

**UNIVERSITÀ DEGLI STUDI DI TRENTO**

**Doctoral School of Physics**

**Dipartimento di Fisica**



---

Tesi di Dottorato di Ricerca in Fisica  
PhD Thesis in Physics

# **Stabilized Optomechanical Systems for Quantum Optics**

**Supervisor**

Prof. G. A. Prodi

**Co-supervisor**

Prof. F. Marin

**Candidate**

Antonio Pontin

DOTTORATO DI RICERCA IN FISICA XXVI CICLO

Trento, March 6th. 2014



# Contents

<b>Introduction</b>	<b>iii</b>
<b>1 Cavity opto-mechanics</b>	<b>1</b>
1.1 Mechanical oscillator . . . . .	1
1.1.1 Classical description . . . . .	1
1.1.2 Quantum description . . . . .	4
1.2 The Fabry-Pérot cavity . . . . .	9
1.2.1 Classical description . . . . .	10
1.2.2 Quantum description . . . . .	14
1.3 Opto-mechanical coupling . . . . .	18
1.3.1 Noise budget . . . . .	27
<b>2 Design and fabrication of low loss MOMS resonators</b>	<b>33</b>
2.1 Design strategy . . . . .	34
2.2 Fabrication . . . . .	45
<b>3 Experimental apparatus</b>	<b>53</b>
3.1 The sample holder . . . . .	56
<b>4 Experimental characterization</b>	<b>59</b>
4.1 Mechanical parameters . . . . .	59
4.2 Optical parameters . . . . .	64
<b>5 Toward squeezed light detection</b>	<b>73</b>
5.1 Frequency noise cancellation . . . . .	73
5.2 Effects of frequency locking on the dynamical backaction . . . . .	85
<b>6 Parametric stabilization of the effective mechanical susceptibility</b>	<b>91</b>
6.1 Parametric control loop model . . . . .	91
6.2 Experimental characterization . . . . .	96

<b>7</b>	<b>Detection of weak stochastic force</b>	<b>105</b>
7.1	Measurement strategies . . . . .	106
7.2	Measurements and data analysis . . . . .	109
<b>8</b>	<b>Squeezing a thermal mechanical oscillator</b>	<b>117</b>
8.1	Stabilized modulation of the optical spring . . . . .	118
8.2	Experimental setup and results . . . . .	121
<b>9</b>	<b>Conclusions and final remarks</b>	<b>127</b>
<b>A</b>	<b>The normal mode expansion</b>	<b>131</b>
<b>B</b>	<b>Additional information on the experimental setup</b>	<b>133</b>
B.1	Laser system . . . . .	133
B.2	The cryostat . . . . .	133
<b>C</b>	<b>The Pound-Drever-Hall technique</b>	<b>135</b>
C.1	Typical noise budget of the cavity frequency locking . . . . .	139
<b>D</b>	<b>General formulas for the homodyne noise spectra</b>	<b>143</b>
	<b>Bibliografia</b>	<b>145</b>

*Is better to remain silent  
and be thought a fool  
than to open one's mouth  
and remove all doubt.*

Mark Twain



# Introduction

The optomechanics field of research has been gathering a lot of momentum during the last couple of years. The technological accomplishments of the last decade have brought a number of very different experimental realizations right on the threshold, or just past it, between classical and quantum visions of reality.

The field was pioneered in the 1970s by Braginsky who investigated the role of radiation pressure coupled to an harmonically suspended end-mirror of a cavity in the context of interferometric gravitational wave detectors. He showed that the radiation pressure can induce damping or anti-damping of the mechanical resonance, an effect that he was able to demonstrate experimentally by using a microwave cavity [1, 2]. He also investigated quantum fluctuations of radiation pressure [3, 4] and, together with later works by Caves (i.e., Ref. [5]), established what is nowadays the standard quantum limit for continuous position detection.

Several theoretical works, published during the 1990s, increased the interest of the scientific community on the field. Many peculiarly quantum phenomena were analyzed. Among these, squeezing of light [6, 7], quantum non-demolition (QND) detection of the light intensity [8], and even the possibility to generate entanglement between the optical and mechanical degrees of freedom [9, 10]. Achieving these results experimentally would provide the means to test quantum mechanics on a macroscopic scale.

However, from an experimental point of view, technological means were not refined enough, at that time, to allow investigation of such phenomena. As a consequence, a race started to develop optomechanical systems with sufficient high performances, typically in terms of losses and mass, to enter the quantum regime. As a result, a large variety of systems have been studied. Among these, thin membranes [11], whispering gallery microdisks [12, 13], photonic crystals [14], micropillars [15] and micro-oscillators [16]. We point out that all these systems reached maturity towards the end of the last decade.

It is only during the last couple of years that some of this quantum phenomena

have been finally observed experimentally: from the direct observation of radiation pressure shot noise [17], to squeezed light generation [18, 19, 20] and to the cooling of the mechanical resonance to its quantum ground state [21]. All these results have opened up the quantum age for the field of optomechanics and opened the way for even more interesting physics such as, for example, the generation of mechanical squeezed states, entanglement (recently observed in a superconducting resonator [22]) and even the possibility to investigate Planck scale physics [23].

In this context, as for all other teams, our effort were initially concentrated on the development of the optomechanical devices. Our progress has been reported in a number of papers, Refs. [24, 25, 26, 27], and we believe that our latest devices present competitive performances. We have worked towards the generation and observation of ponderomotive squeezing and we have identified, and experimentally demonstrated, an optomechanical effect that can ease the achievement of this goal [28]. We have also developed a stabilization technique that have been instrumental for the success of two experiments: the implementation of the Wiener-Kolmogorov data analysis [29] and the squeezing of a mechanical thermal oscillator [30]. In the meanwhile, the research activity for the development of a new generation of devices did not stop; some insight can be found in Ref.[31].

This thesis is structured as follows. In the first chapter we describe from both a classical and a quantum point of view the two building blocks of the optomechanics field, that is, the mechanical and the optical resonators. In particular we discuss the dynamical behavior of such systems subjected to noise and we introduce (quantum) Langevin equations. In its second part, we describe the optomechanical interaction and the physics that derives from it. The model presented here is nowadays well established, it has been used to describe successfully various systems with a very different intrinsic size.

The second chapter is divided into two main sections. In the former we present our design strategy to develop new and competitive devices, while in the latter we focus on their fabrication. As in many of the systems mentioned earlier, the main objective is the reduction of thermal decoherence, that derives from mechanical losses, and that masks, or prevents, the observation of quantum phenomena. We work with relatively thick silicon oscillators with high reflectivity coating. The design and, in particular, the geometry optimization is assisted by numerical simulations based on the finite element method. Our resonators are specifically designed to reach a regime where the dominant loss mechanism, at cryogenic temperatures, is the intrinsic dissipation of silicon. We also show that the developed fabrication process, which integrates the deposition of the high reflectivity coating, does not cause any

degradation of the optical properties of the coating itself.

In Chap. 3 we describe our experimental setup, while in Chap. 4 we present the experimental characterization at room and cryogenic temperatures of the devices whose design and fabrication has been introduced in Chap. 2. We show that, indeed, some of our devices are limited by the mechanical losses of silicon while, at the same time, they present extremely low optical losses. However, some designs presented mechanical performances worse than our expectations. From the experience gained, we present design guidelines for the next generation of devices. We also demonstrate the high reliability of our numerical simulations.

One of the main objectives of the PhD research activity has been the generation of squeezed light. In Chap. 5 we introduce an optomechanical effect that leads to the destructive interference of classical frequency/displacement noise, one of the most detrimental technical noise sources in our system. This effect can strongly facilitate the generation of ponderomotive squeezing for a given set of operating parameters. We demonstrate the effect experimentally and we illustrate its relevance with a detailed theoretical analysis. Despite this identification of the most favorable working point and having developed mechanical resonators with sufficient low losses, we have not yet been able to generate ponderomotive squeezing. In Chap. 5 we discuss why this has been the case.

In Chap. 6 we introduce a novel technique developed to stabilize the effective mechanical susceptibility of the oscillator by direct active control of the optical spring. The scheme implemented affects only one quadrature of the oscillator motion leaving the other unperturbed. We present a theoretical model and the experimental characterization of this parametric feedback. This technique has been instrumental for the realization of the two experiments presented in the following chapters.

In Chap. 7 we study quantitatively the characteristics of our micro opto-mechanical system as detector of stochastic force for short measurement times (for quick, high resolution monitoring) as well as for the longer term observations that optimize the sensitivity. We compare a simple strategy based on the evaluation of the variance of the displacement (that is a widely used technique) with an optimal Wiener-Kolmogorov data analysis. We show that, thanks to the parametric stabilization of the effective susceptibility, we can more efficiently implement Wiener filtering, and we investigate how this strategy improves the performance of our system. We demonstrate the possibility to resolve stochastic force variations well below 1% of the thermal noise.

Finally, in Chap. 8, we report the confinement of an optomechanical micro-oscillator in a squeezed thermal state, obtained by parametric modulation of the

optical spring. We show that the stabilization technique of Chap. 6 can be efficiently used to avoid the onset of the parametric instability of the anti-squeezed quadrature, allowing us to surpass the  $-3\text{ dB}$  limit in the noise reduction, associated with parametric resonance, with a best experimental result of  $-7.4\text{ dB}$ . While the present experiment is in the classical regime, in a moderately cooled system our technique can allow squeezing of a macroscopic mechanical oscillator below the zero-point motion.

# Chapter 1

## Cavity opto-mechanics

In this chapter we will discuss the dynamical behavior of a mechanical oscillator coupled to an optical cavity via radiation pressure. More precisely, we want to arrive, in the end, to a quantum mechanical description of a Fabry-Pérot cavity in which the end mirror is a mechanical oscillator while the input mirror is a standard silica mirror that is supposed to be fixed. Despite this seemingly restricting choice, the results obtained for this system are quite general and can be used to describe more complex ones, like, for example, whispering galleries or photonic crystals, once the peculiarities of such systems are taken into account.

In Sec. 1.1 and Sec. 1.2 we describe the mechanical oscillator and the optical resonator respectively both from a classical and a quantum mechanical point of view. While in Sec. 1.3 we introduce the optomechanical interaction and the quantum dynamical equation for the couple system.

### 1.1 Mechanical oscillator

We are interested in the theoretical description of a realistic mechanical oscillator. In particular we want to describe its dynamical evolution under the action of both deterministic and stochastic forces. The latter are treated in the framework of Langevin equation that we introduce in Sec. 1.1.1 with a classical formalism and with a quantum mechanical one in Sec. 1.1.2.

#### 1.1.1 Classical description

Whatever is the actual opto-mechanical system that one wants to describe, the movable mirror can be considered as a simple harmonic oscillator in most cases.

So let us start discussing the simple lumped element model shown in Fig. 1.1. A massless spring of stiffness  $k$  is connected on one side to an ideal constraint and to a rigid body of mass  $m$  on the other. If  $x(t)$  is the position of the body at time  $t$ , then the equation of motion is:

$$m\ddot{x} = -Kx \quad (1.1)$$

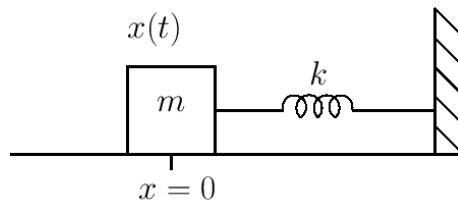


Figure 1.1: *Lumped element model of a mechanical oscillator.*

and the general solution for the free evolution is

$$x(t) = x_0 \cos(\omega_m t + \phi) \quad \text{where} \quad \omega_m = \sqrt{k/m} \quad (1.2)$$

The two parameters,  $x_0$  and  $\phi$ , depend exclusively on the initial conditions  $x(0)$  and  $\dot{x}(0)$ , since no additional external force is considered. The movement of the mirror is an oscillation around the equilibrium position at  $x = 0$  with amplitude  $x_0$  and phase  $\phi$ . The total energy of the system can be calculated as:

$$E_m = \frac{1}{2}m\dot{x}^2 + \frac{1}{2}kx^2 \quad (1.3)$$

it is positive definite and it vanishes for  $x = 0$  and  $\dot{x} = 0$ . The usefulness of this simple model comes from the fact that it is valid for any potential close to a minimum. Its expansion around a stable equilibrium position is equivalent, to the first non-vanishing order, to a quadratic potential. Moreover, it is possible to easily drop the rigid body assumption by means of the Normal Modes Expansion Model [32]. With it, one can forget about the complexity of the dynamics of a three-dimensional body and take into consideration only a limited number of normal modes, if not only one. The mass will be replaced by an *effective mass* that depends on the mode under consideration and on how the displacement is actually measured. For the fundamental mode, however, the effective mass is usually very close to the physical mass. More details can be found in the appendix (Sec. A).

In order to obtain a more realistic model one needs to include the effect of losses and the action of external forces. There are several dissipation mechanisms: clamping losses [33], that are due to the absorption of the oscillator elastic energy

by the environment (constraints, substrate... ); fundamental anharmonic effects such as thermoelastic damping [34], that is, the dissipation of elastic energy into heat. This effect is particularly important in thin structures but is often negligible at cryogenic temperatures; materials-induced losses, that are due to intrinsic defects in the bulk or the surface of the material [35]; at last, viscous damping, that is, energy loss through collisions with the (residual) gas surrounding the oscillator. This mechanism depends strongly on geometry and on the shape of the specific normal mode (see for example Ref. [36]). All these processes add up incoherently so that the total mechanical quality factor is given by  $1/Q_{tot} = \sum Q_i$  with  $i$  identifying individual loss mechanisms.

Let us consider the case of viscous damping. The equation of motion for a single normal mode is

$$\ddot{x}(t) + \gamma_m \dot{x}(t) + \omega_m^2 x(t) = \frac{F_{ext}(t)}{m_{eff}} \quad (1.4)$$

where  $\gamma_m = \omega_m/Q_m$  is the (energy) damping rate while  $F_{ext}(t)$  represents the sum of all external forces acting on the mechanical oscillator. Even when no deterministic force is present, one needs at least to take into consideration stochastic forces. In particular, a term that is always present is the thermal Langevin force.

Since thermal noise is a fundamental noise source it is necessary to discuss it in more details. Assuming thermal equilibrium between the mechanical oscillator and a reservoir at temperature  $T$ , the Langevin force  $F_{th}$  is a stationary Gaussian noise for which the following relations, given by the Fluctuation-Dissipation Theorem (FDT) [37, 38], must hold

$$\begin{aligned} \langle F_{th}(t) \rangle &= 0 \\ \langle F_{th}(t) F_{th}(t') \rangle &= 2k_B T m_{eff} \gamma_m \delta(t - t') \end{aligned} \quad (1.5)$$

-the brackets  $\langle \dots \rangle$  denote the average over the statistical distribution of the noise-

To solve Eq. 1.4 it is convenient to work in the frequency space, thus we define the truncated Fourier transform as

$$x^T(\omega) = \frac{1}{\sqrt{\tau}} \int_0^\tau x(t) e^{i\omega t} dt. \quad (1.6)$$

Averaging over independent realizations of  $x^T(\omega)$  one obtains the spectral density  $\langle |x^T(\omega)|^2 \rangle$ . Now, in the limit of  $\tau \rightarrow \infty$ , under the assumption that  $F_{th}$  is a stationary random process and exploiting the ergodic assumption, the Wiener-Khinchin theorem connects  $\langle |x^T(\omega)|^2 \rangle$  to the Fourier transform of the autocorrelation function, referred to as  $S_{xx}(\omega)$ , also called the Power Spectral Density (PSD).

Using the definition just mentioned, the displacement PSD is given by

$$S_{xx}(\omega) = \int_{-\infty}^{\infty} \langle x(t)x(0) \rangle e^{i\omega t} dt. \quad (1.7)$$

At this point, we can use standard input-output theory for linear time-invariant systems to evaluate the mechanical impulse response function whose Fourier transform<sup>1</sup>, namely the mechanical susceptibility<sup>2</sup>, is

$$\chi(\omega) = \frac{1}{m_{eff}} \frac{1}{(\omega_m^2 - \omega^2) - i\omega\gamma_m} \quad (1.8)$$

so that Eq. 1.7 becomes

$$\begin{aligned} S_{xx}(\omega) &= |\chi(\omega)|^2 \int_{-\infty}^{\infty} \langle F_{th}(t)F_{th}(0) \rangle e^{i\omega t} dt \\ &= |\chi(\omega)|^2 S_{ff,th} \end{aligned} \quad (1.9)$$

where  $S_{ff,th} = 2k_B T m_{eff} \gamma_m$  is evaluated from Eq. 1.5. Looking at Eq. 1.9 is already possible to see that in order to have negligible thermal noise (that is low decoherence) is important to have a high mechanical quality factor. Another important result that can be obtained from Eq. 1.9 is that the area under the spectral peak at  $\omega_m$  gives the variance of the displacement noise, that is

$$\frac{1}{2\pi} \int_{-\infty}^{\infty} S_{xx}(\omega) d\omega = \langle x^2 \rangle. \quad (1.10)$$

In the case of low losses the displacement variance is set by the equipartition theorem, so that  $\langle x^2 \rangle = k_B T / m_{eff} \omega_m^2$

## 1.1.2 Quantum description

When moving to quantum mechanical formalism [39] the physical quantities position  $x$  and momentum  $p$  are replaced by the observables  $\hat{X}$  and  $\hat{P}$  obeying the commutation relation  $[\hat{X}, \hat{P}] = i\hbar$ . Thanks to the principle of equivalence in the Heisenberg representation, the Hamiltonian operator of the system in Fig. 1.1 is obtained by substituting the corresponding observables in the classical expression of the total energy, so that

$$\hat{H}_m = \frac{\hat{P}^2}{2m} + \frac{1}{2} k \hat{X}^2 \quad (1.11)$$

---

<sup>1</sup>Unless otherwise specified the convention used for the Fourier transform is the following:  
 $x(\omega) = \int_{-\infty}^{\infty} x(t) e^{i\omega t} dt$  and  $x(t) = \frac{1}{2\pi} \int_{-\infty}^{\infty} x(\omega) e^{-i\omega t} d\omega$

<sup>2</sup>Note that for an high  $Q_m$  oscillator the near resonance response can be approximated with a Lorentzian curve.

It is convenient to introduce the dimensionless operators  $\hat{x}$  and  $\hat{p}$ , obtained with the normalizations

$$\hat{x} = \sqrt{\frac{m\omega_m}{\hbar}} \hat{X} \quad \hat{p} = \sqrt{\frac{1}{\hbar m\omega_m}} \hat{P} \quad (1.12)$$

satisfying the relation  $[\hat{x}, \hat{p}] = i$ . One can also define the *creation*  $\hat{b}^\dagger$  and *annihilation*  $\hat{b}$  operators as

$$\hat{b} = \frac{1}{\sqrt{2}}(\hat{x} + i\hat{p}) \quad \hat{b}^\dagger = \frac{1}{\sqrt{2}}(\hat{x} - i\hat{p}) \quad (1.13)$$

with commutation relation  $[\hat{b}, \hat{b}^\dagger] = 1$ . Using the latter operators, the Hamiltonian of the system can be rewritten as

$$\hat{H}_m = \hbar\omega_m \left( \hat{b}^\dagger \hat{b} + \frac{1}{2} \right). \quad (1.14)$$

The *number* operator  $\hat{N} = \hat{b}^\dagger \hat{b}$  has the same eigenfunctions as the Hamiltonian and it can be show that its eigenvalues are all the natural numbers. The eigenvalues of the Hamiltonian form a discrete ensemble

$$E_n = \hbar\omega_m \left( n + \frac{1}{2} \right) \quad \text{with} \quad n = 0, 1, 2, \dots \quad (1.15)$$

and corresponding eigenfunctions

$$\psi_n(x) = \frac{1}{\sqrt{2^n n!}} \left( \frac{m\omega_m}{\pi \hbar} \right)^{1/4} e^{-\frac{x^2}{2}} H_n(x) \quad (1.16)$$

where the functions  $H_n(x)$  are Hermite polynomials. The first few eigenfunction are shown in Fig. 1.2. If we denote by  $f_n(x)$  the probability density to find the oscillator between  $x$  and  $x + dx$ , then  $f_n(x) = |\psi_n(x)|^2$ . It is easy to verify that, any given state  $n$ , the mean position  $\langle \hat{X} \rangle_n = \int x f_n(x) dx$  and mean momentum  $\langle \hat{P} \rangle_n = -i \hbar \int f_n d\psi_n$  vanish<sup>3</sup>. On the other hand we can evaluate the root-mean-square value of the position  $\Delta \hat{X}_n$  and of the momentum  $\Delta \hat{P}_n$  for a generic eigenstate  $n$ , and find

$$\begin{aligned} \Delta \hat{X}_n &= \sqrt{\langle \hat{X}^2 \rangle_n - \langle \hat{X} \rangle_n^2} = x_{zpf} \sqrt{\left( n + \frac{1}{2} \right)} \\ \Delta \hat{P}_n &= \sqrt{\langle \hat{P}^2 \rangle_n - \langle \hat{P} \rangle_n^2} = \frac{\hbar}{x_{zpf}} \sqrt{\left( n + \frac{1}{2} \right)} \end{aligned} \quad (1.17)$$

where  $x_{zpf} = \sqrt{\hbar/2m\omega_m}$  is the zero-point motion. From these two equations we can recover, as a consequence of the commutation relation, the Heisenberg inequality

$$\Delta \hat{X} \Delta \hat{P} \geq \frac{\hbar}{2}. \quad (1.18)$$

<sup>3</sup>The eigenfunctions are either symmetric or antisymmetric.

If  $n = 0$ , then equality holds so that the only minimum uncertainty state among the energy eigenstates is the fundamental one. Up until now we have been discussing a

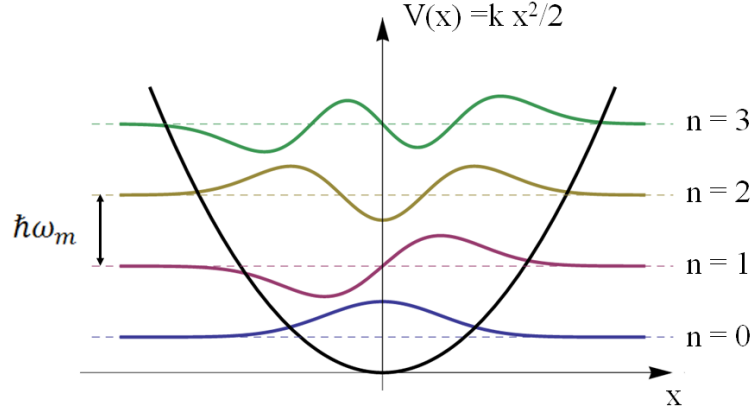


Figure 1.2: Potential energy and contour of the first few eigenfunctions for an harmonic oscillator.

very ideal case. In order to get a more realistic description we need to include in the model some loss mechanism. The first step is to drop the implicit hypothesis that the oscillator is perfectly isolated. A realistic system is always coupled, in some way, to a high (thermal) energy environment. Formally the Hamiltonian of the system is written as  $\hat{H}_m + \hat{H}_{env} + \hat{H}_c$  where

$$\hat{H}_{env} = \sum_i \hbar\omega_i \left( \hat{d}_i^\dagger \hat{d}_i + \frac{1}{2} \right) \quad \hat{H}_c = \sum_i \hbar\kappa_i \hat{d}_i^\dagger \hat{b} + h.c. \quad (1.19)$$

The term  $\hat{H}_{env}$  describes the environment as an infinite ensemble of harmonic oscillators while the term  $\hat{H}_c$  describes the coupling between the two subsystems. Note that this means that a state of the harmonic oscillator is not an eigenstate of the global system. Furthermore, there is never enough information on the environment to allow an analytical description of the system and of its dynamics. The only possible approach is a statistical one.

Assuming thermal equilibrium, the global system state is described with a statistical ensemble of its different eigenstates, characterized by the density operator

$$\hat{\rho} = \frac{1}{Z} e^{-\hat{H}_m/k_B T} \quad (1.20)$$

where  $Z$  is the partition function

$$Z = Tr \left( e^{-\hat{H}_m/k_B T} \right) = \sum_{n=0}^{\infty} e^{-(n+1/2)\hbar\omega_m/k_B T} = \frac{e^{-\hbar\omega_m/2k_B T}}{1 - e^{-\hbar\omega_m/k_B T}} \quad (1.21)$$

from which is possible to calculate the oscillator mean energy at a given temperature  $T$

$$\langle \hat{H}_m \rangle_T = \text{Tr} \left( \hat{H}_m \hat{\rho} \right) = \hbar\omega_m (n_T + 1/2) \quad (1.22)$$

where  $n_T$  is the mean number of thermal phonons of the oscillator and is given by

$$n_T = \frac{1}{e^{\frac{\hbar\omega_m}{k_B T}} - 1} = \frac{1}{2} \coth \left( \frac{\hbar\omega_m}{k_B T} \right) - \frac{1}{2} \quad (1.23)$$

a result quite different from the one obtained with classical statistical physics. Indeed, the equipartition theorem attributes to every degree of freedom an energy contribution of  $\frac{1}{2}k_B T$ . For an harmonic oscillator the kinetic and potential energy sum up to give a mean energy  $\langle H \rangle = k_B T$ . This means that classical and quantum descriptions are equivalent when the temperature is large compared to the *quantum temperature*  $T_Q$ , defined as

$$k_B T_Q = \hbar\omega_m \quad (1.24)$$

while when  $T \ll T_Q$  quantum mechanics predicts a minimum energy, the zero point energy, in keen contrast to the vanishing value predicted by classical physics. This can be seen neatly in Fig. 1.3. At this point we need to discuss how the coupling to the

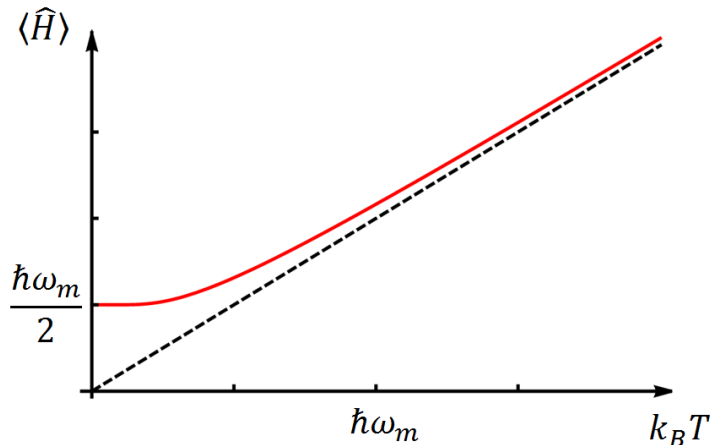


Figure 1.3: Mean energy for an harmonic oscillator as a function of bath temperature. Continuous: quantum evaluation. Dashed: Classical calculation.

reservoir affects the dynamics of the oscillator. This is best done in the framework of the Quantum Langevin Equations (QLEs) [40] that are the generalization to quantum mechanics of the Eq. 1.4 and Eqs. 1.5. A formal derivation of the QLE is outside the scope of this thesis. We will follow Ref. [41] to discuss some key aspects,

in particular concerning the differences with the classical counterpart, but after that, we will assume their validity and directly discuss the results obtained with them.

Eq. 1.4 is the equation of motion of the system that can be retrieved moving to the Heisenberg picture<sup>4</sup>. But, when writing the correlation function  $R_{xx}(t) = \langle \hat{x}(t)\hat{x}(0) \rangle$  is necessary to take into account that the position operator does not commute with itself at different times. Indeed, the correlation function can be expressed as

$$R_{xx}(t) = \langle \hat{x}(0)\hat{x}(0) \rangle \cos(\omega_m t) + \langle \hat{p}(0)\hat{x}(0) \rangle \sin(\omega_m t). \quad (1.25)$$

Classically, the second term in the right hand side (RHS) vanishes since  $x$  and  $p$  are uncorrelated for an oscillator in thermal equilibrium. This is not so in quantum mechanics. Using the commutation relation, one can verify that the cross-correlation term is  $\langle \hat{p}(0)\hat{x}(0) \rangle = -i/2$ , so that, not only is non-vanishing, but is also complex. The correlation then becomes

$$R_{xx}(t) = \frac{1}{2} [n_T e^{i\omega_m t} + (n_T + 1) e^{-i\omega_m t}] \quad (1.26)$$

from which the spectral density can be calculated to be

$$S_{xx}(\omega) = 2\pi x_{xpf}^2 [n_T \delta(\omega + \omega_m) + (n_T + 1) \delta(\omega - \omega_m)] \quad (1.27)$$

where we have restored physical units. Note that this expression is not symmetric in frequency. In the classical case the autocorrelation is always a real function from which follows that  $S_{xx}(\omega)$  is always symmetric in frequency. As expected, in the high temperature limit  $n_T \simeq n_T + 1$  so that classical and quantum predictions coincide. The physical interpretation of this frequency asymmetry can be inferred from the occupation number; the positive frequency part of the spectral density is related to the ability of the oscillator to absorb phonons from the bath, while the negative part is related to the ability to emit phonos<sup>5</sup>. Moreover, when one want to retrieve a classical looking equation that relates a stochastic thermal force noise to a damping term in the equation of motion, it is possible to show that it is the symmetric-in-frequency part of the force noise spectrum  $\bar{S}_{FF}(\omega) = \frac{1}{2}(S_{FF}(\omega) + S_{FF}(-\omega))$  that causes the oscillator to diffuse while the damping rate is proportional to the asymmetric-in-frequency part of the force noise spectrum, that is  $\gamma \propto S_{FF}(\omega) - S_{FF}(-\omega)$ . Note that we introduced the *symmetrized* PSD that for an operator  $\hat{A}(\omega)$  is defined as

$$\bar{S}_{\hat{A}\hat{A}}(\omega) = \frac{1}{2} (S_{\hat{A}\hat{A}}(\omega) + S_{\hat{A}\hat{A}}(-\omega)) \quad (1.28)$$

---

<sup>4</sup>For a generic time independent operator  $\hat{A}$  the equation of motion is  $\dot{\hat{A}}(t) = -\frac{i}{\hbar}[\hat{A}, \hat{H}]$

<sup>5</sup>An even stronger (heuristic) argument for this interpretation resides in the spectral density of the operators  $\hat{b}(t)$  and  $\hat{b}^\dagger(t)$ , since  $S_{\hat{b}\hat{b}}(\omega)$  has a peak centered at  $\omega = -\omega_m$  while for  $S_{\hat{b}^\dagger\hat{b}^\dagger}(\omega)$  the peak is centered at  $\omega = \omega_m$ .

A deeper insight on the physical meaning of the frequency asymmetry and its interpretation can be found again in Ref. [41].

The complete QLEs for a mechanical harmonic oscillator coupled to a thermal bath are given in Eq. 1.29. They retain the familiar form of the classical counterpart, associating a stochastic thermal force to a viscous damping force proportional to the velocity. The complete and rigorous treatment can be found in Ref. [42].

$$\begin{aligned}
 \dot{\hat{x}} &= \omega_m \hat{p} \\
 \dot{\hat{p}} &= -\omega_m \hat{x} - \gamma_m \hat{p} + \xi \\
 \langle \hat{\xi}(t) \rangle &= 0 \\
 \langle \hat{\xi}(t) \hat{\xi}(t') \rangle &= \frac{\gamma_m}{\omega_m} \int \frac{d\omega}{2\pi} e^{-i\omega(t-t')} \omega \left[ \coth \left( \frac{\hbar\omega}{2k_B T} \right) + 1 \right]
 \end{aligned} \tag{1.29}$$

Here,  $\gamma_m$  is the damping rate, as in the classical equation, and  $\hat{\xi}(t)$  is a Gaussian quantum stochastic process; its correlation function, expressed in Eq. 1.29, is given by the quantum FDT. In Fig. 1.4 we show the comparison between quantum and classical predictions for the displacement PSD for three temperature values; for  $T = 0.1 T_Q$  the mean occupation number  $n_T \simeq 0$  and the displacement PSD is given by the zero point fluctuations. The spectra are normalized to the low frequency value calculated for  $T = T_Q$ .

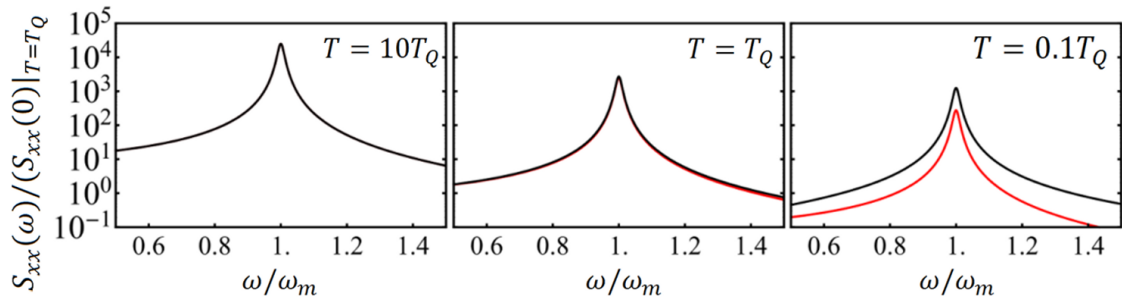


Figure 1.4: Comparison between quantum (black) and classical (red) prediction for the displacement PSD normalized to  $S_{xx}(0)$  evaluated for  $T = T_Q$ .

## 1.2 The Fabry-Pérot cavity

Also in this section we want to keep the parallelism between a classical and a quantum description. As before we start with the former in Sec. 1.2.1 and move to the

latter in Sec. 1.2.2. We are interested in the dynamical equations to describe the Fabry-Pérot resonator under the action of both deterministic and stochastic excitations.

### 1.2.1 Classical description

Consider the simplest cavity composed of two facing partially reflective surfaces with a distance  $L$  between them and an electromagnetic monochromatic plane wave of frequency  $\omega_l$  and with direction of propagation normal to both surfaces. The refractive index, both inside and outside the cavity, is  $n_0 = 1$ . We denote with  $t_i(T_i)$  and  $r_i(R_i)$  the amplitude (power) transmission and reflection coefficients respectively of the  $i$ -th surface and with  $\Sigma_1, \Sigma_2$  the fraction of intensity absorbed or diffused by the surfaces. Conservation of energy requires  $R_i + T_i + \Sigma_i = 1$ . The transmitted and reflected fields are [43]:

$$E_r = E_{in} \left[ -r_1 + \frac{t_1^2 r_2 e^{i2\phi}}{1 - r_1 r_2 e^{i2\phi}} \right] \quad E_t = E_{in} \frac{t_1 t_2 e^{i\phi}}{1 - r_1 r_2 e^{i2\phi}} \quad (1.30)$$

where  $E_{in}$  is the amplitude of the field and  $\phi = L\omega_l/c$  is the phase difference between the fields at the two surfaces. From these two equations it is possible to define the cavity transmission  $\check{T}$  and reflection  $\check{R}$  functions

$$\begin{aligned} \check{T} &= \frac{|E_t|^2}{|E_{in}|^2} = \frac{t_1^2 t_2^2}{(1 - r_1 r_2)^2} \frac{1}{1 + B \sin^2 \phi} \\ \check{R} &= \frac{|E_r|^2}{|E_{in}|^2} = \frac{(\zeta/r_2)^2 + B(1 - \Sigma_1) \sin^2 \phi}{1 + B \sin^2 \phi} \end{aligned} \quad (1.31)$$

where we have defined the coefficient  $B$  and the *coupling parameter*  $\zeta$  as

$$B = \frac{4r_1 r_2}{(1 - r_1 r_2)^2} \quad \zeta = r_2 \frac{r_1 - r_2(r_1^2 + t_1^2)}{1 - r_1 r_2} \quad (1.32)$$

From Eqs. 1.31 we can see that there are resonant peaks (dips) for  $\phi = n\pi$ , and each peak will have a halfwidth  $\kappa_\phi$  defined by

$$4r_1 r_2 \sin^2 \kappa_\phi = (1 - r_1 r_2)^2 \quad (1.33)$$

the distance in frequency between two subsequent peaks is the *Free Spectral Range*<sup>6</sup>  $FSR = c/2L$ , so that we can define  $\kappa_\nu = \kappa/2\pi = \kappa_\phi \frac{FSR}{2\pi}$  and the resonance condition can be expressed as  $\omega_{cav} = 2\pi n FSR$ . The cavity *Finesse* is then  $\mathcal{F} = FSR/2\kappa_\nu$ . The coupling parameter is the fraction of the incident field amplitude that is reflected at resonance. It distinguishes three regimes: for  $0 < \zeta \leq 1$  the cavity is

---

<sup>6</sup>As usual  $c$  is the velocity of light in vacuum.

said *undercoupled*, for  $-1 \leq \zeta < 0$  is *overcoupled* while for  $\zeta = 0$  we have *optimal coupling*.

Particularly important is the case of a cavity with high *Finesse*. This assumption implies  $\kappa_\nu \ll FSR$  and  $(T_i, \Sigma_i) \ll 1$  so that we have

$$\mathcal{F} \simeq \frac{2\pi}{T_1 + T_2 + \Sigma_1 + \Sigma_2} = \frac{2\pi}{T} \quad \zeta \simeq \frac{T_2 - T_1 + \Sigma_1 + \Sigma_2}{T_2 + T_1 + \Sigma_1 + \Sigma_2}. \quad (1.34)$$

The cavity (amplitude) decay rate becomes  $\kappa = cT/4L$  and the transmission and reflection functions of Eqs. 1.31, expressed as a function of the dimensionless detuning  $\Delta_n = \Delta/\kappa = (\omega_l - \omega_{cav})/\kappa$ , can be simplified to

$$\check{T} \simeq \frac{4T_1T_2}{(T_1 + T_2 + \Sigma_1 + \Sigma_2)^2} \frac{1}{1 + \Delta_n^2} \quad \check{R} \simeq \frac{\zeta^2 + \Delta_n^2}{1 + \Delta_n^2}. \quad (1.35)$$

We can also define a reflection response function, that in the high Finesse limit is

$$H^r(\Delta_n) = \frac{E_r}{E_{in}} \simeq \frac{\zeta - i\Delta_n}{1 - i\Delta_n}. \quad (1.36)$$

Moreover, the intracavity power at resonance is  $\mathcal{P}_{cav}(0) = \mathcal{P}_{in} \frac{F}{\pi} (1 - \zeta)$  that gives a clear understanding on the regimes definition according to the coupling parameter. In Fig. 1.5 we show the cavity response function  $\check{T}$  and  $\check{R}$  together with the overall losses  $1 - \check{R} - \check{T}$  for a given set of parameters (see caption). Up until now we used the

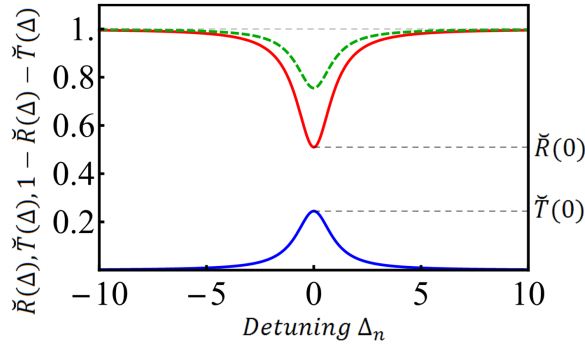


Figure 1.5: *Cavity transmission* ( $\check{T}$ , blue), *reflection* ( $\check{R}$ , red) and *overall losses* ( $1 - \check{R} - \check{T}$ , dashed-green). Values used for the example are  $T_1 = 300ppm$ ,  $T_2 = 25ppm$  and  $\Sigma = \Sigma_1 + \Sigma_2 = 25ppm$ .

plane wave approximation for the input field. A real laser beam is similar in many respects, however its intensity distribution is not uniform but is concentrated near the axis of propagation and its phase fronts are slightly curved. Following Ref.[44], each component of the electric field  $E(x, y, z, t)$  satisfies the scalar wave equation

$$\nabla^2 E + k_0^2 E = 0 \quad (1.37)$$

For a field travelling in the  $z$  direction one writes  $E = \Gamma(x, y, z)e^{-ik_0z}$  where  $\Gamma$  is a slowly varying complex function which represents the difference between a laser beam and a plane wave, that is, a non uniform intensity distribution and its expansion with distance of propagation and the curvature of the phase front. Inserting this expression in the wave equation one obtains

$$\frac{\partial^2}{\partial x^2}\Gamma + \frac{\partial^2}{\partial y^2}\Gamma - 2ik_0\frac{\partial}{\partial z}\Gamma = 0 \quad (1.38)$$

where it has been assumed that  $\Gamma$  varies so slowly with  $z$  that the second derivative  $\partial\Gamma^2/\partial z^2$  can be neglected. We search solutions to Eq. 1.38 of the form

$$\Gamma = \psi(x, y) \cdot \exp\left(-i\left(p(z) + \frac{k_0}{2q(z)}r^2\right)\right) \quad (1.39)$$

where, as usual,  $r^2 = x^2 + y^2$ . Here,  $p(z)$  and  $q(z)$  are complex parameters, the first describing the variation of phase along  $z$  and the beam divergency, the latter describing the variations in beam intensity with the distance  $r$  and the curvature of the phase front.

The solution with  $\psi = \text{constant}$  is the case of a coherent light beam with a Gaussian profile and it is perhaps the most important. For convenience one introduces two real parameters  $R(z)$  and  $w(z)$  related to  $q(z)$  by

$$\frac{1}{q(z)} = \frac{1}{R(z)} - i\frac{\lambda}{\pi w(z)^2} \quad (1.40)$$

$R(z)$  is the radius of curvature of the wavefront the intersects the  $z$ -axis at  $z$  and  $w(z)$  is the decay length of the amplitude with the distance from the axis, called *beam spot*: the intensity profile in every beam cross section is a Gaussian curve with width  $w$ , whose minimum  $w_0$  is called *beam waist*. In Fig. 1.6(left) is shown the physical interpretation of these parameters. For a free propagating beam, setting the waist in  $z = 0$ , we have

$$w^2(z) = w_0^2 \left[1 + \left(\frac{\lambda z}{\pi w_0^2}\right)^2\right] \quad R(z) = z \left[1 + \left(\frac{\pi w_0^2}{\lambda z}\right)^2\right] \quad (1.41)$$

Higher order solutions of Eq. 1.38 are possible and their space profiles are shown in Fig. 1.6(right). In cartesian coordinate  $(x, y, z)$

$$\psi(x, y) = H_m(\sqrt{2}x/w)H_n(\sqrt{2}y/w) \quad (1.42)$$

where  $H_m$  is the  $m$ -th order Hermite polynomial while  $m$  and  $n$  are the (transverse) mode numbers. In cylindrical coordinates  $(r, \phi, z)$

$$\psi(r, \phi) = \left(\sqrt{2}r/w\right)^l \cdot L_p^l[2(r/w)^2] \cdot e^{l\phi} \quad (1.43)$$

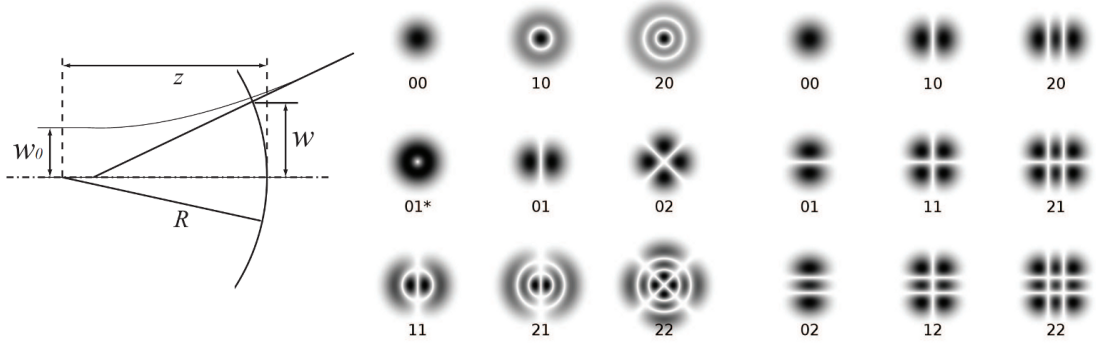


Figure 1.6: *Left: contours of a Gaussian beam and physical interpretation of the parameters  $R(z)$  and  $w(z)$ . Right: Different spatial transverse mode. On the center, Laguerre-Gaussian: labels indicate radial and angular nodes. On the right: Hermite-Gaussian: labels indicate  $x$  and  $y$  nodes.*

where  $L_p^l$  is a generalized Laguerre polynomial while  $p$  and  $l$  are the radial and angular mode numbers respectively. In both cases the parameter  $q$  evolves along  $z$  as it does for a Gaussian beam, while the phase parameter depends on the order of the specific mode.

An ideal lens leaves the transverse field distribution unchanged but modifies the parameters  $R(z)$  and  $w(z)$ . In order to have a resonance in a cavity the beam must return with the same parameters after a roundtrip. This condition is used to calculate the mode parameters that the beam must satisfy in order to be stable inside the resonator. While  $q(z)$  is independent from the mode numbers,  $p(z)$  is not, so that different optical modes resonate at slightly different frequencies. The equations derived in the first part of this section are valid for a Gaussian shaped beam (i.e. the fundamental mode  $TEM_{00}$ ); for higher orders there are increasing deviations [45].

The dynamical equation for the intracavity field is easy to obtain under the assumption of an input field slowly varying on a time scale set by the roundtrip time  $\tau = 2L/c$ , so that  $E(t + \tau) = E(t) + \tau \dot{E}(t)$  is a valid approximation. Considering a high *Finesse* cavity and neglecting losses for the moment, after a roundtrip the intracavity field, in a frame rotating at  $\omega_l$ , is

$$E(t + \tau) = \sqrt{1 - T_1} e^{i\omega_l \tau} E(t) + \sqrt{T_1} E_{in}(t + \tau). \quad (1.44)$$

Applying the approximation just mentioned, expanding the square root in the RHS and assuming  $E_{in}(t + \tau) \simeq E_{in}(t)$  the previous equation became

$$\tau \dot{E}(t) = (-\kappa_\phi + i\psi) E(t) + \sqrt{2\kappa_\phi} E_{in}(t) \quad (1.45)$$

where we used  $\kappa_\phi = T_1/2$  and  $\psi$  is the phase detuning from the cavity resonance, that is  $\omega_l\tau = n2\pi + \psi$ . Note that the phase  $\psi$  could be due either to a mismatch of the cavity length or a mismatch of the light frequency  $\psi = 2\pi \left( \frac{\Delta\nu_0}{FSR} + \frac{\Delta L}{\lambda/2} \right)$ . Eq. 1.45 can be rearranged as

$$\dot{E}(t) = (-\kappa + i\Delta)E(t) + \sqrt{\frac{2\kappa}{\tau}}E_{in}(t) \quad (1.46)$$

where  $\kappa$  is cavity total loss rate. If we drop the assumption of negligible losses, then  $\kappa = \kappa_1 + \kappa_2 + \kappa_\Sigma$ <sup>7</sup> but the input field is still just coupled through the input mirror.

Once solved Eq. 1.46 the reflected and transmitted fields are

$$E_{out}^r(t) = -E_{in}(t) + \sqrt{2\kappa_1}E(t) \quad E_{out}^t(t) = \sqrt{2\kappa_2}E(t) \quad (1.47)$$

## 1.2.2 Quantum description

The quantization of the electromagnetic fields, obtained by expanding the vector potential in terms of cavity modes (see for example [46]), leads to a description based on a simple superposition of independent harmonic oscillators so that quantum states of each mode may be discussed independently. The Hamiltonian of a single cavity mode is

$$\hat{H} = \hbar\omega_{cav} \left( \hat{a}^\dagger \hat{a} + \frac{1}{2} \right) \quad (1.48)$$

with commutation relations appropriate for bosons, that is  $[\hat{a}, \hat{a}] = [\hat{a}^\dagger, \hat{a}^\dagger] = 0$  and  $[\hat{a}, \hat{a}^\dagger] = 1$ . Clearly, Eq. 1.48 is identical to Eq. 1.14. This means that many aspects discussed in the previous section for the mechanical oscillator will remain valid for the cavity mode. However, before moving to the dynamical equation, let us briefly review some key properties of quantum optical fields.

### Some quantum optic basics

In a completely general way, the ensemble of field quadratures can be defined by

$$\hat{a}_\theta = \hat{a}e^{-i\theta} + \hat{a}^\dagger e^{i\theta}. \quad (1.49)$$

The quadrature operators  $\hat{a}_\theta$  and  $\hat{a}_{\theta+\pi/2}$ , aside a global phase factor  $e^{i\theta}$ , allow the identification of the optical phase space with the complex plane with coordinates  $(\langle \hat{a}_\theta \rangle / 2, \langle \hat{a}_{\theta+\pi/2} \rangle / 2)$ . They are analogous to the position  $\hat{x}$  and momentum  $\hat{p}$  operators and since the commutator for  $\hat{a}$  and  $\hat{a}^\dagger$  is non-vanishing there is an Heisenberg

---

<sup>7</sup>Here  $\kappa_i = \frac{cT_i}{4L}$  and  $\kappa_\Sigma = \frac{c\Sigma}{4L}$  with  $\Sigma = \Sigma_1 + \Sigma_2$

inequality imposing a lower bound to the product of their uncertainty, namely

$$\Delta\hat{a}_\theta\Delta\hat{a}_{\theta+\pi/2} \geq 1 \quad (1.50)$$

The eigenstates of the Hamiltonian in Eq. 1.48 are the number or Fock states, in particular, the *vacuum state*, is defined by  $\hat{a}|0\rangle = 0$ . A more appropriate basis for typical optical fields are the *coherent* states. Introduced by Glauber in 1963 [47], these states have an indefinite number of photons which allows them to have a more definite phase than a Fock state where the phase is completely random. Coherent states are generated using the unitary displacement operator  $\hat{D}(\alpha)$ , defined as

$$\hat{D}(\alpha) = \exp(\alpha\hat{a}^\dagger - \alpha^*\hat{a}) \quad (1.51)$$

where  $\alpha$  is a complex number. When  $\hat{D}(\alpha)$  is applied to the vacuum state one obtains

$$|\alpha\rangle = \hat{D}(\alpha)|0\rangle. \quad (1.52)$$

If one calculates the expectation values of the quadrature operators for a coherent state one finds  $\langle\alpha|\hat{a}_\theta|\alpha\rangle = \alpha + \alpha^*$  and  $\langle\alpha|\hat{a}_{\theta+\pi/2}|\alpha\rangle = -i(\alpha - \alpha^*)$  so that  $\alpha = 1/2\langle\hat{a}_\theta + i\hat{a}_{\theta+\pi/2}\rangle = \text{Re}[\alpha] + i\text{Im}[\alpha]$  which makes evident that the state  $|\alpha\rangle$  is merely a translation of the vacuum state to a point  $\alpha$  in phase space. It is easy to verify that for a coherent state  $\Delta\hat{a}_\theta = 1 \forall\theta$ .

In order to better understand the connection between coherent states and laser beams, it is useful to introduce the semiclassical description based on the Wigner distribution. This approximation associate to the generic operators  $\hat{A}$  and  $\hat{A}^\dagger$  two classical pseudo-random variables  $A$  and  $A^*$ , complex conjugate of one another and having a quasi-probability distribution that coincides with the Wigner distribution [46, 48]. In this way, classical and quantum expectation values coincide when the operators are placed in symmetric order. More precisely, for all symmetric functions  $f_S(\hat{A}, \hat{A}^\dagger)$  of the operators  $\hat{A}$  and  $\hat{A}^\dagger$  the quantum expectation value  $\langle f_S(\hat{A}, \hat{A}^\dagger) \rangle = \text{Tr}[f_S(\hat{A}, \hat{A}^\dagger)\hat{\rho}]$  is equal to the mean value  $\overline{f_S(\hat{A}, \hat{A}^\dagger)}$  defined from the semi-classical variables  $A$  and  $A^*$  weighed with the Wigner distribution  $W(A, A^*)$  :

$$\overline{f_S(\hat{A}, \hat{A}^\dagger)} = \int dAdA^* f_S(A, A^*)W(A, A^*) \quad (1.53)$$

The random variable  $A$  completely characterizes the quantum operator  $\hat{A}$ , moreover, it can be decomposed into the sum of its mean value  $\bar{A} = \langle\hat{A}\rangle$  and a fluctuation term  $\delta A = A - \bar{A}$  that derives from the quantum nature of  $\hat{A}$ .

The Wigner distribution for a coherent state is a bivariate Gaussian distribution of the variables  $\alpha_\theta$  and  $\alpha_{\theta+\pi/2}$ , namely, the semi-classical counterpart of the quadratures defined in Eq. 1.49. The distribution is centered in  $\alpha = \frac{1}{2}\langle\alpha_\theta + i\alpha_{\theta+\pi/2}\rangle$ , that

corresponds to the classical amplitude of the field, and has variance equal to 1 for all quadratures (since  $\forall\theta, \Delta\hat{a}_\theta = 1$ ). A possible realization of the quantum field can be written as

$$\check{\alpha} = \sqrt{\bar{I}}e^{i\phi} \quad (1.54)$$

so that  $I = |\check{\alpha}|^2$  is the instantaneous number of photons of the field and  $\phi = \tan^{-1}(\check{\alpha}_{\theta+\pi/2}/\check{\alpha}_\theta)$  is the phase of the field. Upon linearization of Eq. 1.54 around the mean value  $\alpha = \sqrt{\bar{I}}e^{i\bar{\phi}}$  is possible to estimate the fluctuations of the quantum intensity  $\delta I$  and phase  $\delta\phi$ :

$$\delta I = |\alpha| \delta\alpha_{\bar{\phi}} \quad \delta\phi = \frac{1}{2|\alpha|} \delta\alpha_{\bar{\phi}+\pi/2} \quad (1.55)$$

where  $\delta\alpha_{\bar{\phi}}$  are fluctuations parallel to the mean field while  $\delta\alpha_{\bar{\phi}+\pi/2}$  are orthogonal to it. The variance of intensity fluctuations is then  $\Delta I^2 = \bar{I}$  with relative fluctuations  $\Delta I/\bar{I}$  decreasing as  $1/\sqrt{\bar{I}}$ . Since the mean is equal to the variance the statistic is Poissonian, indeed, this is the quantum *shot noise* and is a direct consequence of the discretization of the field. On the other hand, phase variance is inversely proportional to the mean intensity  $\Delta\phi^2 = 1/4\bar{I}$ . Finally, we can recover the phase-intensity Heisenberg inequality

$$\Delta\hat{I}\Delta\hat{\phi} \geq \frac{1}{2} \quad (1.56)$$

for a coherent state the equality holds since both intensity and phase, independently, have the minimum variance.

A more general class of minimum-uncertainty states are the *squeezed states*. In general, a squeezed state may have a sub-shot noise variance in one quadrature. The inequality 1.56 has to hold so that the variance in the other quadrature has to increase accordingly. They can be generated using the unitary squeeze operator

$$S(\varepsilon) = \exp\left(\frac{1}{2}\varepsilon^*\hat{a}\hat{a} - \frac{1}{2}\varepsilon\hat{a}^\dagger\hat{a}^\dagger\right) \quad (1.57)$$

where  $\varepsilon = r e^{2i\varphi}$ , so that  $r$  indicates the strength of the squeezing while  $\varphi$  identifies its direction in the phase space. The squeezed state  $|\alpha, \varepsilon\rangle$  is obtained by first squeezing the vacuum and then displacing it

$$|\alpha, \varepsilon\rangle = D(\alpha)S(\varepsilon)|0\rangle. \quad (1.58)$$

The wigner distribution is a bivariate Gaussian distribution, but in this case the variances are different for the two quadratures. Two special cases are worth discussing. When  $\varphi = \phi$  intensity fluctuations are squeezed while phase fluctuations

are anti-squeezed; viceversa for  $\varphi = \phi + \pi/2$ . If the first case applies, then

$$\Delta I = \sqrt{I} e^{-r} \quad \Delta\phi = \frac{e^r}{2\sqrt{I}} \quad (1.59)$$

where it is evident that the inequality 1.56 holds also in this case. In Fig. 1.7 is shown a schematic representation of a coherent and a squeezed state. The first experimental observation of squeezed light dates back to 1985 [49].

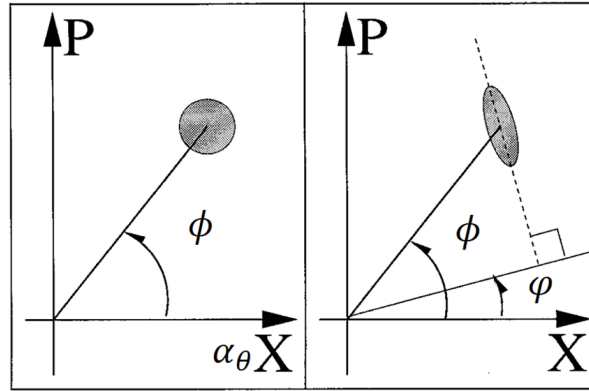


Figure 1.7: *Left: Coherent state. Right: Squeezed state. Here  $X \equiv \alpha_\theta$  and  $P \equiv \alpha_{\theta+\pi/2}$ . The circle and the ellipse are iso-probability curves.*

### Dynamical equation for a quantum Fabry-Pérot cavity

The equation of motion for the intracavity field in a Fabry-Pérot cavity is obtained by moving to the Heisenberg representation of the Hamiltonian of Eq. 1.48, however, as for the mechanical oscillator, for a realistic description of the system dynamics it is necessary to include in the model fluctuation-dissipation processes. Since the Hamiltonian for the optical and mechanical resonators is the same, so could be the treatment in terms of QLEs. The only difference resides in the fact that it is much more convenient to describe the cavity dynamics in terms of the operator  $\hat{a}$  (and  $\hat{a}^\dagger$ ) since coherent states are its eigenstates.

We are interested in the case of a one-sided Fabry-Pérot cavity, since it gives the best description of our experimental setup. This means that we assimilate the output mirror (the oscillator) power transmission coefficient into losses, thus, we define:  $\kappa_e = T_m FSR/2$ , where  $T_m \equiv T_1$ ,  $\kappa_i = \Sigma FSR/2$ , where  $\Sigma = \Sigma_1 + \Sigma_2 + T_2$  and, finally, the cavity amplitude decay rate is  $\kappa = \kappa_e + \kappa_i$ . Assuming a coherent state as input field and in the frame rotating with the laser frequency  $\omega_l$  ( i.e.,

$\hat{a}^{new} = \hat{a}^{old} e^{-i\omega_l t}$ ) the equation of motion for the intracavity field is

$$\begin{aligned} \dot{\hat{a}} &= -(\kappa - i\Delta)\hat{a} + \sqrt{2\kappa_e}\bar{\alpha}_{in} + \sqrt{2\kappa_e}\hat{a}_{in} + \sqrt{2\kappa_i}\hat{a}_{in,v} \\ \langle \hat{a}_n(t)\hat{a}_n(t') \rangle &= \langle \hat{a}_n^\dagger(t)\hat{a}_n^\dagger(t') \rangle = \langle \hat{a}_n^\dagger(t)\hat{a}_n(t') \rangle = 0 \\ \langle \hat{a}_n(t)\hat{a}_n^\dagger(t') \rangle &= \delta(t - t') \quad \text{for } n = in \text{ and } n = in, v \end{aligned} \tag{1.60}$$

Here  $\bar{\alpha}_{in} = \sqrt{\mathcal{P}_{in}/\hbar\omega_l}$  is the input field,  $\mathcal{P}_{in}$  is the incident power,  $\hat{a}_{in}$  are quantum fluctuations coupled to the cavity mode through the input mirror while  $\hat{a}_{in,v}$  is the vacuum input noise describing all other decay channels (optical losses and transmission through the end mirror). To see how the coupling constant ( $\sqrt{\kappa_n}$ ) between the cavity mode and the "photon reservoir" is obtained, look, for example Refs. [50, 51].

Note that the field operators  $\hat{a}$  and  $\hat{a}_{in}$  have a different normalization, the input field is *flux* normalized so that  $\langle \hat{a}_{in}^\dagger \hat{a}_{in} \rangle = \mathcal{P}_{in}/\hbar\omega_l$  while the intracavity field is *number* normalized so that  $\langle \hat{a}^\dagger \hat{a} \rangle = n_c$  is number of photons in the cavity at a given time; this means that the intracavity power is given by  $P_{cav} = \hbar\omega_l n_c/\tau$ . If one compares Eq. 1.60 with the classical counterpart in Eq. 1.46 the only difference that catches the eye is a factor  $\sqrt{\tau}$  that accounts for the different normalizations.

Two final remarks have to be made regarding the correlation functions. First, as already stated they preserve the correct commutation relations between operators during the time evolution. Second, they are formally identical to those involving the creation and annihilation operators of the mechanical oscillators, that is,  $\langle \hat{a}^\dagger(t)\hat{a}(t') \rangle = n_T \delta(t - t')$  and  $\langle \hat{a}(t)\hat{a}^\dagger(t') \rangle = (n_T + 1) \delta(t - t')$ , but at optical frequencies  $n_T \simeq 0$  so that the correlation functions reduce to those listed in Eq. 1.60. Moreover, the cavity mode has more than one decay channel.

### 1.3 Opto-mechanical coupling

In this section we are going to write the quantum mechanical equations to describe the opto-mechanical interaction. As stated in the previous section we are interested in a one-sided Fabry-Pérot cavity. The mechanical oscillator is also the end mirror of the cavity so that it feels the radiation pressure force  $F = 2P/c$  exerted by the intracavity field. Under the action of this force, the cavity length changes from  $L$  to  $L + X$  and in turn the intracavity power is modified since the resonance condition is different. We have already seen the dependence of detuning on length variations. With these two simple considerations it is already possible to write the coupled equations that describe the system in the semiclassical approximation but, since we

have already laid the groundwork, we will directly move to the quantum mechanical case.

In the following we will assume that the mechanical oscillator motion is slow compared to the round trip time of a photon in the cavity (*adiabatic approximation*). In this way it is possible to keep considering only one optical mode. The Hamiltonian operator for the coupled system is

$$\hat{H} = \hbar\omega_{cav}(X)\hat{a}^\dagger a + \hbar\omega_m \left( \hat{b}^\dagger \hat{b} + \frac{1}{2} \right). \quad (1.61)$$

The cavity resonance frequency is modulated by the (small) motion of the mirror, in other words the coupling is parametric. Note that the  $1/2$  term for the optical mode is missing. The reasons are two: first, when moving to the Heisenberg representation its contribution disappears. Note that the same apply to the mechanical mode; second, a more formal derivation (see Ref. [52]) shows that it gives rise to a Casimir term when one accounts for the different density of optical modes inside and outside the cavity. This term, however, can be safely neglected for most opto-mechanical experiments up to date.

Since generally one can safely assume small displacements compared to the cavity length, we can expand  $\omega_{cav}(X)$

$$\omega_{cav}(X) \approx \omega_{cav} + X \frac{\partial \omega_{cav}(X)}{\partial X} + \dots \quad (1.62)$$

generally it is enough to keep the linear term. For the simple cavity we are considering  $\partial \omega_{cav}(X)/\partial X = -\omega_{cav}/L$ , reflecting the fact that we are defining  $X > 0$  for an increase of the cavity length that in turn leads to a decrease in  $\omega_{cav}$ . The Hamiltonian in Eq. 1.61 can be written as

$$\hat{H} = \hbar\omega_{cav}\hat{a}^\dagger a + \frac{1}{2}\hbar\omega_m (\hat{x}^2 + \hat{p}^2) - \hbar g_0 \hat{x} \hat{a}^\dagger a \quad (1.63)$$

where we have defined  $g_0 = \sqrt{2}x_{zpf}\omega_{cav}/L$ . In the previous equation it is easy to identify the interaction Hamiltonian as

$$\hat{H}_{int} = -\hbar g_0 \hat{x} \hat{a}^\dagger \hat{a} \quad (1.64)$$

where it is possible to see that the cavity opto-mechanical interaction is fundamentally a nonlinear process. The radiation pressure force, then, is given by  $\hat{F} = -d\hat{H}_{int}/d\hat{X}$ .

As in the previous sections, it is necessary to include in the description dissipative contributions, both optical and mechanical, and the driving by an external laser,  $\alpha_{in}$ ,

described as a coherent state. We just need to add to the QLEs in Eqs. 1.29 and Eqs. 1.60 the coupling term obtained from Eq. 1.64. In the frame rotating at the laser frequency  $\omega_l$  the coupled equations of motion are

$$\begin{aligned}\dot{\hat{x}} &= \omega_m \hat{p} \\ \dot{\hat{p}} &= -\omega_m \hat{x} - \gamma_m \hat{p} + g_0 \hat{a}^\dagger \hat{a} + \xi \\ \dot{\hat{a}} &= -[\kappa - i(\Delta_0 + g_0 \hat{x})] \hat{a} + \sqrt{2\kappa_e} \bar{\alpha}_{in} + \sqrt{2\kappa_e} \hat{a}_{in} + \sqrt{2\kappa_i} \hat{a}_{in,v}\end{aligned}\quad (1.65)$$

with correlation functions at temperature T

$$\begin{aligned}\langle \hat{a}_n(t) \hat{a}_n(t') \rangle &= \langle \hat{a}_n^\dagger(t) \hat{a}_n^\dagger(t') \rangle = \langle \hat{a}_n^\dagger(t) \hat{a}_n(t') \rangle = 0 \\ \langle \hat{a}_n(t) \hat{a}_n^\dagger(t') \rangle &= \delta(t - t') \quad \text{for } n = in \text{ and } n = in, v \\ \langle \hat{\xi}(t) \rangle &= 0 \\ \langle \hat{\xi}(t) \hat{\xi}(t') \rangle &= \frac{\gamma_m}{\omega_m} \int \frac{d\omega}{2\pi} e^{-i\omega(t-t')\omega} \left[ \coth\left(\frac{\hbar\omega}{2k_B T}\right) + 1 \right]\end{aligned}\quad (1.66)$$

where  $\Delta_0$  is the detuning for a vanishing optomechanical coupling. All noise terms considered are unavoidable fundamental noise sources. However in a realistic scenario two additional technical noises can play a relevant role: (i) amplitude noise, which is taken into account assuming  $\bar{\alpha}_{in} \rightarrow \bar{\alpha}_{in} + \alpha_I(t)$ , where  $\alpha_I(t)$  is a real, zero-mean Gaussian stochastic variable; (ii) phase/frequency noise, which is caused both by the laser frequency fluctuations, and by the fluctuations of the cavity length (and therefore of its resonance frequency) which are not due to the considered mode of the mechanical resonator. The latter are typically much more relevant and can be described writing  $\omega_l - \omega_{cav} \rightarrow \Delta_0 + \dot{\phi}(t)$ , where  $\dot{\phi}(t)$  is a zero-mean frequency noise. As a consequence eqs. 1.65 become

$$\begin{aligned}\dot{\hat{x}} &= \omega_m \hat{p} \\ \dot{\hat{p}} &= -\omega_m \hat{x} - \gamma_m \hat{p} + g_0 \hat{a}^\dagger \hat{a} + \xi \\ \dot{\hat{a}} &= -\left[\kappa - i\left(\Delta_0 + \dot{\phi} + g_0 \hat{x}\right)\right] \hat{a} + \sqrt{2\kappa_e} \bar{\alpha}_{in} \\ &\quad + \sqrt{2\kappa_e} \alpha_I + \sqrt{2\kappa_e} \hat{a}_{in} + \sqrt{2\kappa_i} \hat{a}_{in,v}\end{aligned}\quad (1.67)$$

Amplitude noise acts as additive noise on the cavity modes, while frequency noise is a multiplicative noise, affecting the cavity field in the same manner of the fluctuations of the resonator position  $\hat{x}$ .

We want to generate and manipulate optical quantum fluctuations and therefore we consider the motion of the system around a steady state characterized by the intracavity electromagnetic field in an approximate coherent state of amplitude  $\alpha_s$ , and the micro-oscillator at a new position  $x_s$ , by writing:

$$\hat{x} = x_s + x \quad \hat{p} = p_s + p \quad \hat{a} = \alpha_s + a \quad (1.68)$$

Substituting Eqs. 1.68 in Eq. 1.67, and retaining only the 0 – *th* order contributions one gets

$$p_s = 0 \quad x_s = \frac{g_0}{\omega_m} |\alpha_s|^2 \quad \alpha_s = \frac{\sqrt{2\kappa_e}}{\kappa - i\Delta} \bar{\alpha}_{in} \quad (1.69)$$

where  $\Delta = \Delta_0 + g_0^2 |\alpha_s|^2 / \omega_m$ . The exact QLE for the fluctuation operators  $x, p$  and  $a$  are given by

$$\begin{aligned} \dot{x} &= \omega_m p \\ \dot{p} &= -\omega_m x - \gamma_m p + g_0(\alpha_s a^\dagger + \alpha_s^* a) + \xi + g_0 a^\dagger a \\ \dot{a} &= -(\kappa - i\Delta)a + i g_0 \alpha_s x + i \alpha_s \dot{\phi} + i g_0 x a + i \dot{\phi} a \\ &\quad + \sqrt{2\kappa_e}(\alpha_I + a_{in}) + \sqrt{2\kappa_e} a_{in,v} \end{aligned} \quad (1.70)$$

The nonlinear terms are  $g_0 a^\dagger a$ ,  $i g_0 x a$  and  $i \dot{\phi} a$ . The first two terms have negligible effect when  $|\alpha_s| \gg 1$ , which is usually satisfied, and therefore they can be safely neglected. The last term is a multiplicative noise term and it is not obvious if and when it can be neglected since its evaluation requires the knowledge (or realistic hypotheses) of the frequency and displacement noise spectrum on a wide frequency range. Its treatment is outside the purpose of this thesis and we shall neglect this last term in the following. Keeping only linear terms Eqs. 1.70 become

$$\begin{aligned} \dot{x} &= \omega_m p \\ \dot{p} &= -\omega_m x - \gamma_m p + g_0(\alpha_s a^\dagger + \alpha_s^* a) + \xi \\ \dot{a} &= -(\kappa - i\Delta)a + i g_0 \alpha_s x + \sqrt{2\kappa_e} \tilde{a}_{in} + \Xi \end{aligned} \quad (1.71)$$

where we have introduced two noise terms

$$\begin{aligned} \Xi &= i \alpha_s \dot{\phi} + \sqrt{2\kappa_e} a_{in,v} \\ \tilde{a}_{in} &= a_{in} + \alpha_I \end{aligned} \quad (1.72)$$

describing all detrimental fluctuations acting on the cavity field. At this point we can use Eq. 1.47 to evaluate the reflected field, that is,  $a_{out} = -\tilde{a}_{in} + \sqrt{2\kappa_e} a$ . Taking the Fourier transform of Eqs. 1.71 and solving for  $a(\omega)$  and  $x(\omega)$  one gets

$$\begin{aligned} a_{out}(\omega) &= A_1(\omega) \tilde{a}_{in}(\omega) + A_2(\omega) \tilde{a}_{in}^\dagger(\omega) \\ &\quad + A_3(\omega) \Xi(\omega) + A_4(\omega) \Xi^\dagger(\omega) + A_T(\omega) \xi(\omega) \\ x(\omega) &= B_1(\omega) \left( \sqrt{2\kappa_e} \tilde{a}_{in}^\dagger + \Xi^\dagger \right) + B_2(\omega) \left( \sqrt{2\kappa_e} \tilde{a}_{in} + \Xi \right) \\ &\quad + \chi_{eff}(\omega) \xi(\omega) \end{aligned} \quad (1.73)$$

where we have defined the transfer functions

$$\begin{aligned}
 A_1(\omega) &= \left[ -1 + \frac{2\kappa_e}{K(\omega)} \left( 1 + i g_0^2 |\alpha_s|^2 \frac{\chi_{eff}(\omega)}{K(\omega)} \right) \right] \\
 A_2(\omega) &= \frac{2\kappa_e}{K(\omega)} \left[ i g_0^2 \alpha_s^2 \frac{\chi_{eff}(\omega)}{K^*(-\omega)} \right] \\
 A_3(\omega) &= \frac{\sqrt{2\kappa_e}}{K(\omega)} \left[ 1 + i g_0^2 |\alpha_s|^2 \frac{\chi_{eff}(\omega)}{K(\omega)} \right] \\
 A_4(\omega) &= \frac{1}{\sqrt{2\kappa_e}} A_2(\omega) \\
 A_T(\omega) &= \frac{\sqrt{2\kappa_e}}{K(\omega)} [i g_0 \alpha_s \chi_{eff}(\omega)] \\
 B_1(\omega) &= g_0 \alpha_s \frac{\chi_{eff}(\omega)}{K^*(-\omega)} \\
 B_2(\omega) &= g_0 \alpha_s^* \frac{\chi_{eff}(\omega)}{K(\omega)}
 \end{aligned} \tag{1.74}$$

with  $K(\omega) = \kappa - i(\Delta + \omega)$  and where

$$\chi_{eff}(\omega) = \omega_m \left[ \omega_m^2 - \omega^2 - i \gamma_m \omega + i \omega_m g_0^2 |\alpha_s|^2 \left( \frac{1}{K^*(-\omega)} - \frac{1}{K(\omega)} \right) \right]^{-1} \tag{1.75}$$

is the effective mechanical susceptibility modified by the opto-mechanical coupling.

At this point we are finally ready to discuss some key aspects of the opto-mechanical interaction.

### Bistability

When looking at the steady state solution expressed in Eqs. 1.69 it is possible to verify that trying to calculate the mean number of photons in the optical mode one ends up with a third-degree equation, that is

$$\bar{n}_c \left( \kappa^2 + \Delta_0^2 + \frac{2g_0^2 \Delta_0}{\omega_m} \bar{n}_c + \frac{g_0^4}{\omega_m^4} \bar{n}_c^2 \right) = 2\kappa_e |\alpha_{in}|^2. \tag{1.76}$$

This means that above a certain threshold the system shows a bistable behavior. This is due to the radiation pressure force that modifies the potential felt by the mechanical oscillator to the point where it shows two minima. Note that the same effect can be generated by photothermal forces [53].

### Dynamical backaction

For a given detuning of the input field from the cavity resonance, the intracavity field exerts a radiation pressure force on the mechanical oscillator. Under the action

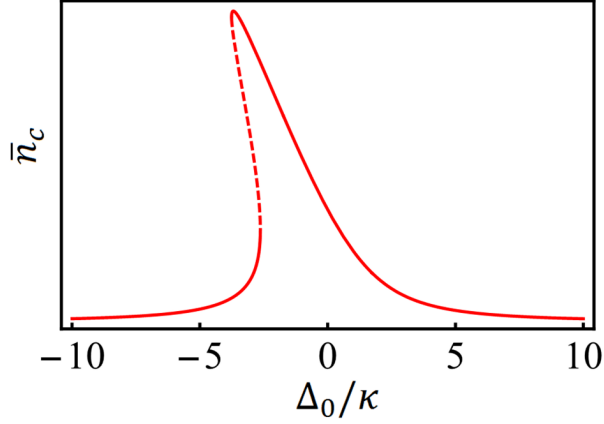


Figure 1.8: *Opto-mechanical bistability.* The curve represents the mean number of intracavity photons  $\bar{n}_c$  as a function of the dimensionless empty cavity detuning  $\Delta_0/\kappa$ . Dashed line indicates the unstable region.

of this force the mean position of the oscillator is changed, in turn this modifies the optical resonance and thus the intracavity power and the radiation pressure that goes with it. This closed loop effect, usually referred to as *dynamical backaction*, is completely described in the definition of the effective mechanical susceptibility in Eq. 1.75. The intracavity field essentially modifies the spring constant felt by the mechanical oscillator. Indeed, we can define the *optical spring* [54, 55] as

$$\begin{aligned}
 K_{opt} &= m \omega_{opt}^2 = m \operatorname{Re} \left[ i \omega_m g_0^2 |\alpha_s|^2 \left( \frac{1}{K^*(-\omega)} - \frac{1}{K(\omega)} \right) \right] \\
 &= 2m \omega_m g_0^2 |\alpha_s|^2 \Delta \frac{\kappa^2 + \Delta^2 - \omega^2}{(\kappa^2 + \Delta^2 - \omega^2)^2 + 4\kappa^2 \omega^2}
 \end{aligned} \tag{1.77}$$

The sign of the optical spring depends on the detuning  $\Delta$  of the input field. When  $\Delta < 0$  (red-detuned) the mechanical spring is "softened" so that the effective mechanical resonance frequency decreases, viceversa, for  $\Delta > 0$  (blue-detuned) the mechanical spring is "hardened".

Moreover, since the cavity field has finite response time, the radiation pressure force will be out phase with the mechanical oscillator motion. As for the optical spring, the sign of this phase depends on the detuning so that the mechanical resonance is *cooled* for  $\Delta < 0$  and is *heated* for  $\Delta > 0$ . Looking again at Eq. 1.75 we

can define the optical damping rate as

$$\begin{aligned}\gamma_{opt} &= -\frac{1}{\omega} \text{Im} \left[ i\omega_m g_0^2 |\alpha_s|^2 \left( \frac{1}{K^*(-\omega)} - \frac{1}{K(\omega)} \right) \right] \\ &= -\frac{4\omega_m g_0^2 |\alpha_s|^2 \kappa \Delta}{(\kappa^2 + \Delta^2 - \omega^2)^2 + 4\kappa^2 \omega^2}\end{aligned}\quad (1.78)$$

so that the total mechanical damping rate becomes

$$\gamma_{om} = \gamma_m + \gamma_{opt} \quad (1.79)$$

the mechanical effective susceptibility can be written as

$$\chi_{eff}(\omega) = \frac{\omega_m}{(\omega_m^2 + \omega_{opt}^2 - \omega^2 - i\omega\gamma_{om})}. \quad (1.80)$$

A clean experimental evidence of these two effects in an opto-mechanical cavity was reported in 2006 by Arcizet *et al.* [56]. In Fig. 1.9 it is possible to see the dependance on the detuning of  $\gamma_{om}$  and of the frequency shift induced by the optical spring, for different values of input power. Note that, when  $\gamma_{om}$  vanishes, the system experiences a parametric instability: any fluctuation grows exponentially up to a saturation value, leading to an oscillation of the mirror at constant amplitude. This effect is also referred to as *self-induced oscillations* (or "*mechanical lasing*"). This instability can be detrimental if one needs to work at small detunings. When the opto-mechanical coupling (or the input power) is strong enough, the minimum achievable detuning will be limited by the combined effect of frequency and displacement noise since, under the action of these noise sources, the oscillator can move to the unstable region even if the mean position is well outside it. For a given detuning, the ratio between frequency shift and optical damping rate depends on the ratio  $\omega_m/\kappa$ : in the *resolved sideband* regime ( $\kappa \ll \omega_m$ ) the backaction effect manifests strongly on the optical damping rate with negligible frequency shift, and viceversa in the *bad cavity* regime ( $\kappa \gg \omega_m$ ).

As for the case of active feedback cooling, the effect of the dynamical back action can be viewed as a change in the thermal bath temperature. We define the *effective temperature*, assuming small frequency shifts, as

$$T_{eff} \simeq T_{init} \frac{\gamma_m}{\gamma_{om}} = T_{init} \frac{1}{1+C} \quad (1.81)$$

where we have introduced the *cooperativity*  $C = \gamma_{opt}/\gamma_m$ , a parameter often used as a figure of merit. Note that this expression derives from classical mechanics and it ceases to be valid for sufficiently low  $T_{eff}$ . A complete quantum mechanical treatment can be found in Ref. [57].

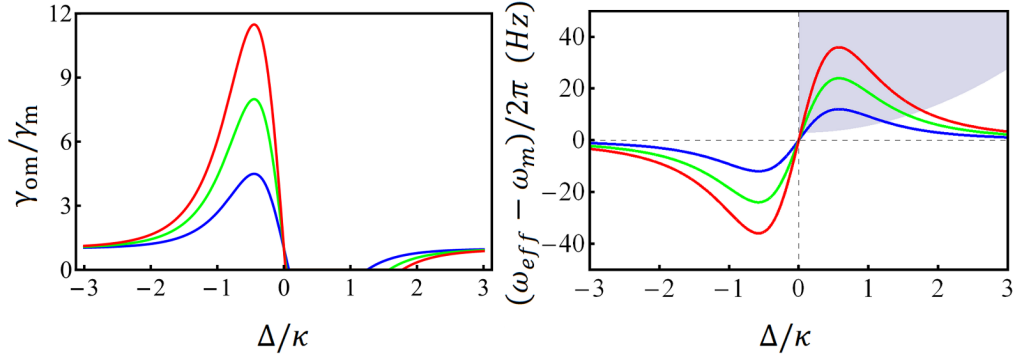


Figure 1.9: *Opto-mechanical damping ratio (left) and frequency shift (right) as a function of the dimensionless empty cavity detuning  $\Delta/\kappa$  for three values of input power. Shaded area corresponds to the unstable domain.*

### Noise properties of the output field quadratures

Another way to see the opto-mechanical backaction starts from the consideration that, in a Fabry-Pérot cavity, displacement and frequency or phase noise are completely undistinguishable so that amplitude fluctuations of the cavity fields generate phase fluctuations (through the mirror motion) that in turn affect amplitude fluctuations. This means that amplitude and phase fluctuations are correlated. In practice, the same process that gives rise to the optical spring and the cooling/heating of the mechanical resonance can generate squeezing. In other words, the output field can present a sub-shot noise statistic. This effect is usually referred to as *ponderomotive squeezing* [6, 7].

The noise spectrum of the quadrature at phase  $\theta$  is defined as

$$2\pi S_{out}^{\theta}(\omega)\delta(\omega + \omega') = \langle a_{\theta}(\omega)a_{\theta}(\omega') \rangle \quad (1.82)$$

where  $a_{\theta}$  is given by Eq. 1.49. Since we are using the correlation functions in the Fourier domain, it is useful to write them here (the non-null ones), even if they are derived from Eq. 1.66. For quantum operators we have

$$\begin{aligned} \langle a_{in}(\omega)a_{in}^{\dagger}(\omega') \rangle &= 2\pi \delta(\omega + \omega') \\ \langle a_{in,v}(\omega)a_{in,v}^{\dagger}(\omega') \rangle &= 2\pi \delta(\omega + \omega') \\ \langle \xi(\omega)\xi(\omega') \rangle &= 2\pi \delta(\omega + \omega') \frac{\gamma_m}{\omega_m} \omega \left[ \coth \left( \frac{\hbar\omega}{2k_B T} + 1 \right) \right]. \end{aligned} \quad (1.83)$$

For the two technical noise sources, we will assume a white noise spectrum. Even if in most experimental system this is not the case, as we will see, we are interested

in a relatively small frequency band centered around the mechanical resonance so that the white noise assumption is a good approximation. The correlation functions in the Fourier domain for the additional amplitude and frequency noise are

$$\begin{aligned}\langle \dot{\phi}(\omega)\dot{\phi}(\omega') \rangle &= 2\pi S_{\dot{\phi}\dot{\phi}} \delta(\omega + \omega') \\ \langle \alpha_I(\omega)\alpha_I(\omega') \rangle &= 2\pi S_{\alpha_I\alpha_I} \delta(\omega + \omega').\end{aligned}\tag{1.84}$$

At this point we have all that we need, we just have to substitute Eq. 1.73 into Eq. 1.49 and calculate  $\langle a_\theta(\omega)a_\theta(\omega') \rangle$ . After some algebraic manipulations one finds

$$\begin{aligned}S_{out}^\theta(\omega) &= S_{a_{in}}(\omega) [|A_1(\omega)|^2 + |A_2(-\omega)|^2 + 2Re [A_1(\omega)A_2(-\omega) e^{-2i\theta}]] \\ &\quad + S_{a_{in,v}}(\omega) 2\kappa_i [|A_3(\omega)|^2 + |A_4(-\omega)|^2 + 2Re [A_3(\omega)A_4(-\omega) e^{-2i\theta}]] \\ &\quad + S_{\xi\xi}(\omega) [|A_T(\omega)|^2 + |A_T(-\omega)|^2 + 2Re [A_T(\omega)A_T(-\omega) e^{-2i\theta}]] \\ &\quad + S_{\alpha_I\alpha_I}(\omega) |\eta_1(\omega)e^{-i\theta} + \eta_1^*(-\omega)e^{i\theta}|^2 \\ &\quad + S_{\dot{\phi}\dot{\phi}}(\omega) |\eta_2(\omega)e^{-i\theta} + \eta_2^*(-\omega)e^{i\theta}|^2\end{aligned}\tag{1.85}$$

where we have defined  $\eta_1(\omega) = A_1(\omega) + A_2(\omega)$  and  $\eta_2(\omega) = i\alpha_s A_3(\omega) - i\alpha_s^* A_4(\omega)$ . Generally the only measurable quantity is the symmetrized spectral density. Using the definition in Eq. 1.28, we have  $\bar{S}_{out}^\theta(\omega) = (S_{out}^\theta(\omega) + S_{out}^\theta(-\omega)) / 2$  from which it is possible to evaluate the angle  $\theta_{min}(\omega)$  that minimizes the quadrature spectrum at every frequency, that is

$$\theta_{min}(\omega) = \frac{1}{2} \arctan \left[ \frac{2\bar{S}_{out}^{\pi/4}(\omega) - \bar{S}_{out}^0(\omega) - \bar{S}_{out}^{\pi/2}(\omega)}{\bar{S}_{out}^0(\omega) - \bar{S}_{out}^{\pi/2}(\omega)} \right]\tag{1.86}$$

and using  $\theta = \theta_{min}(\omega)$  in Eq. 1.85 one can calculate the minimum attainable PSD  $S_{min}(\omega)$ . With our normalizations the output quadrature is squeezed at the frequency  $\omega$  if  $S_{min}(\omega) < 1$ . The first observation of squeezed light generated thanks to the opto-mechanical interaction has been reported by Brooks *et al.* in 2012 [18] who exploited an experimental setup where the role of the mechanical oscillator was played by a cloud of ultra-cold atoms. The same result has been obtained with a macroscopic mechanical oscillator (a photonic crystal) by Chan *et al.* in 2013 [19] and, later on, an even stronger squeezing has been reported by Purdy [20] *et al.*

## Displacement spectrum

The total displacement Spectrum can be evaluate from Eqs. 1.73, Eqs. 1.74 and the definitions of the correlation functions for the various noise sources given previously.

We are going to separate the total spectrum into three contributions:  $S_{th}(\omega)$  due to thermal noise,  $S_q(\omega)$  due to quantum fluctuations of the intracavity field and  $S_{cl}(\omega)$  due to classical amplitude and frequency noise. These can be calculated to be

$$\begin{aligned}
 S_{th}(\omega) &= |\chi_{eff}(\omega)|^2 S_{\xi}(\omega) \\
 S_q(\omega) &= 2\kappa_e |B_2(\omega)|^2 S_{a_{in}}(\omega) + 2\kappa_i |B_2(\omega)|^2 S_{a_{in,v}}(\omega) \\
 S_{cl}(\omega) &= |i\alpha_s B_2(\omega) - i\alpha_s^* B_1(\omega)|^2 S_{\dot{\phi}\dot{\phi}}(\omega) \\
 &\quad + 2\kappa_e |B_1(\omega) + B_2(\omega)|^2 S_{\alpha_I \alpha_I}(\omega)
 \end{aligned} \tag{1.87}$$

with

$$S_{xx}(\omega) = S_{th}(\omega) + S_q(\omega) + S_{cl}(\omega)$$

where, to restore physical unit, one just multiplies  $S_{xx}(\omega)$  by  $2x_{zpf}^2$ . The term  $S_{th}(\omega)$  of the cooled(heated) mechanical resonance, with the right parameters set, can be extremely close to what one would expect from just the zero point motion. The first experimental evidence of a mechanical oscillator on its ground state in an opto-mechanical cavity has been reported only in 2011 by Chan *et al.* [21]. The term  $S_q(\omega)$  represents the effect of the radiation pressure shot noise (RPSN) that can excite the mechanical resonance and in principle give a contribution dominant with respect to thermal force noise. The first direct observation of its effects in an optomechanical cavity has been reported in 2013 by Purdy *et al.* [17].

### 1.3.1 Noise budget

In this section we want to discuss the different contributions of the various noise sources to the quadrature of the reflected field and the displacement spectrum of the mechanical oscillator. To do this, we are going to use opto-mechanical parameters that are relevant to our experimental setup, as we will show in the next chapters. For the mechanical oscillator these are: effective mass  $m = 10^{-7} Kg$ , resonance frequency  $\omega_m/2\pi = 10^5 Hz$  and a quality factor of  $Q = 10^6$ . As for the optical parameters, we are going to consider an input field of wavelength  $\lambda = 1064 nm$  with power  $\mathcal{P}_{in} = 1 mW$ , a cavity of length  $L_{cav} = 0.5 mm$  with optimal coupling, that is  $\zeta = 0$ , and power transmission coefficients  $T_m = T_l = 50 ppm$ , where  $T_l$  includes optical losses due to absorption, diffusion and transmission through the end mirror (oscillator). With these parameters we are considering  $FSR = 300 GHz$  and a cavity half-linewidth  $\kappa/2\pi = 2\kappa_e/2\pi = 2\kappa_i/2\pi = 2.4 MHz$  so that the optical Finesse is  $\mathcal{F} \simeq 63000$ .

We also need to define the spectral densities of the noise sources. With our normalization the shot noise is  $S_{a_{in}}(\omega) = S_{a_{in,v}}(\omega) = 1$ ; for thermal noise we will assume

thermal equilibrium with a bath at the liquid Helium temperature  $T_{bath} = 4.2 K$ . As for the classical amplitude noise we consider an input power PSD that is  $3dB$  over the shot noise at  $\mathcal{P}_0 = 20 mW$ , meaning that we have  $S_{\alpha_I \alpha_I}(\omega) = \mathcal{P}_{in}/4\mathcal{P}_0$ . The overall frequency noise is a combination of displacement noise due to other modes of the system not directly included in the model and the actual excess frequency noise of the input field. We assume for the former  $S_{\dot{\phi}}^{disp}(\omega) = g_0^2 (5 \cdot 10^{-35} m^2/Hz) (rad/s)^2/Hz$  while for the latter we use  $S_{\dot{\phi}}^{\alpha_{in}}(\omega) = 0.5 Hz^2/Hz$ . The total frequency noise PSD is then  $S_{\dot{\phi}}(\omega) = S_{\dot{\phi}}^{disp}(\omega) + (2\pi)^2 S_{\dot{\phi}}^{\alpha_{in}}(\omega)$ . The remaining free parameters are the detuning and the angle  $\theta$  that defines the quadrature we want to analyze. We fix the former to  $\Delta_n = \Delta/\kappa = -0.01$ , in this way the mechanical resonance is cooled and shifted to lower frequencies. The latter is fixed at  $\theta_n = \theta_{min}(\omega_m) = -18 mrad$ . Note that all given spectral densities are bilateral.

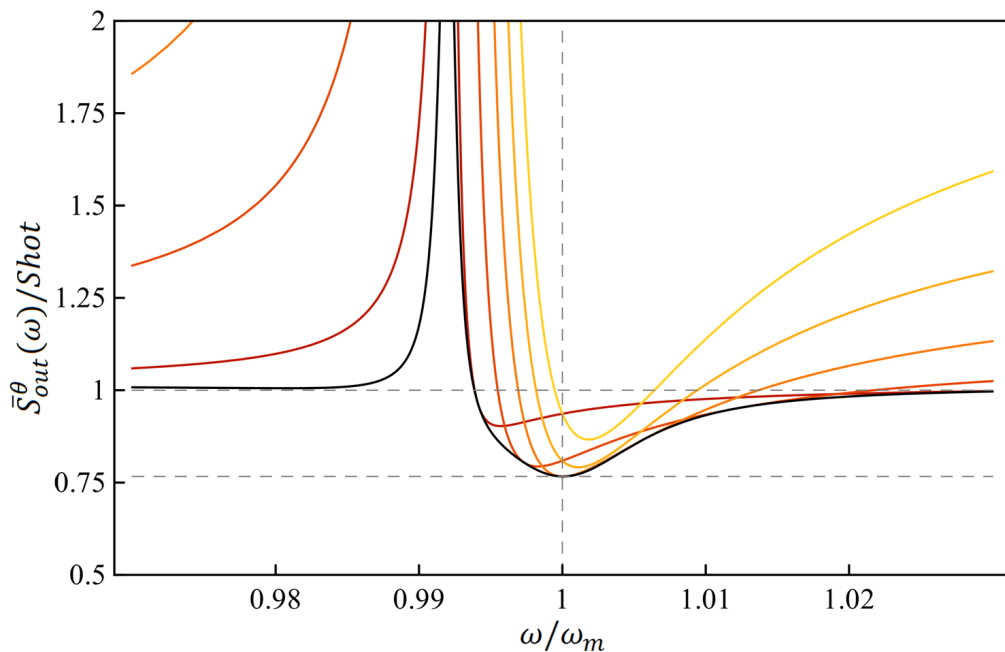


Figure 1.10: The black curve is  $\bar{S}_{min}(\omega)$  while the curves from red to yellow are  $\bar{S}_{out}^\theta$  at fixed values of  $\theta$ , increasing from  $-20 mrad$  (red) to  $-16 mrad$  (yellow) with steps of  $1 mrad$ . All curves are normalized to the shot noise level (dashed gray line). The lower dashed line indicates the maximum squeezing  $\simeq 0.75$ .

Before discussing the noise budget, we show in Fig. 1.10 the optimum spectrum  $\bar{S}_{min}(\omega)$  together with  $\bar{S}_{out}^\theta$  for different values of  $\theta$  around  $\theta_n$ . Note that  $\bar{S}_{out}^\theta$  is the only measurable quantity (for example with homodyne detection) and by changing

$\theta$ , that is choosing a different quadrature of the output field, one can control the maximum measurable squeezing and its bandwidth.

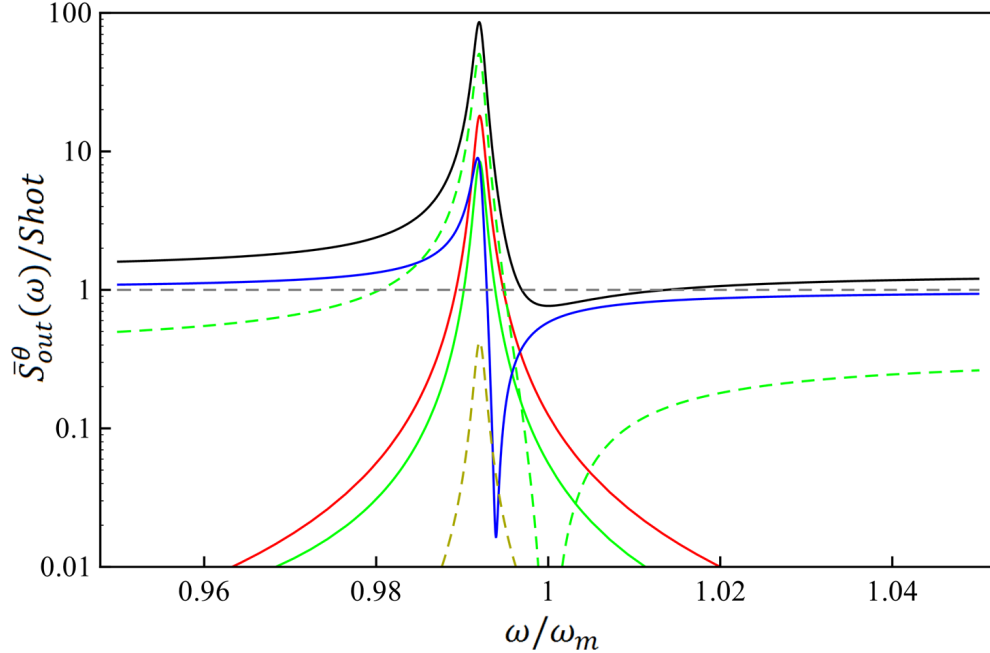


Figure 1.11: Noise budget of  $\bar{S}_{out}^\theta$  (Black) with  $\theta = \theta_n$ . All noise sources contributions are shown: thermal  $\xi$  (red), quantum input  $a_{in}$  (green), vacuum fluctuations  $a_{in,v}$  (blue), classical amplitude  $\alpha_I$  (dashed-dark yellow) and classical frequency noise (dashed-green).

We show in Fig. 1.11 the noise budget for  $S_{out}^\theta(\omega)$  with  $\theta = \theta_n$ . Thermal noise contribution (red) shows a peak at the effective mechanical resonant frequency; a lower Q factor, or bath temperature, would mask all quantum correlations at frequencies close to  $\omega_{eff}$  thus stating the need for a cryogenic environment and justifying efforts to increase the performances of the mechanical oscillator in terms of losses. Vacuum fluctuations give the most detrimental contribution when looking at frequencies far from the mechanical resonance, where the contribution of the quantum noise through the input mirror (green) is extremely small. Reducing its contribution at a given Finesse would not only increase the opto-mechanical coupling thanks to the higher intracavity field but would also increase the bandwidth upon which squeezing is attained. Classical frequency noise (dashed green) has a strong wideband contribution, it becomes the dominant term for a sufficiently low effective temperature (strong input field or large detuning) since the mechanical spectral peak gets buried in the displacement noise floor. However, it has the peculiarity that it gives a vanishing

contribution at the *bare* mechanical resonance frequency (see Chap. 5). Finally, classical amplitude noise (dashed-yellow) gives a negligible contribution for the chosen parameters but particular care has to be taken to reach the assumed value for  $S_{\alpha_I \alpha_I}(\omega)$ .

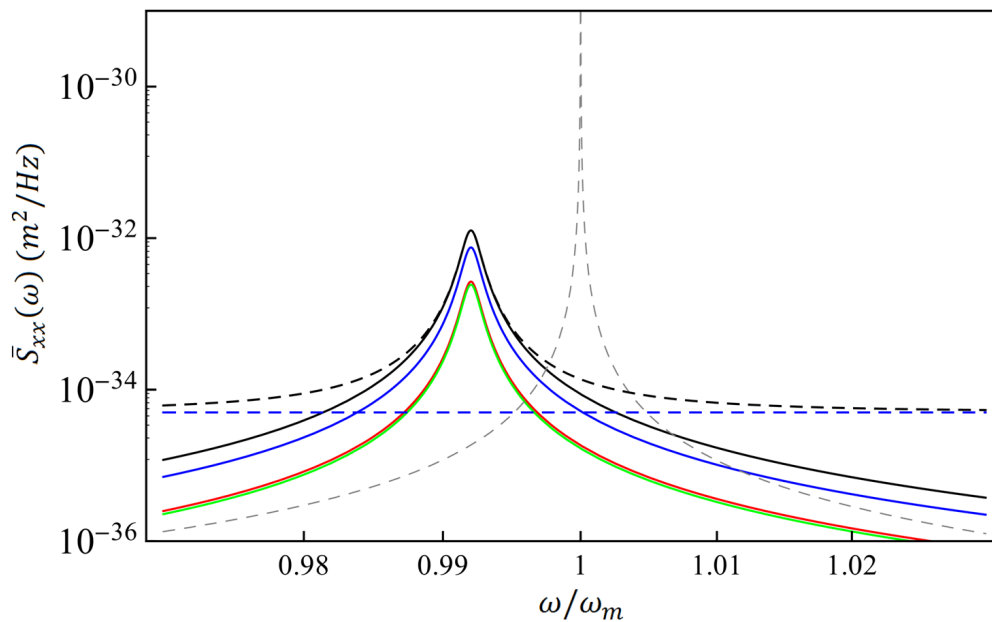


Figure 1.12: Noise budget of  $\bar{S}_{xx}(\omega)$  (Black). All noise sources contributions are shown: thermal (red), quantum (green) and classical (blue). We also show the nominal thermal noise of the free oscillator (dashed-gray), the frequency/displacement noise floor (dashed-blue) and the "measurable" total displacement noise (dashed-black).

We show in Fig. 1.12 the noise budget for  $\bar{S}_{xx}(\omega)$  (black). The mechanical spectral peak is shifted to lower frequencies, with  $\omega_{eff} = 99.2 \text{ kHz}$ , has an effective quality factor  $Q_{eff} = 750$  (cooperativity  $C = 1.33 \cdot 10^3$ ) and an effective temperature of  $T_{eff} = 3.1 \text{ mK}$  ( $\langle n_T \rangle = 650$ ). The quantum backaction  $S_q(\omega)$  (green) and thermal noise  $S_{th}(\omega)$  (red) give an equivalent contribution implying that, in principle, the direct effect of RPSN could be measurable. However, the classical excess noise  $S_{cl}(\omega)$  (blue) is the dominant term and can easily mask the RPSN contribution. As for the quadrature spectra, classical amplitude noise is negligible so that  $S_{cl}(\omega)$  is entirely due to frequency noise.

Measurements of the displacement PSD are usually performed with interferometric techniques, typically the Pound-Drever-Hall (PDH) detection scheme [58, 59], where the frequency noise (dashed blue line in Fig. 1.12) behaves as an additive

noise source to the detection output. A rough estimation of the signal-to-noise ratio is given by the sum  $\overline{S}_{xx}^{meas}(\omega) = \overline{S}_{xx}(\omega) + S_{\dot{\phi}\dot{\phi}}/g_0^2$  (shown in Fig. 1.12 with the dashed black line). However, keep in mind that  $\overline{S}_{xx}(\omega)$  and  $S_{\dot{\phi}\dot{\phi}}$  are correlated so that the correct calculation of the measurable displacement spectra needs to take into account the details of the measurement technique and how this correlation manifests.



## Chapter 2

# Design and fabrication of low loss MOMS resonators

In this chapter we describe the design strategies and the developed fabrication process of opto-mechanical devices specifically designed to ease the detection of ponderomotive squeezing. As we have seen in the previous chapter, the main difficulty for the observation of this phenomenon is due to the overwhelming effects of classical noise sources of thermal origin with respect to the weak quantum fluctuations of the radiation-pressure. Therefore, a low thermal noise background is required, together with a weak interaction between the micro-mirror and this background (i.e., high mechanical quality factors  $Q$ ). The device should also be capable to manage a relatively large amount of dissipated power at cryogenic temperatures (down to a few K).

In the development of our opto-mechanical devices, we are exploring an approach focused on relatively thick silicon oscillators with high reflectivity coating [60, 61]. The relatively high mass is compensated by the capability to manage high power at low temperatures (down to 1 K), owing to a favorable geometric factor (thicker connectors compared to other commonly used devices) and the excellent thermal conductivity of silicon crystals at cryogenic temperatures [62]. Many experiments have demonstrated that silicon mechanical resonators ( $10 \times 10 \times 10 \text{ cm}^3$ ) can show at such temperatures a loss angle, that models structural damping, as small as  $Q^{-1} = 10^{-9}$ , and that in smaller systems this figure reduces proportionally to their characteristic size (either thickness or width) [33, 35, 63]. Therefore, the expected loss angle for a device with a thickness of  $70 \text{ }\mu\text{m}$  is  $Q^{-1} \simeq 10^{-6}$ , provided that all other loss mechanisms are kept under control. In particular, the loss angle of the high reflectivity coating remains of the order of  $\phi_c = 5 \times 10^{-4}$  [64] even at liquid helium

temperature. Indeed, a quality factor of the order of  $\sim 10^6$  should be high enough to allow, in principle, the detection of squeezed light in the  $100\text{ kHz}$  frequency range, as we have shown at the end of Chap. 1.

Actually, for our latest generation of devices, we measured mechanical quality factors up to  $2 \cdot 10^6$  and optical finesse ranging from  $F \simeq 4 \cdot 10^4$  to  $F \simeq 6.5 \cdot 10^4$  at cryogenic temperatures. These results are published in Refs. [24, 25, 26].

In Sec. 2.1 we present the design strategy used to develop the micro-resonators that allowed us to obtain the results just mentioned. In particular, we devised three novel geometries. In Sec. 2.2 we describe the fabrication steps specifically developed to integrate the high-reflective coating deposition (See Ref. [27]).

## 2.1 Design strategy

According to the description of the cavity dynamics, some fundamental requirements for the oscillator may be derived by comparing the power spectral density (PSD) of the radiation-pressure noise and the PSD of the thermal noise. For instance, in view of the production of ponderomotive squeezing, we require that the radiation-pressure force noise, due to quantum fluctuations, dominates over displacement thermal noise at temperature  $T$  [6, 7]:

$$\hbar\omega_l \mathcal{P}_{in} \frac{4}{c^2} \left( \frac{2T_m}{T_m + \Sigma} \right)^2 \left( \frac{\mathcal{F}}{\pi} \right)^2 > 2k_B T \frac{m\omega_m}{Q} \quad (2.1)$$

this simple relation is valid in the bad-cavity regime ( $\omega_m \ll \kappa$ ) and for vanishing detuning. This equation defines the region where the generation of squeezed light can be obtained as a result of the quantum opto-mechanical correlations between field quadratures. Focusing on the right-hand side, we see that the thermal noise should be minimized by reducing the effective mass of the resonator and its frequency (on the contrary, for studying the ground state of the oscillator high frequencies are favored by the requirement  $\hbar\omega_m > k_B T$ ). Furthermore, the quality factor must be enhanced. From the left-hand side, we see that  $\mathcal{F}$  should be as high as possible together with the laser input power  $\mathcal{P}_{in}$ , provided that the device is capable of dissipating the resulting power with a tolerable temperature increase and that one can avoid the rise of static or dynamic instabilities.

Let us start by addressing the enhancement of the quality factor. As we have already mentioned at the beginning of Chap. 1, there are three main loss processes that need to be controlled.

### Inhomogeneous structural damping

Materials-related dissipation, usually referred to as *structural damping*, described by an imaginary part of the Young's modulus in a homogeneous body, is caused by a uniform distribution of impurities and dislocations. However, due to the presence of the high-reflective coating, the typical device has an inhomogeneous loss distribution. Actually, the overall mechanical performances of the device are mainly limited by the optical coating despite its typical thickness being of the order of  $6\ \mu\text{m}$ , small compared to the total thickness of the device that is around  $70\ \mu\text{m}$ . If  $\phi_s(\mathbf{r})$  is the loss factor at position  $\mathbf{r}$ , the energy  $dW$  dissipated in one cycle in the volume element  $dV$  is  $E(\mathbf{r})\phi_s(\mathbf{r})dV$ , where  $E(\mathbf{r})$  is the energy stored in the volume element during the motion. In the device, the total dissipated energy on one cycle is

$$\Delta W_s = \int E(\mathbf{r})\phi_s(\mathbf{r})dV \quad (2.2)$$

where both the energy density and the loss factor depend on the position. As a consequence, the total loss depends on the shape of the displacement within the resonator: modal shapes involving large strain in more dissipative parts imply higher losses than modal shapes where the same part are less strained.

This suggests two courses of action. First and foremost, the coated surface should be as small as possible. How small it depends on the specific Fabry-Pérot cavity that one wants to implement. Since it is necessary to keep negligible diffraction losses, the coated area should be at least several cavity waists. This conclusion may seem trivial, but is challenging from a technological point of view. Second, the device structure has to be designed in such a way that, for the normal mode of interest, the coated substrate is subjected to the smallest strain possible during the motion. This leads to complicated clever geometries.

### Thermoelastic damping

Thermoelastic dissipation was first investigated by Zener [34]. When a solid, with a nonzero coefficient of thermal expansion, undergoes a vibration other than a pure torsion, the strain field generates a thermal gradient and thus a heat flow which dissipates elastic energy. This fundamental mechanism sets the loss in micro opto-mechanical systems (MOMS) devices and precision instrumentation at room temperature. For this reason, it is the subject of an active area of experimental [65, 66], theoretical [67] and numerical [68] research. Just in the case of pure flexure, the loss

factor can be calculated analytically as

$$\phi_Z = \frac{Y\alpha^2 T_{bath}}{\rho C_V} \frac{\omega\tau_Z}{1 + \omega^2\tau_Z^2} \quad (2.3)$$

where,  $\alpha$  is the thermal expansion coefficient,  $C_V$  is the specific heat per unit volume of the material,  $Y$  the Young modulus,  $\rho$  is the density and  $T_{bath}$  is the temperature. The oscillator thickness  $h$  is involved through the material relaxation time  $\tau_Z = \frac{h^2\rho C_V}{\pi^2\kappa}$ , where  $\kappa$  is the thermal conductivity. These equations give some insight on the behavior of this mechanism, even though real losses depend on the geometry and the anisotropy the elastic structure. For instance, in the case of a silicon cantilever with  $h = 70 \mu m$ , we have  $\tau_Z = 0.3 \mu s$  and the expected loss angle at  $250 kHz$  is about  $7 \cdot 10^{-5}$ . This figure limits the  $Q$  factor of a silicon flexure to  $Q < 1.4 \cdot 10^4$  at room temperature, while better performances could be achieved at cryogenic temperatures thanks to the changes in the thermal properties of the material [33]. We also note that at these frequencies the thermoelastic dissipation of the optical coating is negligible, as its average thermal conductivity is 10 times smaller than in silicon [69] and the thermoelastic heat flow is accordingly smaller.

### Clamping losses

The third source of loss in the system is the coupling between the main resonant mode of the device and the internal modes of the wafer. Actually, the loss factor of the wafer is well above the intrinsic loss of silicon, due to the dissipation introduced by the sample holder. Moreover, some kind of coupling with the device is practically unavoidable, as the membrane modes of the wafer cover the full frequency spectrum with a spacing that, in our case, is of the order of  $2 kHz$ . To address this problem, the main resonator is connected to the wafer through a heavy suspended frame that acts as a passive isolation stage. The frame can be seen as a second oscillator with fundamental resonance frequency much lower than that of the mode of interest of the main resonator.

If we consider only a simple one-dimensional model, it is straightforward to solve the three-mode model and evaluate the effective loss factor of the resonator mode when a lossy wafer mode is at a nearby frequency. We assume for the suspended frame a mass of  $M_s = 7 mg$  and a resonant frequency fixed at  $30 kHz$ , while for the mirror we consider  $M_r \simeq 100 \mu g$  and  $\omega_m/2\pi = 130 kHz$ . The equivalent mass of a typical wafer mode at  $100 kHz$  is  $M_W = 0.2 g$ <sup>1</sup>. According to the results shown in Fig. 2.1(a), a resonator with a loss angle  $\phi \simeq 5 \cdot 10^{-6}$  is not affected by a wafer mode

---

<sup>1</sup>These figures are typical results of numerical simulations on our devices, as we will see shortly.

with loss angle  $\phi = 10^{-3}$ , resonating at the same frequency. On the other hand, the loss of the same resonator directly attached to the wafer would be increased up to  $10^{-3}$ (Fig. 2.1 (b)).

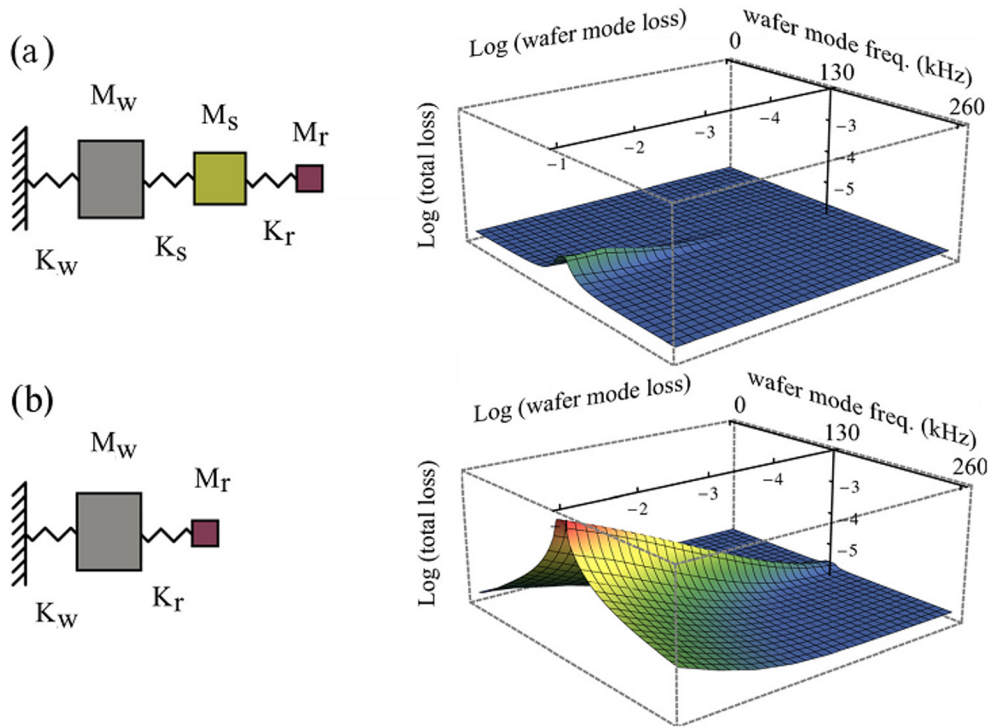


Figure 2.1: *Filtering effect of the suspended frame. (a) Simulated loss factor of the main resonator mode with the isolation wheel. For each mode, elastic constants  $K$  are obtained by the values of resonant frequency and equivalent mass. Even if a loss angle as low as  $5 \cdot 10^{-6}$  is assigned to the resonator and the suspended frame, the resulting total loss factor of the resonator mode can just worsen by less than one order of magnitude, depending on the frequency and the loss of the wafer mode. (b) Simulated loss factor of the main resonator mode without the isolation frame. In this case, the resulting loss factor is strongly correlated to the loss of the wafer mode.*

## Overall mechanical design

From the above discussion, it is clear that the dissipative contribution from different phenomena can be taken into account only by means of numerical simulations. This is usually done with software based on the Finite Element Method (FEM), in our case, ANSYS Multiphysics. The FEM model of the device is based on a three-dimensional

mesh that discretizes the structure, making the problem solvable. The mechanical response of the device is evaluated when it is driven by a harmonic pressure over the surface of the mirror. To be consistent with measurements, the spatial distribution is the same as the laser beam intensity profile (Gaussian shape) and the resulting displacement of the mirror's surface is weighted by the same gaussian profile (see App. A). The model can simulate, separately or in a cumulative way, all the three kinds of dissipation under study. Thermoelastic loss is evaluated from material properties while structural damping requires as input the loss angle of silicon and of the optical coating. When thermoelastic losses can be made negligible, the structural loss of silicon wafers is found well below the value of  $\phi_{Si} = 10^{-6}$  [70, 71], mentioned earlier, and that we assume as reference in our calculation. As for the coating, the loss angle is still in the range  $\phi = (3 - 6) 10^{-4}$  [64, 72] in spite of the large amount of theoretical and experimental developments carried on by scientific community interested in gravitational wave detectors. Therefore, we assume as reference the value  $\phi = 5 10^{-4}$  that well represents the state-of-the-art for optical coatings like the one on top of our silicon surface.

For each resonant mode under study the quality factor is calculated as  $Q = \phi_T^{-1}$ , with  $\phi_T$ , the total loss angle, defined as

$$\phi_T = \frac{\Delta W_T}{2\pi W_T}. \quad (2.4)$$

Here,  $W_T$  is the total energy stored in the resonant mode and  $\Delta W_T$  the total energy loss per oscillation cycle due to all the dissipation processes. In our case, the device is made of subsystems with different, but homogeneous, loss angle, namely the resonator (R), the coating (C) and the frame (F). As a consequence, we can separate the integral in Eq. 2.2 into three contributions

$$\Delta W_T = \phi_F \int_F E(\mathbf{r}) d\mathbf{V} + \phi_R \int_R \mathbf{E}(\mathbf{r}) d\mathbf{V} + \phi_C \int_C \mathbf{E}(\mathbf{r}) d\mathbf{V} \quad (2.5)$$

where the volume integrals are evaluated over each subsystem and  $\phi_F$ ,  $\phi_R$ ,  $\phi_C$  are respectively the loss factors of the frame, the resonator(silicon) and the coating. Therefore, the total loss is given by the sum of the loss angles of each subsystems, weighted by the ratio of the strain energy in the respective subsystem to the total strain energy of the mode

$$\phi_T = \phi_F \frac{W_F}{W_T} + \phi_R \frac{W_R}{W_T} + \phi_C \frac{W_C}{W_T}. \quad (2.6)$$

In the geometry optimization the first and the last terms have to be minimized.

Another aspect that has to be considered, regards higher order modes of the frame. Particular care has to be used in order to avoid that one of these modes ends up with a resonance frequency too close to the mode of interest of the main resonator. If this happens, the two modes become coupled and the quality factor of the mirror's mode is spoiled by the low  $Q$  mode of the frame.

### Optical properties

As stated at the beginning of this section, optical losses are a critical aspect of the device. The finesse  $\mathcal{F}$  is critically dependent from the initial wafer roughness and the mirror's surface cleanliness. Roughness and inhomogeneity of the coating structure are inherent in any integrated optical device and their more conspicuous effect is to scatter light thus leading to power attenuation [73]. As a first step, we set the requirements on the optical losses of the device. Such requirements give rise to an upper limit on the RMS roughness that should be preserved during the fabrication steps. A quantity that we evaluate for controlling the mirror quality is the total integrated scatter (TIS), that is the ratio of the integrated scatter power to the reflected specular power, evaluated from Davies' formula [74, 75]. The TIS is considered together with the relation of the finesse with the transmission and the optical losses

$$\begin{aligned}\Sigma &= \left(\frac{4\pi}{\lambda}\right)^2 \sigma^2 + \mathcal{A} \\ \mathcal{F} &= \frac{2\pi}{T_m + \Sigma}\end{aligned}\tag{2.7}$$

where  $\lambda$  is the wavelength (for our Nd:YAG laser  $\lambda = 1064 \text{ nm}$ );  $\mathcal{A}$  is the contribution to the total optical losses of absorption and diffraction due to finite mirror size;  $\sigma^2 = \int G(\mathbf{r})d(\mathbf{r}) d^2\mathbf{r}$ . Here  $d(\mathbf{r})$  stands for the differences between the mirror surface and the ellipsoidal best interpolated surface, and  $G(\mathbf{r})$  is the Gaussian weight corresponding to the laser beam intensity on the mirror:  $G(\mathbf{r}) = (2/\pi\omega_0^2) \exp(-2r^2/\omega_0^2)$  where  $\omega_0$  is the beam waist.

Equations 2.7 set the constraint for the upper limit of the RMS roughness of the wafer according to the cavity specifications. We consider for instance a Fabry-Pérot cavity with a  $T_m = 50 \text{ ppm}$  silica input mirror having a nominal laser waist of  $43 \mu\text{m}$  and that allows negligible diffraction losses on its surface. According to Equations 2.7, a RMS roughness lower than  $0.5 \text{ nm}$  is needed to obtain an optical loss  $\leq 35 \text{ ppm}$ . This level of roughness must be guaranteed in a circular region with a diameter of about  $250 \mu\text{m}$ , corresponding to 5 – 6 times the laser waist. These

requirements are very tight and a proper choice of the process steps should be taken into account.

### Device geometries

With the strategy and methodology described up until now, we designed three typologies of MOMS. In Fig. 2.2 and Fig. 2.3 we show the scanning electron microscope (SEM) images for typical devices. All three geometry types include the isolation frame realized from the full thickness of the wafer. In Fig. 2.2(a) (and (b)) we show

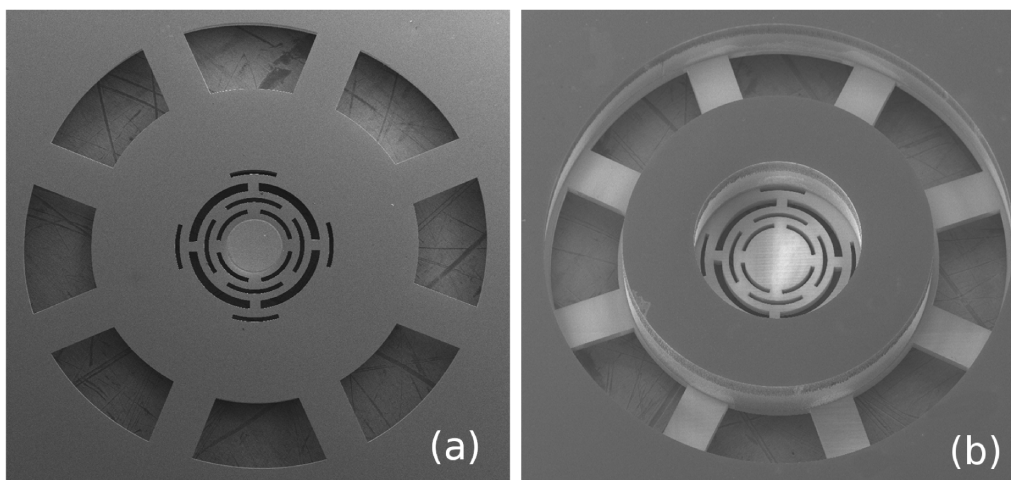


Figure 2.2: SEM images of the double wheel "Low-deformation" oscillator; (a) front and (b) back side. The device has the outer massive frame working as mechanical filtering system and decoupling the inner resonators from the supporting wafer. The mirror can be seen as a bright disk on the resonating structure.

the front (back) side of the "low-deformation mirror" [25] (also called *double wheel oscillator*). The resonator is formed by the central mirror, covered with the highly reflective optical coating (visible as the brighter disk at the center), suspended by a specifically designed elastic structure. This structure made of alternate torsional and flexural springs allows the displacement in the direction orthogonal to the mirror surface with a minimal internal deformation of the mirror itself. For these devices the strain energy ratio of the coating  $W_C/W_T$  is of the order of  $4 \cdot 10^{-3}$ . We produced several different versions of the design, resonating in the range  $35 - 250 \text{ kHz}$  and with equivalent masses in the range  $70 - 250 \mu\text{g}$ . The diameter of the coated surface ranges from  $800 \mu\text{m}$  in larger devices, resonating at low frequencies, to  $400 \mu\text{m}$  in the high frequency versions. Such large mirrors allow negligible diffraction losses even

in non critical cavities. The fundamental modes of the heavy frame is about  $30\text{ kHz}$  for all devices. The second type of resonator, Fig. 2.3(c) (and (d)) is based on the

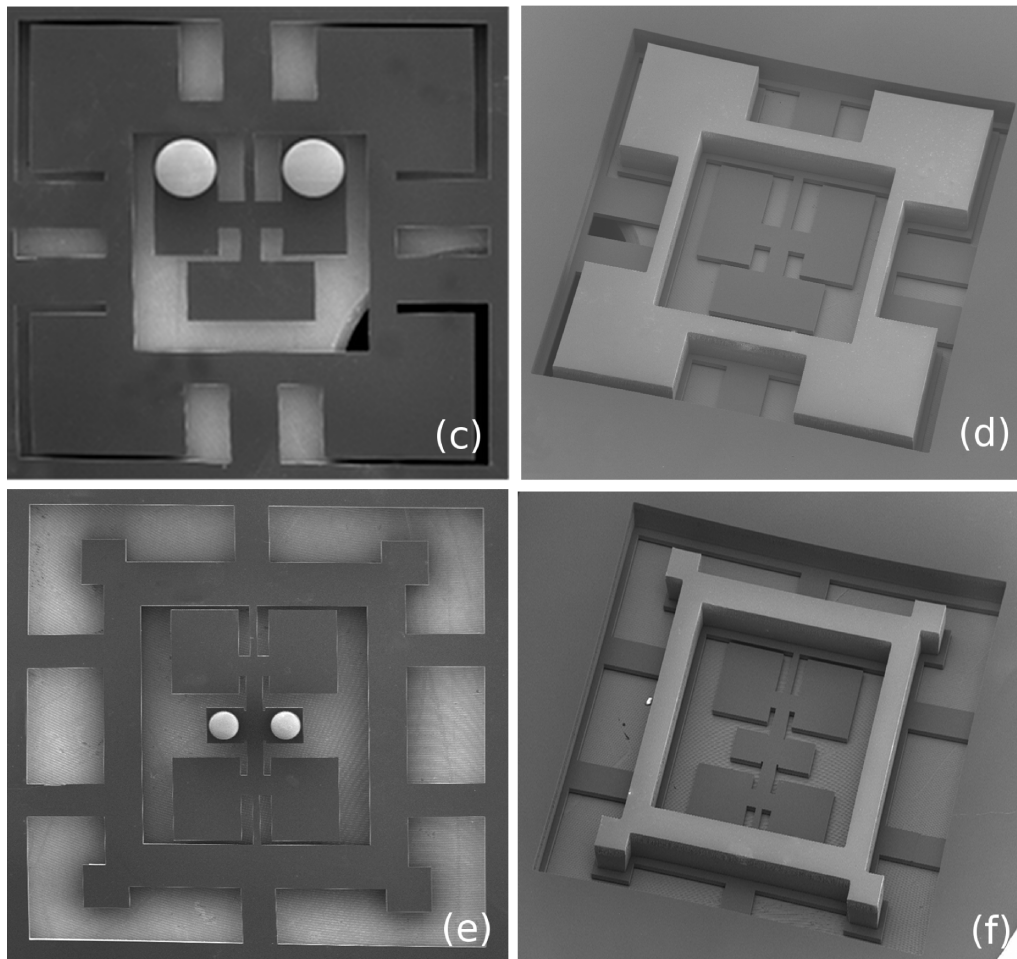


Figure 2.3: *SEM images (front and back side) of: double paddle oscillator (c,d) and quad-paddle oscillator (e,f). Both devices have the outer massive frame working as a mechanical filtering system and decoupling the inner resonators from the supporting wafer. The mirrors can be seen as bright disks on the resonating structures.*

double paddle oscillator (DPO) design [76], and consists of two inertial members, a head and a couple of wings, that are connected by a torsion rod, called the neck (see Fig. 2.4(a)). The wings are connected to the outer frame by another torsion rod, the leg. This system can be visualized as a coupled oscillator consisting of two masses (head and wings) and of two springs (neck and leg) that twist or bend in different directions, originating several composite vibration modes [66]. The antisymmetric torsion modes (AS) consist of a twist of the neck around the DPO symmetry axis

and a synchronous oscillation of the wings. The head rotates around the neck axis while the wings rotate around an axis that is roughly orthogonal to it. The rotation can be concordant (AS1) or discordant (AS2). For these AS modes the elastic energy is primarily located at the neck, where the maximum strain field occurs during the oscillations, while the leg remains at rest and the foot can be supported by the outer frame with negligible energy dissipation. The third type of devices, the quad paddle

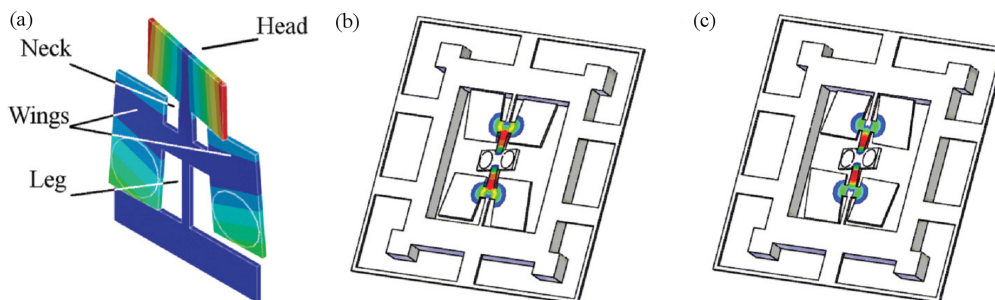


Figure 2.4: *DPO and QPO oscillators. (a) Modal shape of the AS1 mode of the DPO. (b) Modal shape of the AS1 mode of the QPO. (c) Modal shape of the AS2 mode. The contour graph plotted over the modal shapes shows the average elastic energy stored in the device during an oscillation cycle (relative values of energy from 0 to the maximum value). In both cases the maximum value is in the neck.*

oscillator (QPO), is an innovative design derived from the DPO. It consists of three inertial members, the head and two couples of wings, connected by the neck torsion rods (see Fig. 2.4(b) and (c)). Here again, some modes induce only a very small strain in the legs and can be supported by the outer frame with a negligible energy dissipation. We are dealing in particular, again, with the antisymmetric modes (AS1 and AS2). Due to the considerable modal density of this device, special care has been taken to avoid the superposition of the AS with a low-Q flexural modes. It is also possible to exploit the wing torsion (WT) mode, where the head remains at rest because the neck is twisted in opposite directions by the synchronized flapping of the wings. Obviously, the vibration of the WT mode can be detected only by using mirrors placed over the wings.

The remarkable properties of the AS and WT modes is that they are nodally suspended so that the frame strain energy ratio  $W_F/W_T$  is of the order of  $10^{-4}$ . This figure means that only a small fraction of the oscillation energy is stored in the frame and is therefore liable to be transferred to the sample holder. As an order-of-magnitude estimate, from this distribution of strain energy we see that a mode with loss  $Q^{-1} = 10^{-6}$  can tolerate a loss factor of  $10^{-2}$  in the frame without being

spoiled. Concerning the coating energy ratio  $W_C/W_T$ , it is of the order of  $10^{-3}$  for both the DPO and the QPO, so that a mode with loss  $Q^{-1} = 10^{-6}$  can tolerate a loss factor of  $10^{-3}$  in the coating. As we have seen, this value is within the range of what is expected for our coating.

As mentioned at the beginning of this chapter, an important characteristic that must be evaluated in micro-oscillators is their capability to dissipate the relatively large amount of heat produced by the absorbed power. This feature actually determines the maximum field amplitude that can be employed in the experiment. The absorbed power in a resonant Fabry-Pérot cavity is

$$\mathcal{P}_{abs} = \frac{4T_m}{(T_m + \Sigma)^2} \mathcal{A} \mathcal{P}_{in} \quad (2.8)$$

where  $\mathcal{A}$  is the mirror absorption coefficient. For high reflectivity coatings,  $\mathcal{A}$  can be below  $10^{-6}$  [77]; however, we are going to take as reference the more conservative value of  $\mathcal{A} = 4 \cdot 10^{-6}$  measured in Ref. [78] for the same coating as ours, deposited on a silicon substrate. Using FEM simulations we evaluated the thermal gradient

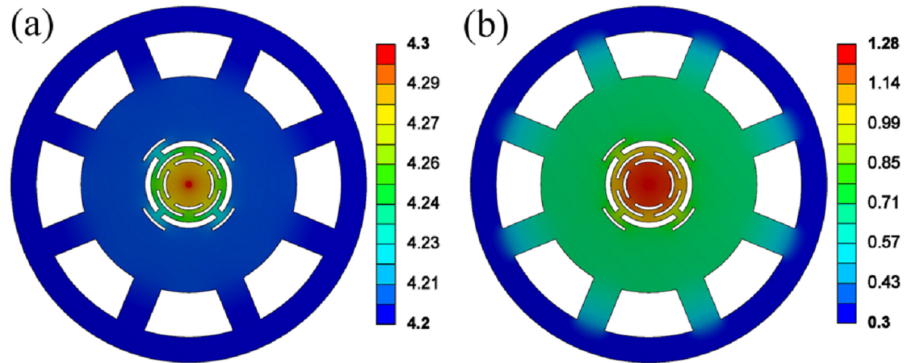


Figure 2.5: *Steady-state thermal analysis of a low deformation mirror: FEM simulation showing the effect of the laser beam power absorption. (a) Temperature mapping with the background at liquid helium temperature, with an absorbed power of 1 mW. (b) Temperature mapping with the background at 300 mK and an absorbed power of 0.1 mW. In both cases, the total laser power is applied on a circular surface of diameter 0.1 mm at the center of the mirror.*

that arises either from an absorbed power of 1 mW, assuming a background at liquid helium temperature, or an ultra-cryogenic environment with  $T_{bath} = 300 \text{ mK}$  and a lower absorbed power of 0.1 mW. In Fig. 2.5 we show the results for a "low deformation mirror", while in Fig. 2.6 those for the QPO. The maximum thermal

gradient, when we consider a  $4.2\text{ K}$  background, is of the order of  $0.1\text{ K}$  for the double wheel oscillator while it reaches  $0.26\text{ K}$  in the case of the QPO. In both cases the temperature increase of the devices is extremely small thanks to their relatively large thickness and to the high thermal conductivity of silicon. Moreover, the temperature is very homogeneous within the main oscillator. This feature is important to avoid effects of non-equilibrium thermal noise [79]. Furthermore, it is clear that even a larger dissipated power could be managed.

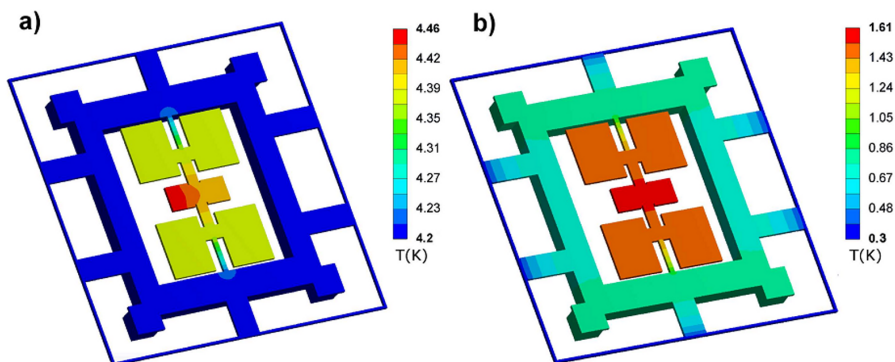


Figure 2.6: *Steady-state thermal analysis of a QPO micromirror: FEM simulation showing the effect of the laser beam power absorption. (a) Temperature mapping with the background at liquid helium temperature, with an absorbed power of  $1\text{ mW}$ . (b) Temperature mapping with the background at  $300\text{ mK}$  and an absorbed power of  $0.1\text{ mW}$ . In both cases, the total laser power is applied on the left of the QPO head on a circular surface of diameter  $0.1\text{ mm}$  at the center of the mirror.*

We remark that, if we consider the optimally coupled cavity of Chap. 1 ( $T_m = \Sigma = 50\text{ ppm}$ ) and the value for  $\mathcal{A}$  chosen as reference, an absorbed power of  $1\text{ mW}$  implies an input power of  $12.5\text{ mW}$  with an intracavity power as high as  $250\text{ W}$ .

When we move to simulations of the ultra-cryogenic environment, the sample temperature remains relatively high, that is  $1.3\text{ K}$  for the double wheel while the QPO reaches  $1.6\text{ K}$ . Thus, there is only a moderate improvement with respect to the previous configuration. This is due to the strong dependance of the thermal conductivity of silicon on temperature (in the cryogenic range, it increases roughly as  $\sim T^3$ ). We also remark that in this range the simulations give just a rough estimation since phononic mean free path is here well over  $\sim 100\text{ }\mu\text{m}$  and thermal conductivity depends on geometric effects, while in our simulations we used the value measured in silicon samples of  $5\text{ mm}$  in diameter [62].

## 2.2 Fabrication

During the development and optimization of the fabrication steps one should keep in mind that any misalignment affects the frequency of the vibrational modes, due to the resulting mass unbalance, and the mechanical losses, since the coating layer would cover areas with higher strain. As the typical alignment error of a mirror obtained by a hard-mask at the end of the process can be as high as  $100\ \mu\text{m}$  [24], we defined the coating by an intermediate lithographic step. The standard projection lithography technique introduces no more than  $2\ \mu\text{m}$  of alignment mismatch between the markers of two consecutive photo-lithographic masks, and an error of no more than  $3\ \mu\text{m}$  from front to back alignment in the lithography. Hence, in the worst case the maximum alignment error is  $7\ \mu\text{m}$  according to the process steps. This mismatch is not critical for the coating centering, as it corresponds to 1.75% of the diameter of the smallest mirror.

Another important factor to be considered is that linear positioning errors could produce a large difference on the effective mass of the external frame, affecting its filtering properties from the vibrations of the wafer's modes. Angular alignment errors can significantly alter the resonant modes of the device and consequently the opto-mechanical coupling, due to the anisotropic properties of silicon crystals.

Finally, the process is made of several steps where the etching of silicon is done by deep-RIE and the oxides are etched by chemical baths that could significantly affect the coating roughness and the geometry of the device. To ensure a good process repeatability we measured the RMS roughness of the coating after the main chemical baths.

For the micro-fabrication of the resonators we have used  $100\ \text{mm}$  diameter  $\langle 100 \rangle$  Silicon-on-Insulator (SOI) wafers ( $400 \pm 5\ \mu\text{m}$  thick handle wafer and  $70 \pm 1\ \mu\text{m}$  device layer wafer) from Icemos Technology Ltd. The buried oxide layer thickness was  $1\ \mu\text{m}$ . These wafers were etched from both sides to realize high-aspect ratio three-dimensional structures, using the buried oxide as etch stop layer. To avoid mechanical losses from doping species or other trapped impurities like oxygen, we employed Floating Zone (FZ) wafers with resistivity higher than ( $1\text{k}\Omega - \text{cm}$ ), both for the handle and the device layers. For the reason described above, to control optical losses due to the surface roughness we selected wafers with a surface roughness RMS (ISO 4287/1) better than  $0.5\ \text{nm}$ , when measured in small areas ( $5\ \mu\text{m} \times 5\ \mu\text{m}$  and  $3\ \mu\text{m} \times 3\ \mu\text{m}$ ) by Atomic Force Microscopy (AFM) in different wafer positions. Measurements results are summarized in Tab. 2.1.

To enhance the process yield and minimize surface roughness deterioration, for

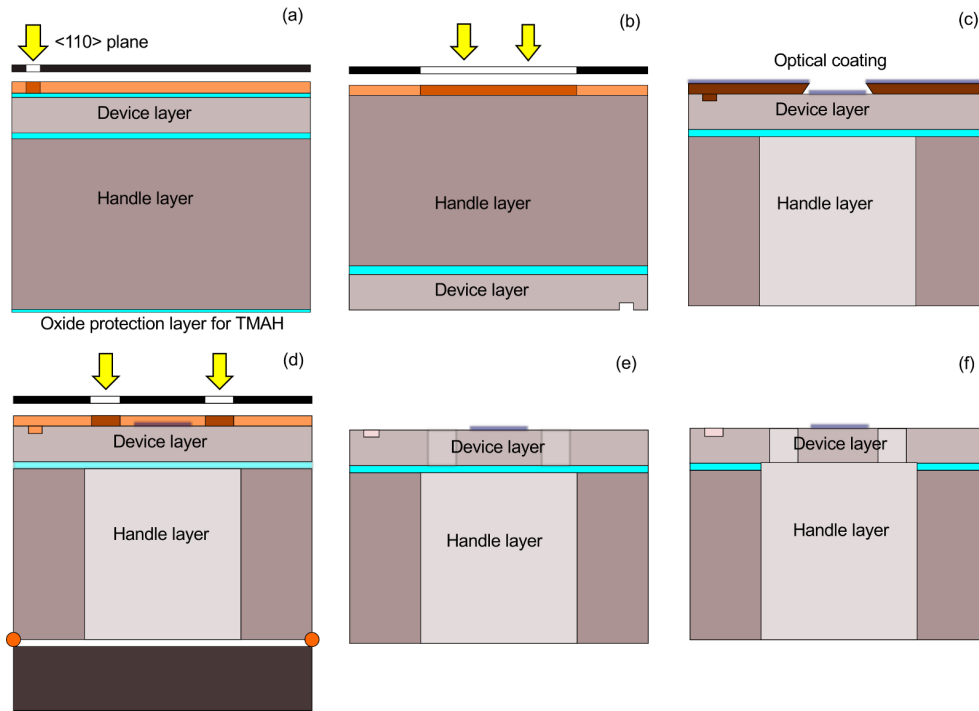


Figure 2.7: Process sequence P1 for the MOMS fabrication: (a) Oxidation - Crystal axis alignment - TMAH (b) Oxide strip - lithography on the handle layer (back SOI wafer) - Deep-RIE on the handle wafer (c) IBS of optical coating - lift-off - coating stabilization (d) lithography on the device layer (front SOI wafer) with the support wafer (e) Deep-RIE on the device layer - resist strip with piraña etch (f) BHF for removing the buried oxide - RCA cleaning.

the fabrication of the resonators we set up two process sequences named P1 (Fig. 2.7) and P2 (Fig. 2.8). Both processes were carried out in a 10 – 100 class clean room facility, performing in appropriate order the fundamental steps detailed below:

1. *Detection of the  $\langle 110 \rangle$  plane.* We aligned our main markers to the  $\langle 110 \rangle$  crystallographic direction by TMAH etching, as the main flat orientation with respect to the crystal is not sufficiently accurate, having a misalignment in the range of 0.2 to 0.8 degrees. The first step consists of an optical lithography with a wagon-wheel based structure in a 200 nm thermally grown oxide. Wafers were then etched in TMAH to a depth of about 8  $\mu\text{m}$  to expose the crystallographic direction  $\langle 110 \rangle$ . The thermally grown oxide was then removed completely by a BHF/BOE 7 : 1 solution in 2 min to free the surface before the mirror deposition. The surface roughness of the silicon surface remains unchanged by this step.

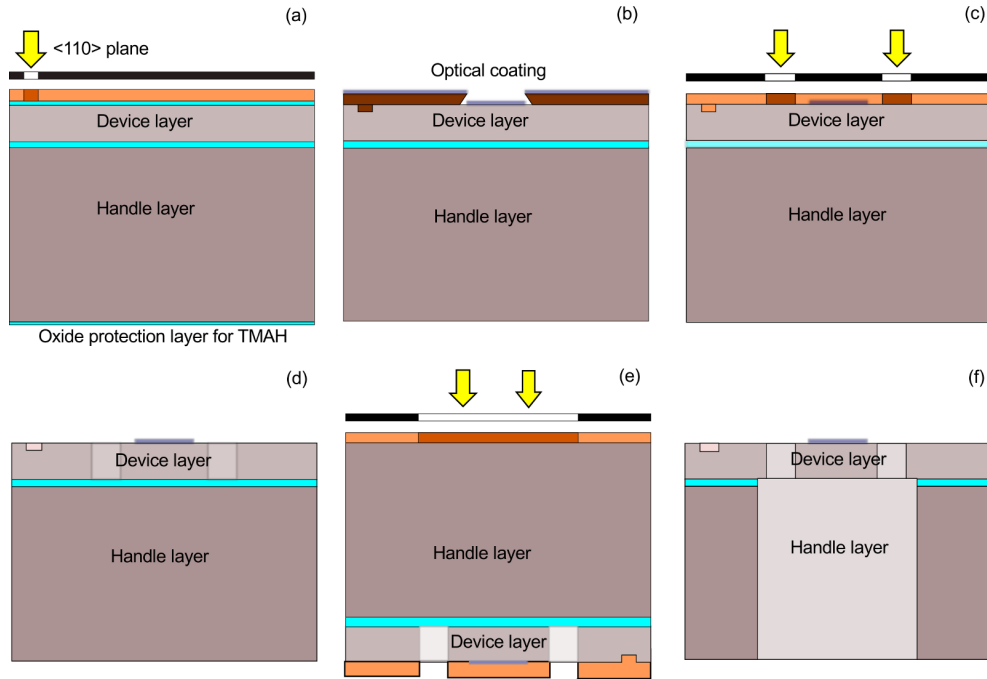


Figure 2.8: Process sequence P2 for the MOMS fabrication: (a) Oxidation - Crystal axis alignment - TMAH (b) IBS of optical coating - lift-off - coating stabilization (c) lithography on the device layer (front SOI wafer) (d) Deep-RIE on the device layer - resist strip with piraña etch (e) lithography on the handle layer (back SOI wafer) (f) Deep-RIE on the handle wafer - BHF for removing buried oxide layer - RCA cleaning.

2. *Deep-RIE of the handle wafer.* The SOI wafer was spin-coated with a AZ4562 resist with a thickness  $10\ \mu\text{m}$  to withstand the etching process. The lithographic mask designed to pattern the handle wafer is optically aligned with the marker prepared in the front side to detect the crystallographic direction. Then an ICP (inductive coupled plasma) Alcatel Deep-RIE AMS 200 machine based on the Bosch process is used to remove the full thickness of  $400\ \mu\text{m}$  of the handle wafer. The etching time is about 32 min (average etching rate  $12.5\ \mu\text{m}/\text{min}$ ). The chuck temperature and He cooling gas pressure are tailored to optimize both etch rate and etch depth uniformity, and to guarantee a good plasma stability, avoiding the formation of any residual structures at the bottom or around the edge of the frame structure, or near the holes. We obtained smooth edges with a scalloping below  $1\ \mu\text{m}$ , as it is shown in Fig. 2.9.
3. *High-reflective coating deposition.* Each mirror has a total thickness of  $5.9\ \mu\text{m}$  and is made of 38 alternate  $\text{Ta}_2\text{O}_5/\text{SiO}_2$  quarter-wave coating layers deposited

by Ion Beam Sputtering (IBS) by ATFilms (Fig. 2.10). The coating procedure makes the films dense (not porous) and harder than the silicon substrate, as covalent bonds are formed during deposition. To integrate the coating deposition with our process we developed a lift-off procedure by using as sacrificial layer a negative high-thickness nLOF2070 resist, patterned by a lithographic mask with circular regions corresponding to the mirrors positions in the wafer. We obtained a  $7.8\ \mu\text{m}$  thick resist (higher than the mirror coating thickness) by using a spin speed of  $3000\ \text{rpm}$ ; the measured undercut is less than  $3\ \mu\text{m}$ . To avoid moisture adsorption during transportation we stabilized the sacrificial resist by a soft baking at  $120\ ^\circ\text{C}$ . The mirrors were then realized by IBS and after the deposition the resist sacrificial layer was removed in a hot acetone bath at  $90\ ^\circ\text{C}$ . A heat treatment at  $430\ ^\circ\text{C}$  was done to reduce the  $\text{Ta}_2\text{O}_5$  dissipation. During the resist removal some small pieces of the coating were released due to the coating edge delamination. For this reason we performed RCA cleaning in our clean room facility to avoid any further contamination during the following steps.

4. *Deep-RIE of the device wafer.* The front side structures were defined by a lithographic step, optically aligned with markers on the back side achieving a maximum alignment error of  $3\ \mu\text{m}$ . The front surface was covered again with a  $10\ \mu\text{m}$  thick layer of AZ4562 resist using a spin coating EVG machine. This resist covers all the surfaces and works as protection layer for the optical coating during the Deep-RIE Bosch process. In addition we glued a support wafer on the back side in four points with resist drops and we performed a soft bake heat treatment to harden this structure. This auxiliary wafer is needed for the protection of the machine chuck. In this way we avoid any chuck damage due to plasma that could break the buried oxide layer on a pass-through hole. We calibrated the etching process with an etch rate of  $7.7\ \mu\text{m}/\text{min}$  to engrave the full thickness of the device layer in  $9\ \text{min}$ .
5. *Wet-etch of the buried oxide.* At the end of this process a piranha etch solution was used to remove the resist, and the residual buried oxide on the device layer was removed by a 15 min BHF wet etch. This chemical bath does not affect the mirror coating because the outer  $\text{Ta}_2\text{O}_5$  reacts very slowly with this acid solution and acts as a protection layer for the mirror coating.

Both process sequences start with the detection of the crystalline plane  $\langle 110 \rangle$   
(i). After that in  $P1$  we performed the back-side etching on the handle layer (ii),

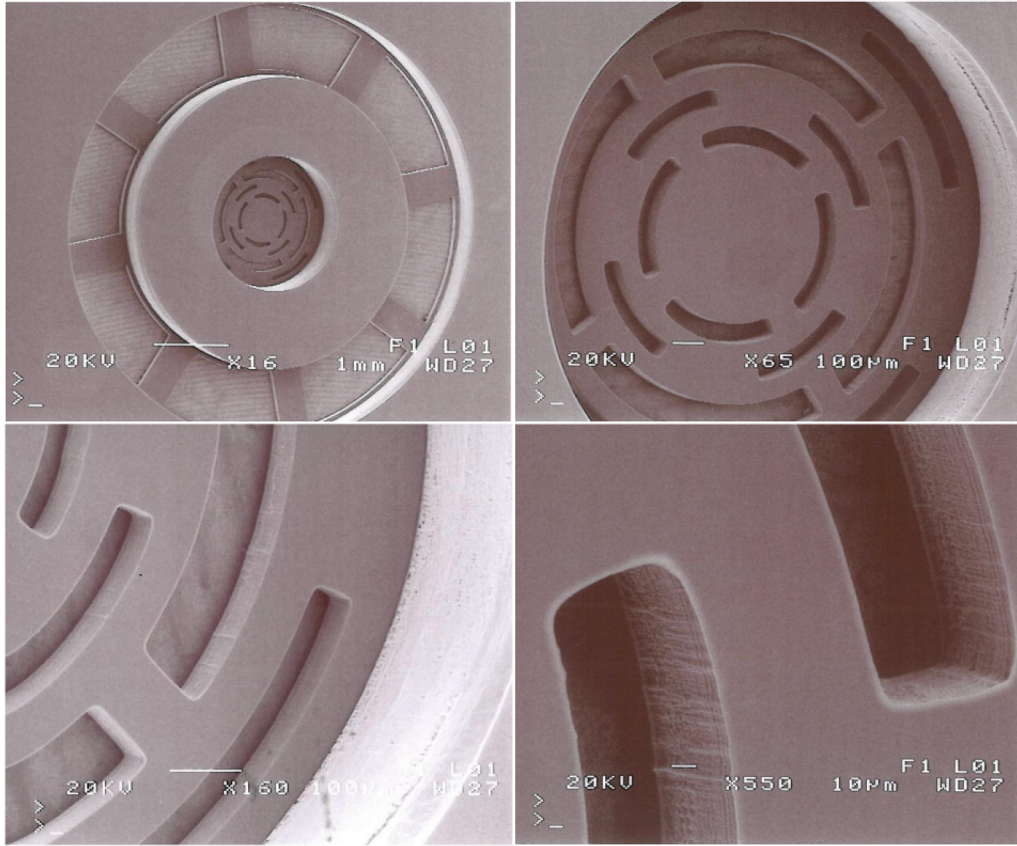


Figure 2.9: SEM image showing details of a double wheel resonator. Sidewall scalloping due to the Deep-RIE Bosch process is lower than  $1\mu\text{m}$ .

the coating deposition (iii), the etching of the resonating structures on the device layer (iv) and the wet etch of the buried oxide (v). In the process *P2* the coating was deposited first (iii), then the resonating structures were etched on the device layer (iv) and the back-side structures on the handle layer (ii); the buried oxide was finally removed by wet etch (v).

To verify the quality of the mirrors, we measured the dimensional characteristics at different scales. First, an AFM scan on a  $5\mu\text{m} \times 5\mu\text{m}$  and a  $3\mu\text{m} \times 3\mu\text{m}$  (Table 2.1) areas show that the RMS roughness is about  $0.5\text{ nm}$  as in the original wafer. Second, we measured with a Zygo NewView 6000 profilometer the roughness on a circular region with a diameter of  $100\mu\text{m}$ , that is, the dimensional scale of the waist of our cavities. Results are in agreement with those obtained with AFM technique, both in the mirror center (Fig. 2.11a) and near the coating edge (Fig. 2.11b). Third, we measured the curvature radius and the diameter of the mirrors by a Leica DCM 3D optical profiler (Figs. 2.12-2.13). The radius of curvature, due to residual stress

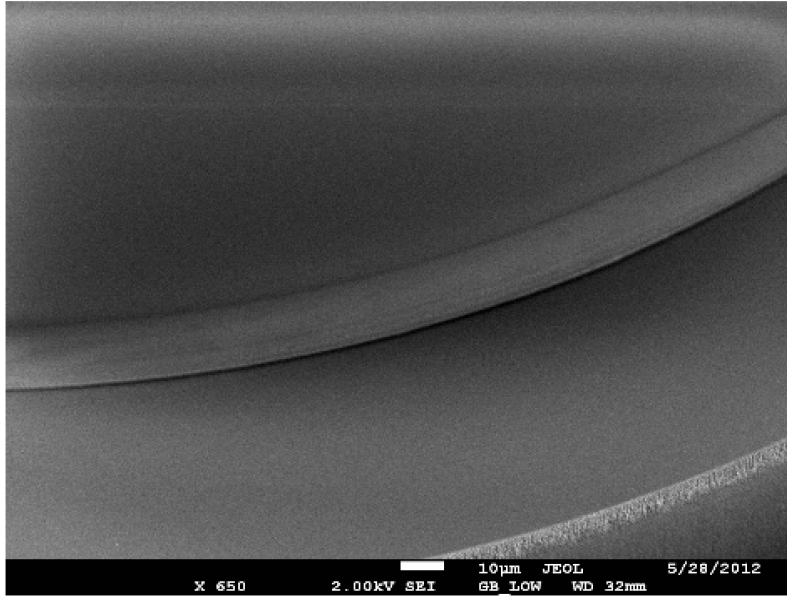


Figure 2.10: SEM image of the mirror over the device layer. The coating is made of 19 pairs of high-low refractive index dielectrics deposited by Ion Beam Sputtering at ATFilms. The thickness is  $5.9 \mu\text{m}$ .

effects, is 100 mm for the small mirrors ( $400 \mu\text{m}$  nominal diameter) and 90 mm for the large mirrors ( $800 \mu\text{m}$  nominal diameter). The actual diameter, measured along two orthogonal directions, ranges from 377 to  $387 \mu\text{m}$  for the small mirrors and from 772 to  $797 \mu\text{m}$  for the large mirrors. These small differences from the nominal value are due to the lift-off process accuracy and the mirrors edge delamination during processing. Both the curvature radius and the diameter variation do not affect the device overall performances because the laser waist in our cavities ranges from  $\sim 40 \mu\text{m}$  to  $\sim 80 \mu\text{m}$ .

Table 2.1: Results of the RMS roughness measurement performed by AFM.

	$5 \mu\text{m} \times 5 \mu\text{m}$	$3 \mu\text{m} \times 3 \mu\text{m}$
Number of sampling points	65536	65536
Max height [nm]	11.80	11.42
Min height [nm]	-1.82	-1.84
RMS roughness [nm]	0.52	0.53
Average height [nm]	0.40	0.39

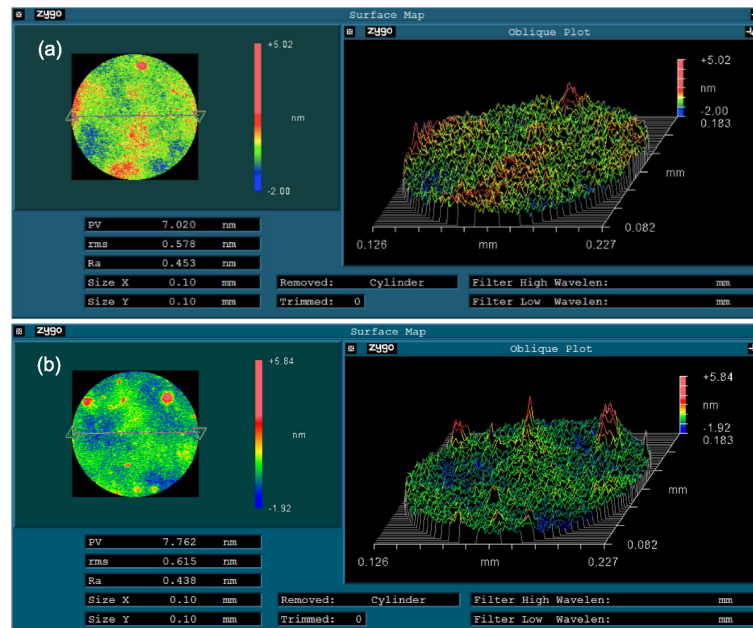


Figure 2.11: Zygo surface profile for a circular area near the mirror center (a) and near the mirror edge (b). Raw data are elaborated subtracting the best fit 3D paraboloid.

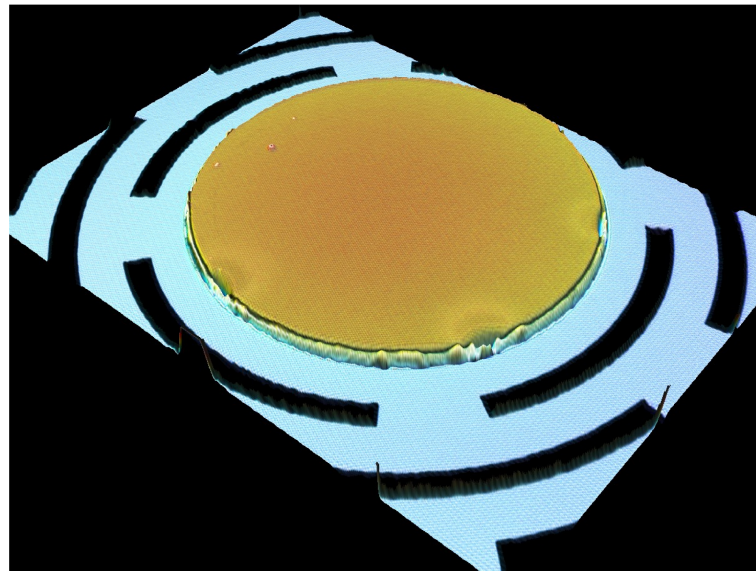


Figure 2.12: The profile of the mirror (diameter 800 μm) is measured by a Leica DCM 3D optical profiler. The figure shows some delamination problems along the edges and some debris over the surface close to the mirror edge (red spots).

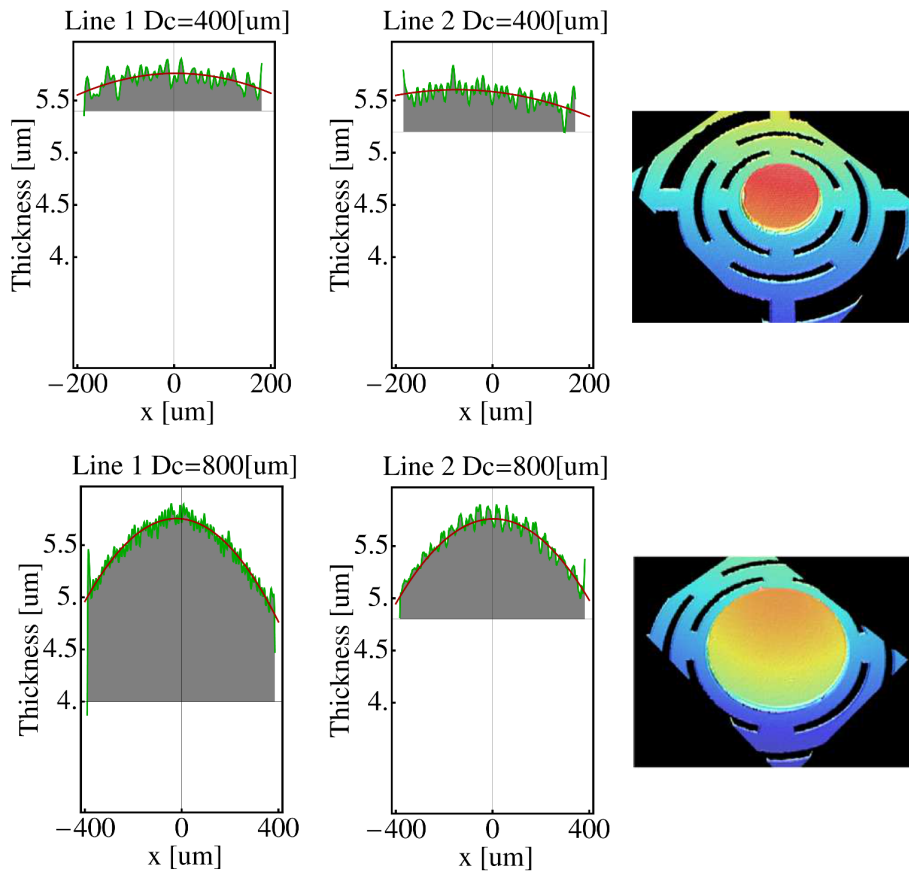


Figure 2.13: 2D and 3D images of the coating curvature and the coating morphology obtained by the Leica DCM 3D optical profiler using confocal mode with blue light with an objective magnification of 100 $\times$ , for the  $D1 = 400\mu\text{m}$  mirror diameter (top) and the  $D2 = 800\mu\text{m}$  mirror diameter (bottom).

# Chapter 3

## Experimental apparatus

In this chapter we are going to describe the typical experimental setup. Clearly, many variations have been used in attaining the results that are presented in the following chapters but the scheme in Fig. 3.1 well represent the backbone of our apparatus. Furthermore, more details are provided in the Appendix for crucial subsystems.

The light source is a Mephisto cw Nd:YAG operating at  $\lambda = 1064 \text{ nm}$  manufactured by InnoLight GmbH<sup>1</sup> with a maximum output power of  $500 \text{ mW}$  (for more details see Sec. B.1). After a  $40 \text{ dB}$  optical isolator, the laser radiation is split into two beams. The first one (beam A) is mainly used to lock the laser frequency to the cavity resonance, while the second one (beam B) is used to inject high power (with respect to beam A) into the cavity. Along the path of beam A, a resonant electro-optic modulator (EOM1) provides phase modulation at  $13.3 \text{ MHz}$  with a depth of about  $1 \text{ rad}$  used for a PDH detection scheme (Sec. C and Refs. [58, 59]). Beam A is also frequency shifted thanks to one or two acousto-optic. This shift is necessary for two reasons: first, we need to finely control the detuning from the cavity resonance of beam B, second, we need to compensate for the difference between the resonance frequencies of orthogonally polarized fields originated by stress-induced birefringence in the cavity. The actual birefringence depends strongly on the specific micromirror under study, with correspondent frequency shifts ranging from a few hundreds of kHz to about  $100 \text{ MHz}$ . As a consequence we use either one or two AOM according to the specific situation. If two AOM are used, they are set to work on opposite first diffraction order (discarding all other orders), allowing a fine control of the frequency difference between the two beams. Along the path of beam B a second, wideband, electro-optic modulator (EOM2) followed by a polarizer allows intensity control with two typical application: coherent mechanical excitation by radiation

---

<sup>1</sup>Nowadays owned by the Coherent group.

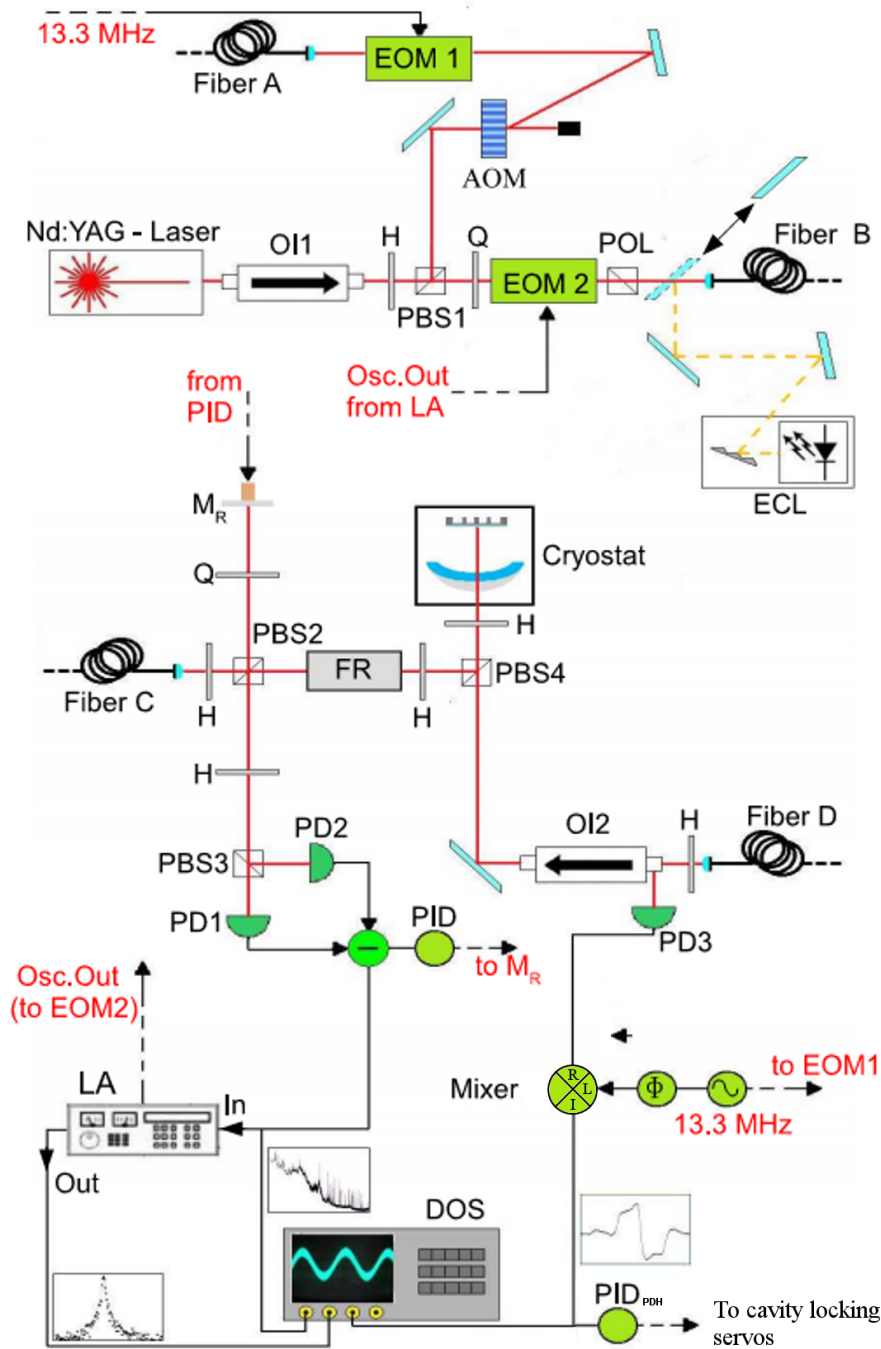


Figure 3.1: Typical basic scheme of the experimental apparatus. Optical isolator (OI); acousto-optic modulator (AOM); electro-optic modulator (EOM); half-wave plate (H); quarter-wave plate (Q); polarizing beam splitter (PBS); polarizer (POL); extended-cavity diode laser (ECL); electromagnetically driven mirror ( $M_R$ ); Faraday rotator (FR); photodiode (PD); servo-loop electronics (PID); Lock-in amplifier (LA); digital scope and acquisition system (DOS); delay line for phase control ( $\Phi$ ). Black lines indicate the electronic part of the setup.

---

pressure or intensity noise reduction by implementing a noise eater feedback loop (not shown in the figure). Both beams are, then, sent to the second part of the apparatus (a second optical bench) by means of single-mode, polarization maintaining, optical fibers whose terminations can be exchanged.

After one fiber, the exit (beam C) is aligned in a Michelson interferometer followed by a balanced homodyne detection. In details, a polarizing beam-splitter (PBS2) divides the beam into two parts, orthogonally polarized, forming the Michelson interferometer arms. At the end of the first one (reference arm) an electromagnetically-driven mirror  $M_R$  is used for phase-locking the interferometer in the condition of maximum displacement sensitivity. A double pass through a quarter-wave plate rotates by  $90^\circ$  the polarization of the this beam, which is then reflected by PBS2. The polarization of the second arm (sensing arm), sent to the sample holder in the cryostat vacuum chamber, is instead rotated by a double pass through a Faraday rotator. The sensing beam is focused with a waist ranging from about 40 to 80  $\mu m$  on the coated oscillator (or mode-matched to the cavity when it is present), and after reflection it is totally transmitted by PBS2, where it overlaps with the reference beam reflected by  $M_R$ . The overlapped beams are then monitored by an homodyne detection, consisting of a half-wave plate, rotating the polarizations by  $45^\circ$ , and a polarizing beam-splitter (PBS3) that divides the radiation into two equal parts sent to the photodiodes PD1 and PD2, whose outputs are subtracted. The signal obtained is a null-average, sinusoidal function of the path difference in the interferometer. Such a scheme (polarization Michelson interferometer: PMI) is barely sensitive to laser power fluctuations. The difference signal is used as error signal in the PMI locking servo-loop (the locking bandwidth is about 1  $kHz$ ) and also sent to the acquisition and measurement instruments (DOS).

The beam exiting from the second fiber (beam D), after an optical isolator, is mode-matched and overlapped to the sensing beam of the PMI, with orthogonal polarization, in a further polarizing beam-splitter (PBS4). The reflected beam is then diverted by the input polarizer of the optical isolator and collected by a fast photodiode for the PDH signal detection. The frequency shift between beams C and D, obtained thanks to the AOM, allows to eliminate any spurious interference and reduce the cross-talk between the two beams in the photo-detection. After the demodulation the PDH signal is sent to both the DOS and, if needed, to the cavity locking servo actuators.

The *standard configuration* sees fiber A connected to the output collimator of fiber D so that beam A-D can be used for the PDH frequency locking while fiber B is connected to fiber C so that beam B-C can be used for high power injection

into the cavity and, at the same time, the Michelson can be exploited to analyze the reflected field quadratures.

For the accurate measurement of the cavity length, we have used an auxiliary extended-cavity semiconductor laser (ECL), with optical feedback from a grating in the Littrow configuration, working around  $1064\text{ nm}$ . This laser can be coarse tuned by rotating the grating in a range covering several hundreds of  $\text{GHz}$ , wide enough to scan  $2 - 3$  FSR of our shortest cavity. Fine tuning is accomplished using the supply current and a piezo-electric transducer which translates the grating.

### 3.1 The sample holder

Each sample contains 9 micro-oscillators, set in a  $3 \times 3$  matrix placed on a  $35 \times 35\text{ mm}^2$  wafer sector. In Fig. 3.2 is shown the design of the sample holder assembly. The sample is housed on the main body (Fig. 3.2(3)), oscillators are not drawn) with the coated surface facing the front and blocked with a locking plate (Fig. 3.2(5)). A thermalization plate (Fig. 3.2(4)), made of OFHC copper, placed in between. Both plates have holes in correspondence of the oscillators, to allow a clear view for a IR CCD camera monitoring the oscillators for TEM modes identification. The main body size is  $54 \times 45 \times 8\text{ mm}$ . The thermalization plate is directly linked to the cold finger with a bundle of thin (diameter  $10\text{ }\mu\text{m}$ ) copper wires for mechanical decoupling, with an overall cross section of  $\sim 3\text{ mm}^2$ . Furthermore, a thin foil ( $0.1\text{ mm}$ ) of OFHC copper is placed between the sample and the main body to increase the cross section of the thermal link. The thermalization plate has also the role of damping wafer modes.

On the front side two translation stages, one vertical (Fig. 3.2(2)) and one horizontal (Fig. 3.2(1)), allow the alignment of the input mirror to form a cavity on the micromirror selected from all nine possibilities. The actual cavity that can be realized depends on the mirror holder and the mirror housed on it. We designed two versions of the mirror holder, one to obtain a cavity of length between  $8$  and  $9\text{ mm}$  and the other one for a shorter cavity with length between  $0.5$  and  $1\text{ mm}$ . In both cases the mirror is a standard silica mirror with high reflectivity coating on one side, an anti-reflection coating on the other side and a concave curvature radius of  $50\text{ mm}$ . Assuming a concave-plane configuration, the maximum cavity waist is nominally  $81\text{ }\mu\text{m}$  for the long cavity and  $49\text{ }\mu\text{m}$  for the short one. In the case of the short cavity, due to the limited tunability of our laser, we need to mount the input mirror on a piezo-electric actuator (see Sec. C for more details) to coarsely tune the cavity resonance by changing its length. The mirror (Fig. 3.3(1)) is glued

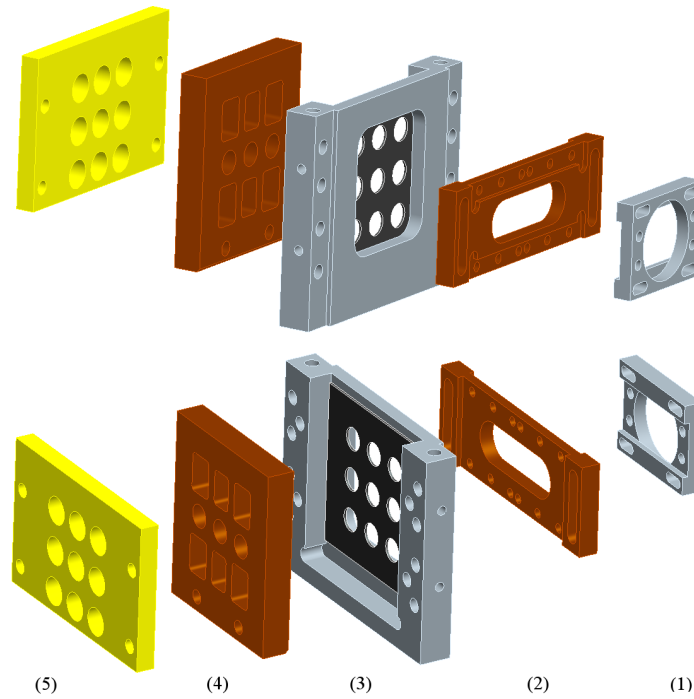


Figure 3.2: (Top) Front view. (Bottom) Back view. (1) horizontal translation stage with seat for the input mirror holder; (2) vertical translation stage; (3) Main body; (4) thermalization plate; (5) locking plate.

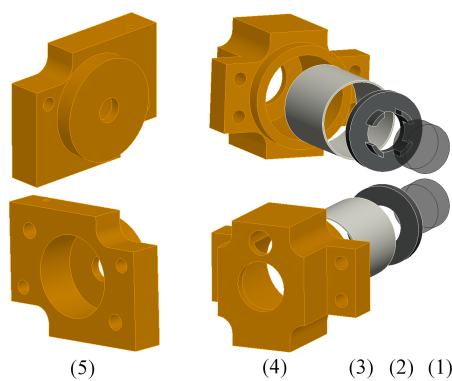


Figure 3.3: Top row: Back view. Bottom row: front view. Short cavity mirror holder (1) to (4). In details: (1) input silica mirror; (2) invar adapter ring; (3) piezo-electrical actuator; (4) main body. (5) Long cavity mirror holder.

to the actuator (Fig. 3.3(3)) that in turn is glued to the main body (Fig. 3.3(4)) of the mirror holder. An adapter ring (Fig. 3.3(2)) is not just required for the different diameter of the mirror and the actuator, but it is also useful to match the coefficient of thermal expansion of silica. For this reason the adapter ring is made of Invar.

On the contrary, the design of the mirror holder for the long cavity (Fig. 3.3(5)) is much simpler since in this case the tuning range of the laser is enough to cover more than one FSR. Clearly, both designs can be directly mounted on the horizontal translation stage of Fig. 3.2(1).

# Chapter 4

## Experimental characterization

In this chapter we are going to describe the experimental results, and the methods used in obtaining them, concerning the opto-mechanical characterization of the devices whose design and fabrication have been described in Cap. 2. We are going to start with the measurement of the mechanical parameters at room and cryogenic temperatures, to move then to the optical ones.

### 4.1 Mechanical parameters

The characterization of the oscillators mechanical parameters is usually performed with the setup in the standard configuration, but with the beam A-D blocked. However, a simple variation is quite useful, especially at low temperature. By reversing the fibers connections and turning off the resonant EOM (EOM1), we can use beam B-D to generate a mechanical excitation by modulating its intensity and, at the same time, perform a displacement measurement with the PMI using beam A-C. We will refer to this configuration as *conf2*. In both cases, the output of the homodyne detection is used to lock the PMI in the position of maximum sensitivity, corresponding to a null average signal. The lock bandwidth is about  $1\text{ kHz}$ .

The output of the PMI can be written as  $V_{out} = (V_{pp}/2)\sin(4\pi\Delta x/\lambda)$ , where  $V_{pp}$  is the peak-to-peak value of the PMI interference fringes and  $\Delta x$  the unbalance between the PMI arms. Once the PMI is actively locked around  $V_{out} \simeq 0$ , the output signal has a linear dependance on the mirror displacement, provided that the residual fluctuations remain within the linear region of the sinusoidal function. Power spectra are calculated and acquired using the integrated Fast Fourier Transform (FFT) analysis software of the digital scope. The measured spectrum  $S_V$ , in  $V^2/Hz$ , is calibrated through the expression  $S_{xx} = S_V(\lambda/2\pi V_{pp})^2$  where  $S_{xx}$  is the displacement

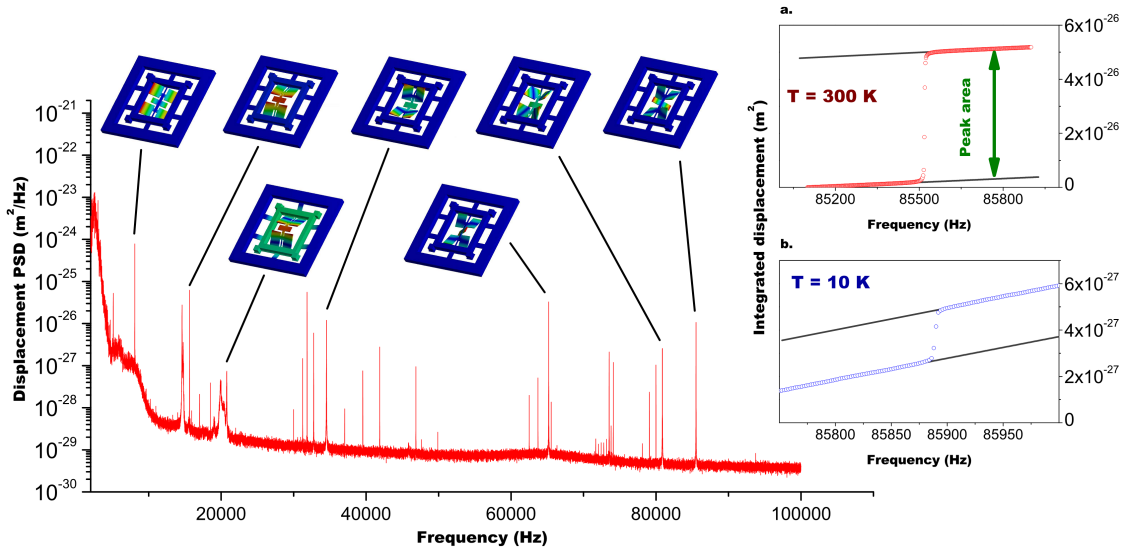


Figure 4.1: *Displacement noise spectrum and area below the mechanical peaks for a QPO design. Also shown are the displacement fields of identified normal modes. Inset: Integrated displacement around the AS2 mechanical resonance, at room (a) and cryogenic temperature (b).*

PSD in  $m^2/Hz$ . An example of such a spectrum is shown in Fig. 4.1. The reported spectra were recorded during the characterization of a QPO. We also show the normal mode identification, accomplished by comparing the spectral peaks with the expected resonance frequencies evaluated with FEM simulations, together with the displacement field of each mode. The sensing beam of the PMI was incident on one of the two coated areas on the head of the QPO so that not all the normal modes were detectable.

As we have shown in Chap. 1, the area  $A$  underlying a mechanical spectral peak is connected to the mechanical parameters through the relation  $A = \frac{k_B T}{m\omega_m^2}$ . This equation can be used to either extract the effective noise temperature or, assuming that the oscillator is at thermal equilibrium with the environment at temperature  $T_{bath}$ , to deduce its effective mass  $m$ . The area of the interesting mechanical peaks is measured by directly integrating over the spectrum, on a region wide several times the peak width. The procedure is illustrated in the inset of Fig. 4.1. The contribution of the (white) background noise is evaluated with a linear fit (dark gray lines) before and after the peak. The offset difference of the two lines provides the value of the peak area. We have verified that the result does not depend on the choice of the FFT windowing and sampling rate. Typical spectra are taken with a record

length of  $250 \text{ kSp}$  and a resolution of  $10 \text{ Hz}$  (sampling at  $2.5 \text{ MSp/s}$ ). Our measurements of  $A$  have an accuracy of about 30% (evaluated from their reproducibility). The ratio between the mass values given by  $A$  and by FEM simulations, evaluated for different oscillators, is on the average  $1.25 \pm 0.30$ , where the uncertainty reflects one standard deviation. This value is compatible with experimental and numerical uncertainty. Such agreement shows the self-consistency of our approach and justifies the assumption on the thermal origin of the excitation. A stronger argument in favor of this assumption is provided by the scaling of  $A$  with temperature. Assuming  $T_{\text{bath}} = 300 \text{ K}$  at room temperature, we first evaluate the effective mass. With its value we calculate the noise temperature of the mode when the oscillator is placed in the cryogenic environment. In order for the assumption to be justified, the calculated temperature and the measured one<sup>1</sup> have to be in agreement. This is always the case, within experimental uncertainties, for modes with a resonance frequency above about  $30 \text{ kHz}$ . A third possibility to test this assumption is to perform a measurement of the effective mass independently from thermal noise. This is done with the setup in *conf2*, in order to measure the mechanical transfer function by recording the coherent response to the radiation pressure excitation. Also in this case the results support the assumption under test.

In order to measure the mechanical quality factors we adopted two methods. For a good Q factor the typical spectral resolution, mentioned earlier, is not high enough. This is clearly visible in Fig. 4.2, where we show the spectral peak of the AS2 mode of our QPO both at room and at cryogenic temperature. Especially at low temperature, the mechanical line is not well resolved. We have used then a digital lock-in amplifier<sup>2</sup>, whose internal local oscillator is tuned at  $110 \text{ Hz}$  from the peak involved in the measurement. The beat note filtered by the output integrator of the lock-in, with a time constant of  $640 \mu\text{s}$ , is then analyzed by the scope with a resolution of  $0.1 \text{ Hz}$ . An example of the spectrum recorded in this way is shown in the left inset of Fig. 4.2 together with the fitting function composed of a mechanical resonance plus a flat background.

However, in some cases, even a resolution of  $0.1 \text{ Hz}$  is not enough. This always happens for the QPO and DPO designs at low temperature. We have therefore adopted a time-resolved detection technique. We used, again, intensity modulation of beam B-D (*conf2*), at a frequency very close to the mechanical resonance, for few minutes. Then, the modulation is switched off and the amplitude of the mechanical oscillation, monitored with the PMI, is measured by the lock-in amplifier whose

<sup>1</sup>We have two sensors, one on the cold finger and one on the sample holder.

<sup>2</sup>A Dual phase DSP lock-in amplifier model 7265 manufactured by Signal Recovery

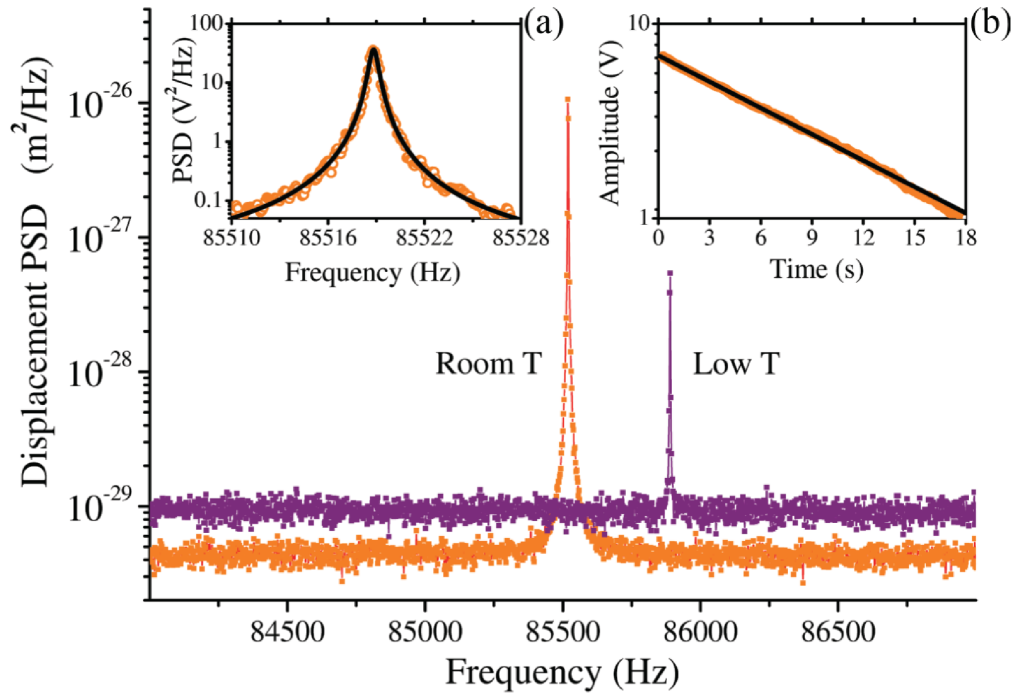


Figure 4.2: *Main panel: PSD around the peak corresponding to the AS2 mode of the QPO; room temperature data are shown in purple and low-temperature in orange. (a) Frequency downshifted spectra of the same spectral line plus fit. (b) Amplitude exponential decay plus fit.*

output quadratures are acquired by the scope. The oscillation amplitude is evaluated off-line and the mechanical quality factor is then given by the simple relation  $Q = \omega_m \tau_m / 2$ , where  $\tau_m$  is the time constant of the amplitude decay. An example of the temporal evolution of the oscillation amplitude is shown in the right inset of Fig. 4.2, where we also display the fitting exponential decay.

We characterized a set of oscillators with different geometrical and mechanical parameters and the results are summarized in Tab. 4.1. The labels  $D1 - 4$  refer to double wheel oscillators. The device that shows the best performances in terms of mechanical losses is the QPO with a  $Q = 2.6 \cdot 10^6$  which indicate that for this design the device can actually reach a regime where the dominating loss mechanism is the intrinsic structural dissipation of silicon, as expected from FEM simulations. However, the situation is a bit different for the double wheel oscillators. The typical quality factor at low temperature is of the order of  $10^4$ , and just in one instance we measured a quality factor that reached the nonetheless remarkable value of  $10^5$ . We point out that this figure represents an improvement of more than one order of

magnitude with respect to our previous generation of double wheel oscillators [24]. Moreover, it indicates that this design is, indeed, effective in reducing losses from the coating layer.

On the other hand, the rather low  $Q$  values observed for other devices suggest that an additional or a stronger than expected loss mechanism is dominating. We attribute this behavior to the coupling of the mirror mode to modes of the wafer/sample holder so that one can infer that the suspended frame does not provide sufficient isolation. Indeed, in some cases we observed a wide range of variation of the  $Q$  factor, at room temperature, depending on the clamping of the sample, especially for those oscillators with quality factors well below expectation. We remark that this is not the case for the DPO and QPO since the AS1 and AS2 modes are nodally suspended. The sample mounting changes the density and overall loss of wafer modes at the resonator frequency in an unpredictable and irreproducible way. We believe that the more effective solution is the improvement of the isolation by introducing a second isolation wheel, or designing a geometry that realizes a nodal suspension for the mirror mode of interest. We could even implement both solutions. As a final remark on the characterization of the mechanical parameters of

		Mass (kg) $\pm 30\%$	Freq. (kHz) $\pm 1\%$	$Q$ $T = 300 K$ $\pm 10\%$	$Q$ $T = 10 K$ $\pm 10\%$
D1		$1.4 \cdot 10^{-7}$	129.0	$2.8 \cdot 10^4$	$1.0 \cdot 10^5$
D2		$2.2 \cdot 10^{-7}$	81.4	$4.8 \cdot 10^3$	$1.2 \cdot 10^4$
D3		$2.0 \cdot 10^{-7}$	94.0	$9.7 \cdot 10^3$	$1.4 \cdot 10^4$
D4		$8.8 \cdot 10^{-8}$	210.6	$1.0 \cdot 10^4$	$2.8 \cdot 10^4$
DPO	AS1	$1.1 \cdot 10^{-6}$	30.4	$6.8 \cdot 10^4$	$1.1 \cdot 10^6$
	AS2	$1.6 \cdot 10^{-6}$	46.2	$8.7 \cdot 10^4$	$8.5 \cdot 10^5$
QPO	AS1	$2.7 \cdot 10^{-7}$	65.2	$8.7 \cdot 10^4$	$8.5 \cdot 10^5$
	AS2	$3.0 \cdot 10^{-7}$	85.5	$1.5 \cdot 10^5$	$2.60 \cdot 10^6$
DPO	AS1	$9.0 \cdot 10^{-8}$	70.9	$1.5 \cdot 10^5$	
	AS2	$1.1 \cdot 10^{-6}$	86.4	$1.5 \cdot 10^5$	

Table 4.1: Parameters of the micro-mirrors measured at room and cryogenic temperature.

our devices, we show in Tab. 4.1 the comparison between FEM predictions and the actual measured values for our best micro-oscillator, namely the QPO. The table

could be extended to all the devices and the agreement would be the same with the only exception of the Q factor for double wheel oscillators other than D1.

		FEM			Low T Exp.		
		Freq. (kHz)	Mass (kg)	Q $T = 4.2 K$	Freq. (kHz)	Mass (kg)	Q $T = 10 K$
		$\pm 5\%$	$\pm 30\%$	$\pm 10\%$	$\pm 1\%$	$\pm 30\%$	$\pm 10\%$
QPO	AS1	67.0	$2.2 \cdot 10^{-7}$	$4.0 \cdot 10^6$	65.2	$2.7 \cdot 10^{-7}$	$8.5 \cdot 10^5$
	AS2	89.0	$2.2 \cdot 10^{-7}$	$2.0 \cdot 10^6$	85.5	$3.0 \cdot 10^{-7}$	$2.6 \cdot 10^6$

Table 4.2: Parameters of the micro-oscillators measured at cryogenic temperature in comparison with FEM simulation results.

## 4.2 Optical parameters

The optical losses are characterized by constructing two cavities. The first one is  $0.6 \text{ mm}$  long (with the mirror holder assembly of Fig. 3.3(1 – 4)), with an input mirror with intensity transmission of  $T_m = 50 \text{ ppm}$ . The second one is  $8.3 \text{ mm}$  long (mirror holder of Fig. 3.3(5)) with  $T_m = 110 \text{ ppm}$ . The characterization consists in determining the overall optical losses by measuring the cavity linewidth  $2\kappa$ .

The cavities are pre-aligned in a nominally class100 laminar flow cabinet. The cleanliness of the surfaces is a critical aspect. Usually, many attempts are necessary in order to attain a good cavity. Prior to each attempt the input coupler and the coated surface of the device are cleaned with spectroscopic grade acetone. We have realized a simple setup inside the cabinet to detect the field reflected from the cavity in order to perform a pre-screening based on a rough estimation of the optical linewidth. If the results are satisfactory, the sample holder with the formed cavity is mounted inside the cryostat vacuum chamber without ever leaving the cabinet. Once the chamber is closed, it is then moved to its seat on the optical bench. For both beam D and C, a mode matching to the cavity of  $85 - 90\%$  is easily attained while a value of  $95 - 96\%$  is usually reached with some effort.

For both cavities, the linewidth measurement is performed by scanning the resonance with the phase-modulated beam A-D and using the sidebands frequencies to calibrate the scan. For the long cavity this is accomplished by scanning the laser wavelength while for the short one we actually change the cavity length with the piezo-actuator that holds the input mirror. In practice, one can fit the PDH signal

(see Chap. C) or the Lorentzian dips in the intensity of the reflected field. An example of the latter is shown in Fig. 4.3. Particular care has to be taken in order to avoid

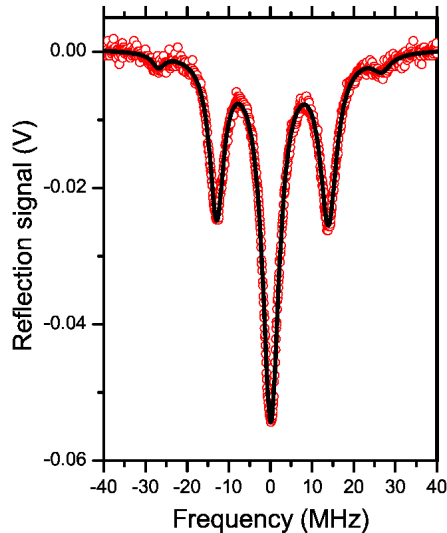


Figure 4.3: *Signal obtained by detecting the laser beam reflected by the short cavity; the dips are fitted with five Lorentzian peaks for the carrier and the FM modulation sidebands used for calibrating the scanning.*

any phenomena that can deform the optical response while performing the scan. In particular, photothermal effects, that deform the Lorentzian in a different way depending from the direction of the scan (blue to red or viceversa), or displacement noise that modulates the cavity resonance. Indeed, the beam intensity should be low enough to avoid the former while, for the latter, the scan should be fast compared to the typical frequencies of acoustic noise (usually  $\leq 1 - 2 \text{ kHz}$ ) but slow compared to the response time of the cavity, or of the photodiode, whichever is the smallest.

An important example of how this aspect can complicate the measurement has been the characterization of the QPO. Indeed, to avoid such deformation effects we had to use a more refined technique. Namely, we used  $\sim 3 \mu\text{W}$  in both beam A-D and B-C (sensing arm) and instead of recording the dips in the reflected intensity, we used the PMI to increase the signal-to-noise ratio: the reference beam of the PMI works as local oscillator for the field reflected from the cavity. The signal detected in the PMI is proportional to  $\sqrt{I_R I_S} \text{Re}[(1 - \eta + \eta H^r) \exp(-i\theta)]$ , where the phase  $\theta = \frac{4\pi}{\lambda} \Delta L$  is determined by the imbalance  $\Delta L$  of the two arms, with intensities  $I_R$  (reference -  $I_R = 1 \text{ mW}$ ) and  $I_S$  (sensing -  $I_S = 3 \mu\text{W}$ ). Normalizing to the fringe amplitude with the cavity out of resonance, i.e., with  $\Delta_n \rightarrow \infty$ , we can write the

PMI signal as

$$S_{PMI} = \cos\theta \left[ 1 - \frac{C}{1 + \Delta_n^2} \right] + \sin\theta \frac{C\Delta_n}{1 + \Delta_n^2} \quad (4.1)$$

with  $C = \eta(1 - \zeta)$ . The coefficient  $\eta$  accounts for the mode-matching both in the coupling to the cavity and between the arms of the PMI. We estimated both, the former from the residual power in the cavity transverse modes while the latter from the fringe contrast seen by the homodyne photodiodes. Both are above 90%.

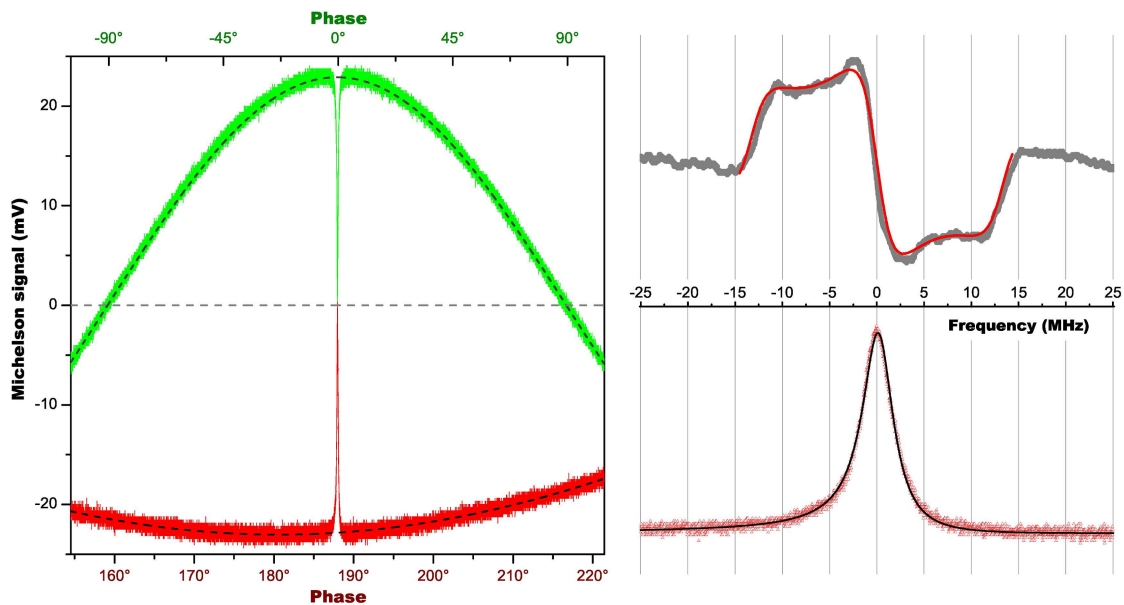


Figure 4.4: *Measurement of the Finesse in a Fabry-Pérot cavity built with a mirror on the head of a QPO. The field reflected from the cavity is measured in a Michelson interferometer, where the cavity resonance appears as a dip on the bright fringe (an upper and a lower bright fringes are shown respectively as green and red traces in the left panel). The depth of the peak gives the coupling coefficient of the cavity, while its width (see on the right an enlarged view of the peak in the lower fringe) gives the cavity linewidth. The frequency calibration in this latter measurement is provided by the distance between the sidebands of the PDH signal (shown above the peak), detected at the same time in a reference beam.*

In Fig. 4.4 we report portions of the PMI signal taken with  $\theta$  around  $0^\circ$  and  $180^\circ$ , when  $\Delta L$  is slowly swept. The  $\theta$  axes are calibrated from fits with a cosine function on signal regions outside the cavity resonance (fitting dashed lines are shown in the figure). During the signal acquisition, the cavity detuning is scanned around resonance; in the shown portions of the signal the cavity resonance condition  $\Delta_n = 0$  happens in near-coincidence with the extremal values of  $\cos\theta$ , therefore the

dip shapes are close to Lorentzian functions. Both dips touch the null value of the signal, visibly demonstrating that the cavity is very close to optimal coupling ( $\zeta \simeq 0$ ). Also in this case, the calibration of  $\Delta_n$  is obtained thanks to the PDH signal, recorded simultaneously to the PMI signal, but the fits of the dip shapes are performed using the complete expression of  $S_{PMI}$ . The fitting procedure gives a cavity resonance full linewidth of  $2\kappa = 3.9 \pm 0.2 \text{ MHz}$ , and a peak depth  $C = 0.96 \pm 0.2$  (uncertainties evaluated from repeated measurements). The linewidth, together with the value of  $\text{FSR} = 252 \text{ GHz}$  (see below the description of the measurement), corresponds to a Finesse of  $65000 \pm 3000$ . Using Eq. 1.34, together with the input coupler transmission of  $T_m = 50 \pm 5 \text{ ppm}$ , allows to calculate cavity losses of  $\Sigma = 47 \pm 10 \text{ ppm}$  and a coupling coefficient of  $\zeta = -0.03 \pm 0.16$ . From this last value and the measured  $C$  we extract  $\eta = 0.93 \pm 0.14$ , in agreement with the independent evaluation of the mode-matching.

The linewidth estimation is usually simpler with the longer cavity since a sufficiently low uncertainty in the measurements is achieved with the fits of the PDH signal. Indeed, we measured a Finesse of  $40000 \pm 4000$  that, together with the nominal input coupler transmission of  $110 \pm 5 \text{ ppm}$ , gives a total cavity loss of  $47 \pm 20 \text{ ppm}$ .

The theoretical transmission of the mirror coated in the oscillators is below  $10 \text{ ppm}$ . This is indeed obtained in a test silica substrate coated together with the Si wafer. The same coating on super-polished silica substrates allowed us to measure finesse exceeding  $2 \times 10^5$ . As we have shown, we observed with the short cavity an overall optical loss of  $\Sigma \simeq 50 \text{ ppm}$ . This value is compatible with the  $\sim 40 \text{ ppm}$  that are calculated using Eq. 2.7 with the roughness measured by AFM: the residual  $10 \text{ ppm}$  is a very satisfactory estimation for the losses due to absorption and transmission on the MOMS mirror and absorption and scattering on the input coupler.

On the other hand, such a value of Finesse, while obtained on different samples, is only achieved on some regions of the MOMS mirrors. Changing the position of the beam on the sample, the measured Finesse of the short cavity varies, indeed, between 60000 and 40000, yielding losses between  $50 \text{ ppm}$  and  $100 \text{ ppm}$ . With the long cavity, the Finesse varies between 40000 and 22000, and the corresponding calculated losses between  $50 \text{ ppm}$  and  $180 \text{ ppm}$ . In any case, the contribution of diffraction losses due to the finite MOMS mirror size is estimated to be negligible. Indeed, we have taken care to avoid beam positions too close to the mirror edge, and the measurements with the long cavity are just taken with the larger mirror diameters.

We point out that the longer cavity has a larger waist, therefore the mirror must be good in a wider region to guarantee a high finesse. Moreover, when one takes into account the MOMS mirrors convexity, the calculated beam size on the mirror

increases from  $43 \mu m$  to  $\sim 50 \mu m$  for the shorter cavity, while for longer one it can reach a value up to  $\sim 90 \mu m$  from the nominal  $79 \mu m$ . Actually, the spread of the loss measurements with the short cavity (i.e., with the smaller waist), as well as the larger losses generally experienced by the long cavity, can in part be attributed to edge debris sticking to the mirror surface (see figure 2.12). An appropriate cleaning sequence for the removal of such debris is still to be developed, as all wet processes, while cleaning the surface, could generate new particles from the edge of the mirror oxide multilayer. A further feature that is probably crucial for explaining our results is the macro-shape of the mirrors, that is determined by the original wafer waviness, on the scale of several tens  $\mu m$ , and by the stress induced by the coating.

A further systematic investigation of this aspect can be performed by comparing surface profiles, weighted over appropriate Gaussian functions, with Finesse measurements along the surface. Such investigation, possibly performed after the different steps of fabrication, would clarify this issue and help to further optimize the process and the final experimental setup.

We also measured the distance between cavity transverse modes that allowed us to deduce the local curvature of the MOMS mirror according to the following equation [44]

$$\frac{\nu_{m,n} - \nu_{0,0}}{FSR} = \frac{1}{\pi} \arccos \left[ \sqrt{\left(1 - \frac{L_{cav}}{R}\right) \left(1 - \frac{L_{cav}}{R_{MOMS}}\right)} \right] (m+n) \quad (4.2)$$

here  $\Delta\nu = \nu_{m,n} - \nu_{0,0}$  is the frequency difference between a longitudinal mode and a transverse mode  $(m, n)$ , where  $m$  and  $n$  are mode numbers (i.e., number of zeros) in the case of a rectangular geometry (for a cylindrical one, the term  $(m+n)$  is replaced by  $(2p+l)$  where  $p$  and  $l$  are the radial and angular mode numbers respectively). We find that the coated MOMS have convex surfaces with radii generally varying between  $0.1$  and  $0.3 m$ . Such evaluations confirm the direct measurements performed with the profilometer, described in Chap. 2.

A fundamental parameter of the cavity is its length. While for the longer cavity mechanical tolerances and simple measurements with a micrometer allows the determination of  $L_{cav}$  with a good accuracy ( $\sim 1\%$ ), the matter is different for the shorter one. In this latter case, to determine  $L_{cav}$  we measured the FSR by means of an auxiliary ECL, sent to the cavity together with the Nd:YAG laser beam. The cavity length is slowly scanned over one FSR, and the ECL is tuned in order to be on resonance at the same time as the Nd:YAG, but on a different longitudinal mode. The two laser frequencies are then measured by means of a wave-meter with an accuracy of  $100 MHz$ . From their difference one obtains the FSR, or a multiple

of it, from which is determined  $L_{cav}$ .

The last relevant parameter is the birefringence that arises from the coating induced stress. We observe large variations from one sample to the other, as well as a dependance on the position within each sample and on the sample mount. The phase difference in the reflection coefficient between orthogonal polarizations is generally in the range  $(0.3 - 10) 10^{-4} rad$ .

In Chap. 2 we described two process sequences developed in order to increase the process yield and to study the effects of different production strategies on the final performances of the devices. Both sequences induce small variations of the mirror's surface roughness with respect to the initial level, whereas the overall performances of the device are not affected. The first sequence ( $P1$ ) allows an easier manipulation of the wafers inside the Deep-RIE chamber, as loading issues may occur when using a resist layer as protection layer in the second process sequence ( $P2$ ). On the other hand, the second sequence eases the handling during the coating deposition by IBS.

With the experimental characterization presented in this chapter we have verified that the processes guarantee both high quality and high aspect ratio structures by preserving the original roughness of the mirror's surfaces.

As an example of the obtained overall performances, considering the mechanical and optical characteristics that we have measured in the cavity with a quad-paddle oscillator, we can infer [26] that at  $4.5 K$  with an input laser power of  $2 mW$ , the radiation pressure quantum noise equals the thermal noise. In table 4.4 we summarize the performance of our devices in comparison with a number of oscillating mirrors described in the literature. Other kinds of opto-mechanical systems (such as refractive membranes, nano-photonics systems, breathing cavities with whispering gallery modes, etc.) are also very useful tools for quantum mechanics [80, 81, 82], however we restrict our analysis to devices allowing a more direct comparison with ours.

The last column reports the ratio between radiation pressure quantum noise and thermal noise at a background temperature of  $4 K$ ,  $S_{qn}/S_{th}$ , evaluated when the input power  $P_{in}$  is such that temperature increase at the mirror due to power absorption is  $\Delta T = 1 K$ . We have used the estimated thermal impedance estimated from the oscillators thickness, a form factor deduced from the shape, and the thermal conductivities at  $4 K$  in Tab. 4.3. For all the mirrors we consider an absorption coefficient of  $10 ppm$ . This is a conservative value for Si substrates (few ppm is a realistic value), it is over-estimated for the silica mirror (where the absorption is probably around  $1 ppm$ ), and probably under-estimated for GaAlAs and gold mirrors. A more accurate evaluation (using FEM simulations) is reported for

our devices in Refs. [25, 26]. To evaluate the thermal noise  $S_{th}$  we have used the parameters reported in Tab. 4.4 even when they are measured at room temperature; some variations are expected at 4 K (in particular a higher  $Q$ ), but we have not tried any extrapolation. Due to the several approximations, this figure must be considered

Table 4.3: Thermal conductivities used for the evaluation of the thermal impedance  $R_{4K}$  at 4 K reported in Tab. 4.4.

	$k \text{ Wm K}^{-1}$
Si [62]	300
Silica [83]	0.12
oxides m.l. <sup>a</sup> [78]	0.07
SiN [84]	0.1
quartz [85]	400
AlGaAs [86]	300

<sup>a</sup> m.l. stands for multi-layer

as an order-of-magnitude estimate. It is however useful to compare different kinds of micro-oscillators. In particular, it shows that thin oscillators allow to obtain a low mass and are useful for several kinds of opto-mechanical experiments, for which they are usually conceived (e.g., on optical cooling, pulsed opto-mechanics, strong opto-mechanical coupling, quantum superposition), while the relatively higher bearable power makes our systems particularly suitable for experiments aiming to create ponderomotive squeezing.

Table 4.4: Comparison of different kinds of oscillating mirrors described in the literature. Unless differently specified, in these devices the mirror is made by a multi-layer of alternate Si/Ti or Si/Ta oxides, or AlGaAs.

Ref	shape <sup>a</sup>	substrate material <sup>b</sup>	thick. ( $\mu\text{m}$ )	T (K)	freq. (kHz)	mass (g)	$Q$	finesse	$R_{\text{AK}}$ (K/W)	$S_{\text{qn}}/S_{\text{th}}$ @ 1 mW	$S_{\text{qn}}/S_{\text{th}}$ @ $\Delta T=1\text{K}$
[87]	torsional	Si	380	4.5	26	$1.0 \times 10^{-2}$	$2.2 \times 10^6$	15000	$3 \times 10^1$	$1 \times 10^{-4}$	$4 \times 10^{-1}$
[56]	beam	Si	60	300	814	$1.9 \times 10^{-4}$	$1.0 \times 10^4$	30000	$1 \times 10^2$	$3 \times 10^{-5}$	$5 \times 10^{-3}$
[88]	cantilever	Si	2	300	12	$2.4 \times 10^{-8}$	$1.4 \times 10^5$	2100	$2 \times 10^4$	$3 \times 10^{-1}$	$8 \times 10^0$
[89]	beam fsl <sup>c</sup>	GaAlAs	5.5	4	1970	-	$2.0 \times 10^4$	5500	$9 \times 10^2$	$2 \times 10^{-2}$	$6 \times 10^{-1}$
[90]	beam	SiN	1	300	950	$1.5 \times 10^{-7}$	$6.7 \times 10^3$	14000	$1 \times 10^7$	$1 \times 10^{-3}$	$9 \times 10^{-6}$
[91]	beam	SiN	1	5.3	945	$4.3 \times 10^{-8}$	$3.0 \times 10^4$	3900	$1 \times 10^7$	$2 \times 10^{-2}$	$1 \times 10^{-4}$
[92]	beam fsl	Si/Ta ox.	5.4	20	350	$4.0 \times 10^{-7}$	$6.0 \times 10^3$	8900	$6 \times 10^6$	$3 \times 10^{-3}$	$2 \times 10^{-5}$
[93]	beam ns fsl <sup>d</sup>	GaAlAs	7	20	3800	$1.5 \times 10^{-7}$	$8.0 \times 10^4$	26000	$1 \times 10^3$	$7 \times 10^{-2}$	$8 \times 10^{-1}$
[94]	plano-convex	silica	2500	300	1130	$7.2 \times 10^{-2}$	$7.6 \times 10^5$	110000	$8 \times 10^3$	$5 \times 10^{-4}$	$9 \times 10^{-5}$
[95]	trampoline	SiN	0.3	300	10	$1.1 \times 10^{-7}$	$9.4 \times 10^5$	29000	$8 \times 10^9$	$3 \times 10^2$	$7 \times 10^{-4}$
[95]	trampoline	SiN	0.3	300	46	$6.0 \times 10^{-8}$	$1.9 \times 10^5$	35000	$8 \times 10^8$	$5 \times 10^1$	$7 \times 10^{-4}$
[95]	trampoline	SiN	0.5	300	158	$6.0 \times 10^{-8}$	$4.3 \times 10^4$	38000	$6 \times 10^7$	$4 \times 10^0$	$8 \times 10^{-4}$
[95]	trampoline	SiN	0.5	0.3	123	$6.0 \times 10^{-8}$	$1.3 \times 10^5$	-	$6 \times 10^7$	-	-
[15, 96]	micropillar <sup>e</sup>	quartz	20	300	3600	$7.0 \times 10^{-5}$	$2.0 \times 10^6$	300	$3 \times 10^2$	$9 \times 10^{-7}$	$4 \times 10^{-3}$
[15, 96]	micropillar	quartz	20	2	3700	$7.0 \times 10^{-5}$	$3.0 \times 10^3$	40000	$3 \times 10^2$	$2 \times 10^{-5}$	$7 \times 10^{-4}$
[26]	<b>quad-pad</b> <sup>f</sup>	Si	70	10	86	$2.2 \times 10^{-4}$	$2.6 \times 10^6$	62000	$2 \times 10^2$	$6 \times 10^{-1}$	$2 \times 10^1$
[25]	<b>wheel</b> <sup>g</sup>	Si	70	10	129	$1.4 \times 10^{-4}$	$1.0 \times 10^5$	55000	$1 \times 10^2$	$1 \times 10^{-2}$	$9 \times 10^{-1}$

<sup>a</sup> ns: oscillator with nodal suspension; fsl: free-standing multi-layer.

<sup>b</sup> Si/Ta ox.: alternate multi-layer of  $\text{SiO}_2$  and  $\text{Ta}_2\text{O}_5$ ; AlGaAs: alternate multi-layer of  $\text{Al}_x\text{Ga}_{1-x}\text{As}$  with different values of  $x$ .

<sup>c</sup> The authors do not give the effective mass of the mode. However, they directly calculate the thermal noise at cryogenic temperature ( $3 \text{ fN}/\sqrt{\text{Hz}}$ ).

<sup>d</sup> The authors do not give the effective mass of the mode, therefore we use here the physical mass of the beam.

<sup>e</sup> The optical coating is a thin layer of gold.

<sup>f</sup> This work, Fig. 2.3(e,f)

<sup>g</sup> This work, Fig. 2.2(a,b)



# Chapter 5

## Toward squeezed light detection

In this chapter we start discussing experimental results achieved in the pursuit of ponderomotive squeezed light generation and detection. In particular we discuss, in section 5.1, an optomechanical effect affecting frequency noise that was already discussed in the literature but whose relevance in aiding squeezing generation was not recognized. The results presented here on this topic can be found also in Ref. [28]. In section 5.2 we discuss how the PDH cavity locking affects the dynamical backaction and we show that it can lead to dynamical instability if a mechanical mode with sufficient low effective mass is inside the frequency lock bandwidth. In this latter section we clarify why, for the moment, we have not been able to generate squeezed light despite having devices with, in theory, sufficiently high performances.

### 5.1 Frequency noise cancellation

Ponderomotive squeezing has been demonstrated experimentally, as we mentioned in Chap. 1, with a maximum noise reduction below the shot noise of 1.7 dB [20] at frequencies in the MHz range. However, quadrature squeezing is particularly useful for improving sensitivity at lower frequencies, in the audio-band, for example for improving the sensitivity of gravitational wave (GW) interferometers [97]. At lower frequencies, however, various sources of technical noise have detrimental effects on squeezing, making low-frequency ponderomotive squeezing much more difficult to achieve. Indeed, we included in the model presented in Chap. 1 classical intensity and frequency/displacement noise. In this section we show that the latter, the strongest technical noise source in our system, can be almost completely canceled around the *bare* mechanical resonance frequency thanks to the destructive interference between the frequency noise directly affecting the cavity and the same frequency noise trans-

duced by the mechanical resonator. We demonstrate such an effect experimentally in a frequency band around  $100\text{ kHz}$ .

The existence of this cancellation can already be predicted looking at Eq. 1.73. Indeed, using the definition in Eq. 1.72, the contribution to the output signal proportional to  $\dot{\phi}$  is

$$a_{out}(\omega) = i [\alpha_s A_3(\omega) - \alpha_s^* A_4(\omega)] \dot{\phi}(\omega) \propto \frac{\chi_{eff}(\omega)}{\chi_0(\omega)} \dot{\phi}(\omega) \quad (5.1)$$

where

$$\chi_0(\omega) = \omega_w (\omega_m^2 - \omega^2 - i\omega\gamma_m)^{-1} \quad (5.2)$$

is the bare susceptibility of the mechanical resonator. In the usual case of a large mechanical quality factor, at the unperturbed mechanical resonance  $\omega = \omega_m$ ,  $\chi_0$  diverges and *the output signal is unaffected by frequency noise*. Therefore we expect a narrow bandwidth around  $\omega = \omega_m$  where noise is strongly suppressed. This cancellation takes place at any cavity detuning except at resonance, when  $\chi_{eff}(\omega) = \chi_0(\omega)$ . In this case in fact, the oscillator is sensitive only to intensity noise and cannot transduce phase/frequency noise.

This frequency noise cancellation is related to the backaction amplification of a signal discussed in Refs. [56, 98] and demonstrated in Ref. [94], that was considered as a possible way to increase the sensitivity GW interferometers. Indeed, both effects are described by the same "amplification" ratio  $\chi_{eff}(\omega)/\chi_0(\omega)$ , because the system responds in the same way to cavity length variations due either to an external signal or to frequency noise modulations. However, here we exploit this interference phenomenon for a different purpose, i.e., for reducing phase/frequency noise in the optical output rather than for amplifying an external signal. We shall see later that such a noise cancellation is essential for the possibility of generating and detecting ponderomotive squeezing at hundreds of  $\text{kHz}$ .

The physical origin of the phenomenon of noise cancellation can be understood also with a simple model. As we have seen, a single classic variable (in our notation,  $\dot{\phi}$ ) describes the fluctuations in the cavity detuning, and it can be used to take into account both the laser frequency noise and the cavity length fluctuations excluding the oscillator modes with low effective mass, for which it is necessary to include in the description their response to radiation pressure. As a consequence, we can consider in this simple model all such noise sources as contributions to effective position fluctuations of the input cavity mirror.

The system can be sketched (see Fig. 5.1) as a first mirror with position  $y(t)$ , that is subjected to displacement noise, linked by the optical spring  $K_{opt}$ , defined in

Eq. 1.77, to the micromirror that in turn is bound, with elastic constant  $K_m$ , to a rigid frame. Assigning a mass  $m$  to the micromirror whose position  $x(t)$  is fluctuating around equilibrium, the equation of motion for  $x$ , neglecting the damping, is

$$m\ddot{x} + K_mx - K_{opt}(y - x) = 0 \quad (5.3)$$

giving the solution, for the Fourier-transformed variables  $\tilde{x}(\omega)$  and  $\tilde{y}(\omega)$ ,

$$\tilde{x} = \frac{K_{opt}}{K_m + K_{opt} - m\omega^2}\tilde{y} = \frac{\omega_{opt}^2}{\omega_m^2 + \omega_{opt}^2 - \omega^2}\tilde{y} \quad (5.4)$$

and for the distance  $(y - x)$ , that corresponds to the cavity detuning in real systems, we have

$$\tilde{y} - \tilde{x} = \frac{\omega_m^2 - \omega^2}{\omega_m^2 + \omega_{opt}^2 - \omega^2}\tilde{y} = \frac{\chi_{eff}}{\chi_0}\tilde{y}. \quad (5.5)$$

We have therefore a cancellation of the effect of the mirror position noise on the cavity length when  $\chi_0 \gg \chi_{eff}$ , i.e., around the bare oscillator resonance. The cancellation on the cavity detuning is effective also on the intracavity and output fields.

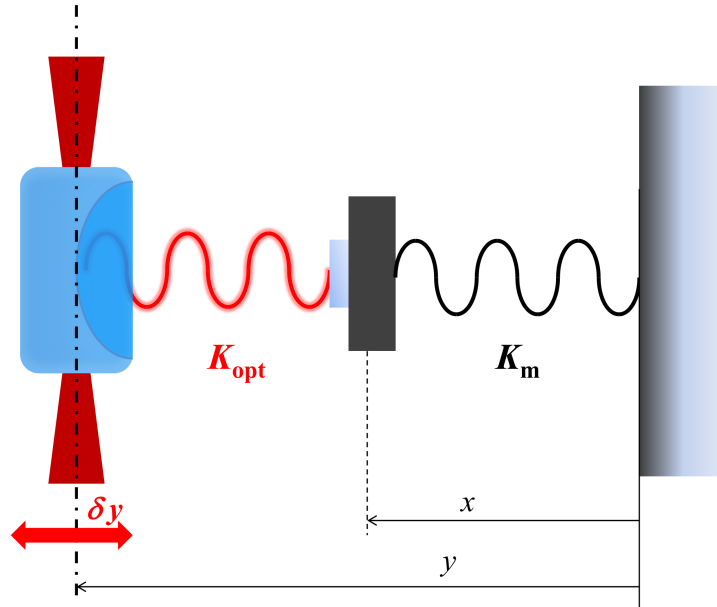


Figure 5.1: Scheme of the simplified model explaining the effect of noise cancellation. The oscillating micromirror is linked by a mechanical spring ( $K_m$ ) to a fixed frame and by the optical spring  $K_{opt}$  to the input mirror, modeled as a rigid fluctuating bound.

### Residual phase noise in homodyne detection

Before moving to the experimental demonstration of the frequency noise cancellation effect, we introduce an additional noise term that is usually unavoidable when measuring the noise properties of a quadrature of the cavity output field, that is, the residual phase fluctuations of the local oscillator. We assume a homodyne detection scheme for the measurements of quadrature spectra.

To evaluate the effects of this additional noise source, it is convenient to express the quadrature output spectra at phase  $\theta$  in the frame defined by the cavity output field. The quadrature noise spectrum  $S_{out}^\theta(\omega)$ <sup>1</sup> is then written in terms of the noise spectra of the amplitude ( $X^{out} \equiv a_0$ ) and phase ( $Y^{out} \equiv a_{\pi/2}$ ) quadratures,  $S_X(\omega)$  and  $S_Y(\omega)$  respectively, and their symmetrized correlation spectrum  $S_{X,Y}(\omega)$ , as

$$S_{out}^\theta(\omega) = \frac{S_X(\omega) + S_Y(\omega)}{2} + \frac{S_X(\omega) - S_Y(\omega)}{2} \cos(2\theta) + S_{X,Y}(\omega) \sin(2\theta). \quad (5.6)$$

We recall that, with our normalizations, the output light is squeezed at phase  $\theta$  when  $S_{out}^\theta(\omega) < 1$ , since 1 represents the shot noise level, and that the Heisenberg uncertainty relation implies the inequality  $S_X(\omega)S_Y(\omega) - [S_{X,Y}(\omega)]^2 \geq 1$ .

When the phase of the local oscillator has residual random fluctuations, the homodyne noise spectrum must be averaged over the distribution of the fluctuating phase  $\theta$ , which we take as a Gaussian variable with variance  $\Delta\theta$  and mean value  $\bar{\theta}$ , i.e.,

$$\bar{S}_{\Delta\theta}^{\bar{\theta}}(\omega) = \frac{1}{\sqrt{2\pi}\Delta\theta} \int_{-\infty}^{\infty} d\theta' \exp\left[-\frac{(\theta' - \bar{\theta})^2}{2(\Delta\theta)^2}\right] S_{out}^{\theta'}(\omega), \quad (5.7)$$

which gives

$$\begin{aligned} \bar{S}_{\Delta\theta}^{\bar{\theta}}(\omega) = & \frac{S_X(\omega) + S_Y(\omega)}{2} + \frac{S_X(\omega) - S_Y(\omega)}{2} e^{-2(\Delta\theta)^2} \cos(2\bar{\theta}) \\ & + S_{X,Y}(\omega) e^{-2(\Delta\theta)^2} \sin(2\bar{\theta}). \end{aligned} \quad (5.8)$$

As a consequence of this additional noise source, the optimum squeezing spectrum is modified and can be expressed as

$$\begin{aligned} 2\bar{S}_{min}(\omega) = & S_X(\omega) + S_Y(\omega) - e^{-2(\Delta\theta)^2} \\ & \times \sqrt{[S_X(\omega) - S_Y(\omega)]^2 + 4[S_{X,Y}(\omega)]^2}. \end{aligned} \quad (5.9)$$

In Appendix D can be found general expressions of the output homodyne noise spectra of: the amplitude quadrature  $S_X(\omega)$ , phase quadrature  $S_Y(\omega)$  and of their correlation  $S_{X,Y}(\omega)$  as a function of the input noise sources spectral density.

---

<sup>1</sup>To ease the notation we shall assume in this section that every spectrum has already been symmetrized so that  $S_x(\omega)$  (without the overline) indicates a symmetrized spectrum.

### Experimental demonstration of frequency noise cancellation

The experiment is carried out with a Fabry-Pérot cavity of length  $L = 0.57 \text{ mm}$  and the  $D1$  double wheel oscillator as end mirror. The cavity Finesse is  $\mathcal{F} = 57000$  so that the half linewidth is  $\kappa_\nu = 2.3 \text{ MHz}$ . Even though the Finesse is slightly lower than the maximum reported in Chap. 4, optical losses are comparable and the cavity is almost optimally coupled also in this case. We report here also the mechanical parameters: resonance frequency  $\omega_m/2\pi = 12891 \text{ Hz}$ , effective mass  $m = 1.35 \cdot 10^{-7} \text{ Kg}$ , and a mechanical quality factor of  $Q = 16000$ , slightly lower than the value reported in Tab. 4.1. This can be attributed to an higher contribution of clamping losses, thus remarking the need of stronger isolation in future generations of devices. We point out that the quality factor has a marginal role in the following measurements as long as  $\gamma_{opt} > \gamma_m$  holds.

We have experimentally verified the cancellation of frequency noise in a narrow band around the bare mechanical resonance in two different ways: (i) looking at the dynamics of the PDH signal, which is approximately proportional to the cavity detuning and is therefore suitable to test the physics of the frequency noise cancellation; (ii) measuring the intensity of the field reflected by the cavity, which is the variable typically observed in ponderomotive squeezing experiments.

In both cases, we have studied the response functions of the system to a modulation of the laser frequency generated by the internal oscillator of the lock-in amplifier, applied to the piezo transducer of the laser cavity (*fast* actuator, see App. B.1). The transduction efficiency of the laser piezo actuator has been calibrated by means of the PMI (that has unequal arm lengths). We express the frequency modulation as

$$\dot{\phi} = \kappa A_{in} \cos(\omega t) \quad (5.10)$$

that is, we are normalizing the modulation amplitude to the cavity damping rate.

The dynamics of the PDH signal has been measured with the setup in the standard configuration but with beam B-C blocked and by measuring the coherent response, of the PDH signal itself, to the frequency modulation with the lock-in amplifier. For a direct comparison between experimental results and theory, the PDH signal is normalized to its peak-to-peak amplitude in order to obtain the frequency modulation of the output field normalized again to  $\kappa$ . Indeed, the PDH signal can be considered as a measurement of the output phase quadrature  $Y_{out}$ , if the detuning and its fluctuations remain small with respect to the cavity linewidth. The amplitude of the measured modulation normalized in this way is  $A_{PDH}$ .

In Fig. 5.2 we show the normalized experimental data  $A_{PDH}/A_{in}$  for three values of steady state detuning  $\Delta_n$  and an input power of  $\mathcal{P} = 0.09 \text{ mW}$ , along

with theoretical predictions. These can be obtained by calculating the frequency noise/modulation transfer function using Eq. 1.73, Eqs. 1.74, and the definition of  $Y_{out}(\omega)$ , that is

$$A_{\dot{\phi}}(\omega) = i(\alpha_s A_3(\omega) - \alpha_s^* A_4(\omega) - h.c.) \quad (5.11)$$

and by normalizing it to its value  $A_{\dot{\phi}}^0$  far from the mechanical resonance. This means calculating the low frequency value of  $A_{\dot{\phi}}(\omega)$  at resonance ( $\Delta = 0$ ) and in the limit of vanishing optomechanical coupling ( $\omega_m \rightarrow \infty$ ), that is,  $A_{\dot{\phi}}^0 = 4\kappa_e \alpha_{in} / \kappa^2$ . Finally, one obtains

$$\frac{A_{PDH}}{A_{in}} = \frac{|A_{\dot{\phi}}(\omega)|}{A_{\dot{\phi}}^0} = \frac{\kappa^2}{4\kappa_e \alpha_{in}} |A_{\dot{\phi}}(\omega)|. \quad (5.12)$$

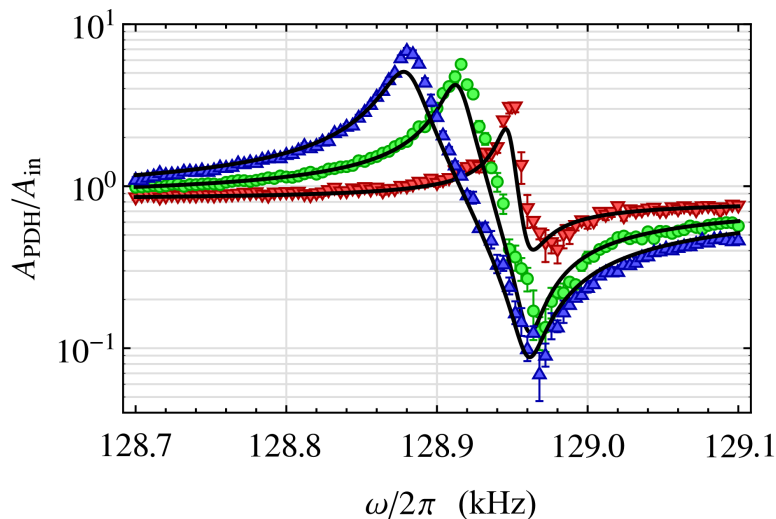


Figure 5.2: *Normalized PDH response functions for three different values of the steady state detuning:  $\Delta_n = -0.0047$  (red inverted triangles),  $\Delta_n = -0.028$  (green dots) and  $\Delta_n = -0.052$  (blue triangles). Error bars express the statistical uncertainty on  $\sim 5$  repeated measurements. The Full lines correspond to the theory prediction with no fitting parameters, but with minor adjustments as explained in the main text.*

Fig. 5.2 shows a dip that is always exactly at  $\omega = \omega_m$ . For increasing detuning, the cancellation bandwidth increases and the dip is more pronounced, as it is expected from the cancellation factor  $\chi_{eff}/\chi_0$  of Eq. 5.1. In fact, the cancellation effect is larger when the effect of the optomechanical coupling on the modified effective susceptibility  $\chi_{eff}$  is larger, i.e., for larger detuning  $\Delta$  and effective coupling  $|g_0 \alpha_s|^2$ . We point out that the theoretical curves in Fig. 5.2 are obtained with no fitting parameters, but with just minor adjustments to the driving power and to the

vertical scale ( $\sim 20\%$ ), both compatible with experimental uncertainties. Moreover, we have added a supplementary detection noise, due to the electronics, that limits the depth of the dips.

To further enhance the dependance of the cancellation effect on the effective coupling strength, we repeated the measurement with beam B-C injected into the cavity, with the higher power of  $\mathcal{P} = 1 \text{ mW}$ . In this case, the PDH beam is maintained on resonance and can thus be considered as a weak probe, compared to the strong and detuned beam B-C. Theoretical predictions can be calculated again from Eq. 5.12 setting  $\Delta = 0$ , but where the effective susceptibility is determined by the dynamical backaction of beam B-C. In Fig. 5.3 we show the same theoretical curves of Fig. 5.2, along with the experimental data and predictions for this second configuration. Here, the beam B-C is injected with a detuning of  $\Delta_n = -0.023$ . The agreement between theory and experiment is very good, the cancellation effect is much stronger and is again centered at  $\omega = \omega_m$ . In the second part of the experiment we have measured

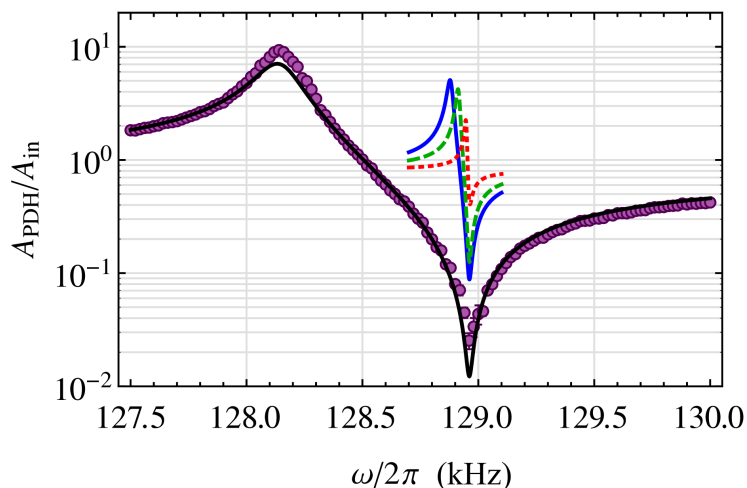


Figure 5.3: *The same three theoretical curves of Fig. 5.2 for the normalized PDH signal, together with an additional data set (purple dots) corresponding to the PDH signal in presence of the strong pump beam B-C ( $\mathcal{P} = 1 \text{ mW}$  and  $\Delta_n = -0.023$ ) which induces a much stronger dynamical backaction. The full black line corresponds to the theoretical predictions with no fitting parameters, except for an additional detection noise due to electronics.*

the response of the system by detecting the intensity modulation of the reflected pump beam B-C. The sum of the photodiodes PD1 and PD2 (with the reference arm of the PMI blocked) were sent to the lock-in amplifier. In this case, the ampli-

tude of the measured intensity modulation normalized to the height of the reflection dip, giving  $A_{PDS}$ . Theoretical predictions can be calculated again using Eq. 1.73 and Eqs. 1.74 as follows. The reflected field is  $\alpha_R = \sqrt{2\kappa_e}\alpha_s - \alpha_{in}$  and the amplitude of the photon flux modulation due to the laser frequency modulation  $\dot{\phi}$  (see Eq. 5.10) is

$$I_{\dot{\phi}}(\omega) = i \{ \alpha_R^* [\alpha_s A_3(\omega) - \alpha_s^* A_4(\omega)] - h.c. \} \dot{\phi}, \quad (5.13)$$

the normalization constant is  $I_0 = 2\alpha_{in}\kappa_i/\kappa$  and, finally, we find

$$\frac{A_{PDS}}{A_{in}} = \frac{|I_{\dot{\phi}}(\omega)|}{I_0} \kappa = \frac{\kappa^2}{2\alpha_{in}\kappa_i} |I_{\dot{\phi}}(\omega)|. \quad (5.14)$$

In Fig. 5.4 we show the normalized experimental data along with theoretical prediction calculated with Eq. 5.14, obtained with three different values of detuning for the pump beam. Also in this case, theoretical curves well reproduce the data without fitting parameters apart the addition of detection noise. This set of measurements

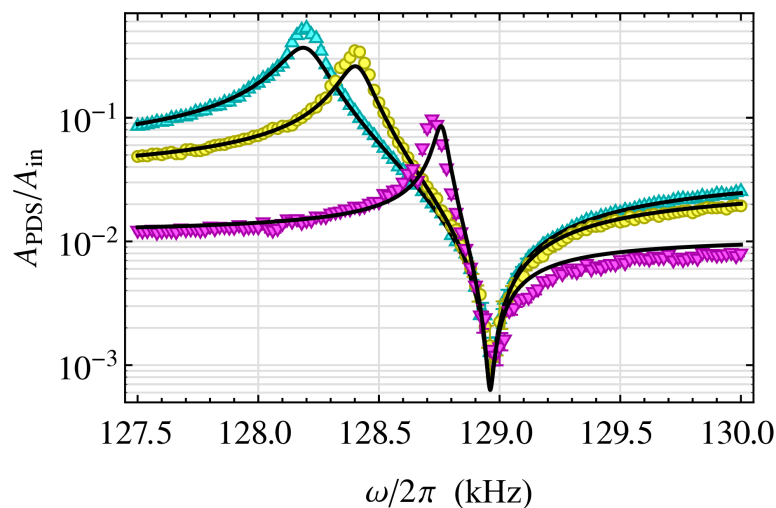


Figure 5.4: Normalized response functions of the reflected field versus frequency for three different values of detuning,  $\Delta_n \simeq 0.0056$  (magenta inverted triangles),  $\Delta_n \simeq 0.015$  (yellow dots) and  $\Delta_n \simeq 0.021$  (cyan triangles). The full lines correspond to the theoretical predictions with no fitting parameters, except for the addition of a detection noise.

is more significative in view of the detection of ponderomotive squeezing, since the reflected field is exactly where quadrature squeezing caused by radiation pressure manifests. Also in these transfer functions we see the same features already underlined in the PDH dynamics: (i) the cancellation dip is exactly at the bare mechanical resonance  $\omega_m$ ; (ii) the cancellation effect is more pronounced for larger detunings and couplings, i.e., for a larger optical spring effect.

## Effect of noise cancellation for generating ponderomotive squeezing at low frequency

In this last section we show that the experimental setup studied above, if slightly improved, can be employed for generating ponderomotive squeezing at frequencies around  $100\text{ kHz}$ , i.e., considerably lower than those of Refs. [19, 20]. We demonstrate that the cancellation mechanism illustrated above is of fundamental importance for the detection of squeezing. This can be seen by considering the prediction for the output homodyne noise spectrum defined by Eq. 1.82 at a fixed phase  $\bar{\theta}$ , which we have chosen as the optimal phase of Eq. 1.86 evaluated at the bare mechanical frequency  $\bar{\theta} = \theta_{min}(\omega_m)$ . We have considered a slightly improved version of the setup, that is, the same optical cavity (i.e., same length and Finesse), the same resonator mass and frequency, and considered only an improved mechanical quality factor,  $Q = 10^5$  as reported in Chap. 4 (and Ref. [25]), liquid He temperatures,  $T = 4\text{ K}$ , and larger input power,  $\mathcal{P} = 30\text{ mW}$ . As we have shown in Chap. 2, the double wheel design is able to work with high intracavity powers without a significant increase of the local temperature. Indeed, the input power considered here would generate a temperature increase with respect to the cold finger of few tenth of  $K$ , and a dissipated power of a couple of  $mW$ , well within reach of a standard liquid He cryostats.

In the device employed here, frequency noise is dominated by background noise and we have observed  $S_{bg} \sim 10^{-34} \div 10^{-33}\text{ m}^2/\text{Hz}$  in the  $\sim 100\text{ kHz}$  region with up to  $25\text{ mW}$  of input power; similar figures are shown by other groups [61]. We have in fact independently verified that laser frequency noise gives a negligible contribution, which amounts to  $0.5\text{ Hz}^2/\text{Hz}$ . For our predictions we take conservatively the upper limit  $10^{-33}\text{ m}^2/\text{Hz}$ , that is equivalent to the frequency noise  $S_{\dot{\phi}} = (d\omega_{cav}/dx)^2 S_{bg} \simeq (2\pi)^2 300\text{ Hz}^2/\text{Hz}$ . For what concerns laser amplitude noise  $\alpha_I$ , the present apparatus, including an additional external noise eater, shows an excess noise  $3\text{ dB}$  above the shot noise for a  $30\text{ mW}$  laser beam (the work described in Ref. [99] has been recently extended in the  $\sim 100\text{ kHz}$  range for this purpose). The excess amplitude noise could be further decreased by  $20\text{ dB}$  using a standard ( $20\text{ cm}$  long,  $30000$  Finesse) filter cavity [100] and at this level, it would provide a negligible contribution to the output spectrum. As a consequence, we have neglected the laser amplitude noise contribution in the predictions below, with the exception of Fig. 5.6.

Fig. 5.5 shows the homodyne noise spectrum  $S_{out}^{\bar{\theta}}$  at phase  $\bar{\theta} = 178.6^\circ$ , together with the various noise contributions, i.e., the quantum noise, the frequency and

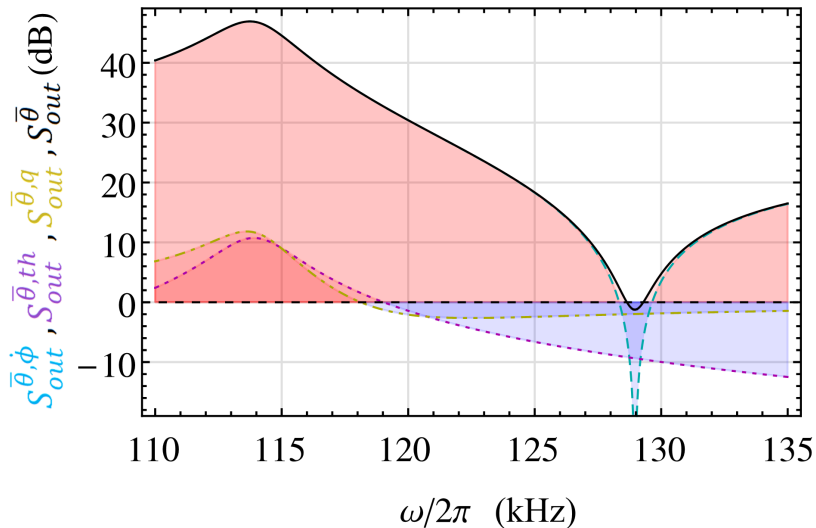


Figure 5.5: Homodyne spectrum  $S_{out}^{\bar{\theta}}$  at the fixed phase  $\bar{\theta} = \theta_{min}(\omega_m)$  (black solid curve), together with its contribution from: quantum noise  $S_{out}^{\bar{\theta},q}$  (yellow dash-dotted curve), due to both input field and vacuum fluctuations, frequency noise  $S_{out}^{\bar{\theta},\dot{\phi}}$  (cyan dashed curve) and thermal noise  $S_{out}^{\bar{\theta},th}$  (magenta dotted curve). Ponderomotive squeezing is achieved in a narrow band around the bare mechanical resonance. The detuning assumed here is  $\Delta = 2\pi 32 \text{ kHz}$  ( $\Delta_n = 0.014$ ).

thermal contributions. It is evident that one generates ponderomotive squeezing in a narrow bandwidth around the bare mechanical frequency  $\omega_m$ , only due to the frequency noise cancellation described above. In fact such noise is dominant everywhere except in this narrow band, where the detected homodyne spectrum is bounded below by the quantum noise contribution, in this set of parameters.

An enlarged view of the homodyne spectrum around  $\omega_m$  is given by Fig. 5.6, where we show  $S_{out}^{\bar{\theta}}$  at different values of the frequency noise  $S_{\dot{\phi}\dot{\phi}}$  (left) and of laser amplitude noise  $S_{\alpha_I\alpha_I}$  (right). A larger  $S_{\dot{\phi}\dot{\phi}}$  implies narrowing the squeezing bandwidth, and we see that one can tolerate an appreciable amount of laser amplitude noise (see the figure caption for details). About 1 dB of squeezing is achievable in this parameter regime, comparable to that achieved in Refs. [19, 20]. Deeper and wider squeezing can be obtained for lower masses, higher Q, lower frequency noise and an overcoupled cavity (with  $\kappa_i \ll \kappa_e$ ) to reduce the effect of vacuum noise entering through optical losses.

The reason why frequency noise (in this case mostly due to background displacement noise) is so important is that it is transformed into strong intracavity laser

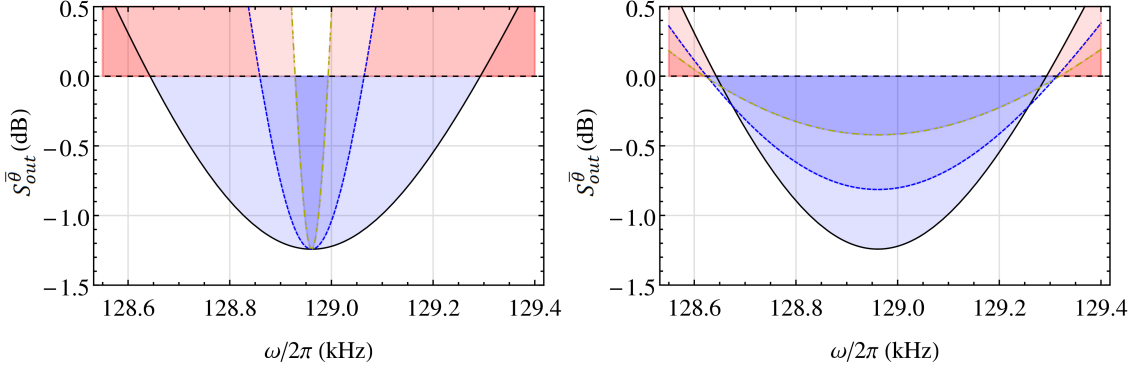


Figure 5.6: *Enlarged view of the homodyne noise spectrum  $S_{out}^{\bar{\theta}}$  around  $\omega = \omega_m$ . In the figure on the left,  $S_{out}^{\bar{\theta}}$  is shown at different values of frequency noise:  $S_{\dot{\phi}\dot{\phi}}/(2\pi)^2 = 3 \cdot 10^2 \text{ Hz}^2/\text{Hz}$  (black solid),  $S_{\dot{\phi}\dot{\phi}}/(2\pi)^2 = 3 \cdot 10^3 \text{ Hz}^2/\text{Hz}$  (blue dotted) and  $S_{\dot{\phi}\dot{\phi}}/(2\pi)^2 = 3 \cdot 10^4 \text{ Hz}^2/\text{Hz}$  (yellow dot-dashed). On the right figure,  $S_{out}^{\bar{\theta}}$  is shown at different values of laser amplitude noise:  $S_{\alpha_I \alpha_I} = 0$  (black solid),  $S_{\alpha_I \alpha_I} = 0.1 \text{ Hz}/\text{Hz}$  (blue dotted) and  $S_{\alpha_I \alpha_I} = 0.5 \text{ Hz}/\text{Hz}$  (yellow dot-dashed). This last value correspond to an excess noise of 3 dB above the shot noise. Other parameters as in Fig. 5.5.*

intensity noise by the frequency-dependent resonance curve of the Fabry-Pérot. The conversion factor is roughly proportional to the derivative of the Lorentzian (at least in the bad cavity limit), therefore typical calculations of achievable squeezing with realistic background noise are forced to consider very small detuning [60, 26]. A similar problem is found when aiming to measure quantum correlations induced by ponderomotive effect [101]. Such a small detuning means that the working point is quite close to the edge of the stability region, and that the requirement on the accuracy and stability of both the detuning and the homodyne phase are very tight. On the other hand, a further and crucial advantage of the frequency noise cancellation mechanism around  $\omega = \omega_m$  is that it allows to significantly relax the requirements on the stability and precision in the detuning and the detection phase in order to get ponderomotive squeezing. This is illustrated in Fig. 5.7, where the homodyne noise spectrum  $S_{out}^{\theta}$  at fixed frequency  $\omega = \omega_m$  is plotted as a function of the normalized detuning and of the homodyne detection phase, with the same set of parameters of Fig. 5.5. The sub-shot noise region becomes wider and wider by increasing the detuning and, consequently, by departing from the phase of the amplitude quadrature  $\theta = 0 = \pi$ . At larger detunings it is sufficient to stabilize the detection phase and the detuning itself at better than 1% level in order to detect squeezing. On the contrary, closer to resonance  $\Delta = 0$ , the sub-shot noise region is much narrower and

one has much more stringent stability requirements on  $\Delta$  and  $\theta$ .

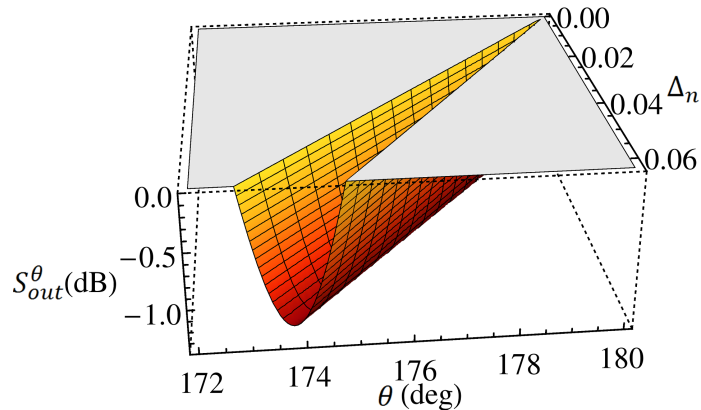


Figure 5.7: Homodyne noise spectrum  $S_{out}^\theta$  at fixed frequency  $\omega = \omega_m$  as a function of detuning  $\Delta_n$  and of the homodyne phase  $\theta$ . Parameters as in Fig. 5.5. The sub-shot noise region widens for increasing detunings and departing from  $\theta = 0 = \pi$ .

The fact that one can tolerate a significantly larger uncertainty in the detection phase by operating around the noise cancellation point  $\omega = \omega_m$ , and at larger detunings, can be seen also in the *averaged* homodyne noise spectrum  $\bar{S}_{\Delta\theta}^\theta(\omega)$  of Eq. 5.8 which takes into account the presence of a detection phase uncertainty  $\Delta\theta$ . This is shown in Fig. 5.8, where  $\bar{S}_{\Delta\theta}^\theta(\omega)$  is plotted versus  $\omega$  and  $\Delta\theta$  at fixed detuning and detection phase (namely,  $\Delta_n = 10^{-3}$  and the corresponding optimal phase  $\bar{\theta} = \theta_{min}(\omega_m) = 179.9^\circ$  in the left panel, and  $\Delta_n = 0.063$  and  $\bar{\theta} = \theta_{min}(\omega_m) = 173.8^\circ$  in the right panel). We see that, at small detunings, squeezing vanishes already for an uncertainty  $\Delta\theta \simeq 0.015^\circ$ , while at larger detunings ponderomotive squeezing is detectable up to a phase detection uncertainty  $\Delta\theta \simeq 1^\circ$ . Further increase of the detuning is not convenient because, at fixed input power, there is an interval of values of  $\Delta$  for which the system is unstable [102]. At larger values of the detuning the system is again stable, but the achievable squeezing is lower. Similar results can be obtained by considering the uncertainty in the detuning  $\Delta$ .

Achieving ponderomotive squeezing with the present optomechanical device presents some practical advantages with respect to the use of the setups of Refs. [19, 20], which are characterized by higher mechanical frequencies and much lower masses. In this latter setups, radiation pressure effects are much stronger and therefore ponderomotive squeezing is easier to achieve. However, the mechanical frequency is much less stable and reproducible, because of significant stress drifts induced by

thermal effects associated with optical absorption [103]. On the contrary, in the present thicker silicon micromechanical mirror, the expected temperature variation is just around  $0.1 K$  in a cryogenic environment, due to the low thermal impedance of the device. This is confirmed by the fact that we could see no relevant drift in the mechanical resonance frequency by illuminating the sample from its back surface (where the light is partially absorbed by silicon) with laser power in the  $mW$  range.

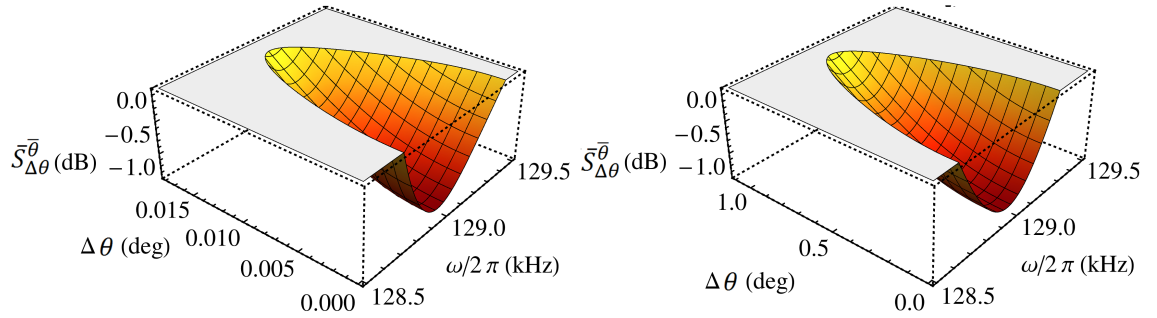


Figure 5.8: Averaged homodyne noise spectrum  $\bar{S}_{\Delta\theta}^{\bar{\theta}}$  as a function of frequency  $\omega/2\pi$  and detection phase uncertainty  $\Delta\theta$  at fixed detuning ( $\Delta_n = -10^{-3}$  in the left panel and  $\Delta_n = -0.063$  in the right panel) and fixed detection phase ( $\bar{\theta} = 179.9^\circ$  in the left panel and  $\bar{\theta} = 173.8^\circ$  in the right panel). Notice the different scale of the  $\Delta\theta$  axes. Other parameters as in Fig. 5.5 )

## 5.2 Effects of frequency locking on the dynamical backaction

In this section we are going to discuss how the frequency lock loop can modify the dynamics of the optomechanical cavity. In particular, we show that: (a) it can introduce the dynamical instability for some mechanical modes, with sufficiently low mass and frequencies, even if the steady state detuning is well inside the stable region; (b) it can affect the dynamical back action even at frequencies much greater than the lock bandwidth. While the latter problem can be addressed rather easily, the former is much more difficult to avoid especially for the QPO designs.

The problem can be discussed starting from Eq. 1.73. Since we want to treat the classical contribution of the control loop, we can neglect the quantum backaction and all additional classical noise terms in the equation for the oscillator position, so

that it can be rewritten as

$$x(\omega) = \chi_0(\omega) [\xi(\omega) + F_{rad}(\omega)] \quad (5.15)$$

where  $F_{rad}(\omega)$  is the position dependent radiation pressure force that is given by

$$\begin{aligned} F_{rad}(\omega) &= -i g_0^2 |\alpha_s|^2 \left[ \frac{1}{K^*(-\omega)} - \frac{1}{K(\omega)} \right] \\ &= -2\Delta_n \frac{g_0^2}{\kappa} \frac{n_c^{max}}{1 + \Delta_n^2} \frac{1}{(1 - i\omega/\kappa)^2 + \Delta_n^2} x \end{aligned} \quad (5.16)$$

where  $n_c^{max}$  is the mean number of intracavity photons at resonance. Note that,  $\chi_{eff}(\omega) = \omega_m [\omega_m^2 - \omega^2 - i\gamma_m \omega - F_{rad}(\omega)/x(\omega)]^{-1}$

The cavity lock loop modifies the laser frequency to maintain the input field at a fixed normalized detuning  $\Delta_n$  from the cavity resonance. Its effect can be included in the model by replacing, in Eq. 5.16,  $\Delta_n$  with its closed loop value, that is

$$\Delta_n \rightarrow \frac{\Delta_n}{1 + G_{lk}(\omega)} \quad (5.17)$$

where  $G_{lk}(\omega)$  is the overall PDH loop gain (see Sec. C). This substitution makes evident that the radiation pressure force is strongly modified by the control loop as long as the frequency is of the order of the lock bandwidth. At higher frequencies the loop contribution rapidly decreases and the radiation pressure is again well described by Eq. 5.16. However, depending on the cavity parameters, residual effects could still be not negligible at  $\omega = \omega_m$ . This is most evident in the optomechanical damping rate  $\gamma_{om}$ . The modified optical damping rate  $\gamma_{opt}^{lk}(\omega)$  is now given by

$$\begin{aligned} \gamma_{opt}^{lk}(\omega) &= \frac{1}{\omega} \text{Im} \left[ \frac{F_{rad}(\omega)}{x(\omega)} \right] \\ &= \frac{1}{\omega} \text{Im} \left[ -\frac{2\Delta_n}{1 + G_{lk}(\omega)} \frac{n_c^{max}}{1 + \left(\frac{\Delta_n}{1 + G_{lk}(\omega)}\right)^2} \frac{1}{(1 - i\omega/\kappa)^2 + \left(\frac{\Delta_n}{1 + G_{lk}(\omega)}\right)^2} \right] \end{aligned} \quad (5.18)$$

so that we have  $\gamma_{om}(\omega) = \gamma_m + \gamma_{opt}^{lk}(\omega)$ . If we take into consideration the cavity parameters given in the previous section and the typical loop gain in Sec. C for a lock bandwidth  $\omega_{lk}/2\pi \simeq 12 \text{ kHz}$ , the resulting  $\gamma_{om}$  is quite different from the one evaluated with Eq. 1.78, as is clearly shown in Fig. 5.9 where the two are compared.

Such a dramatic difference is to ascribe at the fact that, in the bad cavity regime, the imaginary part of  $F_{rad}$  is small compared to its modulus, so that any residual phase contribution from  $G_{lk}$  can result in strong modifications to  $\gamma_{om}$ , even if  $\omega_m/\omega_{lk} \simeq 10$ .

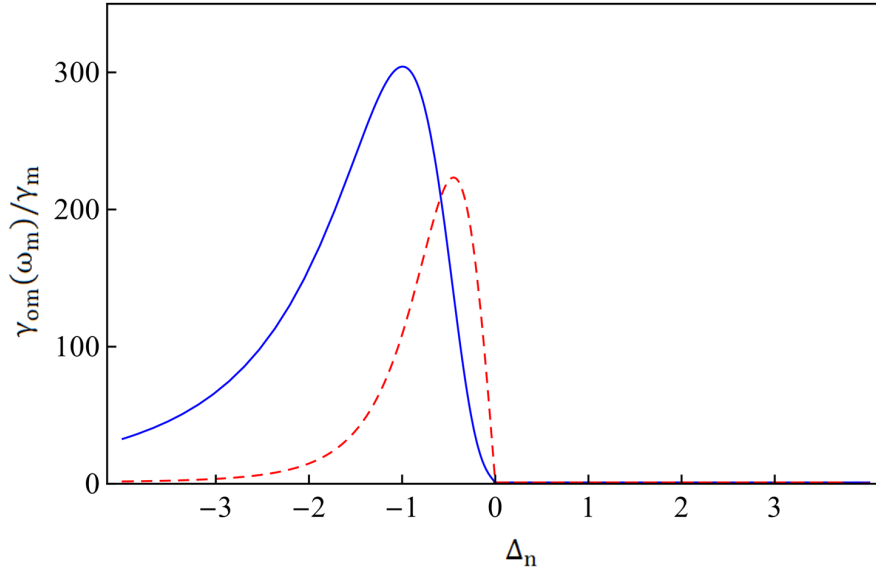


Figure 5.9: *Optomechanical damping rate normalized to the bare mechanical one and calculated at angular frequency  $\omega_m$ , evaluated with  $\gamma_{opt}^{lk}$  (blue) and evaluated without the effects of the frequency lock loop (red dashed).*

The easiest way to deal with this problem is to ensure that  $G_{lk}$  is negligible at  $\omega = \omega_m$  in such a way to avoid the deterioration of the lock loop performances. To do this, we have included in the electronic of the servo loop two passive notch filters in cascade, with a maximum rejection factor of about 100, centered at  $\omega_m$ . Note that the  $Q$  of these filters has to be high enough to provide a sufficient rejection but, at the same time, low enough to guaranty a rejection bandwidth sufficiently wide to comprehend the frequency shift of the mechanical resonance at low temperature.

While the notch filters ensure that  $\gamma_{om}(\omega_m)$  is not affected by the frequency lock loop, at lower frequencies this is not true. Furthermore, the effect of the loop is so strong that the resulting  $\gamma_{om}$  can actually change sign. This means that mechanical normal modes with effective mass comparable to that of the oscillator and resonance frequency  $\omega_0 < \omega_m$  can be brought to the dynamical instability region by the frequency lock loop.

To clarify this concept, we show in Fig. 5.10 the ratio  $\gamma_{opt}^{lk}(\omega)/\gamma_m$  (blue curves) as a function of frequency and at two fixed values of the normalized detuning  $\Delta_n = -0.01$  (left) and  $\Delta_n = -0.003$  (right). The corresponding, roughly constant, ratio calculated for  $\gamma_{opt}(\omega)$  is also shown in both panels (black curves). Note that, thanks to the additional notch filters,  $\gamma_{opt}^{lk}(\omega_m)$  and  $\gamma_{opt}(\omega_m)$  coincide on a reasonably wide

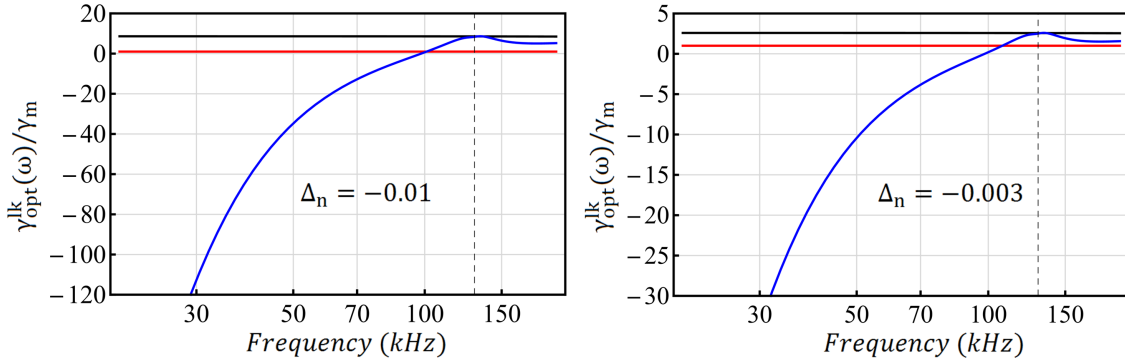


Figure 5.10: Modified optical damping rate, normalized to the bare mechanical one, as a function of frequency for two different values of normalized detuning (blue curves). In both panels: (black curves) nominal  $\gamma_{opt}(\omega)$ ; (red curves) reference value  $\gamma_{opt}^{lk}/\gamma_m = 1$ . The dashed gray vertical lines correspond to  $\omega_m \simeq 129 \text{ kHz}$ .

frequency bandwidth.

We recall that for  $\gamma_{opt}^{lk}(\omega)/\gamma_m \leq -1$  the system is dynamically unstable since the threshold value implies a vanishing optomechanical linewidth. However, here we show  $\gamma_{opt}^{lk}(\omega)/\gamma_m$  also in the unstable region. The reason is simple. The curves shown in Fig. 5.10 are calculated for the effective mass  $m = 1.35 \cdot 10^{-7} \text{ kg}$  of the oscillator mode considered previously. Showing the full range of  $\gamma_{opt}^{lk}(\omega)/\gamma_m$  allows us to roughly estimate how heavier should be the effective mass of a mechanical mode with resonance frequency in the unstable domain. In Eq. 5.18 the mass comes into play through  $g_0^2 \propto 1/m$  so that, for example, if  $\Delta_n = -0.01$ , a mode with resonance frequency  $\omega_0 = 30 \text{ kHz}$  should have an effective mass roughly 120 times higher than that of the main oscillator mode in order to be stable, while at  $\Delta_n = -0.003$  a factor of about 30 would be sufficient.

These figures can be directly compared with actual values of secondary normal modes of the structures presented in Chap. 2. For the double wheel oscillators, the only relevant mode is the fundamental one of the suspension wheel. The effective mass of this mode, that has a resonance frequency  $\omega_0 \simeq 30 \text{ kHz}$  for all designs, is typically in the range  $(0.5 - 1.0) \cdot 10^{-5} \text{ kg}$  indicating that for the  $1 \text{ mW}$  input power considered in evaluating the curves in Fig. 5.10, the fundamental wheel mode would self-oscillate for  $\Delta_n = -0.01$  while it would be stable for  $\Delta_n = -0.003$ . Note that it exists a parameter region for which both, the oscillator and the wheel modes, are stable, but one is cooled and the other is heated, or viceversa. All these effects induced by the frequency lock loop have been observed experimentally. We

remark that additional measures have to be implemented otherwise the parameters region discussed in the previous section would remain out of reach. Fortunately, this can be achieved quite efficiently in two possible ways. The first one requires the implementation of an active feedback cooling on the wheel mode, while the second one consists in modifying the PDH loop. Both have been realized and the latter is found to be the most effective.

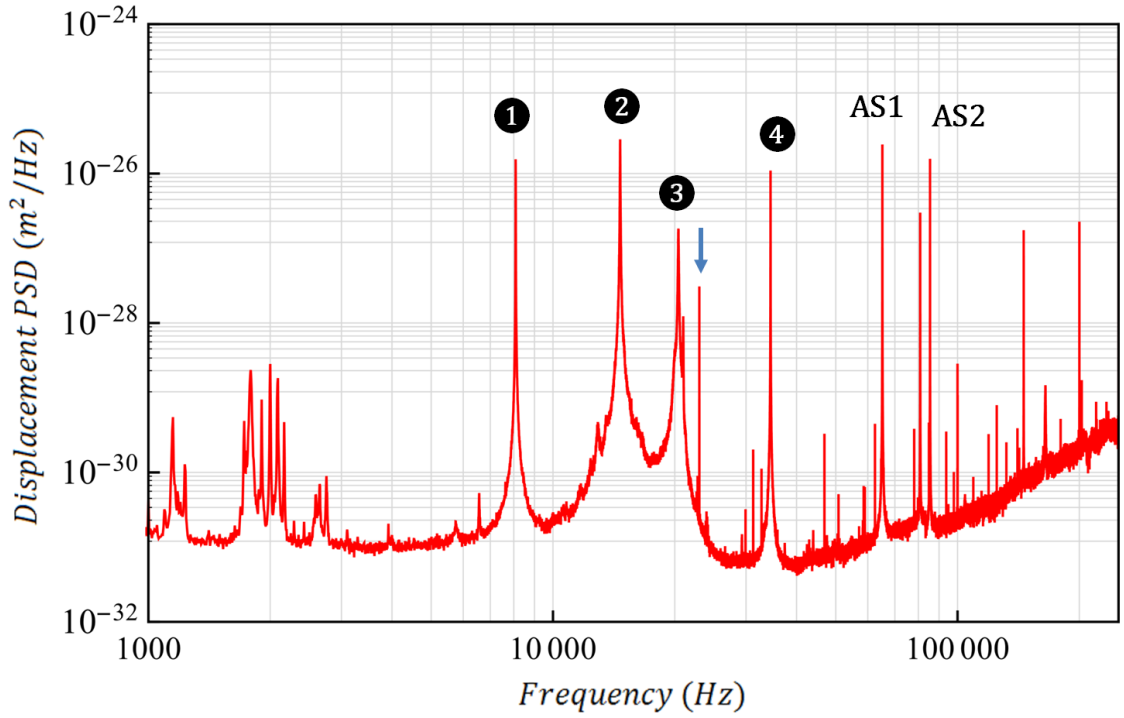


Figure 5.11: *PDH spectrum of our best QPO oscillator acquired with the long cavity at low input power and for a low Finesse cavity. The numbers identify the low frequency normal modes discussed in the text. (1)  $\omega_1/2\pi \simeq 8\text{ kHz}$  and  $m \sim 1 \cdot 10^{-6}\text{ kg}$ . (2)  $\omega_2/2\pi \simeq 15\text{ kHz}$  and  $m \sim 2 \cdot 10^{-7}\text{ kg}$ . (3)  $\omega_3/2\pi \simeq 20\text{ kHz}$  and  $m \sim 4 \cdot 10^{-7}\text{ kg}$ . (4)  $\omega_4/2\pi \simeq 34\text{ kHz}$  and  $m \sim 4 \cdot 10^{-7}\text{ kg}$ . Also identified are the AS1 and AS2 modes. The blue arrow indicates the calibration spectral line (see Sec. C).*

The situation is quite different for the QPO and DPO designs. For these oscillators, a relevant number of normal modes are present at frequencies lower than those of the AS modes. This was already clear in the PMI spectrum of our best QPO shown in Fig. 4.1 where 4 of these modes were identified. To remark the importance of this aspect we show in Fig. 5.11 a PDH spectrum of the same QPO acquired with the long cavity ( $L_{cav} = 8.3\text{ mm}$ ). In this case, the low input power and the low Finesse

(we had  $\mathcal{F} \simeq 10000$ ) have assured that the dynamical backaction, both the naturally occurring and the PDH loop induced, was negligible. The lowest frequency mode, at about  $8\text{ kHz}$ , has an effective mass of  $\sim 1\ 10^{-6}\text{ kg}$  while the following three modes have masses in the range  $(2 - 4)\ 10^{-7}\text{ kg}$ . These figures essentially assure that no stable configuration can be found when the Finesse reaches the value of  $\mathcal{F} = 65000$  measured with the short cavity.

The gravity of this problem was not foreseen in the development phase but for the following generation we added the requirement that the lowest mode of the structure should have a resonance frequency greater than  $\sim 40\text{ kHz}$ .

# Chapter 6

## Parametric stabilization of the effective mechanical susceptibility

Opto-mechanical systems are suitable to investigate a large variety of quantum phenomena that involve the degrees of freedom of both the optical field and the mechanical motion. In many instances, however, the precise knowledge of the effective mechanical parameters is a crucial aspect. For the typical experimental setup this may not be trivial. Indeed, the effective susceptibility can be influenced in many ways. For example, slow thermal drifts of the environmental temperature can modify the resonance frequency of the oscillator or, more subtle, they change the cavity overall birefringence limiting the possibility of maintaining a fixed detuning when a two beam setup, like ours, is used.

The issue of the stabilization of the effective mechanical parameters has been recently considered by few groups [104, 105]. In this chapter we introduce the implementation of a control loop that stabilizes the effective mechanical susceptibility by controlling the optical spring effect, thus realizing a *parametric feedback*. In Sec. 6.1 we introduce the theoretical model to describe it and its experimental realization. To do so, we use a model based on the semiclassical approach that is sufficient to describe all the experimental results presented here. Finally, we discuss, in Sec. 6.2, its characterization.

### 6.1 Parametric control loop model

We consider the experimental setup in the standard configuration so that the weak *probe* beam (A-D) measures the position  $x(t)$  of the oscillator with detection noise  $n(t)$  and back action force  $f_{BA}(t)$ , that are considered uncorrelated and with spectra

$S_n$  and  $S_{BA}$  bounded by  $S_n S_{BA} \geq \hbar^2/4$ . The *pump* beam (B-C) is used for high power injection into the cavity, actually determining the effective mechanical parameters. We want to describe the dynamical evolution of the optomechanical oscillator under the action of a stochastic force noise and an additional coherent oscillating force of constant amplitude  $F_e \cos \omega_e t$ . Then, Eq. 1.4 becomes

$$\ddot{x}(t) + \gamma_{om}\dot{x}(t) + \omega_{eff}^2 x(t) = \frac{1}{m} [f_{st} + F_e \cos \omega_e t] \quad (6.1)$$

where  $\gamma_{om}$  and  $\omega_{eff} = \sqrt{\omega_m^2 + \omega_{opt}^2}$  are the effective mechanical parameters and  $f_{st}$  is the stochastic noise force term that includes the thermal noise contribution and the backaction of the measurement. The result of the position measurement is  $x_m(t) = x(t) + n(t)$ .

The motion of the oscillator can be decomposed into two quadratures  $X(t)$  and  $Y(t)$  in a frame rotating at angular frequency  $\omega_e$ , according to

$$x(t) = X(t) \cos \omega_e t + Y(t) \sin \omega_e t. \quad (6.2)$$

Assuming  $|\omega_e - \omega_{eff}| \ll \omega_{eff}$  and  $\gamma_{om} \ll \omega_{eff}$ , the evolution equations for the two slowly-varying quadratures, derived from Eq. 6.1, can be written as

$$\begin{aligned} \dot{X} + \frac{\gamma_{om}}{2} X - (\omega_{eff} - \omega_e) Y &= \frac{1}{m\omega_e} f_{st}^{(1)} \\ \dot{Y} + \frac{\gamma_{om}}{2} Y + (\omega_{eff} - \omega_e) X &= \frac{1}{m\omega_e} \left[ f_{st}^{(2)} + \frac{F_e}{2} \right] \end{aligned} \quad (6.3)$$

where the stochastic force term has a correlation function  $\langle f_{st}^{(i)}(t) f_{st}^{(j)}(t') \rangle = \delta_{ij} \delta(t - t') S_{st}/2$  ( $i, j=1, 2$ ) and where all noise sources in  $f_{st}$  are assumed uncorrelated with each other. In the experiment, the two quadratures are measured by sending  $x_m(t)$  to a lock-in amplifier whose reference signal is derived from the oscillator modulating the coherent force  $F_e$ . The outputs of the lock-in are  $X_m = X + n^{(1)}$  and  $Y_m = Y + n^{(2)}$  with  $\langle n^{(i)}(t) n^{(j)}(t') \rangle = \delta_{ij} \delta(t - t') S_n/2$ .

The steady state solutions of Eqs. 6.3 are the usual components of the oscillator response, as a function of the frequency difference between resonance and excitation  $\delta\omega = \omega_{eff} - \omega_e$ :

$$\begin{aligned} \bar{X}(\delta\omega) &= \frac{F_e}{2m\omega_e} \frac{\delta\omega}{\frac{\gamma_{om}^2}{4} + (\delta\omega)^2} \\ \bar{Y}(\delta\omega) &= \frac{F_e}{2m\omega_e} \frac{\delta\omega}{\frac{\gamma_{om}^2}{4} + (\delta\omega)^2}. \end{aligned} \quad (6.4)$$

We remark that  $\bar{X}$  is an odd function of  $\delta\omega$ , therefore it can be efficiently exploited to control and lock  $\omega_{eff}$ . The  $X_m$  quadrature is indeed integrated and sent to control the

resonance frequency  $\omega_{eff}$  by modifying the optical spring constant. This is obtained in the experiment by acting on the detuning of the pump beam according to

$$\omega_l(t) = \omega_l^0 - \int_{-\infty}^t \mathcal{G}(t, t') X_m(t') dt' \quad (6.5)$$

where  $\omega_l^0$  is the initial detuning and the kernel  $\mathcal{G}(t, t')$  is constant in the case of an integral feedback loop. Given that  $\omega_l$  determines the effective frequency  $\omega_{eff}$  via Eq. 1.77, we can write

$$\omega_{eff}(t) = \omega_{eff}^0(t) - \int_{-\infty}^t \bar{\mathcal{G}}(t, t') X_m(t') dt' \quad (6.6)$$

where  $\omega_{eff}^0(t)$  is the free-running optomechanical frequency and  $\bar{\mathcal{G}} \propto \mathcal{G}$ . We point out that, in the bad cavity limit, the optomechanical damping rate can be expressed as  $\gamma_{opt} = 2K_{opt}/m\kappa$  so that the shift in the resonance frequency  $\omega_{eff}$  due to the optomechanical backaction is larger than the variation in the total damping rate  $\gamma_{om}$ , as mentioned in Chap. 1. This means that, when considering small variations of  $\Delta$  around the working point, the variations of  $\gamma_{eff}$  due to the feedback loop can be neglected. We also remark that the control of the optical spring can be considered as a classical effect, and its noise neglected in a first order treatment. In any case, such noise (for us, the radiation pressure noise of the pump beam) can be included in  $f_{st}$ . At the purpose of analyzing the effect of the control loop, we first consider slow fluctuations in the opto-mechanical resonance frequency  $\omega_{eff}$ , that can be treated as adiabatic changes of the system, keeping the validity of Eqs. 6.3. In the absence of drift in  $\omega_{eff}^0(t)$ , the steady-state solution is  $\delta\omega = 0$ , i.e.,  $\omega_{eff} = \omega_e$  (long term drifts in  $\omega_{eff}^0(t)$  can be corrected by additional integrators, as in standard servo-loop systems). In the phase plane of a reference frame rotating at  $\omega_e$ , the oscillator motion is now represented by a vector  $\mathbf{R} = (X, Y)$  fluctuating around the average value  $(0, Y_0)$  with  $Y_0 = \bar{Y}(0) = F_e/m\omega_e\gamma_{om}$  (in Fig. 6.1 we report an experimental example). The feedback loop corrects the fluctuations by counter-rotating  $\mathbf{R}$  towards the  $Y$  axis. If  $\mathbf{R}$  remains close to  $(0, Y_0)$ , i.e., if  $\langle X^2 + (Y - Y_0)^2 \rangle \ll Y_0^2$ , we can approximate the angle  $\theta$  between  $\mathbf{R}$  and the  $Y$  axis with  $\theta \approx X/Y_0$ . In this limit, the feedback loop (that acts on  $\theta$ ) just influences the fluctuations in the  $X$  quadrature, leaving free  $Y$  fluctuations. This is expressed by a linear expansion of Eqs. 6.3 around

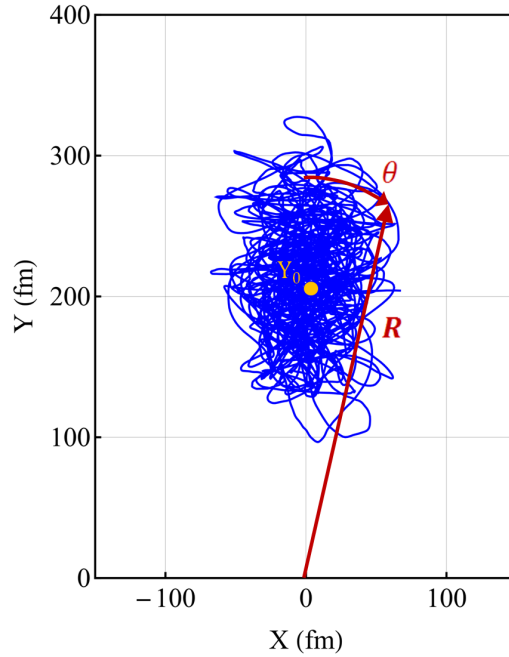


Figure 6.1: *Experimental measurement of the temporal evolution of the mechanical oscillator in the phase plane with active parametric control.*

the steady state, with  $\omega_{eff} = \omega_e + \delta\omega(t)$ ,  $X = \bar{X} + \delta X$  and  $Y = Y_0 + \delta Y$ :

$$\begin{aligned}
 \delta\dot{X} + \frac{\gamma_{om}}{2}\delta X - \delta\omega(t)Y_0 &= \frac{1}{m\omega_e}f_{st}^{(1)} \\
 \delta\dot{Y} + \frac{\gamma_{om}}{2}\delta Y &= \frac{1}{m\omega_e}f_{st}^{(2)} \\
 \delta\omega(t) &= \delta\omega_{eff}^0(t) - \int_{-\infty}^t \bar{\mathcal{G}}(t, t') [\delta X(t') + n^{(1)}(t')] dt'.
 \end{aligned} \tag{6.7}$$

We have few important remarks on the above relations. The first one is that the equation governing the fluctuations of the  $Y$  quadrature is the same that we would have without feedback, therefore  $\delta Y$  behaves as in a free oscillator and, for example, it can be used to reliably measure any external force. Second point, we have a well defined phase plane: the oscillator is not just frequency stabilized, but also phase-locked to the reference. Third issue, the response function of the  $Y$  quadrature is stable, with a peak frequency defined a priori (at  $\omega = 0$ , corresponding to  $\omega_e$  for the evolution of  $x$ ) and, as a consequence, stable width  $\gamma_{om}$  and peak signal-to noise ratio.

The spectrum of the measured  $Y_m$  quadrature calculated from Eq. 6.7 can be

written in the form

$$S_{Y_m} = \mathcal{L}(\omega)S_{st} + S_n/2 \quad (6.8)$$

with

$$\mathcal{L}(\omega) = \mathcal{A} \frac{\gamma_{om}}{\omega^2 + (\frac{\gamma_{om}}{2})^2} \quad (6.9)$$

where  $\mathcal{A} = \int_{-\infty}^{\infty} \mathcal{L}(\omega)d\omega/2\pi = 1/(2\gamma_{om}m^2\omega_e^2)$  and  $S_{st}$  is the total force noise spectral density.

Concerning the measured  $X_m$  quadrature, its spectrum can be calculated assuming an integral feedback loop. As mentioned earlier, in this case the kernel is constant, that is,  $\bar{\mathcal{G}}(t, t') = G_0$ . The equation for  $\delta\omega(t)$  in Eqs. 6.7 becomes

$$\delta\omega = \delta\omega_{eff}^0(t) - G_0 \int_{-\infty}^t [\delta X(t') + n^{(1)}(t')] dt'. \quad (6.10)$$

Moving to Fourier<sup>1</sup> space and solving for  $\delta X(\omega)$  we find that the spectrum of the measured  $X_m$  quadrature is

$$S_{X_m} = \mathcal{R}(\omega)S_{st} + \mathcal{B}(\omega) S_n/2 + \mathcal{D}(\omega) S_{\delta\omega_{eff}^0}/2 \quad (6.11)$$

where  $S_{\delta\omega_{eff}^0}$  is the spectral density of the fluctuations of  $\delta\omega_{eff}^0(t)$  and where we defined

$$\begin{aligned} \mathcal{R}(\omega) &= \gamma_{om} \mathcal{A} \left| \frac{1}{i\omega + \frac{\gamma_{om}}{2} + \frac{G_0 Y_0}{i\omega}} \right|^2 = \gamma_{om} \mathcal{A} |r(\omega)|^2 \\ \mathcal{B}(\omega) &= \left| 1 - r(\omega) \frac{Y_0}{i\omega} \right|^2 \\ \mathcal{D}(\omega) &= |r(\omega)Y_0|^2. \end{aligned} \quad (6.12)$$

It is possible to show that for sufficiently high gain in the feedback loop  $\mathcal{B}(\omega) \simeq 1$ . As a consequence Eq. 6.11 simplifies to

$$S_{X_m} \simeq \mathcal{R}(\omega)S_{st} + S_n/2 + \mathcal{D}(\omega) S_{\delta\omega_{eff}^0}/2 \quad (6.13)$$

The treatment presented here includes slow fluctuations of  $\omega_{eff}^0$  as well as its fast, although weak, variations that can be considered as phase fluctuations. The case of strong and fast variations of  $\omega_{eff}^0$ , producing trajectories in the phase plane that take  $\mathbf{R}$  far from the region with  $\theta < 1$ , requires numerical integration of Eq. 6.3 and the approximation of a free  $Y$  quadrature is no longer reliable.

<sup>1</sup>To comply with the conventions for the Fourier transforms used in electronics we use in this chapter the following definition:  $x(\omega) = \int_{-\infty}^{\infty} x(t)e^{-i\omega t}dt$  and  $x(t) = \frac{1}{2\pi} \int_{-\infty}^{\infty} x(\omega)e^{i\omega t}d\omega$

By excluding the coherent excitation and the frequency control, the spectrum of both quadratures, for an opto-mechanical resonance at  $\omega_{eff}^0 = \omega_e + \delta\omega$ , is

$$S_{X_m} = S_{Y_m} = \frac{1}{2} [\mathcal{L}(\omega - \delta\omega) + \mathcal{L}(\omega + \delta\omega)] S_{F_{st}} + \frac{S_n}{2} \quad (6.14)$$

and, in case of slow fluctuations of  $\delta\omega$ , the spectral peaks assume the shape of a Voigt profile, maintaining a constant area.

## 6.2 Experimental characterization

The optomechanical system that has been used for the characterization of the control loop is the same described in Chap. 5. We report here its fundamental parameters, cavity length  $L_{cav} = 0.57 \text{ mm}$ , Finesse 57000, coupling parameter  $\zeta = 0.09$ , mode matching 96%, mechanical resonance frequency  $\omega_m/2\pi = 128961 \text{ Hz}$ , effective mass  $m = 1.4 \cdot 10^{-7} \text{ Kg}$  and a mechanical quality factor of  $Q = 16000$ . The measurements are performed at room temperature with a probe beam power in the carrier of  $\mathcal{P}_{PDH} \simeq 0.040 \text{ mW}$  and a pump power of  $\mathcal{P}_{pump} = 1.0 \text{ mW}$ .

The coherent excitation is generated by sending the internal oscillator of the lock-in amplifier to the EOM2 along the pump beam path. The PDH signal is sent to a digital scope and to the lock-in for demodulation. In order to obtain the dispersive curve of Eq. 6.4 for the  $X$  quadrature, the phase of the coherent excitation has to be properly adjusted. This is achieved by measuring the transfer function of the  $X$  quadrature itself and by determining the required phase through a fit of the data. The control of the optical spring is obtained by sending the  $X$  quadrature output of the lock-in to the driver of the AOM after it has been integrated. Both the  $X$  and  $Y$  output signal of the lock-in amplifier are acquired by a digital scope with a resolution of 12 bit and a sampling interval of  $21 \mu\text{s}$ . During the data analysis the time traces, that are about 20 second long (corresponding to  $\sim 10^6$  data points), are divided into 1 s long segments. For each segment the power spectrum is calculated using a FFT algorithm, and corrected for the transfer function of the lock-in amplifier.

We can rewrite Eq. 6.12 (and Eq. 6.13) taking the inverse of a high pass filter as transfer function for the integrator, that is

$$\frac{1}{i\omega} \rightarrow \frac{1 + i\omega/\omega_c}{i\omega/\omega_c} \quad (6.15)$$

where  $\omega_c/2\pi = 160 \text{ Hz}$  is the filter cut-off angular frequency, and replacing  $Y_0 G_0 \rightarrow \check{Y}_0 G_{AOM} G_{opt}$ . Then,  $\mathcal{R}(\omega)$  can be expressed as

$$\mathcal{R}(\omega) = \gamma_{om} \mathcal{A} \left| \frac{1}{i\omega + \frac{\gamma_{om}}{2} + G_{loop}(\omega)} \right|^2 \quad (6.16)$$

where

$$G_{loop}(\omega) = \check{Y}_0 \frac{1 + i\omega/\omega_c}{i\omega/\omega_c} G_{AOM} G_{opt}. \quad (6.17)$$

Here,  $\check{Y}_0$  is the average of the time trace of the  $Y$  quadrature expressed in Volts,  $G_{AOM}/2\pi$  is the overall transduction efficiency of the AOM (expressed in Hz/V) and  $G_{opt} = d\omega_{eff}/d\Delta$  is the optomechanical gain, that can be assumed as a constant in the bad cavity regime and for small detuning. This last parameter has been directly measured to attain a good accuracy. Indeed, it could be estimated from the theoretical model and the input parameters, however, the uncertainty would be much higher. Expressing the open loop gain as in Eq. 6.17 allows us to obtain a model for the  $X$  quadrature PSD that is less affected by calibration errors.

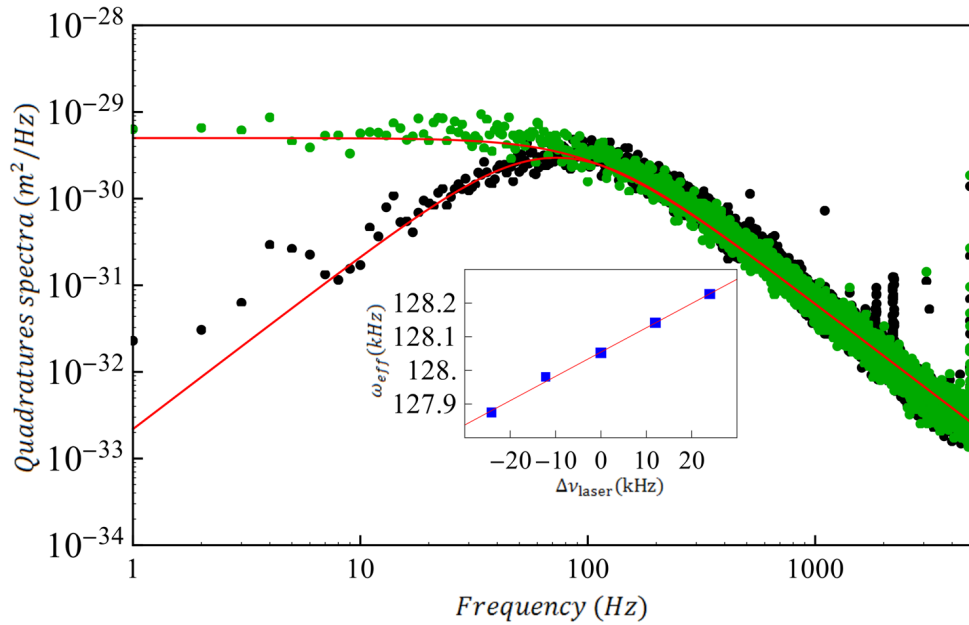


Figure 6.2: Measured  $Y_m$  quadrature (green dots) and  $X_m$  quadrature (black dots) spectra along with theoretical curves (red lines). Inset: calibration of  $G_{opt}$ , we show  $\omega_{eff}$  as a function of small frequency shifts of the pump beam around an initial working point set at  $\Delta\nu_{laser} = 0$ .

In the following measurements the dominant stochastic force is due to thermal noise. In Fig. 6.2 we show an example of the experimental quadrature spectra of the  $Y_m$  quadrature (green dots) and of the  $X_m$  quadrature (black dots) along with theoretical curves obtained with Eq. 6.8 and Eq. 6.13. We remark that, to evaluate these curves, the only free parameter is the effective mechanical damping rate. The model well reproduces the experimental data. In the inset of Fig. 6.2 we show an

example of the calibration of  $G_{opt}$  obtained by shifting the pump beam frequency of a known quantity, with the AOM<sup>2</sup>, and by measuring the resulting effective resonance frequency  $\omega_{eff}$  (blue squares). Also shown is the linear fit of the data (red line).

With the characterization of the control loop we want to define the parameters set that allows the maximum noise reduction in the  $X$  quadrature while remaining stable and maintaining valid the small angle approximation used in the derivation of the model. This second requirement is the most fundamental one since it guaranties that the  $Y$  quadrature can be used for measurement purposes. Keeping constant  $G_{opt}$  we have two ways to change on the loop gain. With reference to Eq. 6.17, we can modify the coherent excitation, to change  $\check{Y}_0$ , and/or modify the electronic gain of the AOM driver thus changing  $G_{AOM}$ . To test their effect on the overall behavior of the loop we have acquired 3 data sets. For the first one we have increased the lock bandwidth of the loop by increasing  $G_{AOM}$ ; we identify this data set as *set1*. For the second one we have increased the lock bandwidth but modifying  $\check{Y}_0$  keeping  $G_{AOM}$  constant (*set2*). For the last set we have increased the coherent excitation while compensating with the reduction of  $G_{AOM}$  (*set3*) in order to keep constant the lock bandwidth. All three data sets are obtained with the mechanical resonance locked at  $\omega_e = 127400 \text{ Hz}$  and with  $G_{opt} = 7.2 \cdot 10^{-3}$ , so that the normalized detuning is  $\Delta_n \simeq 0.09$ .

We show in Fig. 6.3 and in Fig. 6.4 the quadratures spectra of *set1* and *set2* respectively. Qualitatively, in both data sets the low frequency part of the spectral density of the  $X$  quadrature is reduced as the loop gain, and consequently the lock bandwidth, are increased. Over a certain threshold, however, an instability of the control loop appears, manifested by a spurious peak ("servo bump") at about  $1.1 \text{ kHz}$ . The  $Y$  quadrature spectra remains unchanged as the loop gain is increased. Even when the servo bumps are present,  $S_{Y_m}$  is only slightly affected. On the other hand, if the loop gain were to be increased further, the servo bump peak value would increase and its effect on the  $Y$  quadrature spectra would increase as well.

The lock bandwidth (LBW) has been evaluated by fitting the ratio  $S_{X_m}/S_{Y_m}$  with a high pass transfer function to evaluate the cut frequency. As expected, LBW has a linear dependence on the loop gain, as is shown in Fig. 6.5. The maximum value is  $LBW \simeq 260 \text{ Hz}$ , that is greater than the optomechanical half linewidth  $\gamma_{om}/4\pi$ , for both *set1* and *set2*.

In Fig. 6.6 are shown the quadratures spectra for the data *set3*. We recall that,

---

<sup>2</sup>The AOM actually changes the frequency of the probe beam but the cavity lock electronics compensate this shift by modifying the laser frequency, thus keeping the probe beam on resonance. The net result is a shift of the pump beam with respect to the cavity resonance.

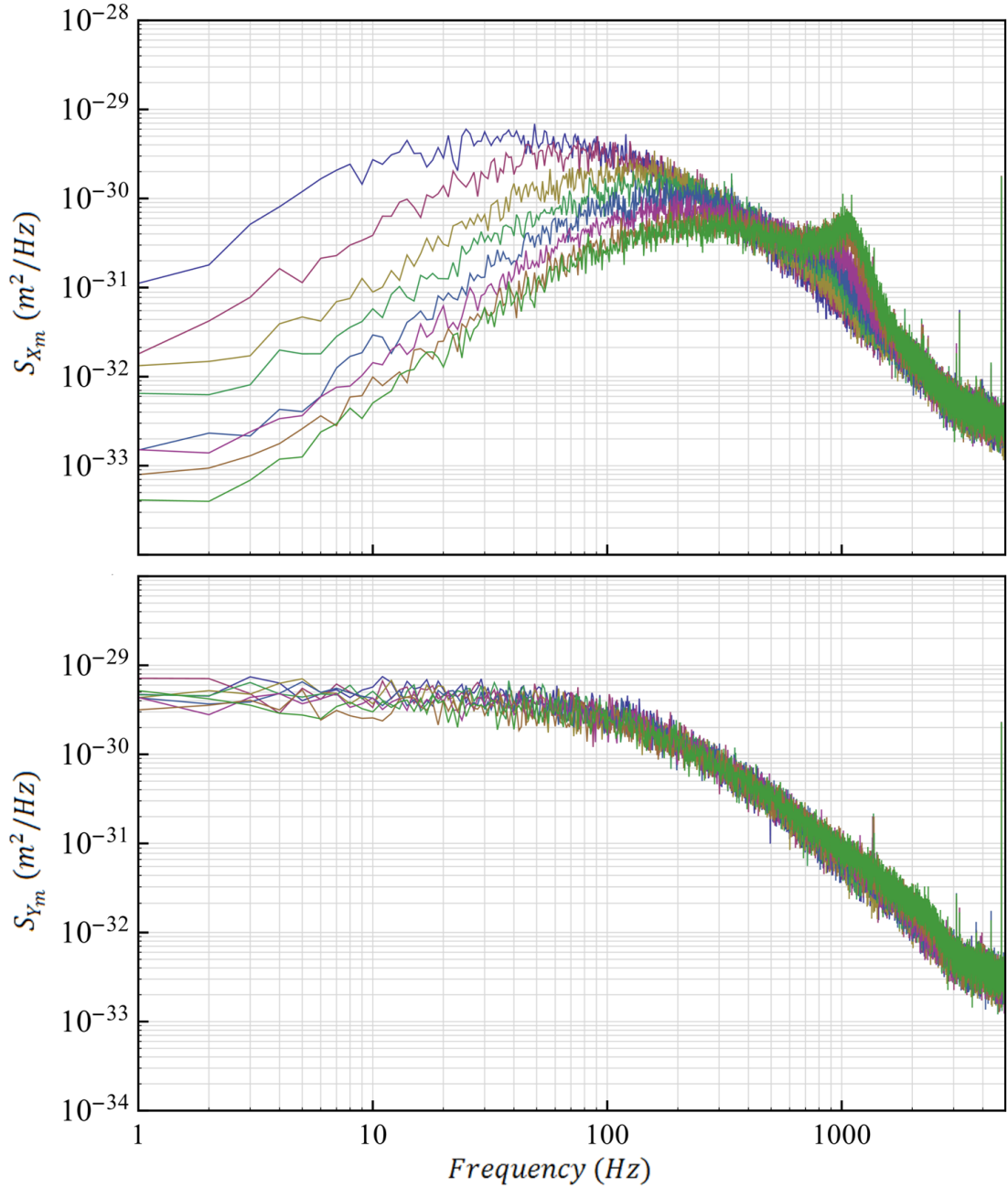


Figure 6.3: *Quadratures spectra of the set1 measurements obtained while increasing  $G_{AOM}$ . Left:  $S_{X_m}$ . Right:  $S_{Y_m}$ .*

for this data set, we wanted to maintain a constant LBW, while increasing  $\check{Y}_0$ . Indeed, in all configurations we obtained  $\text{LBW} = 41 \pm 4 \text{ Hz}$ . An interesting aspect that emerges from these measurements is a nonlinear effect that appears in the  $X$  quadrature spectrum. The low frequency part of the PDH spectrum is up-converted

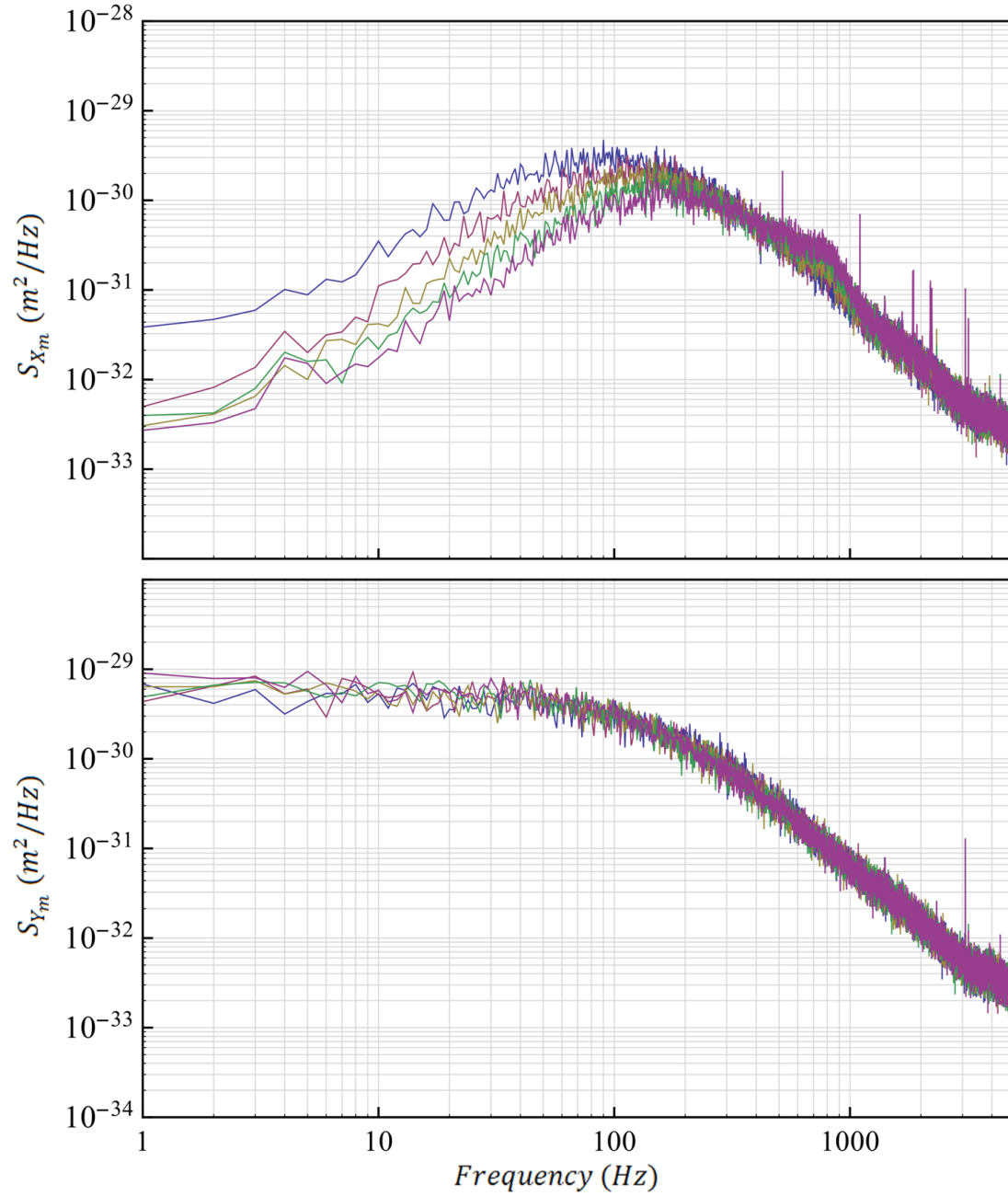


Figure 6.4: Quadratures spectra of the set2 measurements obtained while increasing  $\check{Y}_0$ . Left:  $S_{X_m}$ . Right:  $S_{Y_m}$ .

to the frequency  $\omega_e$  by the strong coherent excitation. Indeed, the amplitude of the peak at  $\sim 4 Hz$  ( a mechanical resonance of the sample holder suspension stage) increases proportionally to  $F_e$  as well as other spectral lines recognizable in the PDH spectra.

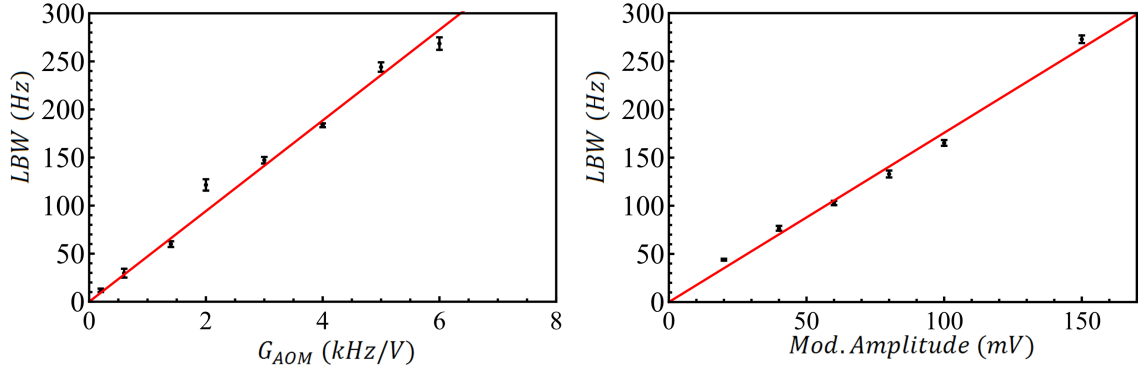


Figure 6.5: Lock bandwidth (LBW) as a function of the relevant parameter determining the overall loop gain, that is,  $G_{AOM}$  for set1 (left) and amplitude of the lock-in reference signal for set2 (right).

To characterize quantitatively the behavior of the control loop we evaluated for every configuration in the three data sets the product  $A\gamma_{om}$ , where  $A$  is the area of the quadratures spectra. This product is independent from the actual dynamical backaction. Indeed, we have

$$A_Z \gamma_{om} = \gamma_{om} \int_{-\infty}^{\infty} S_{Z_m}(\omega) d\omega = \frac{k_B T}{m\omega_e^2} \gamma_m \quad (6.18)$$

where  $Z = X, Y$ . The relevance of this product comes from the fact that we observed a slow drift of  $\gamma_{om}$  during the long time necessary to accumulate the data. This can be attributed to variations of the pump beam intensity, either due to a drift of the laser intensity itself or to a loss of alignment. If the intensity changes while the control loop is active, the mechanical resonance remains locked at  $\omega_e$ , but this implies a change of the steady state detuning, that in turns gives a different optomechanical damping rate. We observed variations of  $\gamma_{om}$  up to 30% over a time period of about 5 hours. Choosing the product  $A\gamma_{om}$  as estimator allows us to get rid of the effects of these slow additional drifts, and evaluate the performances of the control loop. We show, in Fig. 6.7 (left), the  $A_Y \gamma_{om}$  product for the  $Y$  quadrature for all the configurations corresponding to the three data sets, as a function of the ratio  $2\pi LBW/(\gamma_{om}/2)$ . Within the experimental uncertainties, we find a constant value for such product. In particular, for the *set3* (Red) all the points are close together indicating that, indeed, we have been able to keep a constant  $LBW$ . The dashed line in Figs. 6.7 is the nominal value of  $A\gamma_{om} = 2.4 \cdot 10^{-24} m^2 rad/s$ . Despite the fact that all the experimental data are very close to this value, it is possible to infer the presence of a systematic error whose nature is easy to fathom. Indeed, a residual dynamical

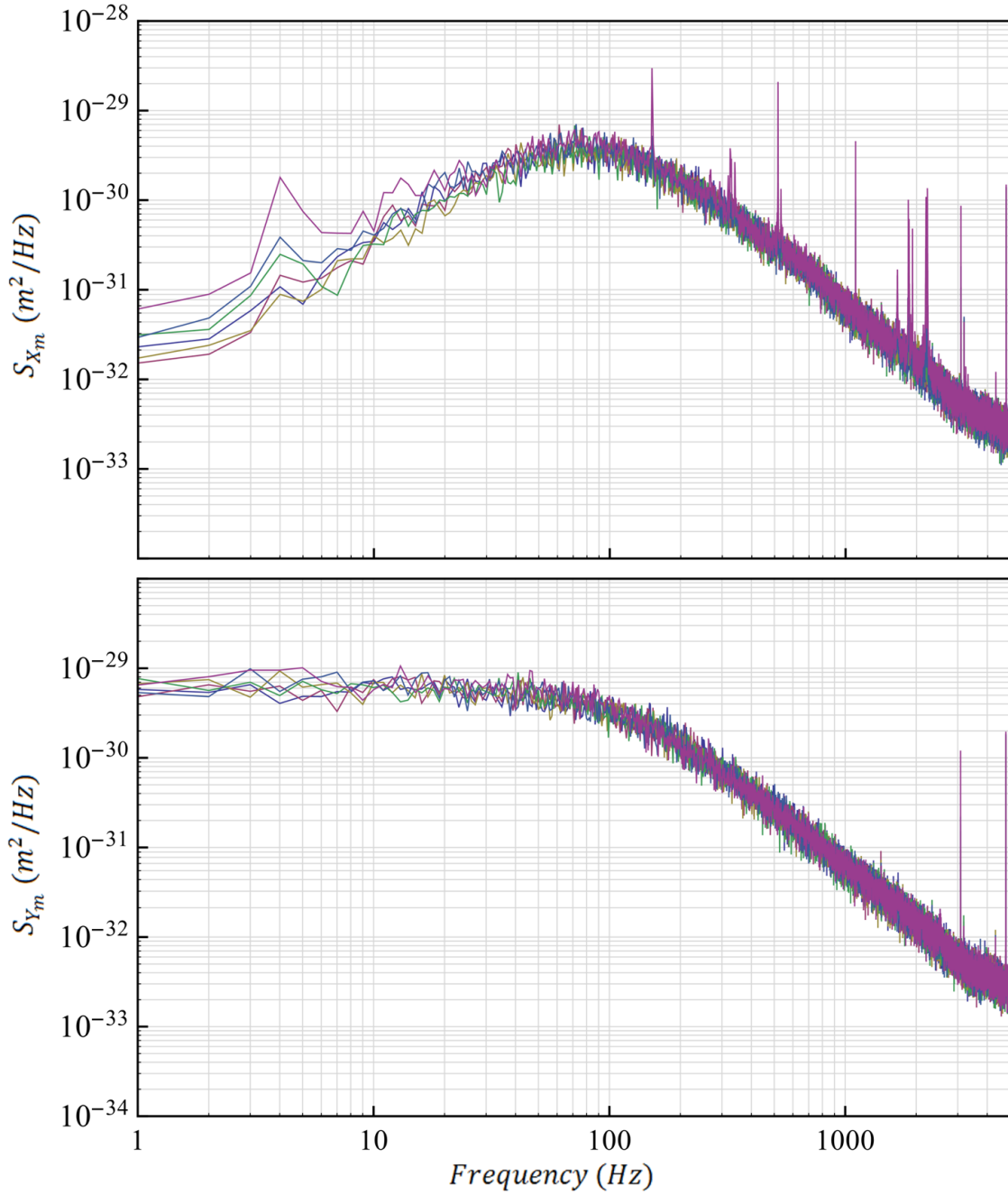


Figure 6.6: *Quadratures spectra of the set3 measurements obtained while increasing  $\check{Y}_0$  and reducing  $G_{AOM}$  in order to maintain constant the lock bandwidth. Left:  $S_{X_m}$ . Right:  $S_{Y_m}$ .*

backaction of the weak probe beam, due to a non vanishing detuning, would explain the difference between experimental data and the theoretical value, since the value

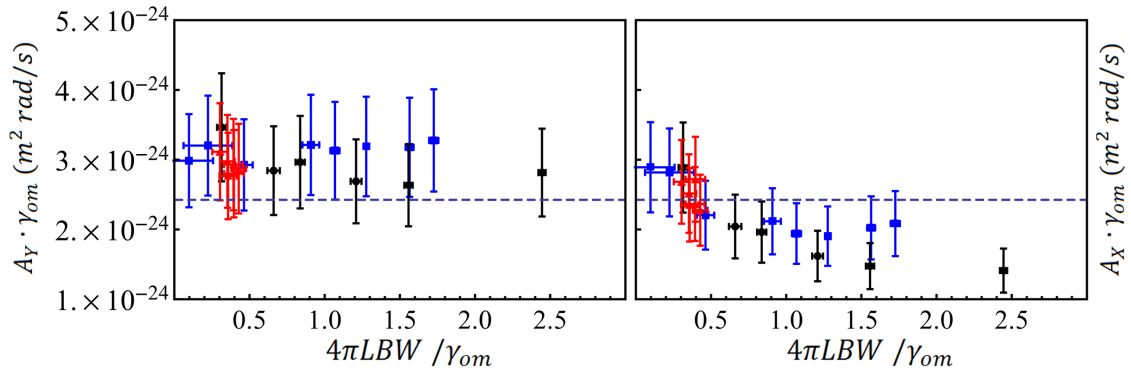


Figure 6.7:  $A \gamma_{om}$  products for all configurations in the three data sets. Left:  $Y$  quadrature. Right:  $X$  quadrature. In both panels: set1 blue points, set2 black points, set3 red points.

of  $\gamma_m$  to consider in Eq. 6.18 would be slightly higher.

In Fig. 6.7 (right), we show the  $A_X \gamma_{om}$  product for the  $X$  quadrature. As the loop gain is increased, the rms fluctuations are reduced up to a factor of 3 dB, except for the the data points of *set3* (red). For both data *set1* (blue) and data *set2* (black), the reduction of  $A_X \gamma_{om}$  saturates roughly when  $4\pi LBW / \gamma_{om} > 1$ . In particular, the saturation value for the data *set1* is slightly higher than that of data *set2* indicating a stronger incidence of the control loop instability.



# Chapter 7

## Detection of weak stochastic force

A frequent crucial task in many applications of optomechanical systems is the detection of weak variations of an external force on a strong background. For instance, this force (that we call *signal force*) can be due to the quantum fluctuations in the radiation pressure, that are usually overwhelmed by background thermal noise (a significant exception is reported in [17]). In this chapter we demonstrate the possibility to resolve stochastic force variations well below 1% of the thermal noise, thanks to the implementation of the Wiener-Kolmogorov filter [106, 107] and the parametric stabilization of the mechanical effective susceptibility described in the previous chapter. These results can be found also in Ref. [29].

To put the problem under a wide, general perspective, let us discuss the task of detecting a weak signal force with flat spectral density (white spectrum) in the presence of a white background force, taking into account a given sensitivity to the displacement of the sensing mass (i.e., a flat readout noise spectrum). These assumptions are meaningful since the sensitive band with respect to a typical input force is limited by the narrow width of the mechanical resonance. The signal force detection can be performed naïvely by measuring the area of the resonance peak emerging from the displacement noise spectrum, as we have done in the previous chapter. With this estimator, the rate of improvement of the statistical uncertainty for increasing measurement time  $t_{meas}$  depends on the correlation time  $\tau_c$  of the oscillator motion, with a relative uncertainty scaling as  $\sim \sqrt{\tau_c/t_{meas}}$ . It seems therefore useful to decrease  $\tau_c$ , i.e., to enhance the damping of the oscillator. However, the fluctuation-dissipation theorem implies that such operation would increase the spectral density of thermal noise. Improved results can instead be achieved by means of a cold damping, e.g. the optical cooling [56, 88, 108], that modifies the effective susceptibility and decreases the correlation time without introducing additional noise

sources. This technique does not increase the signal-to-noise ratio of input excitations, because it changes the response to both signal and background force in the same way. However, as long as the cold damped peak still emerges from the displacement spectral noise, it allows a faster accumulation of statistically independent data bringing therefore, in a given measurement time, to a smaller final uncertainty in the variance of the oscillator motion.

An important remark is that the correlation time of the signal force is by hypothesis very short, therefore the statistics can in principle be much faster than what allowed by the oscillator motion. In other words, the variance of the displacement is not a very efficient indicator, and more refined data analysis can be profitable. In the case of stationary and white input the optimal approach to the measurement is provided by the Wiener-Kolmogorov filtering theory [106, 107]. This technique requires the preliminary knowledge of the exact response function to the input force, and of the signal-to-noise ratio. While the second requirement can be relaxed with a sub-optimal but robust filter using a conservative estimate of the sensitivity [109], the accurate knowledge of the susceptibility is a crucial request. Without its stabilization, the direct measurement of the spectral peak area could be the only applicable strategy in several kinds of opto-mechanical systems, and techniques that reduce the effective coherence time of the oscillator motion, such as cold damping or feedback, represent therefore a way to effectively improve the measurement capabilities of the system [110]. However, it has been remarked that optimal resolution is not really improved in this way [111, 112], and that appropriate data filtering can completely replace these hardware techniques even in the case of non-stationary, non-Gaussian input [113]. In spite of these correct remarks, the problem of the instability in the oscillator parameters and dynamics remains practically difficult to face, and the implementation of optimal analysis requires sophisticated techniques of adaptive filtering. The experimental demonstration in Ref. [113] keeps indeed short ( $\sim ms$ ) measurement times. Therefore, even when willing to apply an efficient data analysis, stabilization and feedback techniques, such as the one presented in Chap. 6, are crucial.

## 7.1 Measurement strategies

In the following we consider the same experimental setup described in the previous chapter, so that the dynamical equation describing the motion of the oscillator is again given by Eq. 6.1 with the difference that we include in the stochastic force term  $f_{st}$  an additional contribution from a stochastic signal force  $f_s$ , with spectral

density  $S_s$ , and whose effects and variations we want to resolve. We consider two possible measurement strategies to detect  $f_s$ , that we assume hidden by the thermal background. In other words, we are seeking for a precise measurement of the stochastic force in order to resolve its weak variations due to changes in  $S_s$ . We are not dealing with measurement accuracy and reproducibility, that both depend critically on absolute calibrations.

The first strategy is simply measuring the area, that we indicate here with  $\sigma^2$ , of the resonance peak. The advantage of this method is that frequency stability of the opto-mechanical oscillator is not crucial: the peak area can be calculated by direct integration of the spectrum of  $x$  within an appropriate frequency interval, provided that  $\omega_{eff}$  is well within the integration band, and the latter is extended to few  $\gamma_{om}$  yet maintaining a negligible contribution of the background noise  $S_n$ . The same measurement can be performed, with equal efficiency, on the spectrum of a quadrature. The estimated force spectral density is  $E\{S_F\} = \sigma^2/\mathcal{A}$ , where  $\mathcal{A}$  is defined as in Eq. 6.9. The drawback of this method is the rather slow improvement of the statistical uncertainty, decreasing as  $\propto \sqrt{\tau_c/t_{meas}}$  where the correlation time is now  $\tau_c = 1/\gamma_{om}$ . The reason is that this strategy does not exploit the full information contained in the signal, whose spectrum around resonance is dominated by the effect of the force fluctuations even well beyond the width  $\gamma_{om}$ .

The second strategy is a close approximation of the Wiener filtering, that represents the optimal choice in case of stationary noise. The non-causal Wiener filter, applied to the spectrum  $S_{Y_m}$  of Eq. 6.8, is defined as

$$|W(\omega)|^2 = \frac{1}{\mathcal{L}(\omega)} \left[ \frac{1}{1 + \Gamma \frac{\mathcal{L}(0)}{\mathcal{L}(\omega)}} \right]^2 \quad (7.1)$$

and the maximum information on  $S_F$  from the experimental  $S_{Y_m}$  is obtained from the filtered spectrum  $S_W = |W|^2 S_{Y_m}$ . The  $1/\mathcal{L}$  factor in Eq. 7.1 is a whitening and calibration function, while the term between the square brackets is a weight function that requires preliminary estimate of the noise-to-peak-signal ratio  $\Gamma$ . Its optimal value is  $\Gamma_{opt} = S_n/2\mathcal{L}(0)S_F$ , but an efficient, even if sub-optimum, filter can choose a  $\Gamma > \Gamma_{opt}$  [109]. In any case, a preliminary fit of a spectrum  $S_{Y_m}$  allows to extract the parameters  $\gamma_{om}$  and  $\Gamma$  for the following application of the Wiener filtering procedure. The correlation time of the filtered signal is now  $\tau_c \sim \sqrt{\Gamma}/\gamma_{om}$ , yielding a faster improvement of the statistics with  $t_{meas}$  with respect to the previous strategy. For an optimum filter (with  $\Gamma = \Gamma_{opt}$ ),  $1/\tau_c$  corresponds to the effective sensitivity bandwidth, i. e., to the frequency band where the effect of force noise falls below the measurement sensitivity (i.e.,  $\mathcal{L}(\omega)S_F = S_n/2$ ). An example of the application of

the whitening function and the complete Wiener filter to a real spectrum is shown in Fig. 7.1.

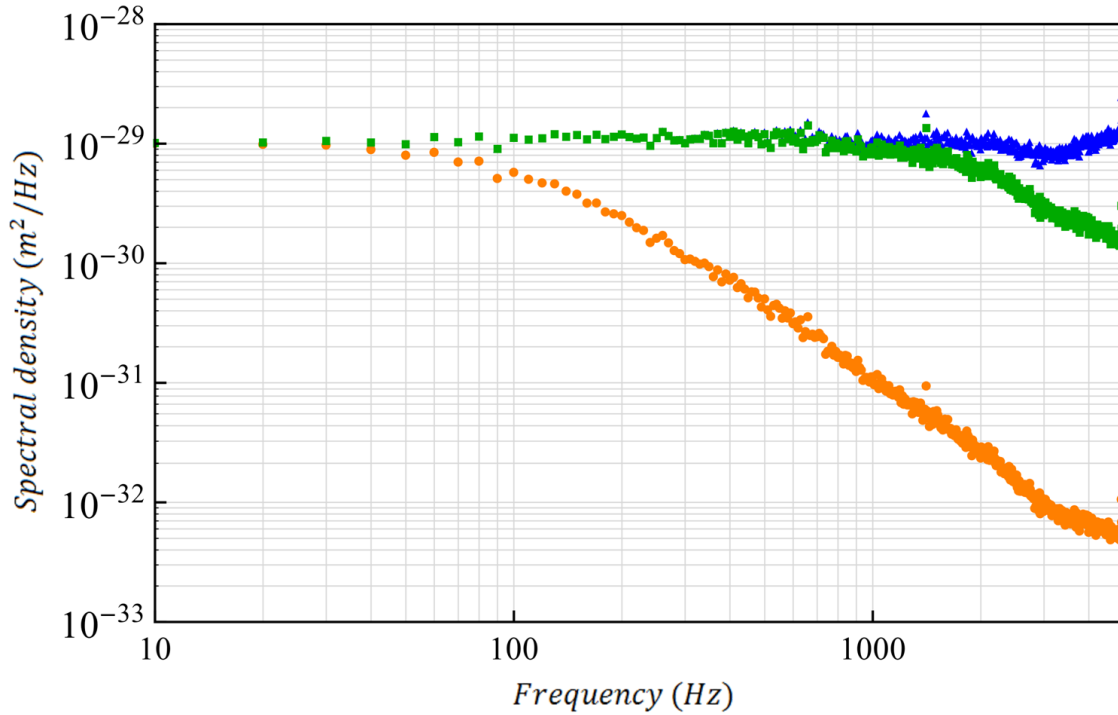


Figure 7.1: Measured spectral density in the  $Y$  quadrature ( $S_{Y_m}$ ) (orange circles); whitened spectrum (blue triangles); with complete Wiener filtering (green squares).

The force spectral density is estimated by integrating the filtered spectrum  $S_W$  and dividing the result by the effective bandwidth  $\sim 1/\tau_c$ . In our real data some spurious peaks appear in the spectrum at few  $kHz$  from the opto-mechanical resonance, therefore the integration is truncated at  $\omega_{cut}/2\pi = 3 kHz$ , slightly below  $1/\tau_c$ .

As we have seen, the application of the Wiener filtering requires the knowledge of the transfer function between force noise and output. For this reason, the parametric control strongly facilitates the filtering procedure, by fixing both the opto-mechanical resonance at  $\omega_{eff} = \omega_e$  and, as a consequence, its width  $\gamma_{om}$ . Without control, optimal filtering would require an adaptive tuning of the parameters, that we are not trying to apply here.

## 7.2 Measurements and data analysis

The experiment has been performed with the same optomechanical cavity and experimental setup used in the characterization of the control loop presented in the previous chapter. In this experiment, however, we want to evaluate the performances of the two measurement strategies presented earlier in two configurations: with and without the parametric control. In this way we can also investigate further the performances of the control loop. When it is active, the effective resonance is fixed, as before, at  $\omega_{eff} = \omega_e = 127400 \text{ Hz}$  with a corresponding resonance width of  $\gamma_{eff}/2\pi = 200 \text{ Hz}$ . Since we wanted to apply a more refined data analysis we have chosen a loop gain for which  $LBW/\gamma_o < 1$ , in this way the control is always stable and in both quadratures the servo bump peak is absent. When the control loop is switched off, the effective mechanical resonance is moved to about  $127400 \text{ Hz}$  by hand tuning the pump beam. In this second configuration the lock-in reference frequency is set at  $127200 \text{ Hz}$ , so that the well defined resonance peak at  $\sim 200 \text{ Hz}$  allows to measure more accurately its parameters.

The  $Y$  quadrature time trace at the output of the lock-in is acquired with the same sampling interval ( $21 \mu\text{s}$ ), but in this experiment data are collected in 35 consecutive time traces, each one lasting about 20 second covering in all nearly 12 minutes, then stored in a hard disk. Several of such series are taken separated by periods of few minutes (necessary to write the data on disk), for a total observation time of several tens of minutes. Here, the time series are divided into  $100 \text{ ms}$  long segments.

The spectra corresponding to the first 20 seconds are averaged, and the averaged spectrum is fitted with Eq. 6.8 (when the parametric control is active) or to Eq. 6.14 (without control). An example of the averaged spectra and the fits are shown in Fig. 7.2. From the fitting procedure we obtain the resonance width, signal maximum and, in the absence of the control, also the resonance frequency. The signal maximum  $Max$  is just exploited to define the value of the parameter  $\Gamma$  to be used for Wiener filtering. At this purpose, we consider a conservative value of the background additive noise on  $Y$ , at  $S_{bg} = 8 \cdot 10^{-33} \text{ m}^2/\text{Hz}$  (one order of magnitude larger than the real  $S_n$ ), and define  $\Gamma = S_{bg}/Max$ . A typical value of  $\Gamma$  is  $10^{-3}$ .

From each of the following spectra (after the first 20 s) we calculate the force spectral density  $S_F$  using the different methods described previously (i.e., from the peak area and using Wiener filtering, both in the configuration with parametric feedback and with free-running oscillator). For the case with the control active, we report in Fig. 7.3 the average  $\bar{S}_F(t_{meas})$  of  $S_F$  accumulated over  $m$  consecutive

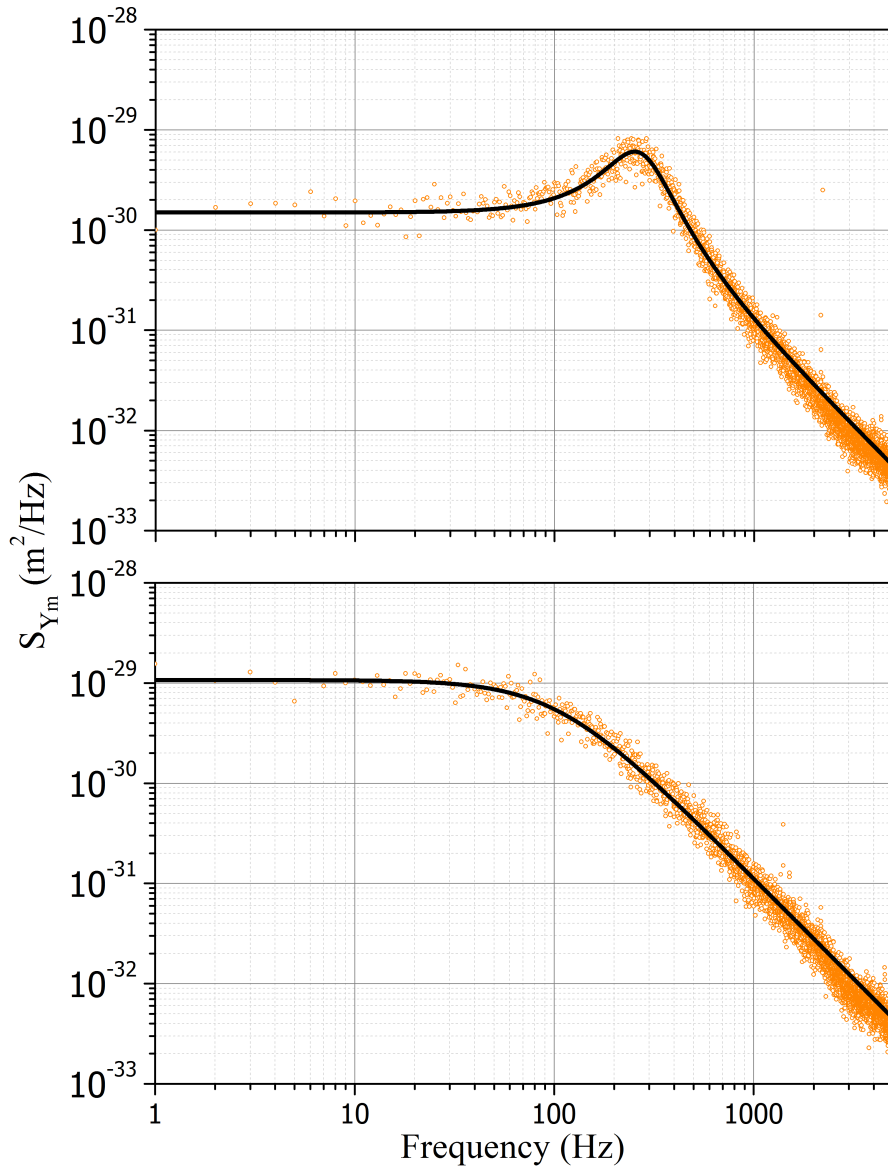


Figure 7.2: *Spectral densities (single-sided) of the Y quadrature ( $S_{Y_m}$ ), for an oscillator without (upper panel) and with (lower panel) parametric control. With a solid line we show the respective fitting functions.*

spectra, corresponding to a measurement time  $t_{meas} = m\tau$ , where  $\tau = 100\text{ ms}$  is the time interval used for calculating each spectrum. The relative standard error  $\sigma_{REL}$  is used to calculate the confidence regions  $(1 \pm \sigma_{REL})\bar{S}_F$ , where  $\bar{S}_F$  is the average at the end of the measurement period. The figure shows the expected convergence of the measured  $\bar{S}_F(t_{meas})$ , which is clearly faster for the filtered data.

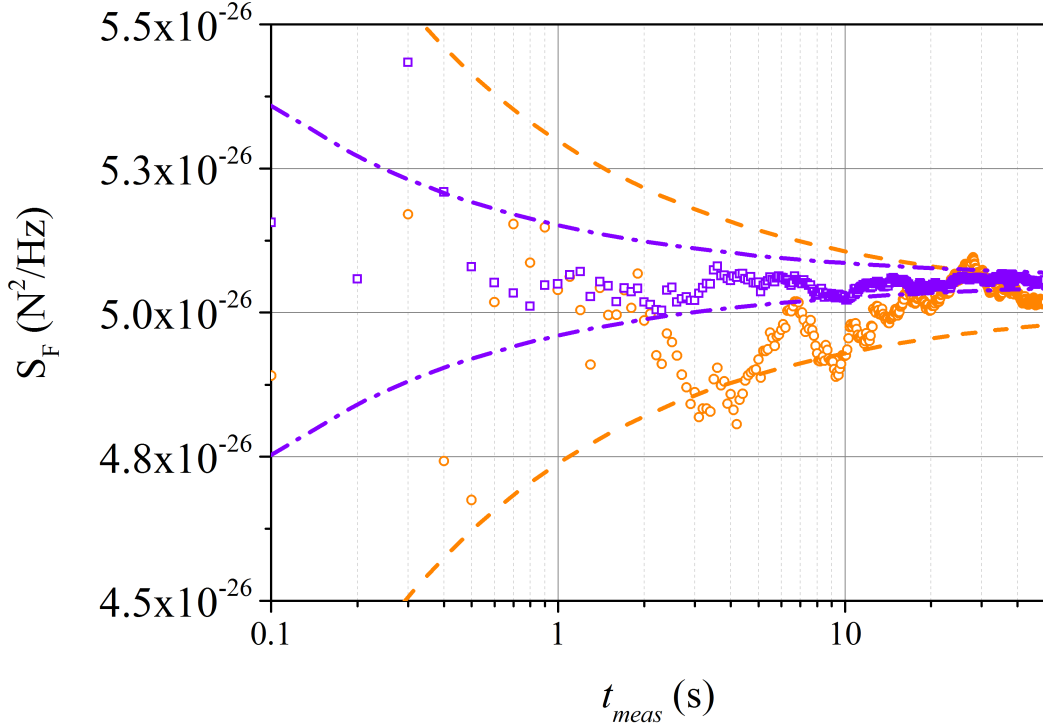


Figure 7.3: Average over a measurement time  $t_{meas}$  of the force noise spectral density  $S_F$ , measured on the oscillator with parametric control using the peak area (orange circles) and the Wiener filtered spectra (violet squares). The confidence bands (respectively dashed and dash-dotted lines), correspond to one standard error.

The relative standard error can be calculated as follows. Generally speaking, we are considering a Gaussian, zero mean stochastic process  $x(t)$  with finite variance  $\sigma_x^2$ , correlation function  $C_{xx}$ , and power spectral density  $S_{xx}$ . The estimate of the mean square of  $x(t)$  in the interval  $[0, t_{meas}]$  has expectation value  $\sigma_x^2$  and standard deviation [109, 114]

$$STD \simeq \left[ \frac{2}{t_{meas}} \int_{-\infty}^{\infty} C_{xx}^2(\tau) d\tau \right]^{\frac{1}{2}}. \quad (7.2)$$

The relative standard deviation is defined as  $\sigma_{REL} = STD/\sigma_x^2$ , and it can be expressed in terms of the spectral densities using

$$\sigma_x^2 = \int_{-\infty}^{\infty} S_{xx}(\omega) \frac{d\omega}{2\pi} \quad (7.3)$$

$$STD \simeq \left[ \frac{2}{t_{meas}} \int_{-\infty}^{\infty} S_{xx}^2(\omega) \frac{d\omega}{2\pi} \right]^{\frac{1}{2}}$$

For a spectrum given by  $S_{xx}(\omega) \propto \mathcal{L}(\omega)$  we obtain the relative standard deviation [109]

$$\sigma_{REL} = \frac{2}{\sqrt{t_{meas}\gamma_{om}}}. \quad (7.4)$$

This expression can be used for the relative uncertainty in the measurement of  $S_F$  using the peak area, since in this case we can neglect the measurement noise  $S_n$  and the finite integration band defined by  $\omega_{cut}$ . Indeed, the one  $\sigma$  confidence region in Fig. 7.3 (dashed lines) for the peak area measurement is calculated using Eq. 7.4. For the Wiener-filtered process, using Eq. 6.8, Eq. 7.1 and the expressions of  $S_W$  and  $\Gamma_{opt}$  we can write the output spectrum in the form

$$S_{xx} \propto \mathcal{L}(\omega) \frac{\mathcal{L}(\omega) + \mathcal{L}(0)\Gamma_{opt}}{(\mathcal{L}(\omega) + \mathcal{L}(0))^2} \quad (7.5)$$

and the relative standard deviation as

$$\begin{aligned} \sigma_{REL} &= \frac{2}{\sqrt{t_{meas}\gamma_{om}}} \left( \frac{\Gamma}{1 + \Gamma} \right)^{\frac{1}{4}} \frac{\sqrt{\pi \int_0^{y_c} \left[ \frac{1+gy^2}{(1+y^2)^2} \right]^2 dy}}{\int_0^{y_c} \frac{1+gy^2}{(1+y^2)^2} dy} \\ y_c &= \omega_{cut} \frac{2}{\gamma_{om}} \sqrt{\frac{\Gamma}{1 + \Gamma}} \\ g &= \frac{\Gamma_{opt}(1 + \Gamma)}{\Gamma(1 + \Gamma_{opt})}. \end{aligned} \quad (7.6)$$

Using these last equations and the parameters given earlier, we evaluated the one  $\sigma$  confidence region in Fig. 7.3 (dashed-dotted lines) for the filtered data.

For the case of the free-running resonator, the spectrum is formed by a couple of symmetric Lorentzian peaks centered at  $\pm\delta\omega$  (see Eq. 6.14). The relative standard deviation, when measuring directly the peaks area, becomes

$$\sigma_{REL} = \frac{2}{\sqrt{t_{meas}\gamma_{om}}} \sqrt{\frac{\gamma_{om}^2 + 2\delta\omega^2}{\gamma_{om}^2 + 4\delta\omega^2}}. \quad (7.7)$$

The Wiener filter is obtained from the expression for a single peak, given in Eq. 7.1, by replacing  $\mathcal{L}(\omega) \rightarrow 0.5(\mathcal{L}(\omega - \delta\omega) + \mathcal{L}(\omega + \delta\omega))$ . Due to the flattening action of the Wiener filter, the filtered output is very similar to the case of the single peak. As a consequence, for our typical parameters, the two theoretical values of  $\sigma_{REL}$  differ by less than 1%.

These calculations, however, are just valid for a stationary system. A more reliable assessment on the measurement stability on the long term and on the achievable

resolution is provided by the Allan variance [115]. In our case, its estimator is defined as

$$\sigma_A^2(m) = \frac{1}{N - 2m + 1} \sum_{k=1}^{N-2m+1} \frac{(\bar{x}_{k+m} - \bar{x}_k)^2}{2} \quad (7.8)$$

$$\bar{x}_k(m) = \frac{1}{m} \sum_{n=k}^{k+m-1} S_F(n)$$

where  $S_F(n)$  is the value of force spectral density calculated from the  $n$ -th spectrum and  $N$  is the total number of spectra. The Allan deviation  $\sigma_A^2(m)$  estimates the one sigma uncertainty that can be obtained with a measurement lasting  $t_{meas} = m\tau$ , and is equal to  $\sigma_{REL}$  in the absence of excess fluctuations (typically, for short measurement times).

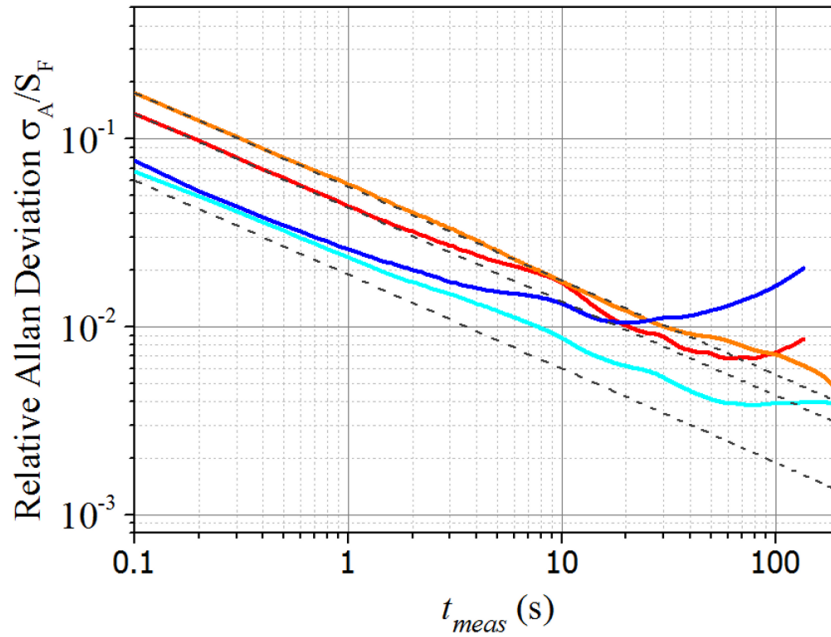


Figure 7.4: *Relative Allan deviation concerning the measurement of the input stochastic force  $S_F$ , performed with four different procedures. Solid lines, from the upper to the lower curve (as seen in the left region of the graph): measurement from the peak area, with parametric control (orange); the same, without control (red); measurement from the Wiener-filtered data, without parametric control (deep blue); the same, with control (light blue). Dashed lines display the expected behavior in the absence of long-term effects, given by Eq. 7.4 (upper line), Eq. 7.7 (middle line), and Eq. 7.6 (considering an implementation of the optimal filter; lower line).*

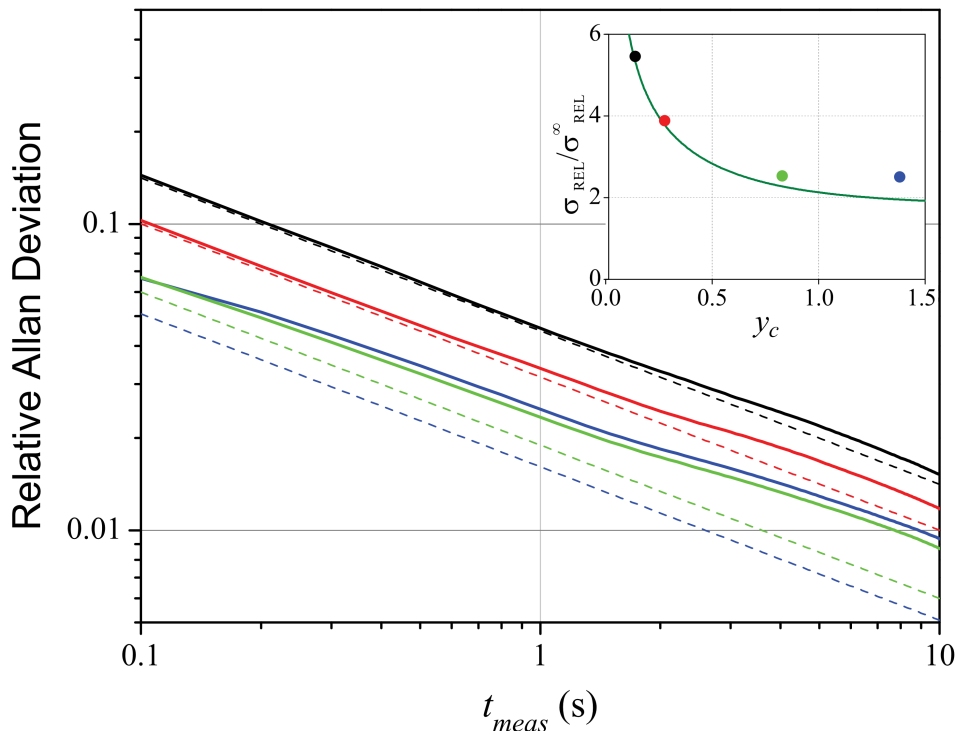


Figure 7.5: *Relative Allan deviation for the measurement of  $S_F$  using the Wiener filtered data, for different values of the cutoff frequency. The dashed lines correspond to the calculated  $\sigma_{REL}$  for  $\omega_{cut}/2\pi = 500$  Hz, 1 kHz, 3 kHz and 5 kHz (from the upper to the lower line). The solid curves are the experimental results for the same cutoff frequencies. In the inset, the experimental relative Allan deviation at  $t_{meas} = 0.1$  s, normalized to the corresponding  $\sigma_{REL}^\infty$ , is reported for the same values of  $\omega_{cut}$  and compared with the theoretical behavior shown with a solid line.*

The calculated relative Allan deviation (i.e.,  $\sigma_A$  divided by  $S_F$ ) is reported in Fig. 7.4 for the different measurement strategies. We can derive two main considerations: a) as expected, the measurement with Wiener filtering improves the statistical uncertainty much faster than the measurement from the peak area. For the former, a 1% resolution is obtained after 10 s and the best resolution of 0.4% is achieved, thanks to the parametric stabilization, after one minute; for the latter, the necessary measurement periods are about three times longer, in agreement with the ratio between the respective  $\sigma_{REL}$ ; b) for measurement periods exceeding 1 s, the parametric control is crucial for the application of Wiener filtering. The measurement resolution does not improve any more after one minute: with the parametric control it remains constant, while it becomes even worse without control. It means that the parametric

control also allows a much more relaxed choice of the optimal measurement time.

The last aspect that has to be discussed is the choice of  $\omega_{cut}$  and its implications. In our experiment,  $y_c = 1$  for  $\omega_{cut}/2\pi \simeq 3600 \text{ Hz}$ . In Fig. 7.5 we report the measured relative Allan deviation as a function of  $t_{meas}$  for different values of the cutoff frequency, together with its expected behavior. When  $\omega_{cut}/2\pi$  surpasses  $3 \text{ kHz}$ , the presence of additional peaks starts to influence the measurement. Indeed, we can see that the data extracted with the cutoff at  $5 \text{ kHz}$  overtake the curve corresponding to  $\omega_{cut}/2\pi = 3 \text{ kHz}$ . It is useful, at this point, to consider the two limits  $y_c \rightarrow \infty$  and  $y_c \ll 1$ , that for  $g \ll 1$  and  $\Gamma \ll 1$  can be written respectively as

$$\sigma_{REL}^{\infty} \simeq \sqrt{\frac{10}{t_{meas}\gamma_{om}/\sqrt{\Gamma}}} \quad (7.9)$$

and

$$\sigma_{REL} \simeq \sqrt{\frac{2\pi}{t_{meas}\omega_{cut}}}. \quad (7.10)$$

In the inset of Fig. 7.5 (solid line) we show the behavior of  $\sigma_{REL}/\sigma_{REL}^{\infty}$  as a function of  $y_c$ . The relative accuracy is just 20% worse if the integration is limited to  $y_c = 1$ . On the other hand, for the  $5 \text{ kHz}$  cutoff frequency, that is with  $y_c > 1$ , the experimental point for  $\sigma_{REL}/\sigma_{REL}^{\infty}$  deviates from the theoretical curve. Indeed, as for the Allan deviation, this is due to spurious peaks that affect  $S_{y_m}$ . In conclusion, with the cutoff at  $\omega_{cut}/2\pi = 3 \text{ kHz}$  we are close to the maximum precision allowed by our background, yet rejecting spurious statistic of the spectrum.



## Chapter 8

# Squeezing a thermal mechanical oscillator

A recent major breakthrough in experimental quantum mechanics is the possibility of preparing macroscopic systems close to their fundamental quantum state. In particular, micro-and nano-oscillators have been recently cooled down to an occupation number close to unity or even below it [21, 116, 117, 118, 119]. While remaining in a thermal state, such systems display peculiar quantum properties such as asymmetric modulation sidebands induced in a probe field [120]. A further interesting development would be the creation of a qualitatively different quantum state, for instance, a mechanical squeezed state. To this purpose, possible techniques are backaction evading measurements [121, 122, 123, 124] and degenerate [125, 126] or nearly degenerate [127, 128, 129] parametric modulation. Mechanical oscillators operate in the degenerate parametric regime when their spring constant is modulated at twice the oscillator resonance frequency. In such a condition, the response of the oscillator to an external excitation acting close to resonance is enhanced, until the parametric modulation depth reaches a threshold marking the birth of self-oscillations (parametric resonance) [130]. More precisely, the response is amplified in the quadrature of the motion in phase with the parametric modulation, and deamplified in the orthogonal quadrature ( $\pi/2$  quadrature). Therefore the distribution of fluctuations in the phase plane caused by stochastic excitation is squeezed and, in particular, its variance is reduced below its free-running value in the  $\pi/2$  quadrature. As a consequence, the parametric effect can be used to produce quadrature squeezed states of a macroscopic oscillator, similarly to what is commonly obtained for the electromagnetic field in optical parametric oscillators [46, 50]. This effect has already been demonstrated for thermal oscillators [125, 126, 129], and is expected even for the

quantum noise [127, 128]. However, since the amplified quadrature evolves into self-oscillations for an excitation strength approaching the threshold, the corresponding noise reduction in the  $\pi/2$  quadrature, monotonic with the parametric excitation, is limited to  $-3\text{ dB}$ . This is a general feature of parametric squeezing [46, 50]. Recent proposals to surpass this limit are based on continuous weak measurements and a detuned parametric drive [127], or unbalanced sidebands modulation [131].

A recent experiment [129] shows, indeed, that the uncertainty in the knowledge of the oscillator trajectory in the phase space (*localization*) is squeezed with a minimal variance reduced by  $-6.2\text{ dB}$  with respect to that of a free thermal oscillator. The authors also suggest that, using the information on the oscillator position in an appropriate feedback loop, even the *confinement* of the oscillator in a strongly ( $> 3\text{ dB}$ ) squeezed state could be obtained, though such a result has not yet been demonstrated. Here, we follow Ref. [129] to identify two very different approaches to the issue. We call *localization* the identification of the location in the phase plane of the oscillator trajectory, achieved through highly refined data analysis, to distinguish it from the *confinement* in a chosen limited (squeezed) region in the phase plane.

In this chapter, we report on the observation of the confinement of a micro-oscillator in a squeezed thermal state, obtained by parametric modulation of the optical spring constant [54, 55]. We exploit the parametric feedback loop introduced in Chap. 6 to stabilize the amplified quadrature allowing us to surpass the  $3\text{ dB}$  barrier on noise reduction, with a best experimental result of  $-7.4\text{ dB}$ . The results that we present here have been recently published and can be found in Ref. [30].

## 8.1 Stabilized modulation of the optical spring

We start with the description of the dynamical evolution of an optomechanical oscillator under the action of the stochastic thermal force  $f_T$ , and whose effective spring constant is modulated at twice its effective resonance frequency. Later on, we discuss, the simultaneous action of the parametric stabilization. The equation of motion we consider is then

$$\ddot{x} + \gamma_{om}\dot{x} + \omega_{eff}^2[1 + \epsilon \cos(2\omega_{eff}t + \theta_{2f})] = \frac{f_T}{m} \quad (8.1)$$

where, as usual,  $\gamma_{om}$  and  $\omega_{eff}$  are the effective mechanical parameters,  $f_T$  is the stochastic thermal force and the modulation depth  $\epsilon$  is assumed to be small compared to 1. As was done in the previous chapters, we decompose the oscillator motion into two quadratures  $X(t)$  and  $Y(t)$  in a frame rotating at angular frequency  $\omega_{eff}$ ,

according to

$$x(t) = X(t) \cos \omega_{eff} t + Y(t) \sin \omega_{eff} t. \quad (8.2)$$

Assuming  $\gamma_{om} \ll \omega_{eff}$  and neglecting terms at  $3\omega_{eff}$ , caused by the spring modulation, the evolution equation for the two quadratures can be written as

$$\begin{aligned} \dot{X} + \frac{\gamma_{om}}{2} X + \frac{\epsilon \omega_{eff}}{4} [\sin(\theta_{2f}) X + \cos(\theta_{2f}) Y] &= \frac{f_T^{(1)}}{m \omega_{eff}} \\ \dot{Y} + \frac{\gamma_{om}}{2} Y + \frac{\epsilon \omega_{eff}}{4} [\cos(\theta_{2f}) X - \sin(\theta_{2f}) Y] &= \frac{f_T^{(2)}}{m \omega_{eff}} \end{aligned} \quad (8.3)$$

where the stochastic force term has correlation function  $\langle f_T^{(i)}(t) f_T^{(j)}(t') \rangle = \delta_{ij} \delta(t - t') S_T / 2$  ( $i, j = 1, 2$ ). By choosing  $\theta_{2f} = -\pi/2$  we can recover two uncoupled equations and, expressing the modulation amplitude as  $\epsilon = \frac{2\gamma_{om}}{\omega_{eff}} g$ , we find

$$\begin{aligned} \dot{X} + \frac{\gamma_{om}}{2} (1 - g) X &= \frac{f_T^{(1)}}{m \omega_{eff}} \\ \dot{Y} + \frac{\gamma_{om}}{2} (1 + g) Y &= \frac{f_T^{(2)}}{m \omega_{eff}} \end{aligned} \quad (8.4)$$

so that, when moving to the Fourier domain, the quadratures PSD are evaluated to be

$$\begin{aligned} S_X &= \sigma_0^2 \frac{\gamma_{om}}{\omega^2 + [\frac{\gamma_{om}}{2} (1 - g)]^2} \\ S_Y &= \sigma_0^2 \frac{\gamma_{om}}{\omega^2 + [\frac{\gamma_{om}}{2} (1 + g)]^2} \end{aligned} \quad (8.5)$$

where  $\sigma_0^2 = k_B T_{eff} / m \omega_{eff}^2$  is the area of the spectra when the modulation is absent. The spectral densities maintain a Lorentzian shape with width multiplied, respectively, by  $(1 - g)$  and  $(1 + g)$ . In the  $X - Y$  plane, we find an elliptical probability distribution thus identifying a *thermal squeezed state* (see Fig. 8.1(d)). The ellipse is aligned so to have the major axis parallel to  $X$ . The area of the spectra, that is, the two quadratures variances, are

$$\begin{aligned} \sigma_X^2 &= \langle X^2 \rangle = \frac{\sigma_0^2}{1 - g} \\ \sigma_Y^2 &= \langle Y^2 \rangle = \frac{\sigma_0^2}{1 + g} \end{aligned} \quad (8.6)$$

From Eqs. 8.5 and Eqs. 8.6 it is easy to see that the variance  $\sigma_X^2$  diverges for  $g \rightarrow 1$ , thus limiting  $\sigma_Y^2$  to values greater than  $0.5\sigma_0^2$  (the mentioned  $-3$  dB limit).

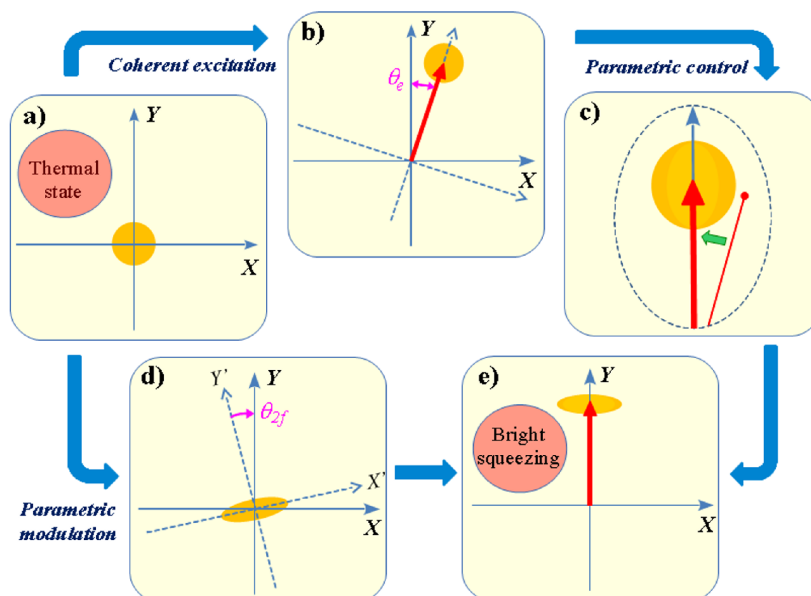


Figure 8.1: Sketch of the experimental techniques applied to the oscillator to obtain the bright squeezed state (e) from the thermal state (a).

When the coherent excitation, necessary for the parametric stabilization, is switched on, the center of the ellipse is just shifted to  $(0, \bar{Y}_0/(1+g))$ , where  $Y_0$ , defined as in Chap. 6, is the steady state value of the oscillator response to the coherent excitation (in the absence of the parametric modulation). The configuration in phase space is now equivalent to that of an optical field with *bright squeezing* [132, 133] (see Fig. 8.1(e)). Moreover, the phase  $\theta_{2f}$  acquires a more definite meaning: it is the phase difference, between the coherent excitation and the modulation at  $2\omega_{eff}$ , necessary to obtain the squeezing of the  $Y$  quadrature in the phase plane  $X-Y$  defined by the coherent excitation. However, we remark that the fluctuations along  $X$  still increase with  $g$  and the squeezing remains limited to  $3\text{ dB}$ . On the other hand, by activating the parametric feedback we can depress the parametric amplification and prevent the divergence of  $\langle X^2 \rangle$ . As a consequence, the parametric gain can now be increased above unity. As we have shown,  $S_X$  depends on the electronic servo loop, but its standard deviation can be maintained close to its thermal value. The crucial issue is that the  $Y$  quadrature is not affected by the feedback loop, as we showed in Chap. 6. The fluctuations on  $Y$  maintain a Gaussian distribution,  $S_Y$  keeps a Lorentzian shape and the  $Y$  variance  $\sigma_Y^2 = \langle (Y - Y_0)^2 \rangle$  can be reduced below the  $-3\text{ dB}$  barrier, continuing to follow Eq. 8.6.

## 8.2 Experimental setup and results

The experiment is performed with the same optomechanical cavity used in the experiments described in the previous chapters. For completeness, and to help the readability, we report here again the fundamental parameters: cavity length  $L_{cav} = 0.57 \text{ mm}$ , Finesse 57000, coupling parameter  $\zeta = 0.09$ , mechanical resonance frequency  $\omega_m/2\pi = 128961 \text{ Hz}$ , effective mass  $m = 1.35 \cdot 10^{-7} \text{ Kg}$  and a mechanical quality factor of  $Q = 16000$ . The measurements are performed at room temperature with a probe beam power in the carrier of  $\mathcal{P}_{PDH} \simeq 0.040 \text{ mW}$  and a pump power of  $\mathcal{P}_{pump} = 1.0 \text{ mW}$ .

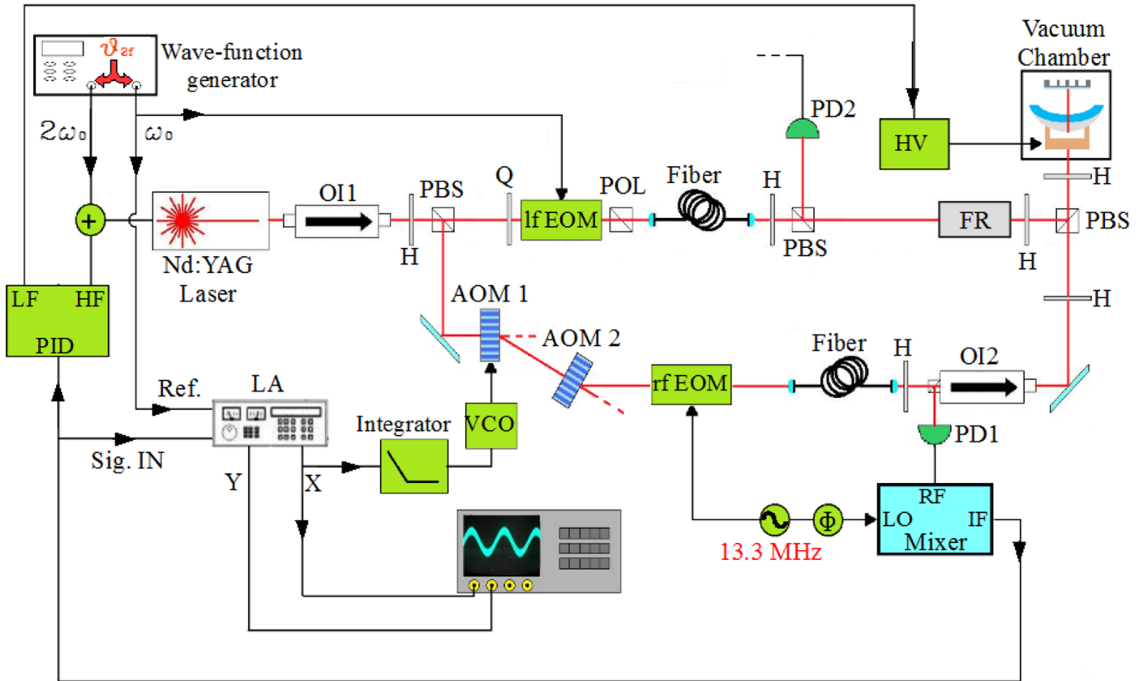


Figure 8.2: Scheme of the experimental apparatus. Optical isolator (OI); acousto-optic modulator (AOM); electro-optic modulator (EOM); half-wave plate (H); quarter-wave plate (Q); polarizing beam splitter (PBS); polarizer (POL); Faraday rotator (FR); photodiode (PD); lock-in amplifier (LA); voltage controlled oscillator (VCO); delay line for phase control ( $\Phi$ ); high voltage amplifier (HV). Black lines indicate the electronic part of the setup.

The experimental setup, shown in Fig. 8.2, is an extension of the two beam standard configuration to implement the parametric control and the  $2\omega_{eff}$  modulation of the optical spring. As before, the PDH signal is sent to the lock-in amplifier for

demodulation to obtain the two quadratures of the oscillator motion. The feedback loop is implemented as described in Chap. 6, that is, the  $X$  quadrature output signal is integrated and sent to the AOM driver to control the detuning of the pump beam. The main difference, here, is that we use an external reference for the lock-in, provided by a two channels wave-function generator. The signal of the first channel, in addition to being used for the reference at  $\omega_e$ , is also used to generate the coherent excitation. The maximum modulation depth used is 0.5% peak-to-peak, giving an intracavity modulated force with amplitude  $F_e^{max} \simeq 2 \cdot 10^{-10} N$ . The signal of the second channel, set at angular frequency  $2\omega_e$ , is sent to the fast actuator of the laser to generate a modulation of the detuning, that is, of the optical spring. The two channels are phase locked to each other so that an arbitrary phase difference  $\theta_{2f}$ , between the two signals can be set. The  $X$  and  $Y$  quadrature signals are simultaneously acquired by a digital scope with a resolution of 12 bit, sampling interval of  $21 \mu s$  and a total observation time of about 20 s ( $\sim 10^6$  data).

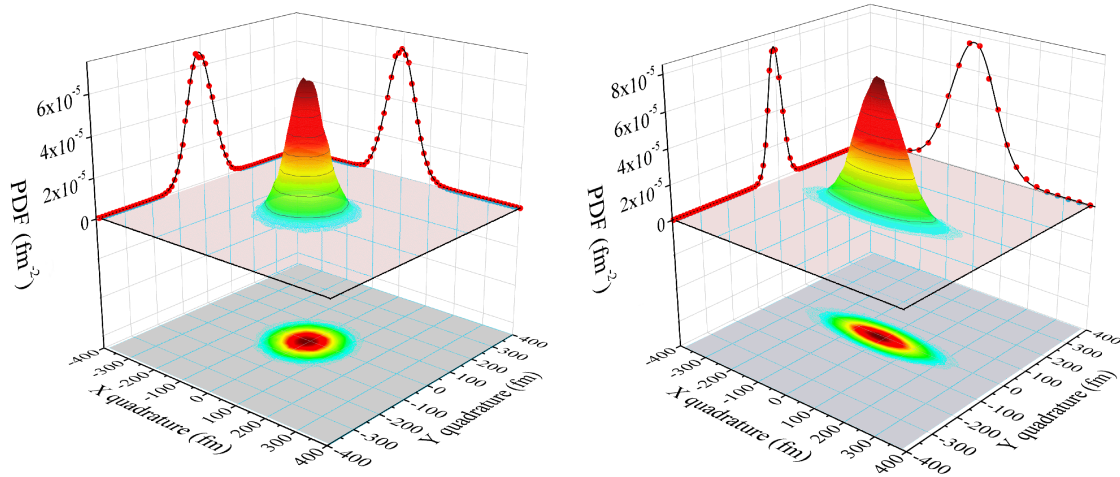


Figure 8.3: Phase space PDFs for the two configurations named, respectively (a) and (d) in Fig. 8.1. Left: thermal oscillator (a) at the effective temperature  $T_{eff} \simeq 15 K$  ( $\gamma_{eff}/2\pi = 110 Hz$ ). Right: parametrically squeezed oscillator (d), with parametric gain  $g = 0.83$ .

The stabilization loop and the  $2\omega_{eff}$  modulation are independent of each other and can be activated simultaneously or one at a time. Indeed, the first stage of the experiment has been the generation of a squeezed thermal state without the feedback loop. We acquired several time series with an increasing parametric gain  $g$ . For these measurements the initial (at  $g = 0$ ) effective mechanical parameters were  $\omega_{eff} = 127400 Hz$  and  $\gamma_{om}/2\pi = 160 Hz$ , corresponding to an effective temperature

of  $10 K$ . In Fig. 8.3, we show the phase space probability density functions (PDFs) for the maximum achieved parametric squeezing (right) and, for comparison, of the thermal oscillator (left). Also shown are the marginal distributions for the oscillator quadratures.

In the second stage of the experiment we activate also the parametric control. In this case the measurements have been performed in two different working points: the first is identical to the one used in the first stage, that is, at  $\omega_{eff}/2\pi = 127400 Hz$ , while, in the second point, the effective resonance is at  $\omega_{eff}/2\pi = 128000 Hz$  where  $\gamma_{eff}/2\pi = 110 Hz$ , corresponding to an effective temperature of  $T_{eff} \simeq 15 K$ . In both cases, the amplitude of the coherent excitation has been adapted during the measurement in order to keep a constant value of the coherent component in the oscillator motion, i.e., a constant  $\langle Y \rangle \simeq Y_0$ , compensating the parametric de-amplification. This value is  $\langle Y \rangle \simeq 300 fm$ , i.e., at least 6 times larger than the standard deviation of the thermal distributions. This assures, together with the stabilization of the  $X$  quadrature, that the condition  $\phi \simeq X/Y_0 \ll 1$  is satisfied. In Fig. 8.4, we show the phase space PDFs for the maximum achieved parametric squeezing with coherent excitation and frequency feedback (right) and, for comparison, of the thermal oscillator (left). Also shown are the marginal distributions for the oscillator quadratures.

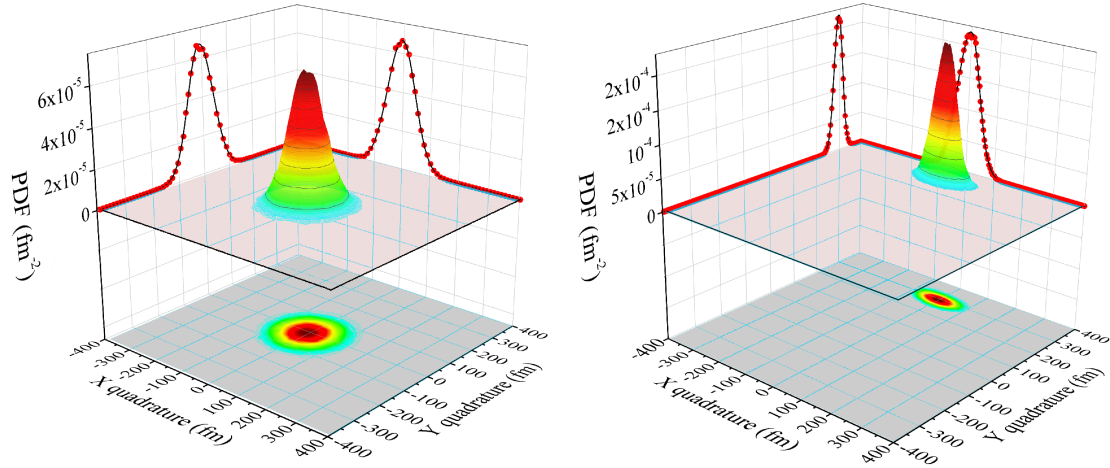


Figure 8.4: Phase space PDFs for the two configurations named, respectively (a) and (e) in Fig. 8.1. Left: thermal oscillator (a) at the effective temperature  $T_{eff} \simeq 15 K$  ( $\gamma_{eff}/2\pi = 110 Hz$ ). Right: parametrically squeezed oscillator with coherent excitation and frequency feedback (e), with parametric gain  $g = 5.4$ .

In Fig. 8.5, we plot the variances for the  $X$  and  $Y$  quadratures, normalized to their free-running value in the absence of parametric modulation, for all data collected in the two phases of the experiment. These are calculated from the integral of the spectra with a statistical uncertainty typically around 3%, calculated from several independent time series. For the second stage of the experiment we just give the feedback-independent  $Y$  variance. The solid lines are given by the expression  $1/(1-g)$  and  $1/(1+g)$  (see Eqs. 8.6) with  $g = V_{2f}/V_{th}$ , where  $V_{2f}$  is the amplitude of the modulation sent to the laser fast actuator, and the threshold  $V_{th}$  is obtained by fitting Eq. 8.6 to the variance of  $Y$ . The maximum noise reduction is  $-7.4 \pm 0.2 \text{ dB}$ , limited by the appearance of instabilities in the control loop, namely, the servo bumps discussed in Chap. 6. An optimization of the loop parameters, not yet performed, would likely allow a wider working range and a stronger squeezing.

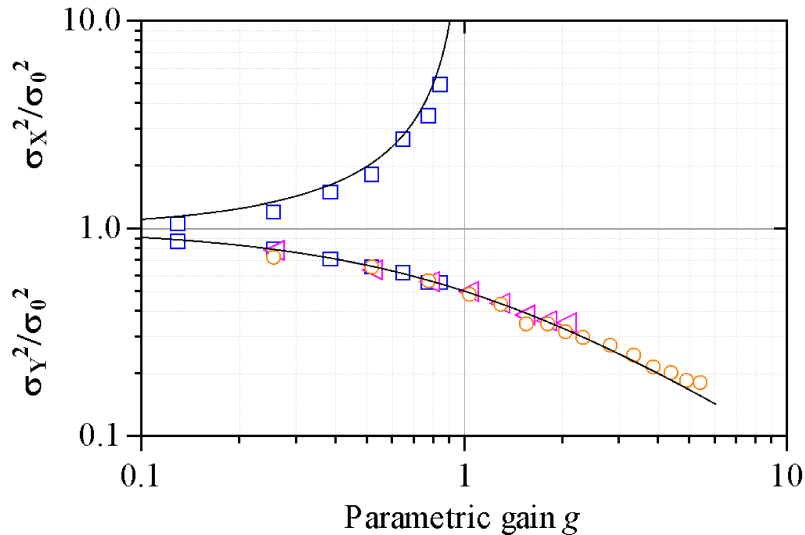


Figure 8.5: *Normalized measured variances of the  $X$  and  $Y$  quadratures, as a function of the parametric gain  $g$ . Squares: parametric modulation without coherent excitation and parametric feedback:  $\omega_{eff}/2\pi = 127400 \text{ Hz}$  ( $\gamma_{om}/2\pi = 160 \text{ Hz}$ ,  $T_{eff} = 10 \text{ K}$  at  $g = 0$ ). Circles: parametric modulation in the presence of coherent excitation and parametric feedback for  $\omega_{eff}/2\pi = 127400 \text{ Hz}$ ; triangles:  $\omega_{eff}/2\pi = 128000 \text{ Hz}$  ( $\gamma_{om}/2\pi = 110 \text{ Hz}$ ,  $T_{eff} = 15 \text{ K}$  at  $g = 0$ ). Solid lines represent the theoretical curves.*

In order to emphasize that the  $Y$  quadrature behaves, indeed, as for a squeezed free-running oscillator, even for the strongest  $2\omega_{eff}$  modulation amplitude used and even with the parametric feedback active, we show in Fig. 8.6(b) the PSD measured with  $g = 5.9$ ; also shown is the spectrum for the free thermal state and, for both

spectra, the Lorentzian fit to the data that allow to deduce the correlation times of each time series.

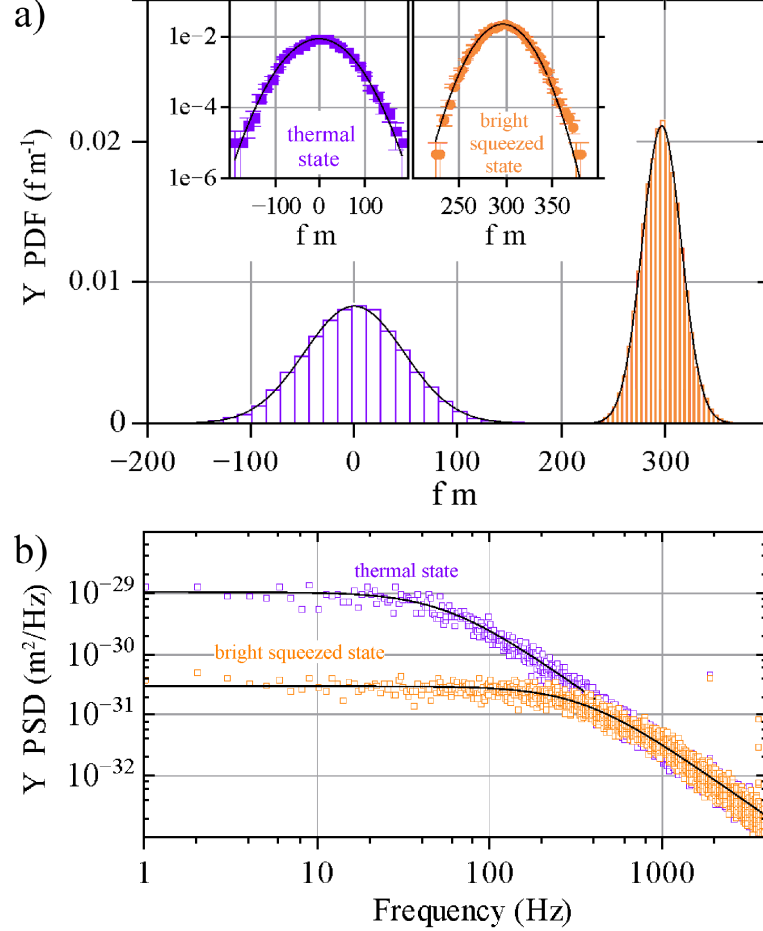


Figure 8.6: Upper panel: experimental PDFs of the  $Y$  quadrature. Violet histogram: thermal oscillator at  $T_{eff} = 15 K$ . Orange histogram: squeezed oscillator with  $g = 5.9$ . Solid lines show Gaussian fitting functions. In the inset the same histograms are shown in logarithmic scale, with statistical error bars. Lower panel: corresponding PSD with Lorentzian fitting functions.

In Fig. 8.6(a) are reported the histograms representing the experimental PDFs of the  $Y$  quadrature for both thermal and squeezed state. For the latter the mean value is shifted to  $\langle Y \rangle \simeq 300 fm$  by the coherent excitation. Also shown are the Gaussian fitting functions (solid lines). For calculating these histograms we have first applied to the time series an additional digital low-pass filter at  $\sim 1 kHz$  to reduce the effect of spurious peaks that appear above  $5 kHz$ . This cutoff is still well above the half-width of the opto-mechanical resonance, that even with the largest

parametric gain is around  $300 Hz$ . We have then reduced the number of samples by keeping one data point every correlation time, in order to obtain sets of uncorrelated samples that have been used to calculate the probability distributions (PDFs). In the inset of Fig. 8.6(a) the same histograms are shown in logarithmic scale with error bars that reflect the standard error on each bin. The reduced  $\chi^2$  of a Gaussian fit is around unity for both the PDFs of the thermal state and that of the Y quadrature in the squeezed state, indicating that, indeed, even in the latter case the fluctuations are stochastic with Gaussian-Lorentzian statistics [134].

# Chapter 9

## Conclusions and final remarks

We have presented in this thesis our research activity in the field of optomechanics performed, during my PhD program, over a two years period. As customary, we have started, in Chap. 1, with a theoretical description of the optomechanical interaction. The quantum mechanical model, that has been presented here, is nowadays well established, thus we have given a compact, but complete and general description, that does not rely on too many assumptions regarding the considered parameters regimes. We also have included in the model the principal (classical) technical noise sources in a fully consistent way.

We have shown in Chap. 2 and Chap. 4 the development and the characterization of our micro-oscillators. We have presented two novel designs, the "low deformation" *double wheel* and the *quad/double paddle oscillators*, that represent an improvement of more than one order of magnitude (two in the case of the QPO) in terms of mechanical losses with respect to our previous generation of devices, while keeping the same high optical performances. We have also identified possible ways to increment even further the achievable quality factors especially for what concerns the double wheel species. Preliminary experimental results, on the third generation of devices realized with these guidelines<sup>1</sup>, show that, indeed, quality factors in the range of  $10^6$  can be achieved even for the double wheel type.

One of the major goals in the field of optomechanics has been, for quite a long time, the generation and detection of ponderomotive squeezed light whose first theoretical analysis (Refs. [6, 7]) dates back to 1994. This result has been achieved, almost 20 years later, initially using a mechanical mode of an ultracold atomic gas inside an optical cavity and, later on, using a silicon micromechanical resonator and a thin semi-transparent membrane within a Fabry-Pérot cavity (Refs. [18, 19, 20]).

---

<sup>1</sup>See Ref. [31] for some insight on the third generation designs.

However, quadrature squeezing (in a cw beam) is particularly useful for improving sensitivity in the audio-band, while the mentioned experimental demonstrations are achieved around the mechanical resonance in the  $MHz$  range. At lower frequencies, obtaining ponderomotive squeezing is much more difficult due to the presence of typically stronger technical noise sources, in particular, frequency/displacement noise.

In Chap. 5 we have identified an optomechanical effect that leads to the cancellation of frequency noise around the bare mechanical resonance frequency. This cancellation is due to the destructive interference between the frequency noise directly affecting the cavity and the same frequency noise transduced by the mechanical resonator. We have demonstrated experimentally this effect and we have shown that it could strongly facilitate the generation and detection of ponderomotive squeezing in the audio-band.

However, we have also shown, in the second part of Chap. 5, that we have not been able to exploit the exceptional optomechanical properties of our best micro-oscillator, namely, the QPO. The cause is to ascribe to the cavity locking feedback loop that changes the radiation pressure phase in a frequency dependent way and that leads to the dynamical instability of low frequency normal modes that would otherwise be stable. This effect can be avoided for the double wheel designs but not for the QPO and DPO ones. The third generation of devices has been designed taking this aspect into account and we are confident that it will allow us to generate ponderomotive squeezing.

In the final chapters, we have presented two relevant experiments that rely on the stabilization technique described and characterized in Chap. 6. This technique consists in a feedback loop that directly acts on the *optical spring* to lock the effective mechanical resonance at the desired frequency. We have shown that the control loop affects only one quadrature of the oscillator motion, leaving the other one unperturbed.

In the first of these experiments (Chap. 7), we have exploited the stabilization of the effective mechanical susceptibility to implement the Wiener-Kolmogorov filtering, a data analysis technique that, in this context, allows a fast accumulation of statistics in the measurement of the stochastic forces acting on the micro-oscillator. This method requires the precise knowledge of the mechanical transfer function, so that the stabilization of the effective mechanical parameters is of fundamental importance for its application. We have shown that, by combining these techniques, we are able to resolve stochastic force variations below 1% of the thermal noise after 10 s of observation time, and about 0.4% after 60 s, with a sensitive bandwidth

---

of about  $3\text{ kHz}$ . This experiment has been carried out at room temperature, we remark that a comparable peak-signal to noise ratio can be achieved at cryogenic temperatures by choosing a working point with a smaller detuning with respect to the one used to obtain the reported figures. The same techniques can be applied in a large variety of micro- and nano-mechanical systems, including those based on electric measurements and microwave radiation. Detecting a weak stochastic signal on a stronger background is an important task in the research field of quantum mechanics with macroscopic oscillators, in particular when exploring the properties of oscillators with low occupation number, or, e.g., in a squeezed state or other peculiarly quantum states.

In the second experiment (Chap. 8), we have performed the parametric excitation of the mechanical oscillator at twice its resonance frequency by directly modulating the optical spring. When applied to a thermal noise driven oscillator, the excitation generates a reduction in the variance of one quadrature of the oscillator motion and an increase in the other one, resulting in a squeezed thermal state. However, the maximum noise reduction in the squeezed quadrature is normally limited to a  $-3\text{ dB}$  factor due to the rise of a dynamical instability in the anti-squeezed one. Also in this case the stabilization technique of Chap. 6 has been instrumental. Indeed, by carefully selecting the phase of the parametric excitation, we can squeeze the quadrature unaffected by the control loop and anti-squeeze the other. Then, the parametric feedback avoids the rise of the instability allowing to break the  $3\text{ dB}$  barrier. We have observed a maximum noise reduction of  $-7.4\text{ dB}$ .

The model for the stabilization loop, presented here, is based on a classical description. Furthermore, the conclusion that one quadrature of the oscillator motion is not affected by the control loop, it is true only to first order. A complete quantum mechanical description, that we are currently developing, must include quadratic terms. Indeed, the backaction introduced by the feedback loop will ultimately sets a limit to the maximum achievable noise reduction. Nevertheless, we remark that the technique is based on a weak measurement with sensitivity well below the standard quantum limit, so that the effects of the measurement backaction should become relevant only for high parametric gain. Thus, we are convinced that the achievable squeezing will be enough to allow to start from a moderately cooled oscillator, with an occupation number significantly above unity, a condition that can even be reached in the bad cavity configuration exploited throughout this thesis. As a consequence, the scheme described in Chap. 8 can be efficiently exploited to produce a macroscopic mechanical oscillator in a bright squeezed state, opening the way to further studies of quantum phenomena in macroscopic systems.



# Appendix A

## The normal mode expansion

The equation of motion of an elastic body of density  $\rho$ , forced by a force density  $\mathbf{F}(\mathbf{r}, t)$ , can be summarized as [32]

$$\rho \frac{\partial^2 \mathbf{u}(\mathbf{r}, t)}{\partial t^2} - L[\mathbf{u}(\mathbf{r}, t)] = \mathbf{F}(\mathbf{r}, t) \quad (\text{A.1})$$

with the appropriate initial and boundary conditions. Here,  $\mathbf{u}(\mathbf{r}, t)$  is the displacement field of the elastic body and  $L[\mathbf{u}(\mathbf{r}, t)]$  is defined as

$$L[\mathbf{u}] = (\lambda + \mu) \nabla(\nabla \cdot \mathbf{u}) + \mu \nabla^2 \mathbf{u}. \quad (\text{A.2})$$

The Lamè coefficients  $\lambda$  and  $\mu$  depend on the Poisson ratio  $\sigma_p$  and on the Young modulus  $Y$  of the material

$$\lambda = \frac{Y \sigma_p}{(1 + \sigma_p)(1 - 2\sigma_p)}, \quad \mu = \frac{Y}{2(1 + \sigma_p)}. \quad (\text{A.3})$$

The displacement normal modes  $\mathbf{w}_n(\mathbf{r})$  are defined as the solutions of the eigenvalue equation

$$-\rho \omega_n^2 \mathbf{w}_n = L[\mathbf{w}_n] \quad (\text{A.4})$$

with the boundary conditions defined by the requirement that components of the stress normal to the body surfaces vanish on the body surfaces. The normal modes constitute a complete ortho-normal basis and the solution of Eq. A.1 can be written as

$$\mathbf{u}(\mathbf{r}, t) = \sum_{n=1}^{\infty} \mathbf{w}_n(\mathbf{r}) q_n(t). \quad (\text{A.5})$$

The determination of the coefficients  $q_n(t)$  is simple if the excitation can be factorized as  $\mathbf{F}(\mathbf{r}, t) = G_t(t) \mathbf{G}_r(\mathbf{r})$ . Indeed, using the eigenvalue equation and taking the projection on the mode  $\mathbf{w}_m$ , Eq. A.1 can be rewritten as

$$M \frac{\partial^2 q_m(t)}{\partial t^2} + M \omega_m^2 q_m(t) = G_t(t) \int_V dV \mathbf{G}_r(\mathbf{r}) \cdot \mathbf{w}_m(\mathbf{r}) \quad (\text{A.6})$$

where it is easy to see that the  $m$ -th mode has the same dynamic of a driven harmonic oscillator.

When measuring the position of the mass, or of a smaller surface of it, the observable physical quantity  $X(t)$  may be defined as

$$X(t) = \int_S ds \mathbf{P}(\mathbf{r}) \cdot \mathbf{u}(\mathbf{r}, t) = \sum_n q_n(t) \int_S ds \mathbf{P}(\mathbf{r}) \cdot \mathbf{w}_n(\mathbf{r}) . \quad (\text{A.7})$$

Here,  $\mathbf{P}(\mathbf{r})$  is a weighting function and the integral is performed on the chosen surface  $S$ . The spatial form of  $\mathbf{P}(\mathbf{r})$  reflects the measurement strategy, and in our case, is proportional to the Gaussian beam spot power profile. Notice that for an optical driving force the weighting function is identical. Indeed, in this case the force density in Eq. A.1 reduces to a surface force that can be written as  $\mathbf{F}(\mathbf{r}, t) = \frac{2\mathcal{P}(t)}{c} \mathbf{P}(\mathbf{r})$  (for a reflected beam). Moving to the frequency domain and introducing a damping term, the observable  $X$  can be expressed as

$$X(\omega) = \frac{2\mathcal{P}(\omega)}{cM} \sum_n \frac{[\int_S ds \mathbf{P}(\mathbf{r}) \cdot \mathbf{w}_n(\mathbf{r})]^2}{(\omega_n^2 - \omega^2) + i\omega_n\gamma_n} . \quad (\text{A.8})$$

From this equation it is clear the the effective mass  $m$  of each normal modes depends on the scalar product between the specific normal mode displacement field and  $\mathbf{P}(\mathbf{r})$ . The actual number of normal modes that one needs to consider depends on many factors, such as the frequency separation of the modes with respect to the bandwidth of interest or the sensing surface size compared to the wavelength of the modes. In many cases, only a limited number of modes is necessary since, for a given sensing surface, high order modes tend to give a vanishing average displacement and the contribution of modes other than the ones of interest, that are sufficiently separated in frequency, can be limited to their tails and regarded as a displacement noise floor.

# Appendix B

## Additional information on the experimental setup

### B.1 Laser system

The light source is a Mephisto cw tunable Nd:YAG operating at  $\lambda = 1064\text{ nm}$  manufactured by InnoLight GmbH<sup>1</sup> with a maximum output power of  $500\text{ mW}$ . The frequency can be tuned by a temperature controller (*slow*) and a piezo-electric controller (*fast*), both driven by a voltage signal. The slow controller gain is  $G_s = -3\text{ GHz/V}$ , with a response bandwidth of  $\cong 1\text{ Hz}$ , a continuous tuning range of about  $8\text{ GHz}$  (limited by mode hopping) and a total one of about  $30\text{ GHz}$ . The fast controller has a gain of  $G_{fast} = 1.14\text{ MHz/V}$ , with a response bandwidth of  $\sim 100\text{ kHz}$  above which the gain start to decrease and is affected by resonances in the electro-mechanical response of the piezo actuator. The laser electronics has a built-in *noise eater* feedback loop circuit to reduce amplitude noise. In Fig. B.1 we show the measured relative amplitude noise spectra  $S_{laser}/S_{shot}$  for different power levels and with the noise eater switched on and off, from which is clear that additional noise reduction is necessary to approach the shot noise level.

The laser spectral linewidth is of the order of  $1\text{ kHz}$ .

### B.2 The cryostat

The cryostat in our experimental setup is a continuous flow cryostat manufactured by Janis, model ST-100, slightly customized to increase the maximum allowed sample size by modifying the thermal shield diameter. which is  $60\text{ mm}$ . The distance between

---

<sup>1</sup>Nowadays owned by the Coherent group.

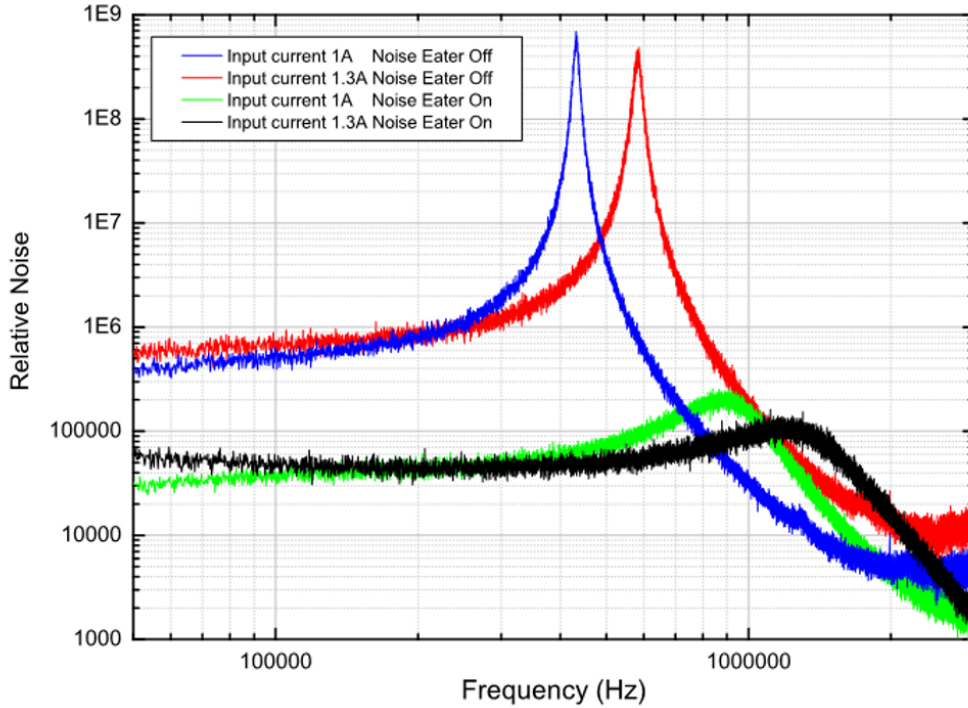


Figure B.1: *Relative noise spectra  $S_{laser}/S_{shot}$  for different power levels (namely, 280 mW for an input current of 1 A and 460 mW for 1.3 A) and with the noise eater switched on and off. The spectra are measured with a power  $\mathcal{P}_{meas}$  of a few mW in a balanced detection, then corrected with the Mandel factor [46] to obtain the relative noise at the laser output.*

the cold finger and the shield bottom is 70 mm for an overall useful volume of 0.2 l. The nominal cooling power is 3 W.

The thermal shield has two 25 mm diameter access holes that allow to explore several oscillators on the same wafer, when working with the Michelson interferometer. Such holes limit the achievable minimum temperature to about 10 K, while limiting the apertures to few mm<sup>2</sup>, when working with the cavity, allows to descend below 4.5 K.

# Appendix C

## The Pound-Drever-Hall technique

The Pound-Drever-Hall technique [58, 59] is nowadays a standard method to lock a laser frequency to the resonance of a Fabry-Pérot cavity, or viceversa. It allows to extract a signal that is proportional to the frequency difference between the light beam and the cavity. However, as we will see shortly, this difference must be small compared to the cavity linewidth. The error signal obtained with the PDH technique can be fed to a servo actuator in a closed feedback loop. If the servo modifies the beam frequency, then the laser frequency will be locked to the cavity resonance, on the contrary, if it modifies the cavity length the cavity resonance will be locked to the laser frequency.

Without loss of generality, we can describe the beam as a plane wave  $E(t) = E_0 e^{i\omega_l t}$  that before entering the cavity is phase modulated (EOM1 of Fig. 3.1) at frequency  $\Omega_s$ , much smaller than the FSR. In the frame rotating at angular frequency  $\omega_l$  the input field can be expressed as

$$\begin{aligned} E_{in} &= E_0 \exp(i\beta \sin(\Omega_s t)) \\ &\simeq E_0 \sum_{n=-\infty}^{\infty} J_n(\beta) e^{i n \Omega_s t} \end{aligned} \tag{C.1}$$

where  $\beta$  is the modulation depth and we used the Jacobi-Anger expansion<sup>1</sup>. The electric field is then composed of a carrier at angular frequencies  $\omega_l$ , and sidebands at angular frequencies  $\omega_l \pm n \Omega_s$ . Before entering the cavity, the field passes through an optical circulator (in our setup we use the OI2) so that we can measure the reflected field intensity with a photodiode (PD3).

If we indicate with  $H^r(\omega)$  the cavity response function for the reflected field,

---

<sup>1</sup>The Jacobi-Anger expansion is defined as  $e^{i z \sin \theta} = \sum_{n=-\infty}^{\infty} J_n(z) e^{i n \theta}$  where  $J_n(z)$  is the  $n$ -th Bessel function.

given by Eq. 1.36, the field incident on the photodiode is

$$E_r(t) \simeq E_0 \sum_{n=-\infty}^{\infty} H_n J_n(\beta) e^{in\Omega_s t} \quad (\text{C.2})$$

where we have defined

$$H_n = H^r(\Delta + n\Omega_s) \quad (\text{C.3})$$

and where  $\Delta = \omega_l - \omega_{cav}$  is, as usual, the laser detuning from the cavity resonance. The intensity impinging on the photodiode is given by the square modulus of the field, thus

$$I_r \propto |E_r|^2 \propto \sum_{n,m=-\infty}^{\infty} J_n J_m H_n H_m^* e^{i(n-m)\Omega_s t}. \quad (\text{C.4})$$

At this point a phase sensitive detection technique is applied. The photodiode voltage output is mixed with the signal that was used to generate the original phase modulation and then low pass filtered. This means that we are interested only in the terms, in Eq. C.4, for which  $n - m = \pm 1$ . The signal at the low pass filter output depends on the phase difference between the photodiode response and the reference. If we write it as

$$V \propto \sum_{n=-\infty}^{\infty} J_n H_n (J_{n-1} H_{n-1}^* e^{i\Omega_s t} + J_{n+1} H_{n+1}^* e^{-i\Omega_s t}) \quad (\text{C.5})$$

and we define

$$A = \sum_{n=-\infty}^{\infty} J_n J_{n-1} H_n H_{n-1}^*, \quad (\text{C.6})$$

the voltage output becomes<sup>2</sup>

$$V \propto A e^{i\Omega_s t} + A^* e^{-i\Omega_s t} = 2\text{Re}A \cos \Omega_s t + 2\text{Im}A \sin \Omega_s t \quad (\text{C.7})$$

where it is possible to see that detecting the component in phase with  $V$  ( $\propto \sin \Omega_s t$ ) one obtains  $2\text{Re}A$ , detecting the component in quadrature one obtains  $2\text{Im}A$ , and, for a generic phase, a linear combination of the two.

We can work a little more on  $A$ . Using the following generic relation

$$\begin{aligned} \sum_{n=-\infty}^{\infty} a_n &= \sum_{n=0}^{\infty} a_n + \sum_{n=-\infty}^{-1} a_n = \sum_{n=0}^{\infty} a_n + \sum_{n=1}^{\infty} a_{-n} = \sum_{n=0}^{\infty} a_n + \sum_{n=0}^{\infty} a_{-(n+1)} \\ &= \sum_{n=0}^{\infty} (a_n + a_{-(n+1)}) \end{aligned} \quad (\text{C.8})$$

---

<sup>2</sup>Note that  $A^* = \sum_{n=-\infty}^{\infty} J_n J_{n-1} H_n^* H_{n-1} = \sum_{n'=-\infty}^{\infty} J_{n'+1} J_{n'} H_{n'+1}^* H_{n'}$ , and by comparison with Eq. C.5 one gets Eq. C.7

and the property  $J_{-n} = (-1)^n J_n$ , we can rewrite Eq. C.6 as

$$A = \sum_{n=-\infty}^{\infty} J_n J_{n-1} H_n H_{n-1}^* = \sum_{n=0}^{\infty} J_n J_{n+1} (H_n^* H_{n+1} - H_{-(n+1)}^* H_{-n}). \quad (\text{C.9})$$

In this last equation, we can see that the terms of the summation becomes smaller and smaller as  $n$  increases. For a small modulation depth, or for a narrow linewidth ( $\kappa \ll \Omega_s$ ) it is possible to keep only the first term. Furthermore, in this limit, we have that  $H(\Omega_s) \simeq 1$ , so that Eq. C.9 reduces to

$$A \simeq J_0 J_1 (-2i \text{Im}[H(\Delta)] + H(\Delta - \Omega_s) - H^*(\Delta + \Omega_s)) \quad (\text{C.10})$$

and is now clear that if one detects the component in phase with  $V$ , the signal vanishes at resonance ( $\Delta = 0$ ), while for the component in quadrature one obtains the imaginary part of  $H$  that has a dispersive shape. Indeed, near resonance, the error signal  $D$  is proportional to the frequency difference  $\Delta$  according to

$$D \simeq -C_\eta |E_0|^2 J_0(\beta) J_1(\beta) (1 - \zeta) \frac{\Delta}{\kappa} \quad (\text{C.11})$$

where  $C_\eta$  is a coefficient that accounts for the efficiency of the photodiode, its sensitivity, the mixer gain and other possible electronic gains. Note that the slope of  $D$  is proportional to the Finesse, so that a higher one implies an higher sensitivity even though at the expenses of the dynamic range.

Experimentally, the detection phase is selected by means of a delay line on the path of the reference signal, and the resulting delay time can be adjusted until one obtains the needed value  $T = \frac{2\pi}{4\Omega_s}$ .

By scanning the laser frequency and acquiring the demodulated signal  $D(\Delta)$ , one get the picture in Fig. C.1, where we show an experimental measurement (black dots) along with a fit to the data (red line) for a  $0.57 \text{ mm}$  long cavity with Finesse  $\mathcal{F} = 57000$  and a half linewidth of  $\kappa/2\pi = 2.3 \text{ MHz}$ , and where the modulation frequency is  $\Omega_s/2\pi = 13.3 \text{ MHz}$ . One should keep in mind that, in order to have also the contributions from the  $\pm 2\Omega_s$  sidebands in the expression for  $D(\Delta)$  higher order terms in the expansion of Eq. C.9 must be included in the calculations. While the first order approximation is good as long as  $\kappa \ll \Omega_s$ , higher order terms become increasingly more relevant as  $\kappa$  approaches  $\Omega_s$ . Note that a very good and useful approximation for the near resonance behavior of  $D$  is (blue line in Fig. C.1)

$$D \simeq -\frac{V_{pp}^{PDH}}{\kappa} \Delta \quad (\text{C.12})$$

where  $V_{pp}^{PDH}$  is the maximum peak-to-peak voltage measured while scanning the laser frequency.

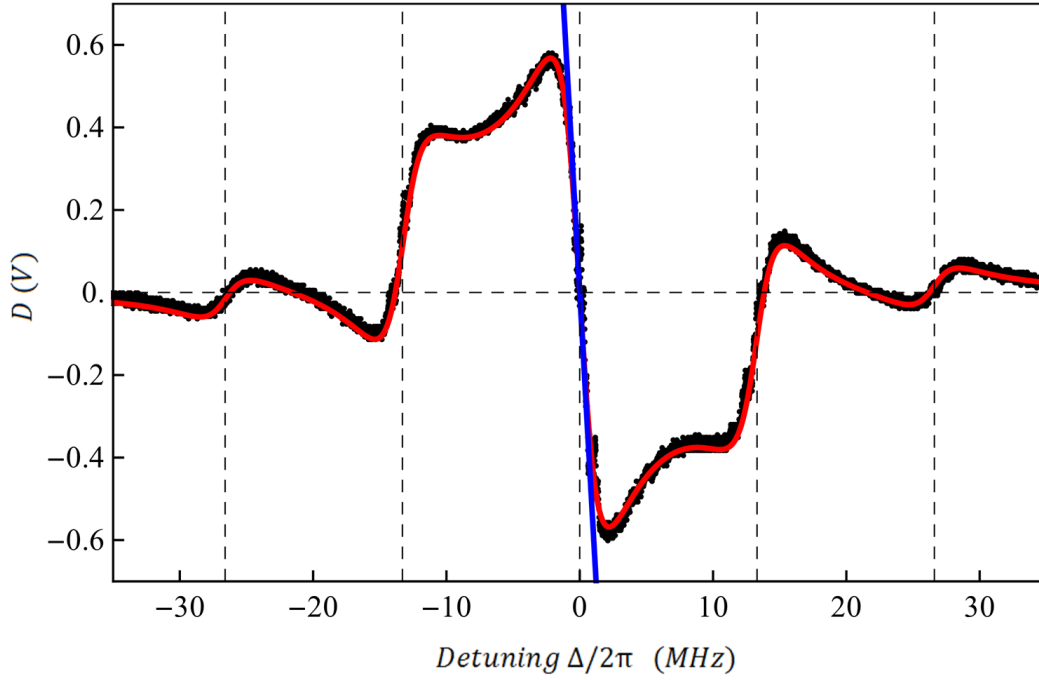


Figure C.1: *Pound-Drever-Hall signal. Experimental data (black dots), best fit of data (red) and near resonance approximation (blue). Vertical dashed lines are sidebands central frequencies at multiples of  $\Omega_s/2\pi = 13.3$  MHz.*

The PDH spectra are calibrated by means of a sinusoidal modulation at  $f_{cal} \sim 20$  kHz sent to the laser fast actuator. The ratio between the laser frequency and the cavity length allows to convert the detuning into cavity displacement. The calibration spectral line is affected by the servo loop, therefore, it is necessary to always acquire simultaneously the PDH and the error signal. If  $S_{PDH}(f)$  is the PSD of the PDH signal and  $S_{err}(f)$  is the PSD of the error signal, both expressed in  $V^2/Hz$ , the PDH spectrum  $S_{xx}^{PDH}(f)$  expressed in  $m^2/Hz$  is given by

$$S_{xx}^{PDH}(f) = \frac{n_c}{n_p} \left[ G_{fast} \frac{2\pi L_{cav}}{\omega_l} \right]^2 S_{PDH}(f) \quad (C.13)$$

where  $n_c = S_{err}(f_{cal})$ ,  $n_p = S_{PDH}(f_{cal})$  and  $G_{fast}$  is the transduction efficiency of the fast actuator of the laser assembly (see Sec. B.1). The overall calibration has an accuracy of  $\sim 20\%$ .



care has to be taken for the crossover between the two actuators.

We take into consideration four noise sources, all of them measured at the output of their respective generating element and assumed to be additive and uncorrelated to each other. The noise sources are: laser frequency noise with (monolateral) PSD  $S_{ff} = \frac{2\pi 10^4}{\omega} Hz^2/Hz$ , PDH detection noise with a PSD of  $S_{V,PDH} = 3 \cdot 10^{-13} V^2/Hz$ , output voltage noise of the PID electronics with a PSD of  $S_{V,servo} = 7 \cdot 10^{-13} V^2/Hz$ , and HV amplifier output voltage noise with a PSD of  $S_{V,HV} = 2 \cdot 10^{-8} V^2/Hz$ , that is by far the strongest noise source.

The PDH gain, as described earlier, is  $G_{PDH} = D = -V_{pp}^{PDH}/\kappa_\nu$ ,  $G_{amp}^{HV} = 36$ , the piezo electric transduction coefficient is  $G_{PZT} = 3.8 \cdot 10^{-9} m/V$ , while the cavity gain is  $G_{cav} = g_0/2\pi = \omega_l/2\pi L_{cav}$ . The low pass filters and PID transfer functions are<sup>3</sup>

$$H_{LPF}(f) = \left[ \frac{1}{1 + i\frac{f}{1.6}} \right]^2 \frac{1 + i\frac{f}{500}}{1 + i\frac{f}{10000}} \quad (C.14)$$

$$G_{lock}(f) = 0.8 \frac{1 + i\frac{f}{32900}}{i\frac{f}{32900}} \frac{1 + i\frac{f}{143000}}{1 + i\frac{f}{27400}} \frac{1}{1 + i\frac{f}{300000}}$$

for the sake of simplicity we also define the overall actuators transfer function as

$$G_{att}(f) = G_{fast} + G_{amp}^{HV} H_{LPF}(f) G_{PZT} G_{cav} \quad (C.15)$$

The total closed loop frequency noise is then

$$S_{ff,cl}(f) = \frac{S_{ff} + S_{V,PDH} |G_{att} G_{lock}|^2 + S_{V,servo} |G_{att}|^2 + S_{V,HV} |H_{LPF} G_{PZT} G_{cav}|^2}{|1 + G_{att}(f) G_{lock}(f) G_{PDH}|^2} \quad (C.16)$$

however, we are more interested in the equivalent total displacement PSD that is  $S_{xx,cl}(f) = S_{ff,cl}(f)/|G_{cav}|^2$ .

In Fig. C.3 we show the noise budget calculated with Eq. C.16. Relevant cavity parameters for the case under study are:  $\mathcal{F} = 57000$ ,  $L_{cav} = 0.57 \text{ mm}$  and an almost optimally coupled cavity with  $\zeta = -0.09$ . The peak-to-peak voltage of the PDH signal used in the calculation is  $V_{pp}^{PDH} = 1 \text{ V}$ , giving a lock bandwidth of about  $12 \text{ kHz}$ . The total equivalent displacement noise is well below the typical actual displacement noise measured in our opto-mechanical cavities (dashed gray line).

---

<sup>3</sup>As in Chap. 6 we use the same conventions for the Fourier transform used in electronics.

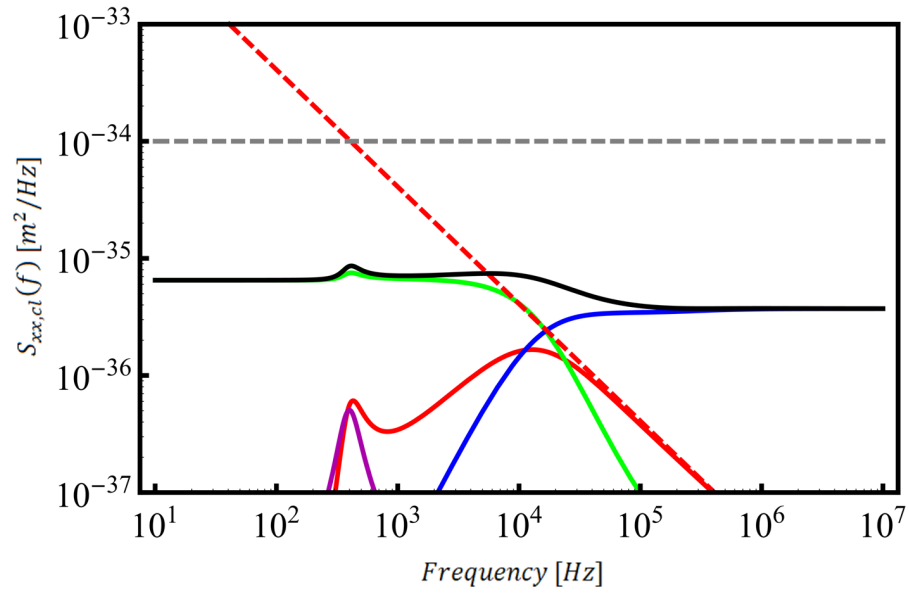


Figure C.3: *Equivalent cavity displacement noise. Total (black) and individual contribution:  $S_{ff}$  (red),  $S_{V,servo}$  (blue),  $S_{V,PDH}$  (green) and  $S_{V,HV}$  (violet). Dashed red line is the open-loop frequency noise while dashed gray line is typical displacement noise.*



# Appendix D

## General formulas for the homodyne noise spectra

Using Eq. 1.73 and the definition for the  $X_{out}$  and  $Y_{out}$  quadratures of the reflected field given in Chap. 5 we can decompose the total noise in each quadrature into the contribution from the various input noise sources. This approach does not really add new information with respect to the treatment given in Chap. 1 but it has two advantages: first, it allows to write a direct expression for the cross-spectral densities coming from the optomechanical interaction; second, the treatment of the phase noise in the homodyne detection is made rather easy. The decomposition is obtained as follows.

Here, we identify four input noise sources, quantum, which includes input and vacuum fluctuations, frequency, amplitude and thermal. For the  $X_{out}$  quadrature the symmetrized spectral density is<sup>1</sup>

$$S_X(\omega) = S_X^q(\omega) + S_X^{freq}(\omega) + S_X^{ampl}(\omega) + S_X^{th}(\omega) \quad (\text{D.1})$$

we also define the following additional function

$$\lambda_{ij}^{\pm} = A_i(\omega) \pm A_j^*(-\omega) \quad (\text{D.2})$$

---

<sup>1</sup>To simplify notation we drop from here on in this section the subscript *out*.

using which we have

$$\begin{aligned}
 S_X^q(\omega) &= \frac{1}{2} [|\lambda_{12}^+(\omega)|^2 + |\lambda_{12}^+(-\omega)|^2] + \kappa_i [|\lambda_{34}^+(\omega)|^2 + |\lambda_{34}^+(-\omega)|^2] \\
 S_X^{freq}(\omega) &= \{|\lambda_{34}^+(\omega) + \lambda_{34}^{+,*}(-\omega)|^2 - 2 \operatorname{Re}[(1 + e^{2i\theta_\Delta})\lambda_{34}^+(\omega)\lambda_{34}^+(-\omega)]\} |\alpha_s|^2 S_{\dot{\phi}\dot{\phi}}(\omega) \\
 S_X^{ampl}(\omega) &= |\lambda_{12}^+(\omega) + \lambda_{12}^{+,*}(-\omega)|^2 S_{\alpha_I \alpha_I}(\omega) \\
 S_X^{th}(\omega) &= |A_T(\omega) + A_T^*(-\omega)|^2 \frac{\gamma_m}{\omega_m} \omega \coth\left(\frac{\hbar\omega}{2k_B T}\right).
 \end{aligned} \tag{D.3}$$

in the same way,

$$S_Y(\omega) = S_Y^q(\omega) + S_Y^{freq}(\omega) + S_Y^{ampl}(\omega) + S_Y^{th}(\omega) \tag{D.4}$$

where

$$\begin{aligned}
 S_Y^q(\omega) &= \frac{1}{2} [|\lambda_{12}^-(\omega)|^2 + |\lambda_{12}^-(-\omega)|^2] + \kappa_i [|\lambda_{34}^-(\omega)|^2 + |\lambda_{34}^-(-\omega)|^2] \\
 S_Y^{freq}(\omega) &= \{|\lambda_{34}^-(\omega) + \lambda_{34}^{-,*}(-\omega)|^2 - 2 \operatorname{Re}[(1 + e^{2i\theta_\Delta})\lambda_{34}^-(\omega)\lambda_{34}^-(-\omega)]\} |\alpha_s|^2 S_{\dot{\phi}\dot{\phi}}(\omega) \\
 S_Y^{ampl}(\omega) &= |\lambda_{12}^-(\omega) + \lambda_{12}^{-,*}(-\omega)|^2 S_{\alpha_I \alpha_I}(\omega) \\
 S_Y^{th}(\omega) &= |A_T(\omega) + A_T^*(-\omega)|^2 \frac{\gamma_m}{\omega_m} \omega \coth\left(\frac{\hbar\omega}{2k_B T}\right).
 \end{aligned} \tag{D.5}$$

To write the cross-spectra it is convenient to define three additional functions, that is

$$\begin{aligned}
 \xi_{ij}(\omega) &= A_i(\omega)A_j(-\omega) + A_i(-\omega)A_j(\omega) \\
 \eta_{ij}(\omega) &= A_i(\omega)A_i(-\omega) - A_j^*(\omega)A_j^*(-\omega) \\
 \mu_{34}(\omega) &= [A_3(\omega) + A_4(\omega)][A_3(-\omega) + A_4(-\omega)].
 \end{aligned} \tag{D.6}$$

Finally, the total cross spectral density is

$$S_{X,Y}(\omega) = S_{X,Y}^q(\omega) + S_{X,Y}^{freq}(\omega) + S_{X,Y}^{ampl}(\omega) + S_{X,Y}^{th}(\omega) \tag{D.7}$$

where

$$\begin{aligned}
 S_{X,Y}^q(\omega) &= \operatorname{Im}[\xi_{34}(\omega)] + 2\kappa_i \operatorname{Im}[\xi_{34}(\omega)] \\
 S_{X,Y}^{freq}(\omega) &= 2|\alpha_s|^2 \operatorname{Im}[\mu_{34}(\omega) - (1 + e^{2i\theta_\Delta})\eta_{34}(\omega)] S_{\dot{\phi}\dot{\phi}} \\
 S_{X,Y}^{ampl}(\omega) &= 2\operatorname{Im}[\mu_{12}(\omega)] S_{\alpha_I \alpha_I} \\
 S_{X,Y}^{th}(\omega) &= 2\operatorname{Im}[A_T(\omega)A_T(-\omega)] \frac{\gamma_m}{\omega_m} \omega \coth\left(\frac{\hbar\omega}{2k_B T}\right).
 \end{aligned} \tag{D.8}$$

In all previous equations  $\theta_\Delta = -\arctan(\Delta/\kappa)$  is the argument of  $\alpha_s$ .

# Bibliography

- [1] V. Braginsky and A.B. Manukin, *Sov. Phys. JETP* Vol. **25**, 653 (1967)
- [2] V. Braginsky *et al.*, *Sov. Phys. JETP* Vol. **31**, 829 (1970)
- [3] V. Braginsky and A.B. Manukin, *Measurement of weak forces in Physics experiments*, University of Chicago Press (1977)
- [4] V. Braginsky and F.Y.A. Khalili, *Quantum Measurements*, Cambridge University Press (1995)
- [5] C.M. Caves, *Phys. Rev. Lett.* Vol. **45**, 75 (1980)
- [6] C. Fabre *et al.*, *Phys. Rev. A* Vol. **49**, 1337 (1994)
- [7] S. Mancini and P. Tombesi, *Phys. Rev. A* Vol. **49**, 4055 (1994)
- [8] M. Pinard *et al.*, *Phys. Rev. A* Vol. **51**, 2443 (1995)
- [9] S. Bose *et al.*, *Phys. Rev. A* Vol. **56**, 4175 (1997)
- [10] S. Mancini *et al.*, *Phys. Rev. A* Vol. **55**, 3042 (1997)
- [11] J.D. Thompson *et al.*, *Nature (London)* Vol. **452**, 72 (2008)
- [12] X. Jiang *et al.*, *Opt. Express* Vol. **17**, 20911 (2009)
- [13] G.S. Wiederhecker *et al.*, *Nature (London)* Vol. **462**, 633 (2009)
- [14] M. Eichenfield *et al.*, *Nature (London)* Vol. **459**, 550 (2009)
- [15] A.G. Kuhn *et al.*, *Appl. Phys. Lett.* Vol. **99**, 121103 (2011)
- [16] M. Siciliani de Cumis *et al.*, *J. Appl. Phys.* Vol. **106**, 013108 (2009)
- [17] T.P. Purdy *et al.*, *Science* Vol. **339**, 801 (2013)

- [18] D.W.C. Brooks *et al.*, *Nature* Vol. **488**, 476 (2012)
- [19] A.H. Safavi-Naeini, *et al.* *Nature (London)* Vol. **500**, 185 (2013)
- [20] T.P. Purdy *et al.*, *Phys. Rev. X* Vol. **3**, 031012 (2013)
- [21] J. Chan *et al.*, *Nature* Vol. **478**, 89 (2011)
- [22] T.A. Palomaki *et al.*, *Science* Vol. **342**, 710 (2013)
- [23] I. Pikovski *et al.*, *Nature Physics* Vol. **8**, 393 (2012)
- [24] E. Serra *et al.*, *J. Appl. Phys.* Vol. **111**, 113109 (2012)
- [25] E. Serra *et al.*, *Appl. Phys. Lett.* Vol. **101**, 071101 (2012)
- [26] E. Serra *et al.*, *Phys. Rev. A* Vol. **86**, 051801(R) (2012)
- [27] E. Serra *et al.*, *J. Micro-mech. Microeng.* Vol. **23**, 085010 (2013)
- [28] A. Pontin *et al.*, *arXiv:1308.5176* (2013) (accepted for publication on *Phys. Rev. A*)
- [29] A. Pontin *et al.*, *arXiv:1312.4867* (2013) (accepted for publication on *Phys. Rev. A*)
- [30] A. Pontin *et al.*, *Phys. Rev. Lett.*, Vol. **112**, 023601 (2014)
- [31] A. Borrielli *et al.*, *Microsyst. Technol.*, DOI [10.1007/s00542-014-2078-y](https://doi.org/10.1007/s00542-014-2078-y) (2014)
- [32] M.H. Sadd, *Elasticity. Theory, Applications and Numerics.*, Elsevier Academic Press (2005)
- [33] J.P. Zendri *et al.*, *Rev. Sci. Instrum.* Vol. **79**, 033901 (2008)
- [34] C. Zener, *Phys. Rev.* Vol. **53**, 90 (1938)
- [35] X. Liu *et al.*, *J. Appl. Phys.* Vol. **97**, 023524 (2005)
- [36] R.G. Christian, *Vacuum* Vol. **16**, 175 (1966)
- [37] H.B. Callen & T.A. Welton, *Phys. Rev. D* Vol. **83**, 34 (1951)
- [38] R. Kubo, *Rep. Prog. Phys.* Vol. **29**, 255 (1966)
- [39] C. Cohen-Tannoudji, *Quantum mechanics*, Hermann (1998)

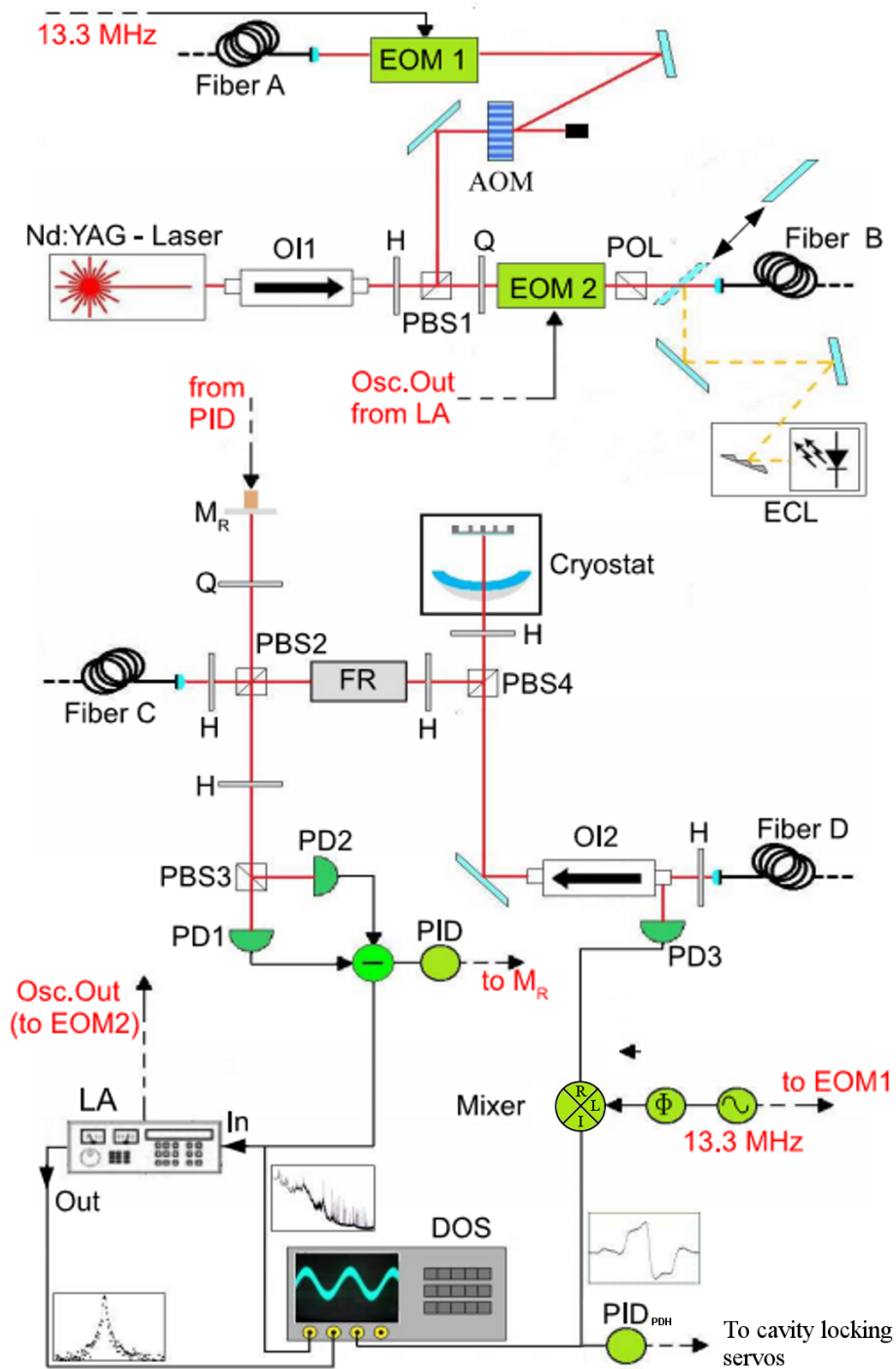
- [40] G.W. Ford, *Phys. Rev. A* Vol. **37**, 4419 (1988)
- [41] A.A. Clerk, *Rev. Mod. Phys.* Vol. **82**, 1155 (2010)
- [42] V.A. Giovannetti & D. Vitali, *Phys. Rev. A* Vol. **63**, 023812 (2001)
- [43] M. Born & E. Wolf, *Principles of Optics*, Pergamon, New York (1965)
- [44] H. Kogelnik & T. Li, *Appl. Opt.* Vol. **5**, 1550 (1966)
- [45] O. Svelto, *Principles of Laser*, Plenum Press, New York (1998)
- [46] D.F. Walls & G.J. Milburn, *Quantum Optics*, Springer, (1993)
- [47] R.J. Glauber, *Phys. Rev.* Vol. **131**, 2766 (1963)
- [48] E. Wigner, *Prog. in Opt.* Vol. **30**, 1 (1992)
- [49] R.E. Slusher *et al.*, *Phys. Rev. Lett.* Vol. **55**, 2409 (1985)
- [50] M.J. Collet & C.W. Gardiner, *Phys. Rev. A* Vol. **30**, 1386 (1984)
- [51] M.J. Collet & C.W. Gardiner, *Phys. Rev. A* Vol. **31**, 3761 (1985)
- [52] C.K. Law, *Phys. Rev. A* Vol. **51**, 2537 (1995)
- [53] F. Marino, *et al.* *Phys. Rev. Lett.* Vol. **98**, 074104 (2007)
- [54] V.B. Braginsky *et al.*, *Phys. Lett. A*, Vol. **232**, 340 (1997)
- [55] B.S. Sheard *et al.*, *Phys. Rev. A*, Vol. **69**, 051801(R) (2004)
- [56] O. Arcizet *et al.*, *Nature* Vol. **444**, 71 (2006)
- [57] F. Marquardt, *et al.* *Phys. Rev. Lett.* Vol. **99**, 093902 (2007)
- [58] R.V. Pound, *Rev. Sci. Instr.* Vol. **17**, 460 (1946)
- [59] R.W.P. Drever, J.L. Hall *et al.*, *Appl. Phys. B* Vol. **31**, 97 (1983)
- [60] F. Marino *et al.*, *Phys. Rev. Lett.* Vol. **104**, 073601 (2010)
- [61] O. Arcizet *et al.*, *New J. Phys.* Vol. **10**, 125021 (2008)
- [62] T. Klitstener *et al.*, *Phys. Rev. B* Vol. **38**, 7576 (1988)
- [63] P. Mohanty *et al.*, *Phys. Rev. B* Vol. **66**, 085416 (2002)

- [64] K. Yamamoto *et al.*, *Phys. Rev. D* Vol. **74**, 022002 (2006)
- [65] A. Grib *et al.*, *J. Appl. Phys.* Vol. **107**, 013504 (2010)
- [66] A. Borrielli *et al.*, *J. Micro-mech. Microeng.* Vol. **21**, 065109 (2011)
- [67] S.A. Chandorkar *et al.*, *J. Appl. Phys.* Vol. **105**, 043505 (2009)
- [68] E. Serra *et al.*, *Int. J. Numer. Methods Eng.* Vol. **78**, 671 (2009)
- [69] M.M. Fejer *et al.*, *Phys. Rev. D* Vol. **70**, 082003 (2004)
- [70] D.F. McGuigan *et al.*, *J. Low Temp. Phys.* Vol. **30**, 621 (1978)
- [71] L. Khine and M. Palaniapan, *J. Micro-mech. Microeng.* Vol. **19**, 015017 (2009)
- [72] D.R.M. Crooks and M. Palaniapan, *Class. Quantum Grav.* Vol. **27**, 084030 (2010)
- [73] F. Ladouceur, *J. Light Technol.* Vol. **15**, 1020-5 (1997)
- [74] D.Z. Anderson *et al.*, *Appl. Opt.* Vol. **23**, 1238-45 (1984)
- [75] H. Davies *et al.*, *Proceedings of the IEE - Part IV: Institution Monographs* Vol. **101**, 209-214 (1954)
- [76] C.L. Spiel *et al.*, *Rev. Sci. Instrum.* Vol. **72**, 1482 (2001)
- [77] K. An *et al.*, *Int. J. Numer. Methods Eng.* Vol. **78**, 671-691 (2009)
- [78] A. Farsi *et al.*, *J. Appl. Phys.* Vol. **111**, 043101 (2012)
- [79] L. Conti *et al.*, *Class. Quantum Grav.* Vol. **27**, 084032 (2010)
- [80] T.J. Kippenberg *et al.*, *Science* Vol. **321**, 1172 (2008)
- [81] F. Marquardt and S.M. Girvin, *Physics* Vol. **2**, 40 (2009)
- [82] I. Favero and K. Karrai, *Nature Photon.* Vol. **3**, 201 (2009)
- [83] G.X. Mack and A.C. Anderson, *Phys. Rev. B* Vol. **31**, 1102 (1985)
- [84] B.L. Zink and F. Hellman, *Solid State Commun.* Vol. **129**, 199 (2004)
- [85] G.W. Gardner and A.C. Anderson, *Phys. Rev. B* Vol. **23**, 474 (1981)
- [86] N. Chaudhuri *et al.*, *Phys. Rev. B* Vol. **8**, 4668 (1973)

- [87] I. Tittoonen *et al.*, *Phys. Rev. a* Vol. **59**, 1038 (1999)
- [88] D. Kleckner and D. Bouwmeester, *Nature* Vol. **444**, 75 (2006)
- [89] G.D. Cole *et al.*, *Appl. Phys. Lett.* Vol. **92**, 261108 (2008)
- [90] S. Groeblacher *et al.*, *Nature* Vol. **460**, 724 (2009)
- [91] S. Gröblacher *et al.*, *Nature Phys* Vol. **5**, 485 (2009)
- [92] D. Brodoceanu *et al.*, *Appl. Phys. Lett.* Vol. **97**, 041104 (2010)
- [93] G.D. Cole *et al.*, *Proc. IEEE 23rd Int. Conf. on Microelectromechanical Systems* p 847(2010)
- [94] P. Verlot *et al.*, *Phys. Rev. Lett.* Vol. **104**, 133602 (2010)
- [95] D. Kleckner *et al.*, *Opt. Express* Vol. **19**, 19708 (2011)
- [96] P-F. Cohadon *private communication*(2013)
- [97] H.J. Kimble *et al.*, *Phys. Rev. D* Vol. **65**, 022002 (2001)
- [98] A. Buonanno and Y. Chen, *Phys. Rev. D* Vol. **64**, 042006 (2001)
- [99] L. Conti *et al.*, *Appl. Opt.* Vol. **39**, 5732 (2000)
- [100] L. Conti *et al.*, *J. Opt. Soc. Am. B* Vol. **20**, 462 (2003)
- [101] P. Verlot *et al.*, *Com. Ren. Phys.* Vol. **12**, 826 (2011)
- [102] C. Genes *et al.*, *Adv. At. Mol. Opt. Phys.* Vol. **57**, 33 (2009)
- [103] A. Jöckel *et al.*, *Appl. Phys. Lett.* Vol. **99**, 143109 (2011)
- [104] D. Antonio *et al.*, *Nature Commun.*, Vol. **3**, 806 (2012)
- [105] E. Gavartin *et al.*, *Nature Commun.*, Vol. **4**, 3860 (2013)
- [106] A.N. Kolmogorov, *Bull. Acad. Sci. U.S.S.R. Scr. Math.* Vol. **5**, 3 (1941)
- [107] N. Wiener *Extrapolation, Interpolation, and Smoothing of stationary Time Series*, The MIT Press, Cambridge, Wiley and Sons, New York, Chapman and Hall, London (1949)
- [108] S. Gigan *et al.*, *Nature* Vol. **444**, 67 (2006)

- [109] P. Astone *et al.*, *Rev. Sci. Instrum.*, Vol. **61**, 3899 (1990)
- [110] E. Gavartin *et al.*, *Nature Nanotech.*, Vol. **7**, 509 (2012)
- [111] J. Tamayo, *J. App. Phys.*, Vol. **97**, 044903 (2005)
- [112] A. Vinante *et al.*, *Nature Nanotech.*, Vol. **8**, 470 (2013)
- [113] G.I. Harris *et al.*, *Phy. Rev. Lett.*, Vol. **111**, 103603 (2013)
- [114] J.S. Bendat and A.G. Piersol, *Random Data: Analysis and Measurement Procedures*, Wiley, New York (2010)
- [115] D.W. Allan, *Proceedings of the IEEE*, Vol. **54**, 221 (1966)
- [116] A.D. O'Connell *et al.*, *Nature*, Vol. **464**, 697 (2010)
- [117] J.D. Teufel *et al.*, *Nature*, Vol. **475**, 359 (2011)
- [118] E. Verhagen *et al.*, *Nature*, Vol. **482**, 63 (2012)
- [119] T.P. Purdy *et al.*, *New J. Phys.*, Vol. **14**, 115021 (2012)
- [120] A.H. Safavi-Naeini *et al.*, *Phys. Rev. Lett.*, Vol. **108**, 033602 (2012)
- [121] V.B. Braginsky *et al.*, *Science*, Vol. **209**, 547 (1980)
- [122] A.A. Clerk *et al.*, *New J. Phys.*, Vol. **10**, 095010 (2008)
- [123] J.B. Hertzberg *et al.*, *Nature Phys.*, Vol. **6**, 213 (2009)
- [124] M.R. Vanner *et al.*, *Nat. Commun.*, Vol. **4**, 2295 (2013)
- [125] D. Rugar and P. Grütter, *Phys. Rev. Lett.*, Vol. **67**, 699 (1991)
- [126] T. Briant *et al.*, *Eur. Phys. J. D*, Vol. **22**, 131 (2003)
- [127] A. Szorkovszky *et al.*, *Phys. Rev. Lett.*, Vol. **107**, 213603 (2011)
- [128] A. Szorkovszky *et al.*, *New J. Phys.*, Vol. **14**, 09526 (2012)
- [129] A. Szorkovszky *et al.*, *Phys. Rev. Lett.*, Vol. **110**, 184301 (2013)
- [130] L.D. Landau and E.M. Lifshitz, *Mechanics*, chap. 5, page 80(Pergamon Press, Oxford,1976)
- [131] A. Kronwald *et al.*, *arXiv:1307.5309*, (2013)

- [132] F.A.M. de Oliveira and P.L. Knight, *Phys. Rev. Lett.*, Vol. **61**, 830 (1988)
- [133] R. Paschotta *et al.*, *Phys. Rev. Lett.*, Vol. **72**, 3807 (1994)
- [134] R. Loudon, *The Quantum Theory of Light*, Oxford University Press (2000)
- [135] B. Friedland *Control System Design: An Introduction to State Space Methods*, McGraw Hill (1986)
- [136] G.F. Franklin *et al.* *Feedback Control of Dynamic Systems* , Addison-Wesley, Reading, Massachusetts (1987)
- [137] T. Day *Frequency Stabilized Solid State Lasers for Coherent Optical Communications* , Ph.D. thesis, Stanford University (1990)



Typical basic scheme of the experimental apparatus. Optical isolator (OI); acousto-optic modulator (AOM); electro-optic modulator (EOM); half-wave plate (H); quarter-wave plate (Q); polarizing beam splitter (PBS); polarizer (POL); extended-cavity diode laser (ECL); electromagnetically driven mirror ( $M_R$ ); Faraday rotator (FR); photodiode (PD); servo-loop electronics (PID); Lock-in amplifier (LA); digital scope and acquisition system (DOS); delay line for phase control ( $\Phi$ ). Black lines indicate the electronic part of the setup.